University of Bath

UNIVERSITY OF BATH

PHD

An Experimental Study of Gas Turbine Rim Seals

Scobie, James

Award date:
2014

Awarding institution:
University of Bath

[Link to publication](#)

An Experimental Study of Gas Turbine Rim Seals

James Andrew Scobie

A thesis submitted for the degree of Doctor of Philosophy

University of Bath

Department of Mechanical Engineering

May 2014

Abstract

Gas turbines are one of the most widely-used power generating technologies in the world today. In the face of climate change and continued global financial pressures placed on industries, one of the biggest challenges facing engine designers is how to continually improve turbine efficiencies.

Rim seals are fitted in gas turbines at the periphery of the wheel-space formed between rotor discs and their adjacent casings. These seals reduce the ingestion of hot gases that can cause catastrophic damage to some of the most highly stressed components in the engine. In gas turbine engines this ingestion is principally caused by circumferential pressure asymmetries in the mainstream annulus, radially outward of the rim seal. A superposed sealant flow, bled from the compressor, is used to reduce or, at the limit, prevent ingestion. As the use of this sealing air can reduce the cycle efficiency, it is important to know how much flow is required to prevent ingestion and to understand the associated fluid dynamics and heat transfer when ingestion occurs.

This thesis presents experimental results from a specifically designed research facility which models an axial turbine stage with generic, but engine-representative, rim seals. The test section featured stator vanes and symmetrical rotor blades. Measurements of pressure, CO_2 gas concentration and swirl ratio are used to assess the performance of different seal designs. Although the ingestion through the rim seal is a consequence of an unsteady, three-dimensional flow field, and the cause-effect relationship between pressure and the sealing effectiveness is complex, the experimental data is shown to be successfully calculated by simple effectiveness equations developed from a theoretical orifice model.

Effectiveness data were collected at the design condition for a datum radial-clearance single seal, and compared with a double overlap equivalent and a further derivative with a series of radial fins. The benefit of using double rim seal configurations was demonstrated, where the ingested fluid was shown to be predominately confined to the outer wheel-space between the two sets of seals. The radial fins increased the level of swirl in this outer wheel-space, rotating the captive fluid with near solid body rotation. This improved the attenuation of the pressure asymmetry which governs the ingress, and improved the performance of the inner geometry of the seal. A criterion for ranking the performance the different seals was proposed, and a performance limit was established for double seals, in which the inner seal is exposed to rotationally induced ingress only.

Experiments were also performed at off-design conditions, where the effect on ingress of varying the flow coefficient (C_F) was demonstrated for both under-speed and over-speed conditions. The correlated effectiveness curves were used to predict the required levels of sealant flow to prevent ingestion, and the variation with C_F was in mainly good agreement with the theoretical curve for combined ingress, which covers the transition from rotationally induced to externally induced ingress. Departure of the measured values from the theoretical curve occurred at very low values of C_F for all the seals tested. This was attributed to flow separation at large deviation angles between the flow and the symmetric turbine blades.

The effectiveness measurements determined from gas concentration were then used to establish a new effectiveness based on pressure. A hypothetical location on the vane platform was assumed to exist where the measured pressures would ensure consistency between the two definitions. Experimental measurements for a radial clearance seal showed that as predicted, the normalised pressure difference across the seal at this location was linearly related to the pressure difference at an arbitrary location on the vane platform. When compared to the original concentration effectiveness measurements, good agreement was found with the values of effectiveness determined by the theoretical pressure model. It was shown in principle how parameters obtained from measurements of pressure and concentration in a rig could be used to calculate the sealing effectiveness in an engine.

The design of a novel 1.5-stage facility, complete with representative turned rotor blades, is then described. The rig experimentally models hot gas ingestion in a downstream, as well as an upstream wheel-space. The methodology behind the design process was outlined, and details were given on the proposed design operating conditions. Experience gained from conducting experiments in the previous facility heavily influenced the design of the new rig. The instrumentation capabilities have been summarised and an explanation of the intended measurements given.

Acknowledgements

Contents

List of figures

List of tables

Nomenclature

Symbols

A	area
b	characteristic radius of seal
B	constant
c	concentration; chord length
C	resultant velocity at exit from vanes; constant
$C_{d,e}\ C_{d,i}$	discharge coefficients for egress, ingress
C_F	flow coefficient $[\ = W/\Omega b\ ]$
c_p	specific heat
C_p	pressure coefficient $[\ = (p - \bar{p})/(^1\!/_2\,\rho\Omega^2 b^2)\ ]$
C_w	non-dimensional flow rate $[\ = \dot{m}/\mu b\ ]$
$C_{w,i}$	non-dimensional ingress flow rate
$C_{w,0}$	non-dimensional sealing flow rate
$C_{w,min}$	minimum value of $C_{w,o}$ to prevent ingress
$C_{\beta 1}$	modified internal swirl ratio $[\ = \beta_1^2/(1-r_1^2/r_2^2)\ ]$
e	imbalance offset
E	modulus of elasticity
F	force
g	normalized pressure difference across seal clearance $[\ = (p_1-p_{2min})/\Delta p\ ]$
g^*	value of g when $C_{w,0} = 0$
$\hat{g}$	value of g to ensure $\varepsilon_p = \varepsilon_c$
G	gap ratio $[\ = S/b\ ]$
G_c	seal-clearance ratio $[\ = s_c/b\ ]$
h_{buffer}	depth of buffer cavity
I	second moment of area
$K,\ k_a,\ k_c$	empirical constants
L_e	entrance length
$\dot{m}$	mass flow rate
M	Mach number

p	absolute static pressure
p_0	total pressure
r	radius
Re_w	axial Reynolds number in annulus [$= \rho W b / \mu$]
$Re_w{}^*$	alternative definition of axial Reynolds number in annulus [$= \rho W c_x / \mu$]
Re_ϕ	rotational Reynolds number [$= \rho \Omega b^2 / \mu$]
s	entropy
s_c	seal clearance
$s_{overlap}$	axial overlap of radial clearance seal
S	axial clearance between stator and rotor
T	temperature; torque
U	bulk-mean velocity through rim-seal clearance [$= \dot{m} / 2\pi \rho b s_c$]; linear blade speed
v	Poisson's ratio
V	velocity relative to blades
V_ϕ	tangential component of velocity
W	axial velocity in annulus
W_s	work generated by stage
x	nondimensional axial distance in annulus [$= 2z / s_c$]
z	axial distance
α	vane exit angle
β	blade angle; swirl ratio in wheel-space [$= V_\phi / \Omega r$]
$\beta - \beta_0$	deviation angle
δ	uncertainty; interference
δ^*	displacement thickness of boundary layer
ΔC_p	non-dimensional pressure difference [$= \Delta p / (\frac{1}{2}\rho \Omega^2 b^2)$]
Δp	peak-to-trough pressure difference in annulus [$= p_{max} - p_{min}$]
Γ_c	ratio of discharge coefficients [$= C_{d,i} / C_{d,e}$]
$\Gamma_{\Delta p}$	ratio of driving force for EI and RI ingress [$= \Delta C_p / C_{\beta 1}$]
ε	sealing effectiveness [$= C_{w,0} / C_{w,e} = \Phi_0 / \Phi_e$]
ε_c	concentration effectiveness [$= (c_s - c_a) / (c_o - c_a)$]

ε_p	pressure effectiveness
$\hat{\varepsilon}_p$	value of ε_p equal to ε_c
ζ	similarity parameter
η_s	isentropic efficiency of stage
Φ	non-dimensional sealing parameter [$= C_w / 2\pi G_c Re_\phi$]
Φ_i	value of Φ when $C_w = C_{w,i}$
Φ_{min}	value of Φ when $C_w = C_{w,min}$
Φ_{min}'	value of Φ_0 when $\varepsilon = 0.95$
Φ_0	value of Φ when $C_w = C_{w,0}$
θ	angular coordinate, non-dimensional vane pitch
λ_N	isentropic coefficient of vanes
λ_R	isentropic coefficient of blades
λ_T	turbulent flow parameter [$= C_{w,o} Re_\phi^{-0.8}$]
Λ	degree of reaction [$= (T_2 - T_3) / (T_1 - T_3)$]
μ	dynamic viscosity
ρ	density
σ	standard deviation
χ	similarity parameter
ψ	blade loading coefficient [$= 2c_p \Delta T_0 / U^2$]
Ω	angular velocity of rotating disc

Subscripts

a	annulus
ax	axial
A	location A on vane platform in annulus
c	concentration
CI	combined ingress
e	egress
EI	externally-induced ingress
i	ingress; inner
max	maximum

min	minimum
o	outer
rad	radial
RI	rotationally-induced ingress
s	stator
0	superposed flow; design condition
1,2	locations in wheel-space and annulus
ϕ	angular coordinate

Superscripts

$^-$	average value
$+$	value for upper 95% uncertainty limit
$-$	value for lower 95% uncertainty limit
$*$	value with zero ingress
'	value at $\varepsilon_c = 0.95$

Chapter 1: Introduction

1.1 History of the gas turbine

In 1791 British coalmaster and inventor John Barber filed a patent for a gas turbine entitled "A method of Rising Inflammable Air for the Purposes of Procuring Motion". Working fluid was produced from heated coal mixed with air, which was compressed and then burnt. This produced a high speed jet that impinged on radial blades located on a turbine wheel rim (Figure 1.1). Unfortunately due to the technological restrictions of the time, nothing practical ever came of his patent. However Barber was credited as the first man to describe in detail the principle behind the modern day gas turbine.
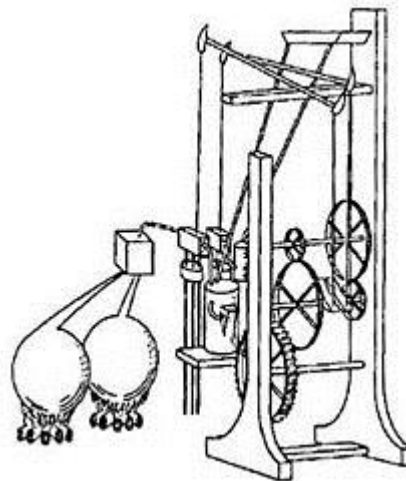
Figure 1.1: Sketch from John Barber's patent (1791)

For the next century development was focused on the reciprocating steam engine, and efforts were made to improve the efficiency of the steam process. In around 1850 Ferdinand Redtenbacher, regarded by many as the founder of scientific mechanical engineering, wrote to German physicist and leading expert in technical thermodynamics at the time, Gustav Zeuner stating:

"The fundamental principle of the generation and use of steam is wrong. It is hoped steam engines will disappear in a not far distant future, as soon as we know more about the nature and effects of heat."

In the early 1900's, various engineers across Europe worked independently to develop a practically functioning gas turbine, as previously described theoretically by John Barber.

One of the biggest challenges that existed was the design of an efficient compressor to raise the pressure of the air. The efficiency of turbo compressors available at the time was simply too low to make gas turbines designs feasible.

Franz Stolze in Germany took out a patent in 1872 featuring the first multi-stage axial flow compressor driven by a multi-stage reaction turbine. The 'fire turbine' was the first gas turbine to be built and tested between 1900 and 1904 with limited success; the cycle thermal efficiency was too low as the compressor consumed the majority of the energy produced by the turbine.

In 1903, Rene Armengaud and Charles Lemale also built and successfully tested the first of several experimental gas turbines with internally water cooled discs and blades. Their design featured a Rateau rotary compressor and a Curtis stage impulse turbine. However the operational efficiency of their early power turbine was limited to less than three percent.

German engineer Hans Holzwarth attempted to get around the compression problem by developing a design that worked using a constant volume, or isochoric process. Similar to an internal combustion engine, valves were used to supply air to a closed combustion chamber featuring spark plugs, then expanded through a 2-stage Curtis turbine. The design, developed in 1905 was the first large scale industrially usable gas turbine. Although in theory the turbine was expected to deliver 1000 hp, large heat losses resulted in this value being closer to 200 hp.

The Swiss company Brown, Boveri & Cie (BBC) took up the manufacture of an advanced Holzwarth gas turbine in 1928. The first unit went into operation in 1933 at a German steel plant with blast furnace exhaust gas used as fuel (Figure 1.2). However the success of the constant volume gas turbine was short lived; with the improvement of axial flow compressors, constant pressure (isobaric) gas turbines with continuous combustion prevailed due to their significant advantages.
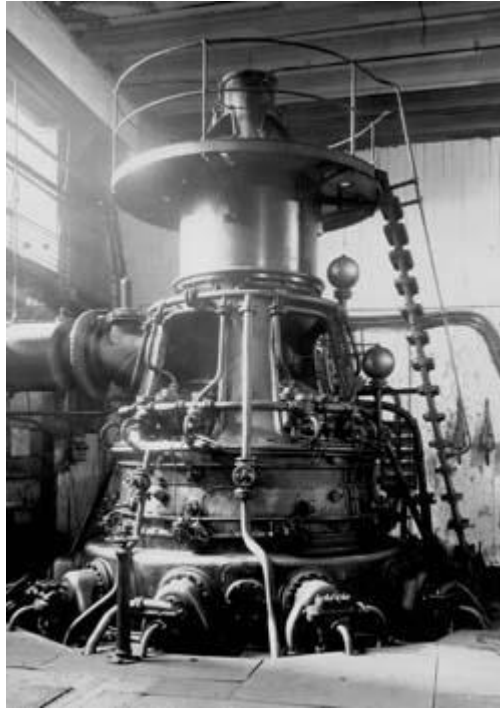
Figure 1.2: Holzwarth gas turbine in operation at Thyssen & Co 1933

In 1939, the director of Brown Boveri, Dr Adolf Meyer presented a paper on "The Combustion Gas Turbine: Its History, Developments and Prospects" to the Institution of Mechanical Engineers in London. In his address, Dr Meyer foresaw the numerous future applications for the gas turbine and also predicted the benefits of a combined cycle gas turbine steam plant. A dominant role for the development of cooling technology, high temperature materials, and turbine aerodynamics was outlined.

This presentation coincided with the introduction of the first practical, commercially used industrial gas turbine for electric power generation. Built by BBC, it was situated in Neuchâtel, Switzerland. The design featured an axial compressor, axial turbine and generator arranged in line and coupled along a common shaft, a concept similar to that of today's modern gas turbines. The turbine had a power output of 4 MW at the generator terminals, and a thermal efficiency of 17.4%. The plant stayed operational for 63 years, serving as a standby unit until 2002 when after 1,908 cycles a damaged generator unit finally caused its withdrawal from service. In 1988 ASME designated it an International Historic Mechanical Engineering Landmark. Today it is on display in Birr, Switzerland near the Alstom R&D site (Figure 1.3).

Figure 1.3: The world's first industrial gas turbine, GT Neuchâtel 1939 – ASME (2007)

The development of the gas turbine aero-engine took place in parallel with their stationary counterparts. In the early days of powered flight, piston engines were predominately used to power propeller driven aircraft. However, military designers in the 1930s soon realised that their aircraft were limited both in velocity and maximum altitude. The competing mechanism of using larger engines to produce more power whilst increasing the weight of the aircraft resulted in maximum speeds of around 350 mph. Attempts to spin propellers faster came up against compressibility effects as the tips approached the speed of sound, and climbing in altitude was limited as the decreased density reduced both engine and propeller efficiency.

Sir Frank Whittle and Dr Hans Von Ohain are jointly credited with independently inventing the jet engine. It was Whittle in 1930 that first realised that the future of aircraft propulsion would require a new power-plant capable of forcibly expelling air through an exhaust. However he received no support from the British Air Ministry, who deemed his design unworkable. Whittle persisted and filed a patent entitled "Improvements in Aircraft Propulsion", featuring a compound axial centrifugal compressor and a single stage axial turbine. It was not until 1937 that Whittle's work was realised through public financing for his company, Power Jets Ltd. The W.1 eventually flew in the Gloster E.28/39 in May, 1941.

Meanwhile in Germany, Von Ohain had put forward his idea for a turbojet engine, similar to Whittle's design, in 1935. His engine, named the HeS 3B, was built by aircraft manufacturer Ernst Heinkel to power the He 178 aircraft. This resulted in the first jet-powered flight taking place in Germany in August, 1939, exactly one week before the outbreak of the Second World War. Von Ohain's work influenced the world's first

operational production turbojet, the Junkers JUMO 004 which powered the Messerschmitt Me 262.

Hunt (2011) presents a detailed account of the history of the industrial gas turbine from 1940 to 1990. The first industrial gas turbine to run in the United Kingdom was in 1945. The 500 bhp experimental machine was built by C A Parsons, the company behind the modern steam turbine. Westinghouse made significant contributions to the development of the industrial gas turbine in the United States, including the first combustion turbine used commercially. The W21 was installed in 1949 at the Mississippi River Fuel Corporation and was fuelled by natural gas. It became the world's first engine to operate for more than 100,000 hours.

In 1950, Siemens obtained permission from the Allied Control Council to resume development of gas turbines. The first Siemens gas turbine was named VM 1, VM for the German word "verbrennungsmaschine" meaning combustion engine. It was designed for an output of 1.5 MW and the compressor shared many similar features with the JUMO 004.

Driakunchak *et al.* (2011) and Hunt (2011) describe the Siemens VM 5 as the world first truly commercial gas turbine. Shown in Figure 1.4, the 5.4 MW gas turbine was installed in 1958 at the Dortmund-Horder-Hutten-Union smelting plant. With uncooled turbine blading, turbine inlet temperatures were limited to 700°C, resulting in an efficiency of 29%.
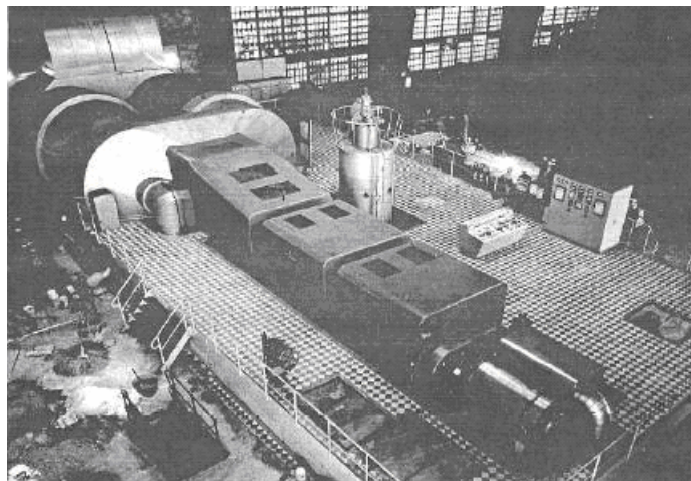
Figure 1.4: Siemens VM 5 blast furnace gas turbine

Improvements continued into the 1960's when Siemens decided to build what was then the largest single-shaft gas turbine in the world. The VM 80 had a mass flow rate of 184 kg/s and a pressure ratio of 6:1, generating 23.4 MW at an efficiency of 32%. It commenced

commercial operation in 1962 acting as a peaking plant and supplying district heating to the city of Munich.

The Westinghouse 501 series of heavy duty gas turbine engines were developed from 1968 up to 1998. During this period, power output increased from 45 to 249 MW as turbine entry temperature was raised from 963 to 1500°C through advances in turbine cooling. Combined cycle configurations allowed efficiencies of up to 58% to be realised. Similar advancements were made at both Siemens and GE during the same timeframe. Siemens purchased the Westinghouse turbine business in 1998, consolidating the engine programmes under one common nomenclature.

Recently, the Siemens SGT5-8000H (Figure 1.5) set the record for the most powerful gas turbine in the world. Rated at a gross power output of 375 MW in simple cycle operation and 570 MW in combined cycle, the power plant can achieve a combined cycle efficiency of 60.75%.
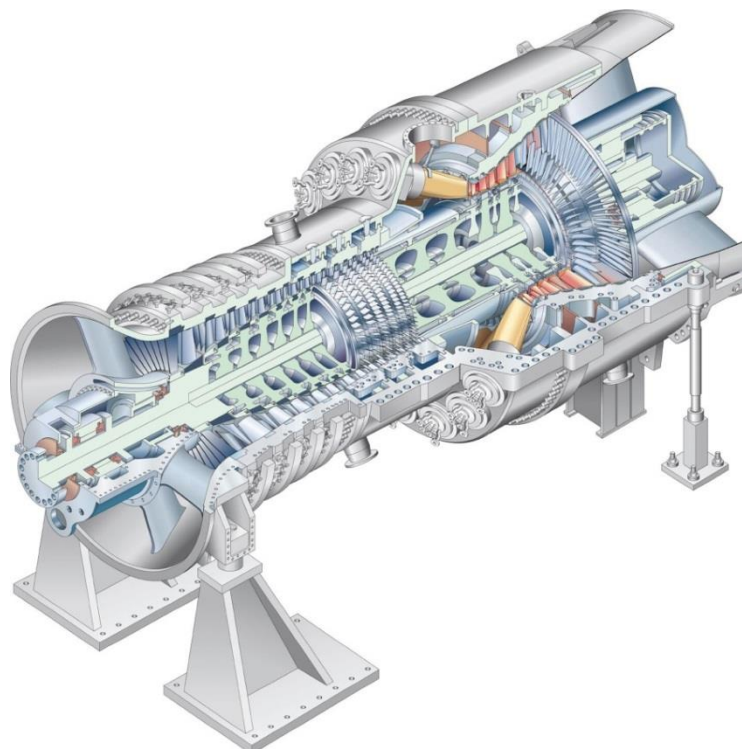
Figure 1.5: Siemens SGT5-8000H gas turbine engine

1.2 Industrial Gas Turbine Applications

Today gas turbines have developed into one of the most proven and reliable power generation technologies. The lower weight and size per unit of power output gives the gas turbine significant advantages in comparison to other power generation devices. Gas turbines used for producing shaft power fall into two main categories, heavy frame and aero-derivative engines:

Heavy frame engines are physically large power generation units ranging from 3 to 375 MW in simple cycle configuration, with typical efficiencies from 30 to 48%. They are used in applications where space and weight restrictions are not an issue. The advantages of heavy frame gas turbines are long life, high availability, and slightly higher efficiencies in comparison to aero-derivate equivalents. They are characterised by low pressure ratios (usually below 20:1) and low noise levels. When coupled to a steam turbine and operated in combined cycle configuration, thermal efficiencies of greater than 60% are achievable.

Aero-derivative engines are adapted for electrical generation by removing the bypass fan and adding a power turbine at the exhaust. Typical power ranges are from 2.5 to 50 MW and efficiencies from 35 to 45%. The ability to start-up, shut down and handle load changes more quickly than industrial machines is one of their biggest advantages. They are also more compact and useful for smaller power outputs. Whilst they produce fewer emissions than other gas turbines due to design restrictions, they tend to operate using more expensive fuels.

In single spool gas turbines, power can be extracted mechanically from an output shaft, either at the front (cold) or the rear (hot) end of the turbine, and used to drive an electrical generator. These engines operate at either 3000 or 3600 rpm to match either 50 or 60 Hz generators. Alternatively a free power turbine coupled aerodynamically at the rear of the engine can be used. This configuration allows for easier starts on the turbine components, as the power turbine can be allowed to run at different speeds to the gas generator. This has a significant impact on off-design performance, allowing far greater flexibility in output speed at a given power.

Power generation turbines for supply to national grid systems are categorised in three ways, depending on their utilization:

Peak loppers (peaking power plants) have low utilization, typically less than 10%. They are employed to satisfy the peak demand for electrical power. Unit cost is crucial, response time onto full load is very important and thermal efficiency is relatively unimportant. For this reason simple gas turbine cycles burning natural gas or diesel are usually employed in

this role. Peak loppers can be single spool or free power turbine, aero-derivative or heavy frame type.

Base load power plants achieve as near to 100% utilization as possible to supply the continuous demand for electrical power. The emergence of the combined gas and steam cycle in the 1960's has enabled the gas turbine to be considered as a primary power generator. Gas turbines are used in combined cycle configuration for maximum possible thermal efficiency; start and acceleration times are therefore unimportant. They compete with coal and nuclear fired steam plants, where the availability of natural gas and lower emissions has made them ever more increasingly popular.

Mid merit (intermediate) power stations have typically 30-50% utilisation and serve the extra requirement for electrical power which is seasonal, typically in the winter period where demand increases for domestic heating and lighting. They employ simple cycle gas turbines of a higher technology level than those used for peak lopping. The higher unit cost is justified by higher thermal efficiency, given the higher utilisation. Most engines are aero-derivative adjusted for optimum simple cycle thermal efficiency.

Gas turbines are also extensively found in pipeline pumping and compression applications in some of the harshest environments in the world. Turbines operating on natural gas pipelines can typically consume 7 to 10% of the fluid being pumped as fuel, tapped off the pipeline itself.

In addition, gas turbine engines have been successfully used for marine propulsion applications. In 1967, the Royal Navy took the strategic decision that all future propulsion of their warships would be gas turbine based. The new Queen Elizabeth-class aircraft carriers currently under construction will be principally powered by two Rolls-Royce Marine Trent 36 MW gas turbine generators.

1.3 Gas Turbine Theory
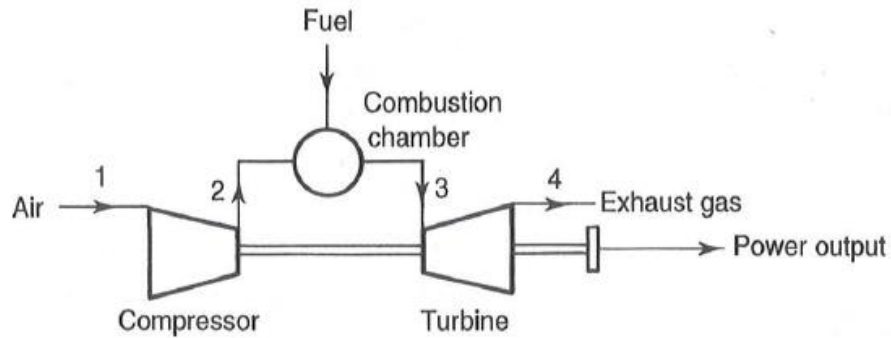
Figure 1.6: Simple gas turbine system - adapted from Saravanamuttoo *et al.* (2001)

A simple gas turbine system is depicted graphically in Figure 1.6. The working fluid is first accelerated through a compressor raising the pressure of the flow. In an ideal system this process is isentropic, where no energy is lost to heat due to friction and aerodynamic losses. The addition of energy in the form of fuel then takes place in the combustion chamber, where the compressed air is ignited to raise the working temperature. As ideally this occurs at constant pressure, the specific volume of the fluid increases. Expansion of this hot gas through a turbine then allows for work to be extracted, providing useful energy in addition to driving the compressor. Again, ideally this expansion occurs isentropically in the ideal case and the fluid leaves the gas turbine at the same pressure it entered at. The useful energy can either be accelerated through a nozzle to create thrust, as in a turbojet aircraft engine, or used to drive an additional turbine to generate mechanical power or electricity. This process can be described thermodynamically by the Brayton cycle, of which the corresponding *T-s* and *p-v* diagrams are shown in Figure 1.7 (a) and (b).
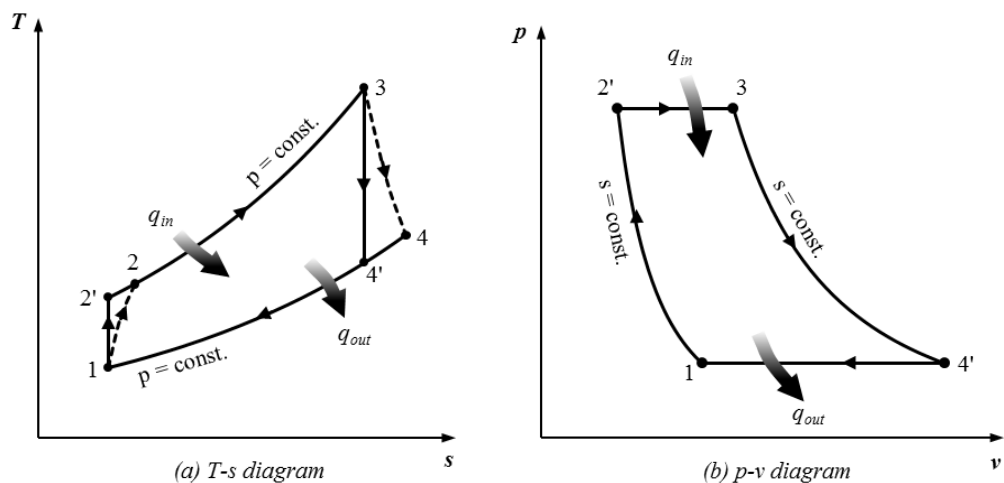
Figure 1.7: Temperature-entropy and pressure-volume plots for Brayton cycle

In reality the compression and expansion process are non-isentropic, resulting in a change in entropy as the fluid flows through the compressor and turbine sections. This is shown in Figure 1.7 (a) by the diagonal dotted lines connecting 1 to 2 and 3 to 4, for the compression and expansion processes respectively.

In the ideal case, the overall efficiency of the gas turbine is primarily dependent upon the pressure ratio of the compressor. However when component losses are taken into account, the cycle efficiency becomes dependent on the turbine entry temperature (TET) as well as pressure ratio, as a result of more work output for the same amount of fuel.

1.4 Internal cooling
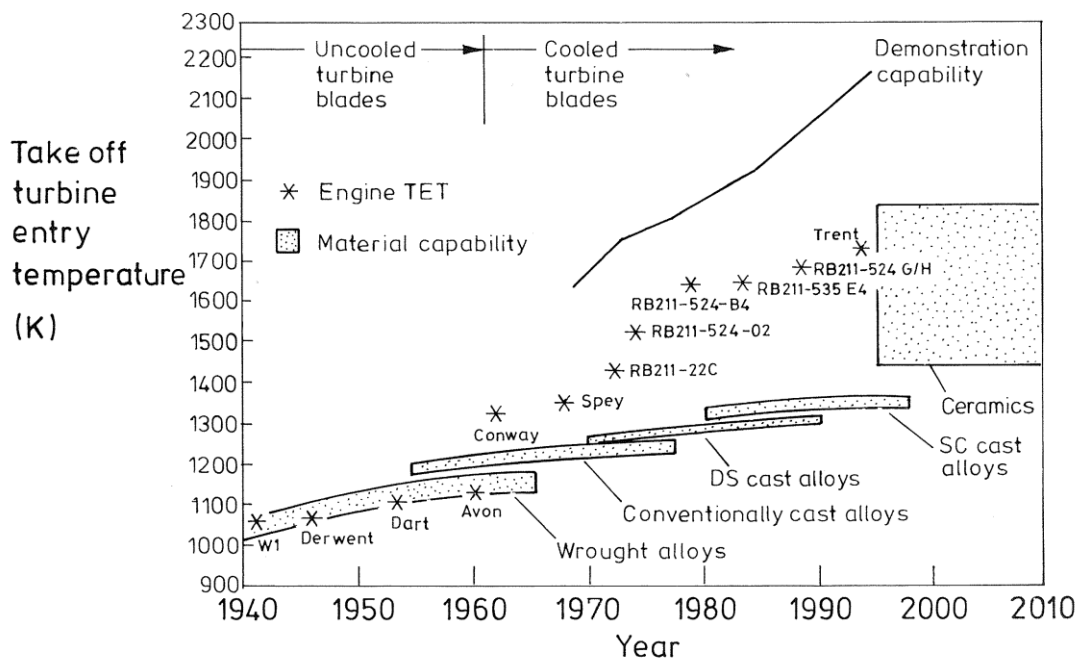
Figure 1.8: The progress of turbine entry temperature for Rolls-Royce engines since 1940 (Cumpsty (2003))

Figure 1.8 illustrates the progress of TET for Rolls-Royce aero engines since 1940. Typical turbine entry temperatures for modern day gas turbines are in excess of 1800 K. This has pushed the limits of metallurgic technology, as even the most advanced single-crystal Nickel alloys used to manufacture turbine blades would melt at 1550 K. In order to reduce temperatures downstream of the combustor to acceptable levels, cooling air is bled

off from the main-gas path at several axial locations upstream in the compressor. A complicated internal network, known as the secondary air system, is used to distribute this relatively cool air (900 K) for sealing and purging of blades, discs, shafts, cavities and bearing chambers. A typical turbine cooling and sealing arrangement is shown in Figure 1.9.
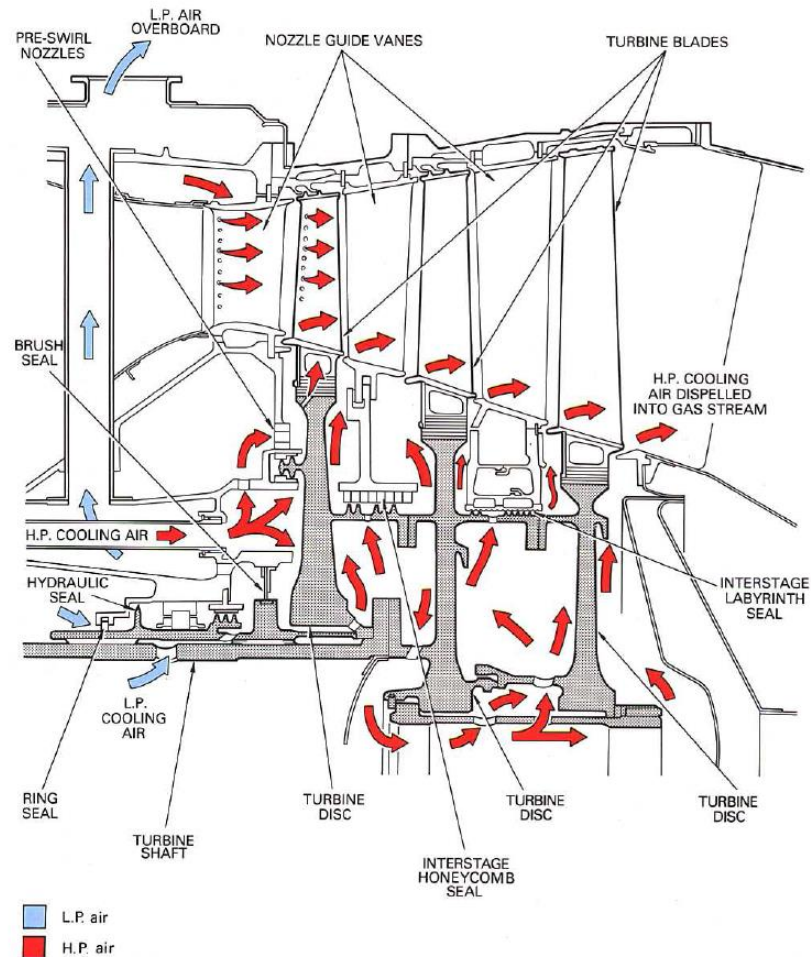
Figure 1.9: Typical turbine cooling and sealing arrangement – Rolls-Royce (1996)

The continued striving for improved gas turbine efficiency and performance has placed an increasing significance on the capability of the secondary air system to manage this *expensive* cooling air in the most effective way. Anywhere between 15 to 25% of the flow through the engine may be bled off for this purpose, in turn reducing the efficiency and specific work output. At a constant TET, the specific fuel consumption (sfc) can be said to increase by about 4% for a 5% increase in cooling flow (Cumpsty (2007)). However the benefits of an increased TET are substantial, even when the additional losses introduced by the cooling system are taken into account.

1.5 Introduction to Ingress

An important function of the secondary air system is to reduce the ingress of hot mainstream gas into the wheel-space between the stationary and rotating discs. This is principally caused by the non-axisymmetric pressure variation as the flow passes over the vanes and blades. This type of ingestion, known as externally-induced (EI) ingress, occurs at the locations where the external pressure in the annulus is greater than that in the wheel-space, as shown in Figure 1.10.
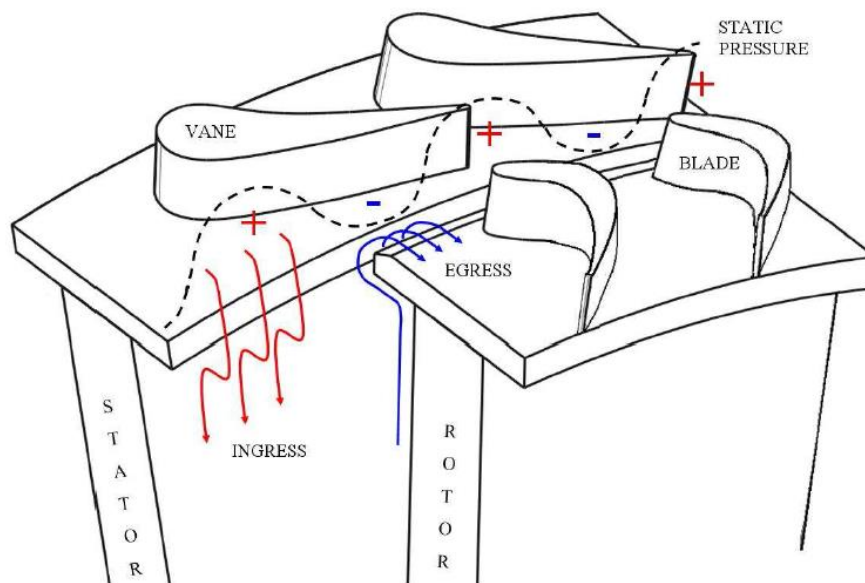
Figure 1.10: Variation of static pressure in the annulus that leads to externally induced ingress

Even if the external flow were axisymmetric however, ingress can still occur due to rotational effects. The rotating fluid in the wheel-space creates a radial pressure gradient which can cause the pressure to drop below that of in the mainstream annulus. This 'disc-pumping effect' causes the egress of fluid near the rotating disc, where the centrifugal effects are greatest. To conserve radial mass flow, ingress of external fluid through the rim seal occurs near the stator disc. This type of ingestion is known as rotationally-induced (RI) ingress.

When the effects of both EI ingress and RI ingress are significant, the term combined ingress (CI) is used. This type of ingestion can be of practical relevance when an engine is operating at 'off-design' conditions.

A non-contacting rim seal, shown in Figure 1.11, is used to reduce the ingested fluid, in conjunction with sealing air supplied from the compressor to pressurise the wheel-space. Too much sealing air will reduce the performance of the turbine through the interaction of the discharging sealing air (known as the egress) and the mainstream gas path, creating aerodynamic losses. Conversely, too little sealing air can cause the overheating of critical components, resulting in disastrous consequences. As noted by Johnson *et al.* (1994), for an advanced 2-stage gas turbine, a 50% reduction in rim seal coolant purge flow could increase turbine efficiency by 0.5%, corresponding to a reduction in sfc of 0.9%.

In terms of internal air systems, the engine designer wants to know the following: the most effective seal geometry; how much sealing air is required to limit ingestion to an acceptable level; when ingress occurs, how much hot gas enters the wheel-space; how this ingested fluid affects the temperatures on the rotating and stationary components.
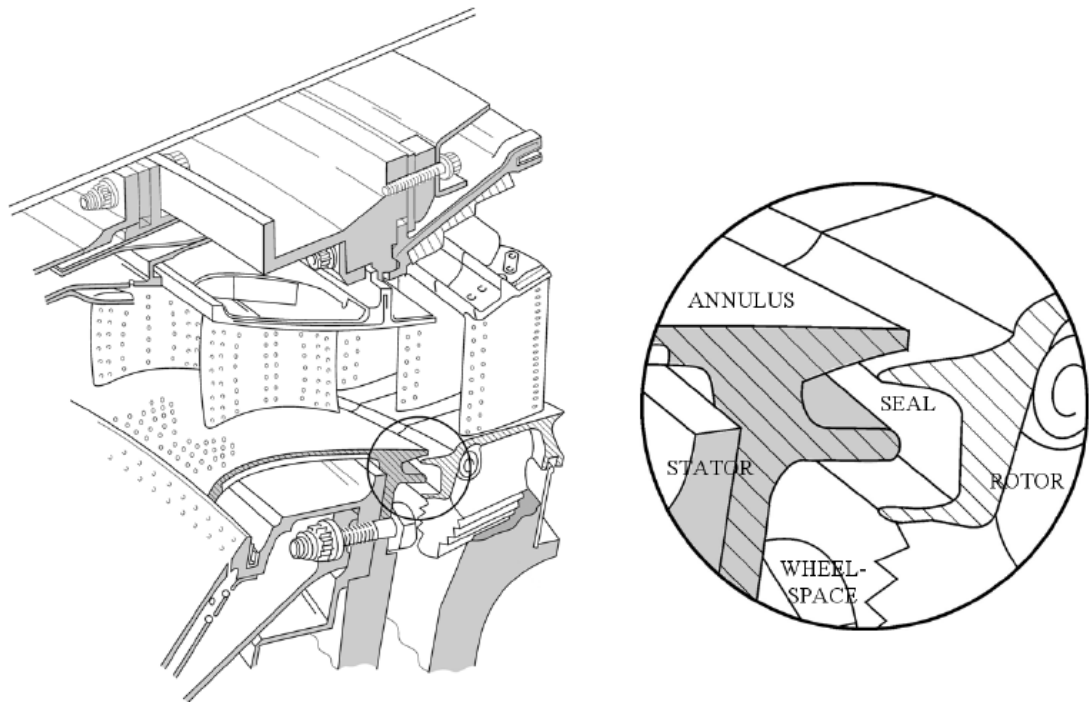
Figure 1.11: Typical rim seal configuration in a high pressure turbine stage

1.6 Thesis Aims

The main experimental aim of this thesis is to measure the sealing characteristics of a series of generic rim-seal geometries, which will better inform the gas turbine engine designer. It is hoped that these experimental measurements will provide a fundamental insight into the ingress problem and inform improvements for future internal air system designs.

The experimental data will allow the engine designer to estimate the initial effect of ingress without the need for extensive computational research. An extensive range of seal effectiveness measurements aimed at better informing the designer will be presented.

The experimental sections of this thesis aim to address the following questions:

- What is the most effective rim seal configuration to help prevent hot gas ingestion into the upstream wheel-space of a gas turbine?

- What is the effect on ingress of varying the flow coefficient from the design condition?

- How can experimental data measured using a test facility be used to inform the design of gas turbine rim seals?

An additional aim of this PhD is the design of a novel 1.5 stage experimental facility. The design methodology, as well as an outline of future experimental measurements, is documented as part of this thesis. The rig was designed as an engine representative model of both the upstream, as well as the downstream wheel-space of a gas turbine, from which experimental correlations could be scaled and applied to a full sized engine. The test facility will allow for detailed investigations into the sealing characteristics and wheel-space fluid dynamics of various generic and company proprietary rim seal configurations.

The rig has been specifically designed to accommodate infrared temperature probes for heat transfer measurements on the rotor surface. This novel approach will enable the effects of ingress on the rotor side of both wheel-spaces to be established.

The addition of turned rotor blades and an energy absorbing dynamometer will allow for more engine representative and engine relevant measurements to be made. A larger mainstream gas path annulus will also enable the interaction of the main and secondary flows to be studied in greater detail. It is envisaged the experimental measurements made using this facility will form the basis for future theses from the University of Bath.

1.7 Thesis Outline

Chapter 1 gives an introduction to the historical development of the industrial gas turbine and their application in the power generation industry. The basic theory and principles behind the operation of a gas turbine is explained, and the hot gas ingestion problem faced by engine designers is introduced. The aims and objectives of this thesis and a list of publications resulting from this work are given.

Chapter 2 provides a review of the current literature relevant to the phenomenon of hot gas ingestion. The fundamental fluid dynamics of a free disc and a rotor-stator cavity are discussed. This is followed by an extensive review of the existing experimental and theoretical research into rotationally-induced, externally-induced and combined ingress. The previous research into ingress conducted at Bath is also considered.

Chapter 3 outlines experimental data collected using the Bath single stage research facility operating at the design condition. Measurements of pressure and effectiveness determined using a CO_2 gas concentration technique, were used to compare the relative performance of three different rim seal configurations. The data were shown to agree well with a previously published theoretical orifice model.

Chapter 4 presents ingestion measurements at off-design conditions, were the flow coefficient in the annulus was varied either side of the design point. The effect on the minimum sealing flow required to seal the wheel-space against ingress was demonstrated for three rim seal designs. The variation of the experimental data was in mainly good agreement with the theoretical curve for combined ingress, which covers the transition from rotationally induced to externally induced ingress.

Chapter 5 presents an alternative definition of effectiveness based on pressure measurements. A theoretical model was developed and validated using experimental data for a radial-clearance seal. It was shown in principle how parameters obtained from measurements of pressure and gas concentration in a rig could be used to calculate the sealing effectiveness in a gas turbine engine.

Chapter 6 describes the design of a novel 1.5 stage facility which experimentally models hot gas ingestion in a downstream, as well as an upstream wheel-space. The rig capability is outlined, and the technical aspects of the design are documented. An explanation of the intended measurements is also provided.

Chapter 7 provides the conclusions of this thesis and recommendations for future research into the ingress problem to be conducted using the new facility.

1.8 Generic versus Confidential Seal Geometries

In addition to the generic seal designs presented in this thesis, many additional geometries were tested that could not be included due to their confidential nature. An extensive series of tests on Siemens complicated seal profiles were omitted as these could not have been published in the open domain without a thesis embargo. However, one set of Siemens proprietary seals, currently under consideration for patent protection, will appear in a future publication.

1.9 Publications

This thesis has produced six publications in total; four conference papers and two journal manuscripts. Two additional papers based on the work of this thesis are expected to be published at the 2015 ASME Turbine Technical Conference in Montreal. These include: (i) a paper based on the design of the 1.5 stage facility (as outlined in Chapter 6), and (ii) a paper on the performance of proprietary rim seals (currently under patent) supported by CFD work of Teuber (2014) at Siemens. Data for (ii) was not included here to avoid a thesis embargo. Two unrelated publications have also been completed during this PhD.

Conference publications:

1. Sangan, C. M., Pountney, O. J., **Scobie, J. A.**, Wilson, M., Owen, J. M. and Lock, G. D., 2012, "Experimental Measurements of Ingestion Through Turbine Rim Seals. Part 3: Single and Double Seals," ASME Paper GT2012-68493.
2. **Scobie, J. A.**, Sangan, C. M., Teuber, R., Pountney, O. J., Owen, J. M., Wilson, M., and Lock, G. D., 2013, "Experimental Measurements of Ingestion Through Turbine Rim Seals. Part 4: Off-Design Conditions," ASME Paper No. GT2013-94147.
3. Sangan, C. M., **Scobie, J.A.**, Owen, J. M., Lock, G. D., Tham, K. M., and Laurello, V. P., 2014, "Performance of a Finned Turbine Rim Seal," ASME Paper GT2014-25626. To appear in ASME Journal.

4. Owen, J. M., Wu, K., **Scobie, J. A.**, Sangan, C. M., Cho, G., and Lock, G. D., 2014, "Use of Pressure Measurements to Determine Effectiveness of Turbine Rim Seals," ASME Paper GT2014-25200. To appear in ASME Journal.

5. **Scobie, J. A.**, Sangan, C. M., and Lock, G. D., 2014, "Flow visualisation experiments on sports balls," To be presented at The Engineering of Sport 10 conference, Sheffield 2014.

Journal publications:

1. Sangan, C. M., Pountney, O. J., **Scobie, J.A.**, Wilson, M., Owen, J. M., and Lock, G. D., 2013, "Experimental Measurements of Ingestion Through Turbine Rim Seals. Part 3: Single and Double Seals," ASME J. Turbomach., 135, p.051011.

2. **Scobie, J. A.**, Sangan, C. M., O. J., Owen, J. M., Wilson, M., and Lock, G. D., 2014, "Experimental measurements of hot gas ingestion through turbine rim seals at off-design conditions," Proc. IMechE Part A: J. Power and Energy, published OnlineFirst on March 25, 2014.

3. **Scobie, J. A.**, Pickering, S. G., Almond, D. P., and Lock, G. D., 2013, "Fluid dynamics of cricket ball swing," Proc. IMechE Part P: J. Sports Engineering and Technology, 227 (3), pp. 196-208.

Chapter 2: Literature Review

This chapter will give a succinct overview of the fluid dynamics found in rotating systems, before moving on to look at the ingress problem in greater detail. The case of rotationally induced ingress is considered, followed by externally induced and combined ingress. A review of the current experimental facilities looking into the ingress problem is provided, along with a summary of the previous ingestion research work carried out at the University of Bath.

2.1 The Free Disc

One of the simplest rotational flow scenarios is a disc spinning with uniform angular velocity (Ω) in free air (Figure 2.1). To satisfy the no-slip condition within the rotor boundary layer, the fluid must accelerate by friction from zero at the free-stream to the tangential disc speed, $V_\phi = \Omega r$, at the surface. The so called 'disc-pumping', caused by the centrifugal forces acting on the fluid leads to a radial outflow, V_r. To satisfy the conservation of mass, it is necessary that fluid is entrained axially (V_z) into the boundary layer to facilitate this radial fluid flow. The flow near the axis of rotation tends to be laminar. For large values of angular velocity the flow can become turbulent even at low radius, and a transition region will exist.
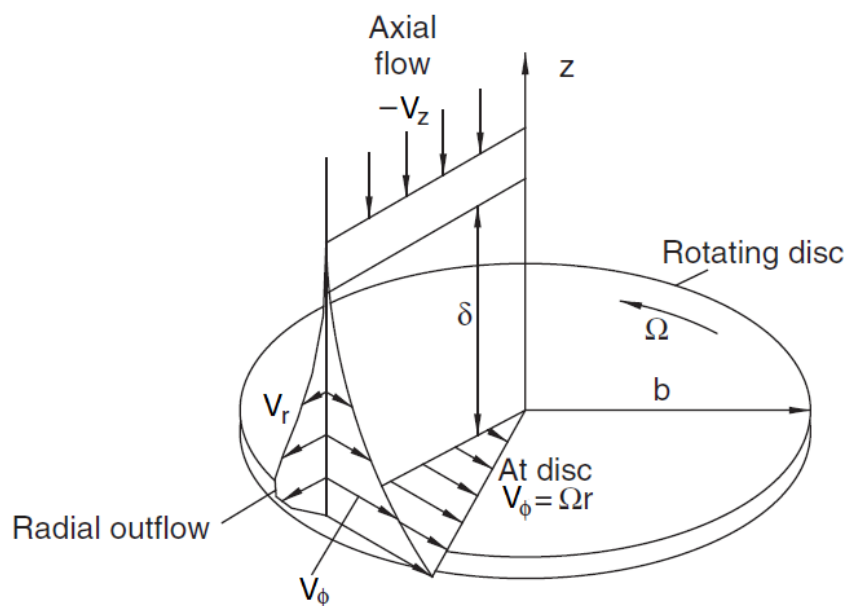
Figure 2.1: Local velocity profiles for a simple disc spinning in free air – adapted from Childs (2011)

2.2 Stationary disc in a rotating fluid

Figure 2.2 shows the local velocity profiles for a stationary disc in a rotating fluid. The flow rotating outside the boundary layer is in equilibrium under the influence of the centrifugal force which results in a radial-pressure gradient. Near the disc surface the tangential velocity, V_ϕ, decreases with a corresponding decrease in the local centrifugal force. The radial pressure gradient causes the flow near the surface to flow radially inwards, and for reasons of continuity this motion is compensated by an axial flow (V_z) away from the surface.
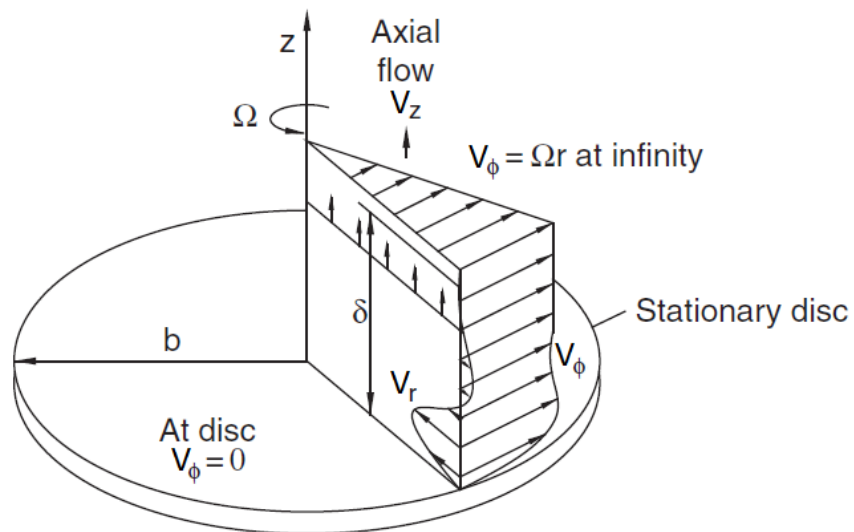
Figure 2.2: Local velocity profiles for a stationary disc in a rotating fluid - adapted from Childs (2011)

2.3 Rotor-Stator Systems

A rotor-stator system consists of a rotating disc and a stationary disc separated by an axial clearance that forms a cavity known as a wheel-space, as shown in Figure 2.3. This type of configuration is commonly found in gas turbines between rotor discs and their adjacent casings. The flow physics of rotor-stator systems is more complex than the individual cases; the characteristics will vary with the proximity of the stator and rotor, the presence of a stationary or rotating shroud, and the supply of any imposed flow.
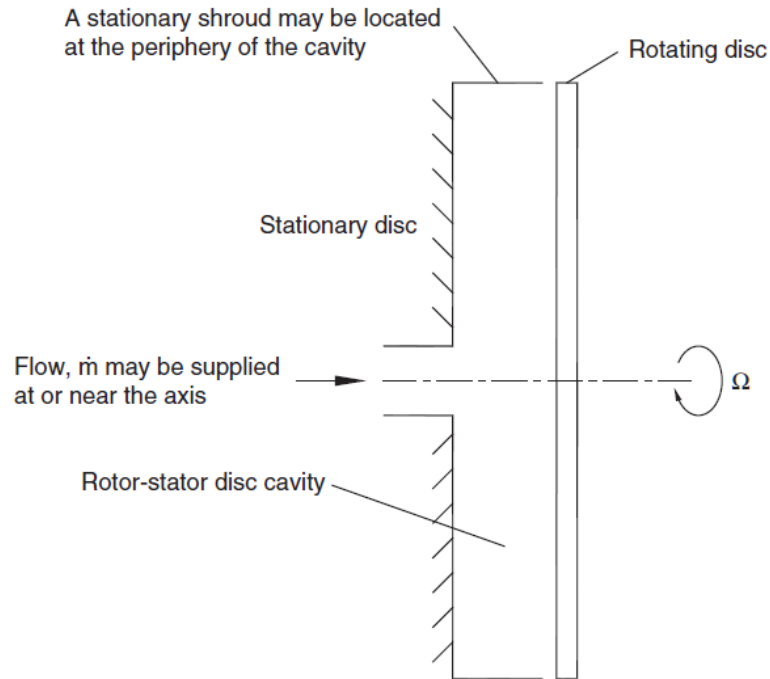
Figure 2.3: Rotor-stator system – adapted from Childs (2011)

Before the existence of extensive experimental data and numerical solutions, Batchelor (1951) proposed that an inviscid core of fluid existed between the rotating and stationary discs, which rotated in solid body rotation at an angular velocity somewhere between that of the stator and rotor. The core is confined between the two boundary layers which develop on the rotor and stator surfaces. In order to supply the rotor boundary layer, fluid is entrained from the core and pumped radially outward. At the stator surface there is a radial inflow, and movement of fluid from the boundary layer to the core. The characteristic velocity profiles for Batchelor flow are shown in Figure 2.4.
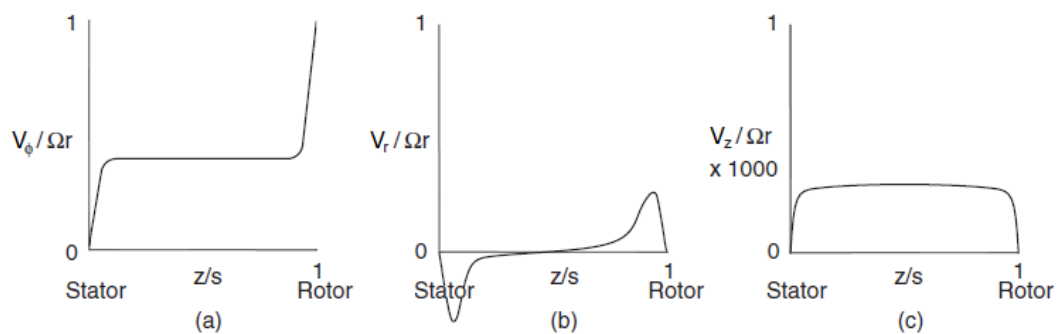
Figure 2.4: Characteristic velocity profiles in a rotor-stator system for Batchelor flow: (a) tangential velocity, (b) radial velocity, and (c) axial velocity – adapted from Childs (2011)

In contrast to Batchelor, Stewartson (1953) suggested that the flow was more like that of the free disc, where the tangential velocity in the rotor boundary layer reduces from the rotor speed (Ωr) to zero away from the boundary layer. He concluded that no boundary layer was necessary on the stator surface and no core rotation existed. The characteristic velocity profiles for Stewartson flow are shown in Figure 2.5.
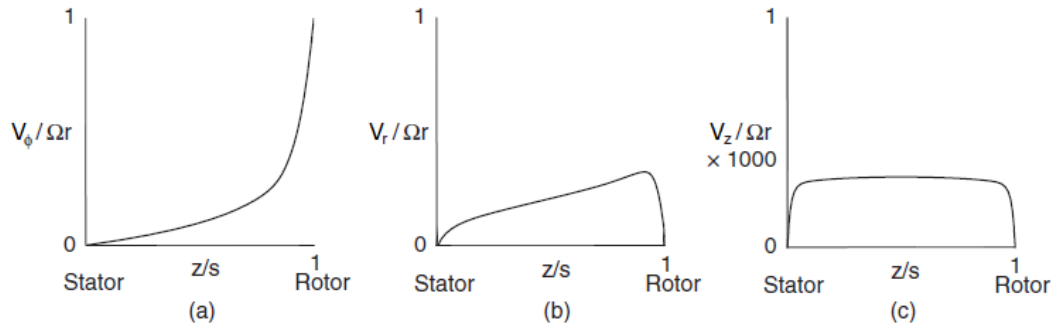
Figure 2.5: Characteristic velocity profiles in a rotor-stator system for Stewartson flow: (a) tangential velocity, (b) radial velocity, and (c) axial velocity – adapted from Childs (2011)

This paradox became known as the Batchelor-Stewartson controversy, and only when experimental measurements were made was it shown that each model is valid depending on the flow conditions. For an enclosed rotor-stator system with no superposed flow, a rotating core will exist and Batchelor flow best describes the flow structure. For an open system with no shroud, or an enclosed system subjected to a superposed flow rate greater than the free disc entrainment rate which suppresses the core, Stewartson flow will best describe the flow structure.
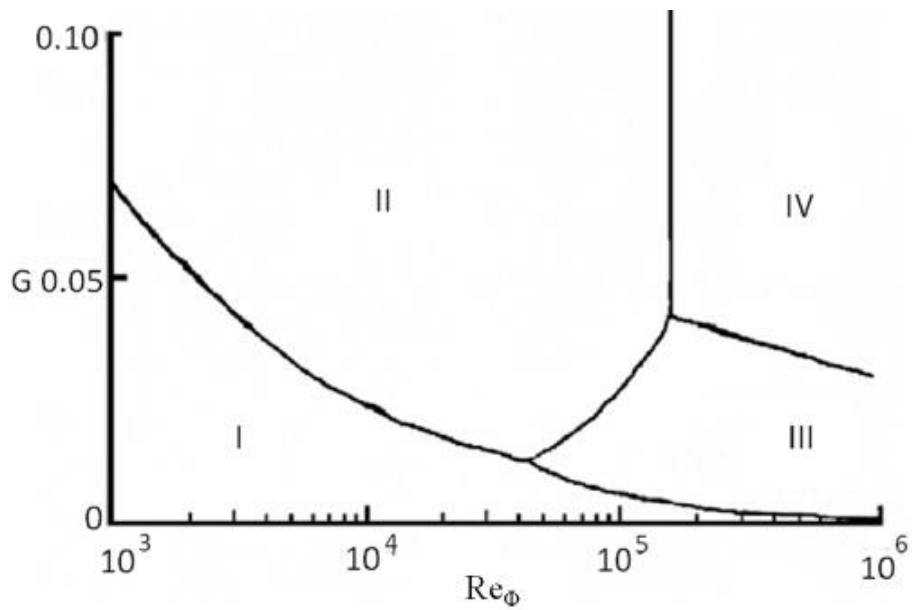
Figure 2.6: Flow regimes for an enclosed rotor-stator system – Daily and Nece (1960)

Daily and Nece (1960) carried out an experimental and theoretical study which enabled rotor-stator flow to be categorised by the gap-ratio, G, and the rotational Reynolds number, Re_ϕ, as shown by Figure 2.6. Velocity profile measurements in an enclosed rotor-stator system revealed four regimes, defined as followed:

- Regime I: Laminar flow, with a small clearance and merged rotor-stator boundary layers (Couette flow). For a constant Re_ϕ, the frictional heating on the rotor will decrease with an increase in G.

- Regime II: Laminar flow, with a large clearance and separated rotor-stator boundary layers resulting in a rotating core between the two discs. The presence of the stator reduces the core rotation, and hence the frictional heating, below that of a free disc. However as G increases, the influence of the stator reduces and the frictional heating will increase. For $G > 0.1$, the stator will have no effect and the frictional heating will be equivalent to that of a free disc.

- Regime III: Turbulent flow, with a small clearance and merged rotor-stator boundary layers. This regime is similar in nature to Regime I.

- Regime IV: Turbulent flow, with a large clearance and separated rotor-stator boundary layers resulting in a rotating core between the two discs. This regime is similar in nature to Regime II.

2.4 RI ingress

One of the earliest experimental studies of ingestion was performed at the University of Sussex by Bayley and Owen (1970). They investigated a shrouded stator separated axially from a rotor disc, similar to setup shown in Figure 2.3. A superposed radial flow of air, $C_{w,o}$, was supplied to the wheel-space at the centre of the stator disc and flowed radially-outward, discharging through the seal clearance into a quiescent atmosphere. Owing to the sub-atmospheric pressure created by the rotating fluid in the system, external air could be drawn into the wheel-space. Static pressure measurements were made on the stator wall; sub-atmospheric readings indicated ingestion had taken place. Increasing the superposed radial flow rate increased the relative pressure inside the wheel-space and consequently reduced the amount of ingested air. At sufficiently high flow rates, ingress did not occur and the system was said to be "sealed". The authors showed that $C_{w,min}$, the minimum non-dimensional sealant flow rate required to prevent ingestion, was proportional to Re_ϕ and G_c. For $G \gg G_c$ and $Re_\phi < 4 \times 10^6$, the following empirical relationship, now termed the Bayley-Owen criterion for RI ingress, was proposed:

$$C_{w,\min} = 0.61 G_c \, \mathrm{Re}_\phi \qquad (2.1)$$

This criterion has been widely quoted and has often been used in situations, such as EI ingress, where it has no validity.

Further research into rotationally induced ingress in rotor-stator systems was performed by Phadke and Owen (1983) using five different seal configurations. Using pressure measurements and flow visualisation experiments, $C_{w,min}$ was found to be lower for radial-clearance seal geometries in comparison to the axial-clearance equivalent with a common clearance. Unlike the axial-clearance configurations, the radial-clearance seals exhibited a pressure-inversion effect at large sealant flow rates, where the pressure inside the wheel-space increased with increasing rotational speed. The greater the overlap the larger the magnitude of this pressure inversion effect, therefore improving the performance. Suggestions were made for why this effect had occurred, although no definitive explanation was given.

In Hartford Connecticut, Graber *et al.* (1987) pioneered sealing effectiveness measurements in turbine rigs using a gas concentration technique. Experiments were performed in rotating rig facility with a shrouded rotor and a shroudless stator disc. Four peripheral seal geometries and two different swirl ratios in the annulus were investigated. Due to the flow rate in the annulus being very small (< 0.03 m/s), and in the absence of any

evidence of a circumferential variation in pressure, it is likely that the flow was very close to axisymmetric and therefore any ingestion that occurred would have been due to rotational effects. The sealant flow was seeded with CO_2 and concentration measurements were made on the stator wall to determine how much unseeded air from the annulus had been ingested. In the absence of ingress, the value of concentration measured on the stator wall would have been equal to the seeded value in the sealant flow. Measurements were made at multiple radial locations on the stator and the mean of these samples was taken as the level of concentration in the wheel-space, c_s. The cooling effectiveness parameter was therefore defined as:

$$\varepsilon_c = \frac{c_s - c_a}{c_0 - c_a} \tag{2.2}$$

where c_a and c_0 are the measured concentration levels in the annulus and sealant flow line respectively. The typical variation of cooling effectiveness with sealant flow rate is shown in Figure 2.7.
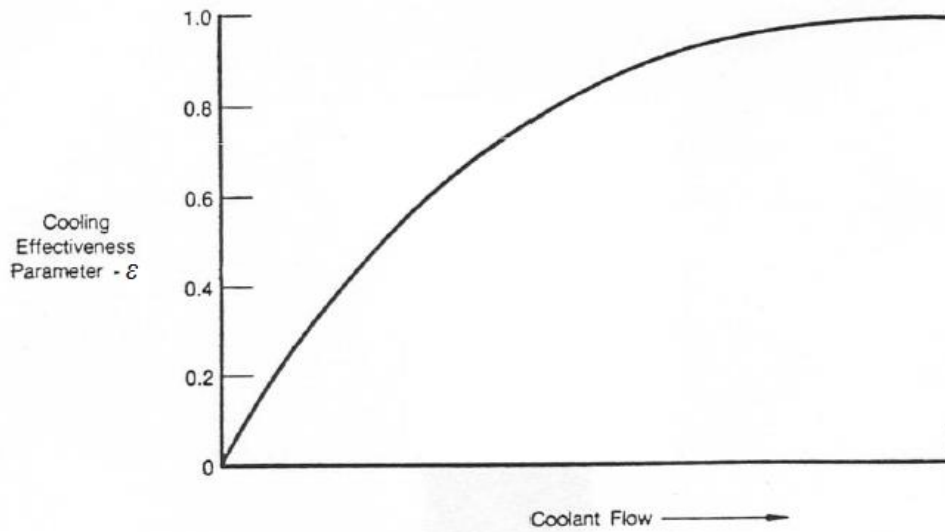
Figure 2.7: Typical seal cooling effectiveness parameter as a function of purge flow rate – adapted from Graber *et al.* (1987)

Figure 2.7 shows that increasing the cooling effectiveness above 80% becomes a law of diminishing returns. If acceptable disc temperatures can be tolerated at conditions less than the no ingestion rate, large amounts of sealing flow can be saved. Therefore it is apparent a designer must be aware of not only the minimum amount flow rate required to prevent ingestion, but also the shape of this distribution/relationship. The results of Graber *et al.* (1987) were in reasonable agreement with the findings of Phadke and Owen (1983). The

degree of external swirl in the annulus was found to have little impact upon sealing effectiveness.

Phadke and Owen (1988a) expanded on their earlier work with a three part series of papers, the first of which once again looked at ingestion in the absence of external flow. Inspired by the work of Graber *et al.* (1987), the authors added CO_2 gas concentration measurements to their previously implemented techniques. Flow visualisation showed that the previously unexplained pressure inversion effect was due to impingement of the radially pumped flow on the periphery of the stator. This impinging jet formed a protective fluid curtain that helped prevent ingress.

Chew (1991) questioned the validity of some of the Phadke and Owen (1983) results at small seal clearances. Analysis of the pressure difference across the seal with no rotation implied discharge coefficients greater than unity. It was concluded that the most likely explanation for this was from errors that occurred in setting the seal gap, G_c. A mathematical model was developed by linking boundary layer flow in the wheel-space through momentum integral analysis, to a simple orifice model for the seal clearance. The model was used to predict the amount of ingested flow and minimum sealing flow to prevent ingestion. The turbulent flow parameter, λ_T, was used as the boundary layer flow in the rotor-disc system depends on it. By using the empirical constant $k = 0.65$, determined from Phadke and Owen (1983), the theory agreed with the measurements of Graber *et al.* (1987), as shown in Figure 2.8. It was shown that the ingested flow, C_w, is approximately 20% of the minimum sealant flow rate to seal the system, $C_{w,min}$.

$$\varepsilon = \lambda_T / (0.8\lambda_T + 0.2\lambda_{min})$$

Graber et al (1987) $\begin{cases} \odot \ v_{ex} = \Omega b \\ \triangle \ v_{ex} = 2\Omega b \end{cases}$
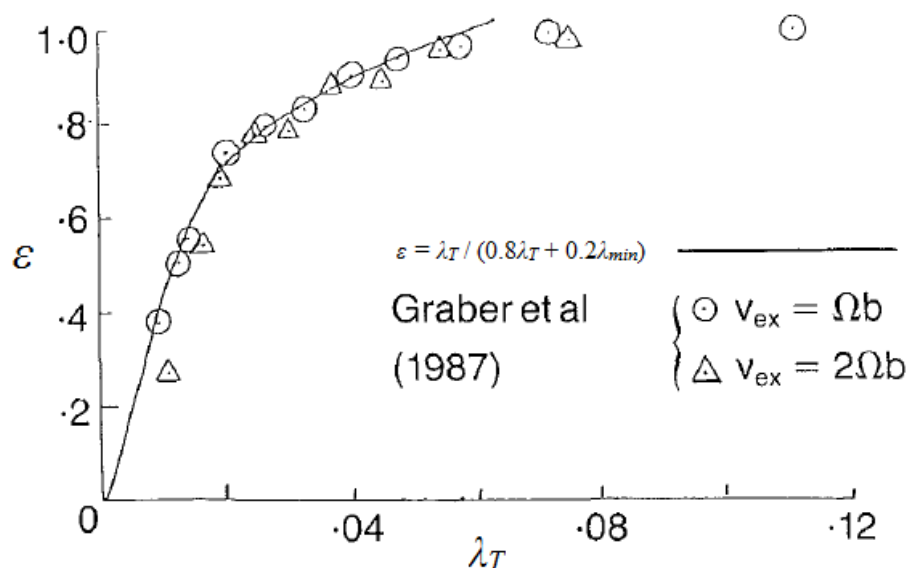
Figure 2.8: Comparison of model prediction with data of Graber *et al.* – adapted from Chew (1991)

Chew *et al.* (1992) made further comparisons of the mathematical model with several geometries including the radial-clearance seal configurations tested by Dadkhah *et al.* (1992), and the experimental data of Daniels *et al.* (1992). The importance of further research to account for the influence of external flow was identified.

2.5 EI ingress

Abe *et al.* (1979) performed the first investigation that showed ingress could be governed by the external flow in the annulus rather that the rotational speed of the disc. Where in previous studies measurements had been made at atmospheric conditions with simplified geometries, the study featured actual turbine disc geometries and an external flow supply. The presence of 27 vanes positioned upstream of the seal clearance on the stator platform turned the flow approximately 50°. This created the required pressure asymmetries for EI ingress to take place, in the absence of rotor blades. Measurements of pressure, velocity and the density of propane gas were used to determine the performance of several complex rim-seal designs. The authors concluded ingress was predominantly governed by the ratio of sealing to annulus air flow rate, the rim-seal clearance, and the shape of the rim-seal. Wheel-space and disc temperatures of a real engine compared well with calculated temperature distribution from the experiment. The results highlighted ingress was under-predicted by tests conducted at atmospheric conditions and paved the way for future investigations into the effects of external flow.

Phadke and Owen (1988b, c) investigated the effect on ingress in the presence of quasi-asymmetric and non-asymmetric annular flows. In the absence of vanes and blades, these circumferential pressure asymmetries were created by blocking off segments of the annulus with honeycomb sections attached to wire mesh. Tests were conducted with three rim-seal geometries, including both axial and radial clearance seals, at Re_w and Re_ϕ values up to 1.2×10^6. Three experimental criterions were used to establish $C_{w,min}$, the minimum non-dimensional sealant flow rate required to prevent ingress. Pressure readings provided an indirect measurement of ingress by comparing the pressure inside the wheel-space to that outside in the annulus. Qualitative flow visualisation was achieved by seeding the external flow with smoke particles and observing the level of smoke that entered the wheel-space. Finally, gas concentration measurements were made with nitrous oxide at a fixed location on the stator wall. The three methods were found to give qualitatively similar results, although the pressure measurements tended to overestimate $C_{w,min}$.

The findings of the quasi-asymmetric experiments showed two regimes existed, a rotationally dominated regime at small values of Re_w / Re_ϕ and an external flow dominated regime at large values. In the rotational regime, where $Re_w \rightarrow 0$, $C_{w,min}$ increased with Re_ϕ (consistent with the findings of Phadke and Owen (1988a)). For the largest values of Re_w, $C_{w,min}$ was proportional to Re_w and independent of Re_ϕ. At small values of Re_w, there was a decrease in $C_{w,min}$ with increasing Re_w creating an undershoot. This behaviour was attributed to the sealing effect of an axisymmetric external flow. For both regimes and all seals tested, $C_{w,min}$ increased with increasing clearance ratio, G_c.

In Phadke and Owen (1988c), the results of tests conducted with non-axisymmetric external flow were presented. Variations of asymmetry were created by using different combinations of honeycomb mesh, which allowed the effects of pressure asymmetry to be separated from Re_w. The results showed in the externally induced regime, $C_{w,min}$ increased linearly with $C_{p,max}{}^{1/2}$, the non-dimensional maximum circumferential pressure difference in the annulus. Phadke and Owen correlated their results using the following relationship:

$$C_{w,\min} = 2\pi G_c K P_{\max}{}^{1/2} \tag{2.3}$$

where K is an empirical constant and:

$$P_{\max} = \frac{1}{2} C_{p,\max} \, \mathrm{Re}_w{}^2 \tag{2.4}$$

As shown by Figure 2.9, the experimental data correlated well with a value of $K = 0.6$. It was suggested a conservative estimate of $C_{w,min}$ could be found by assuming the larger value determined for the two regimes. The results also indicated a double-shrouded radial clearance seal would outperform other seal geometries in minimising the amount of ingested fluid into the wheel-space.
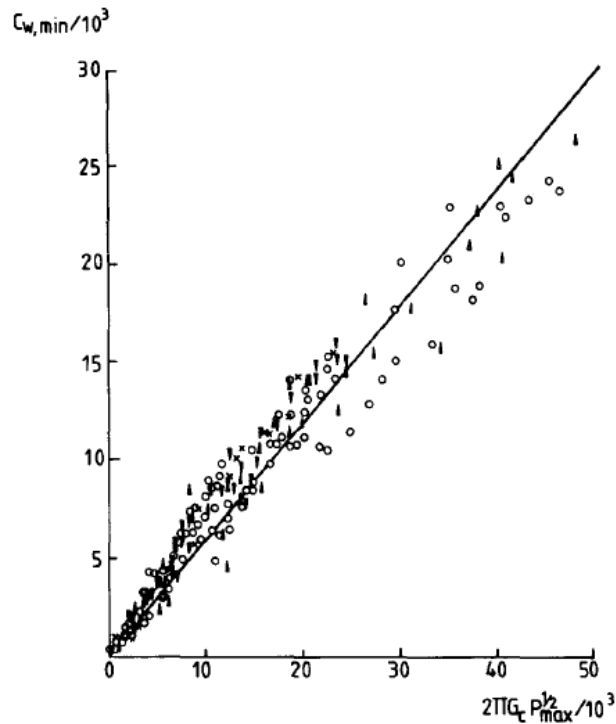
Figure 10   The variation of $C_{w,min}$ with $2\Pi G_c P_{max}^{1/2}$

Symbol	○	×	△	▽
Seal	1	2	3	5

Equation 4 with $K = 0.6$ ————————

Figure 2.9: The variation of $C_{w,min}$ with $2\pi G_c P_{max}^{1/2}$ - Phadke and Owen (1988c)

Hamabe and Ishida (1992) made gas concentration measurements to determine the sealing effectiveness in a single stage turbine rig featuring upstream stator vanes but no downstream rotor blades. The authors used a previously developed orifice model to predict the distribution of effectiveness with sealing flow rate. It was found that the shape of the external circumferential pressure profile affects the sealing effectiveness considerably. In the model, the pressure profile was estimated using three simplified wave forms, labelled A, B and C at the top of Figure 2.10. Although none of the estimations gave exact correlation with the measurements of effectiveness, the saw-tooth model (C) gave the best prediction. As shown in Figure 2.10, only by using the measured external pressure distribution did good agreement occur. It was therefore concluded that knowledge of the pressure in the annulus was required to accurately predict the sealing effectiveness.
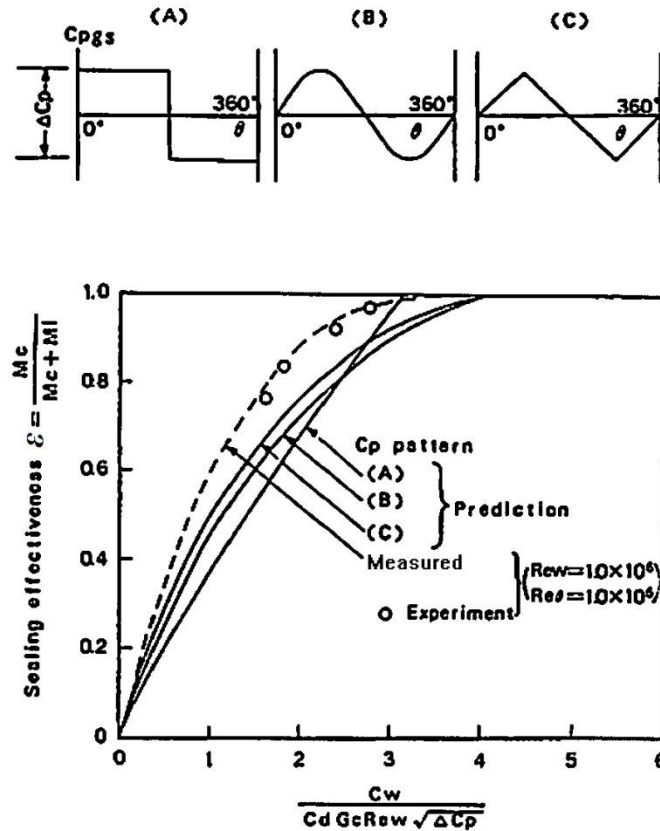
Figure 2.10: Sealing effectiveness as a function of sealing flow parameter – adapted from Hamabe and Ishida (1992)

A new experimental test facility at the University of Sussex was presented by Dadkhah *et al.* (1992), capable of reaching rotational Reynolds numbers of 3×10^6. The rig featured external flow, in the absence of vanes and blades, and reversible disc assemblies to allow investigation into upstream and downstream wheel-space cavities. Gas concentration and pressure measurements took place to determine ingestion levels. The results suggested that if a value of $\varepsilon = 0.95$ could be tolerated the sealing flow rate could be reduced by as much as 35%. Figure 2.11 shows the relative tangential velocity in the core plotted against the parameter $\lambda_t(r/b)^{-13/5}$, obtained by several methods including the momentum-integral solution of Chew (1991). The empirical correlation shows the core rotation is completely suppressed at a value of 0.486, twice the free disc entrainment value.
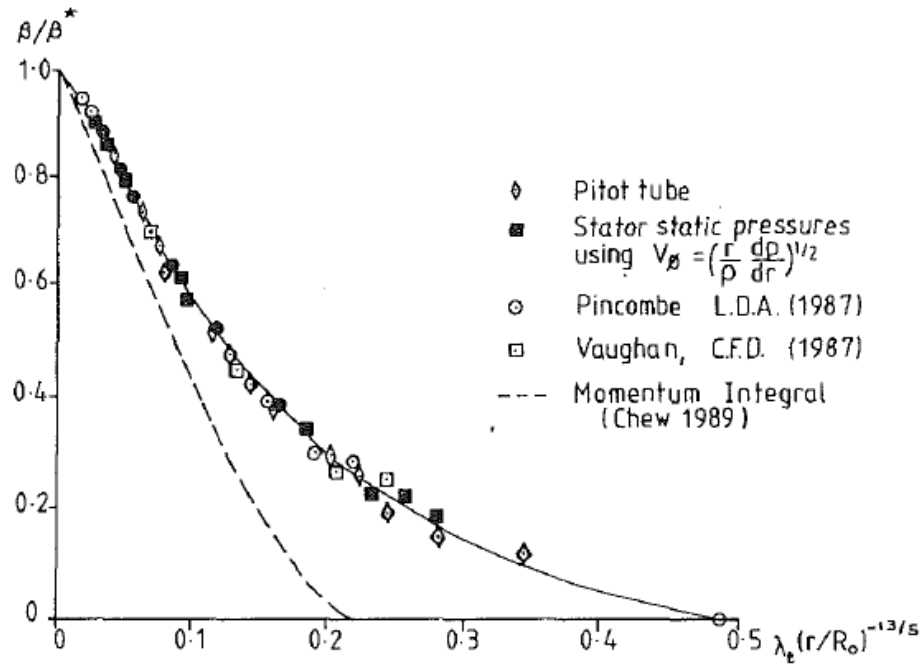
Figure 2.11: Variation in relative tangential velocity of the wheel-space core flow at *r/b* = 0.658 and *x/s* = 0.5 - Dadkhah *et al.* (1992)

Stator guide vanes were then fitted to the Sussex rig to create pressure asymmetries in the annulus for the investigation of Chew *et al.* (1994). Once again, N_2O gas concentration measurements were used to determine sealing effectiveness. They confirmed this effectiveness was dependent on the hub static pressure distribution downstream of the vanes for a simple axial-clearance seal. Discharge coefficients for egress and ingress were measured without vanes and with a stationary rotor disc. The results were used to solve a simple orifice model, similar to that used by Hamabe and Ishida (1992). In comparison to the experimental measurements, the orifice model overestimated the level of ingestion, possibly due to the neglect of inertial effects. Steady CFD calculations demonstrated encouraging agreement with experimental values, and allowed the effect of ingestion on the rotor side of the wheel-space to be examined. However, ingress levels at high sealant flow rates were under-predicted. Reasons for this were attributed to a lack of detailed modelling in the annulus, unsteady effects not captured by the computations and insufficient spatial resolution. The long term goal of unsteady calculations, including all features of the turbine stage was established.

The first published experimental investigation for a turbine rig with both vanes and blades was presented by Green and Turner (1994). The rig was adapted from Chew *et al.* (1994), with the addition of 32 rotor blades close to the seal clearance, and the same

measurement techniques were employed. Surprisingly, the results showed the inclusion of the blades caused a reduction in ingestion rather than an increase (Figure 2.12). It was suggested at low sealant flow rates, the effect of the blades could be to smooth out the pressure asymmetries caused by the vanes, thus decreasing ingestion. The authors concluded that the blades, together with the vanes play an important role on ingestion, and that future experiments should be performed at conditions close to engine operating levels if the results are to contribute to design practices.
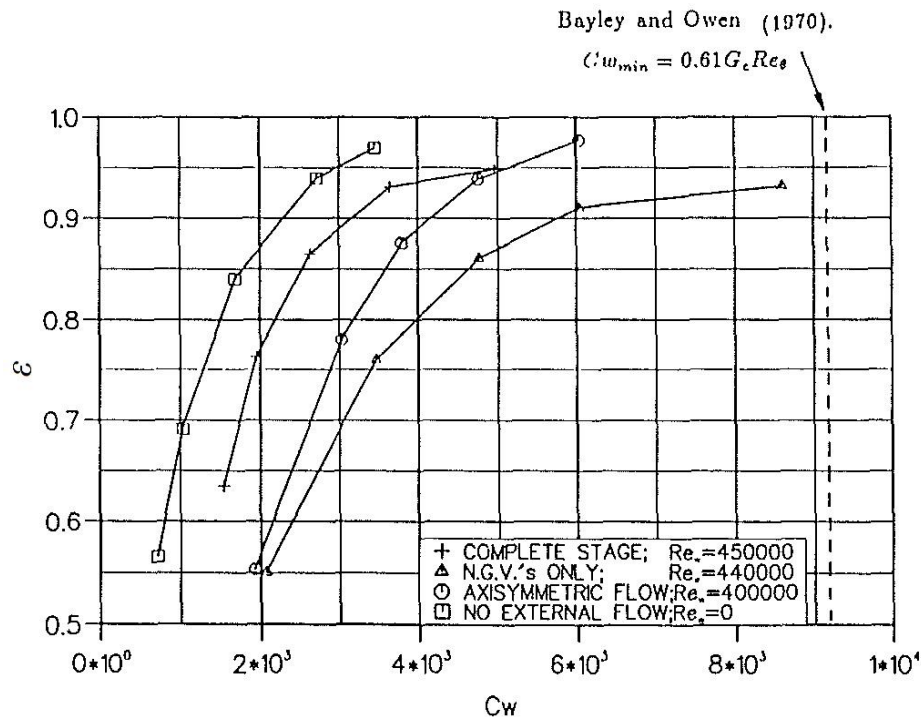
Figure 2.12: Variation of sealing effectiveness with non-dimensional sealant flow rate for four external flow conditions – adapted from Green and Turner (1994)

A detailed review of the hot gas ingestion mechanisms found in gas turbines was given by Johnson *et al.* (1994). Amongst the physical mechanisms discussed are:

- Disc pumping (equivalent to RI ingress)
- Periodic and unsteady pressure fields due to vanes and blades (equivalent to EI ingress)
- Asymmetry in the seal geometry
- Turbulent transport
- Flow entrainment

Bohn *et al.* (1995) made pressure and velocity measurements using Laser Doppler Velocimetry (LDV) in a 1-stage rig complete with 30 vanes in Aachen, Germany. This high speed test facility was capable of operating at near engine conditions, with vane exit Mach numbers reaching up to 0.7 and rotor speeds of 15,000 rpm. It was shown through velocity measurements in the wheel-space that ingress could occur not only on the stator, but also on the rotor side of the wheel-space under certain conditions. Circumferential static pressure measurements in the annulus at three axial locations downstream of the trailing edge of the vanes were presented. The results showed the axial decay in magnitude of the peak-to-trough pressure difference over two vane pitches. This was responsible for the increase in ingestion levels as the vanes were moved closer to the rim-seal. In addition, by comparing the radial static pressure distribution in the wheel-space to the average vane pitch pressure in the annulus, a pressure criterion, *p**, was used to determine when ingress occurs. The measurements also showed the pressure in the wheel-space was non-axisymmetric at radius ratios larger than 0.972, as shown in Figure 2.13.
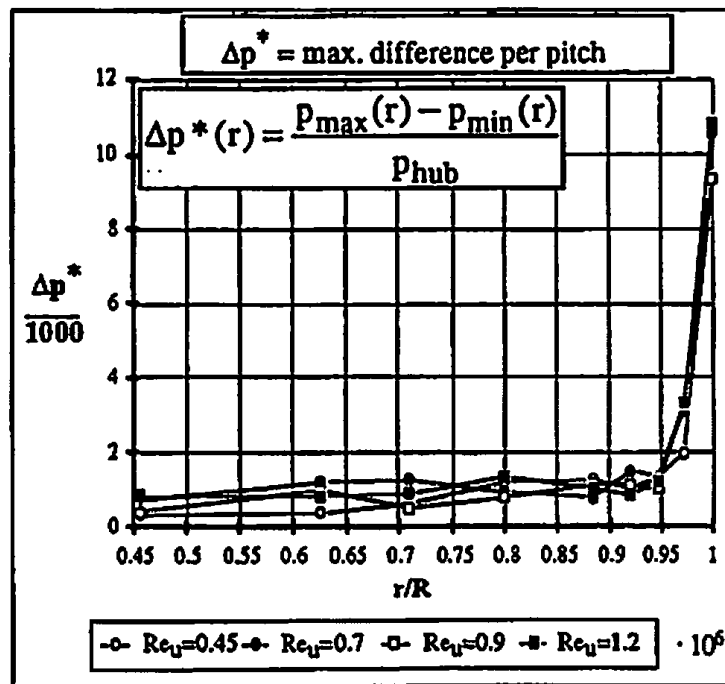
Figure 2.13: Maximum circumferential pressure difference in wheel-space - Bohn *et al.* (1995)

Hills *et al.* (1997) compared 3D steady CFD predictions with experimental pressure measurements made in the rig described by Chew *et al.* (1994), with redesigned guide vanes and pegs to represent the rotor blades. At high sealant flow rates the experimental and

computational results diverged; this was attributed to interaction of the sealing and mainstream flows. It was concluded a combined CFD calculation featuring annulus and cavity flows may be required to capture this effect.

The rig at Aachen was then adapted into a 1.5 stage turbine, including 62 twisted rotor blades and a dynamometer to remove the excess power that was consequently generated. Bohn *et al.* (1999) used the pressure criterion, p^*, and CO_2 gas concentration measurements to determine the effects of Re_w and Re_ϕ on the sealing effectiveness of two seal geometries (shown in Figure 2.14). The results showed increasing Re_w had a detrimental effect on sealing performance for both geometries due to the increase in pressure asymmetry in the annulus. The effect of Re_ϕ was shown to be dependent on geometry. 3D numerical simulations performed without blades, identified Gap Recirculation Zones (GRZs) near the rotating disc which varied in diameter with circumferential position.
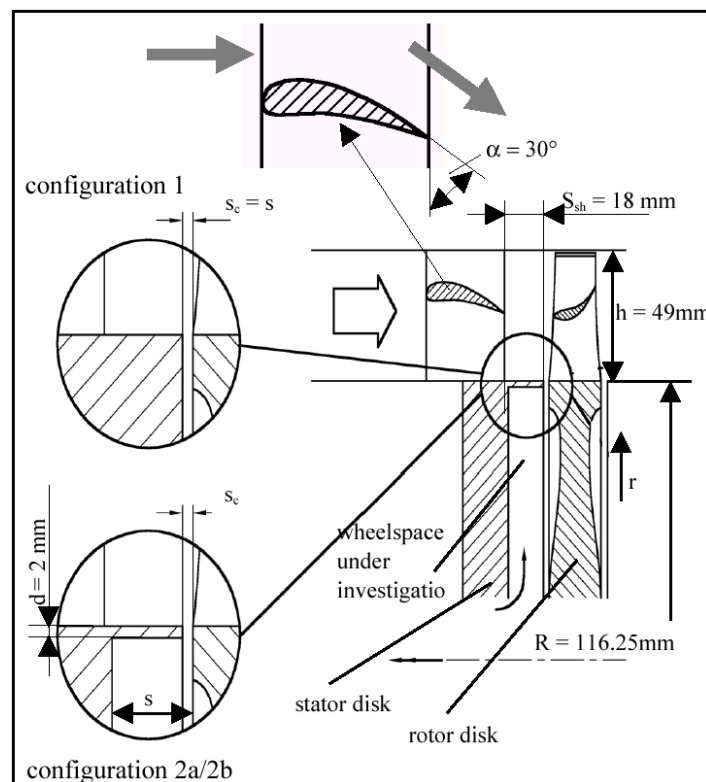
Figure 2.14: Geometric configurations tested by Bohn *et al.* (1999, 2000) and Bohn and Wolff (2003)

The influence of rotor blades on ingestion was examined by Bohn *et al.* (2000) by comparing their results with previous experiments by Bohn *et al.* (1995) without rotor blades. The peak-to-trough magnitude of the circumferential pressure difference in the

annulus, measured 1.5 mm downstream from the vane trailing edge, was larger when the rotor blades were present. For configuration 1, the rotor blades were shown to have a detrimental effect on effectiveness. However, for configuration 2, the opposite was observed where an improvement took place with the rotor blades included. Numerical 3D unsteady computations also showed an improvement in sealing efficiency when compared to steady calculations for the same configuration without blades.

Khilnani and Bhavnani (2001) investigated the sealing performance of simple and engine realistic geometries in an external flow rig without vanes or blades. Measurements of CO_2 gas concentration and static pressure were used to determine $C_{w,min}$ for a range of Re_w and Re_ϕ values (Figure 2.15). The results showed good agreement with the findings of Phadke and Owen (1998c), although the results did not become completely independent of Re_ϕ due to the limits of Re_w. The measurements were therefore said to be conducted within the combined ingress regime.
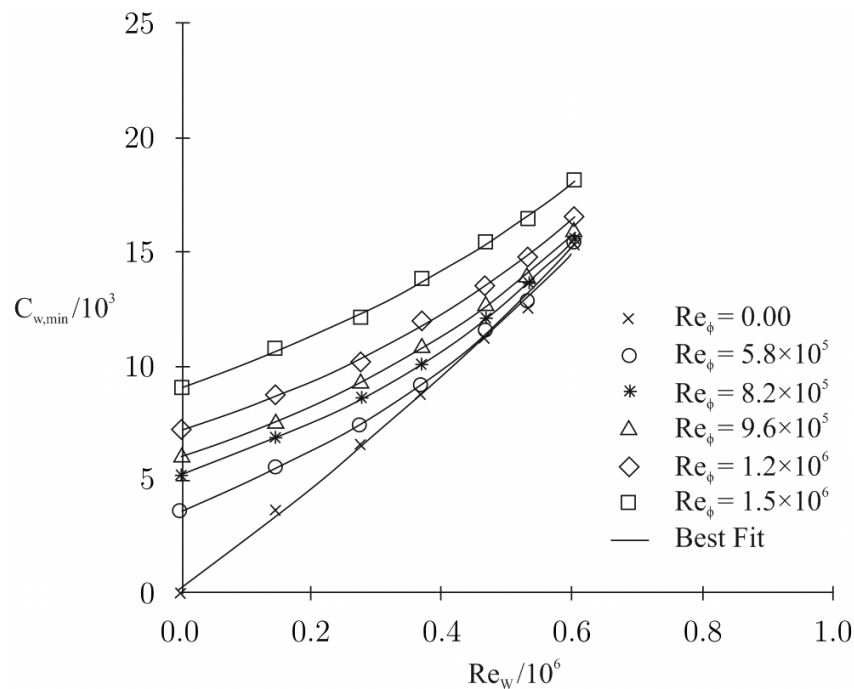
Figure 2.15: Effect of Re_ϕ on variation of $C_{w,min}$ with Re_w – adapted from Khilnani and Bhavnani (2001)

An unsteady CFD model simulating hot gas ingestion was presented by Hills *et al.* (2002), who showed considerably better agreement with the previously published experimental data presented in Hills *et al.* (1997), than was achieved with steady models. Circumferential pressure asymmetries caused by the rotating blades were shown to have a

large influence on ingestion despite being considerably smaller than the pressure asymmetries due to the stationary vanes. The authors concluded the vane only measurements presented in Green and Turner (1994), shown in Figure 2.12, were made in error and the rotor blades do in fact contribute to ingestion. The simple orifice theory model presented by Chew *et al.* (1994) was extended to include inertial effects due to swirl velocity. The model had some success in capturing the experimental trends.

Bohn and Wolf (2003) developed a new approximation for sealing effectiveness based on $C_{w,min}$, G_c and $C_{p,max}$. CO_2 gas concentration and steady pressure measurements were made for four different rim-seal geometries. The correlations display a linear variation of $C_{w,min}$ with $C_{p,max}^{1/2}$. It was also showed that the performance of rim-seals could be ranked using different values of the empirical constant K, based on the least squares error when fitted to the experimental data (Figure 2.16). It was suggested that the single value of $K = 0.6$ used by Phadke and Owen (1988c) to correlate their data for multiple seals was overly conservative. The influence of vane exit angle was shown to have marginal effect on ingestion.
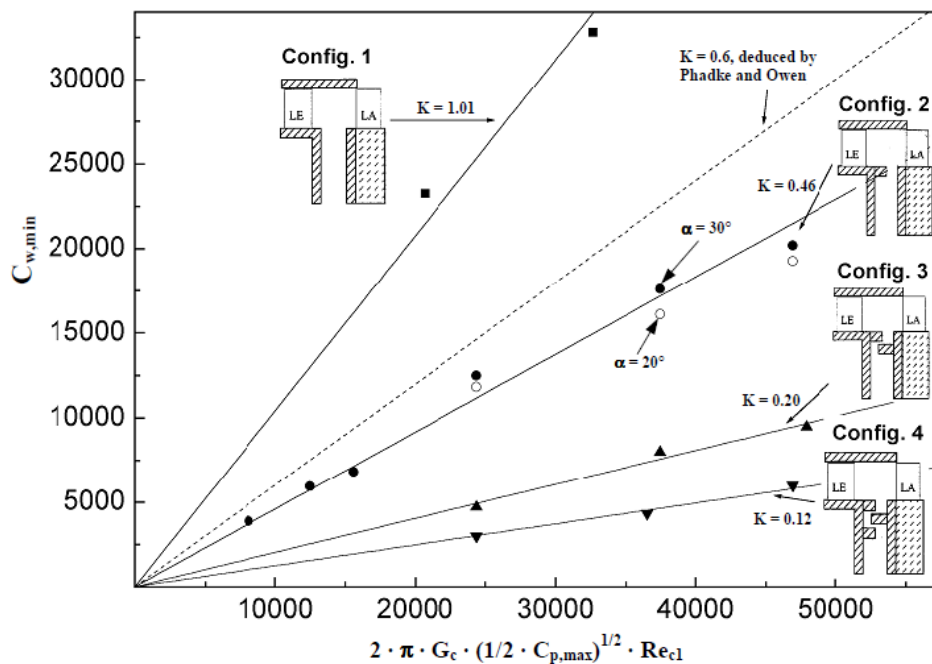
Figure 2.16: Comparison of *K* values for different rim-seal geometries - Bohn and Wolf (2003))

Gentilhomme *et al.* (2003) presented measurements of ingestion in a single-stage turbine rig complete with vanes and blades. Two operating conditions were tested covering a wide range of vane exit Mach numbers. The authors concluded the amount of ingress will depend

on the vane, blade and seal geometries, as well as the relative location of the seal clearance. As shown in Figure 2.17, the sealing effectiveness data for each test condition collapsed with the seal gap to annulus velocity ratio, U/W. CFD predictions of pressure asymmetry at the seal were used in the simple ingestion model described by Hills *et al.* (2002). The results severely underestimated ingestion levels in comparison to the experimental measurements, and showed strong sensitivity to the swirl velocity assumed for the seal flow.
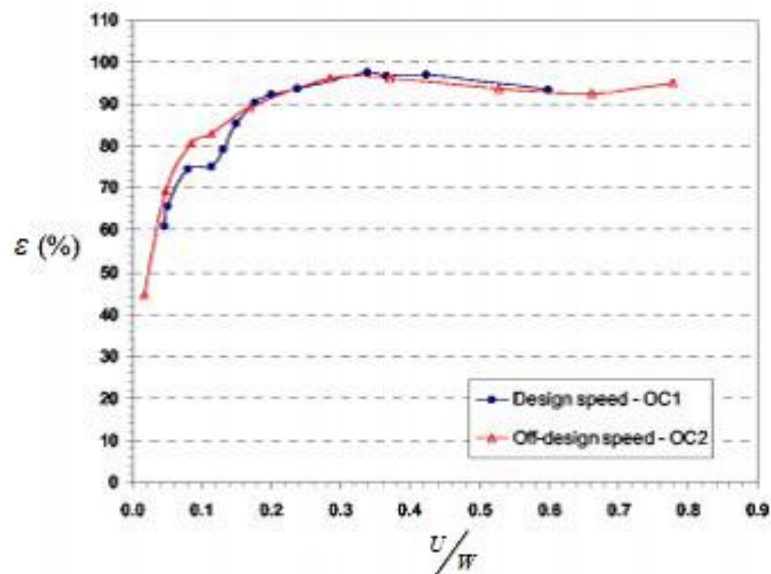
Figure 2.17: Concentration measurements made at two operating conditions – adapted from Gentilhomme *et al.* **(2003)**

Further 2D LDV measurements were presented by Bohn *et al.* (2003) with the Aachen rig in a new configuration featuring 16 stator vanes on either side of 32 blades. The unsteady measurements indicated a strong effect of both the stator vanes and rotor blades on ingestion in the upstream cavity. It was shown even for large sealant flow cases, ingestion occurs in the high pressure regions directly in front of the rotor blades. These regions intensified when the blades passed by the stator wake compared to the ingestion when the blades pass by the stator passage.

Results of different numerical approaches were presented by Jakoby *et al.* (2004), using data from the Aachen test rig for validation. A 360° simulation of the time-dependent flow field, including the main gas path, was used in an attempt to find large scale structures discovered in the experiments. When the sealant flow rate was small enough, low-pressure zones, which rotated at approximately 80% of the rotor speed, were found to strongly

influence the hot gas ingestion. Although, with the 360° model, comparisons with effectiveness data were better than those achieved using sector models, the CFD still significantly under-predicted the ingestion.

Cao *et al.* (2004) presented a combined CFD and experimental study which also featured an unsteady 3D 360° simulation without vanes or blades. The computations showed alternating regions of ingress and egress rotating at just below the rotor speed. Fast response unsteady pressure transducers, installed in a 2 stage axial turbine rig located in Rugby, UK, were used to measure the pressure in the wheel-space and confirm the CFD prediction.

The influence of axial and radial-clearance seal geometries on ingestion into the upstream cavity of the new Aachen rig configuration was investigated experimentally by Bohn *et al.* (2006). Circumferential and radial distributions of pressure and CO_2 gas concentration measurements in the wheel-space were presented for different operating conditions and sealant flow rates. As expected, the radial-clearance seal outperformed the axial seal in preventing ingestion. The radial-clearance seal measurements also indicated a compact rotating core extending radially outwards to the rim seal region.

Johnson *et al.* (2006) used an orifice model to calculate effectiveness measurements from the Aachen turbine rig described in Bohn *et al.* (2003). They used 2D time-dependent CFD for the annulus hub circumferential pressure distribution in their model, which allowed the effects of the vanes and blades to be taken into account. A single 'lumped' discharge coefficient (C_d) of 0.4 gave good agreement with the experimental data obtained from the rig. The importance of the time-dependent pressure field over the rim seal on ingestion was shown when the vanes and blades are closely spaced.

Roy *et al.* (2007) performed sealing effectiveness and Particle Image Velocimetry (PIV) experiments in a low-speed single-stage turbine rig at Arizona State University. Tangential velocity measurements showed ingress and egress occurring concurrently at different regions of the cavity. The results of a 3D unsteady CFD sector analysis detected large scale unsteady structures in the wheel-space.

Johnson *et al.* (2008) modified the orifice model presented in Johnson *et al.* (2006) to include two discharge coefficients, $C_{d,i}$ for ingress and $C_{d,e}$ for egressing flow. Comparison made with sealing effectiveness data obtained from the Arizona State rig showed an improvement in the agreement. It was concluded the effects of swirl could be compensated for by adjusting the discharge coefficients, therefore it was not necessary to complicate the model by adding a swirl term. Figure 2.18 demonstrates the best correlation with the ASU single overlap seal was achieved using $C_{d,i} = 0.2$ and $C_{d,e} = 0.27$.
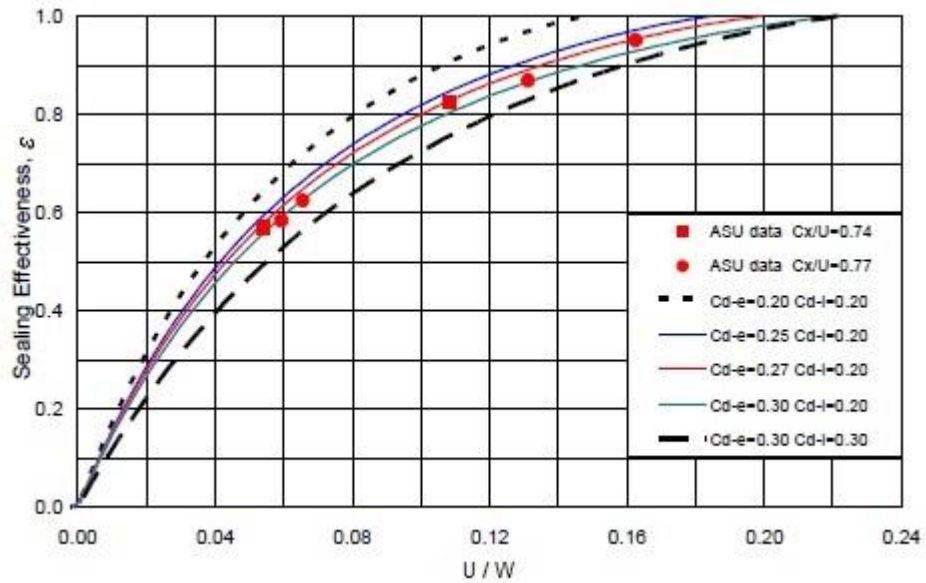
Figure 2.18: Comparison of ASU experimental data and orifice model predictions – adapted from Johnson *et al.* **(2008)**

Further experimental measurements performed at ASU were published by Zhou *et al.* (2011). Three rim-seal configurations were tested, including a double seal, to determine the influence of seal geometry on ingestion. The instantaneous fluid velocity field was mapped using PIV at multiple circumferential positions, and CO_2 gas concentration measurements were used to determine the effectiveness. At low sealant flow rates, the measured radial and tangential velocity components identified areas where ingress and egress occurred. An unsteady 3D CFD sector model under-predicted ingestion, as the circumferentially rotating low pressure zones, predicted by 360° simulations, could not be captured.

Additional rim-seal configurations, featuring an inner labyrinth seal, were then tested by Balasubramanian *et al.* (2011) in an aft-cavity rig. The ingestion measurements indicated that the inner wheel-space was completely purged at the highest sealant flow rate, but ingress still occurred in the outer wheel-space.

Wang *et al.* (2012) performed numerical simulations of the ASU rig geometry using a radial clearance seal and a 360° time-dependent approach. Circumferential distributions of ingress and egress flows in the wheel-space were found to rotate at the rotor speed. For lower sealant flow rates where ingestion was significant, the flows were not associated with the numbers of vanes or blades. Such a computationally expensive approach is time consuming and requires significant expertise and insight. This highlights the important role

experiments play not only in providing economically viable data, but also validation of these complicated CFD codes.

Eastwood *et al.* (2012) investigated re-ingestion of sealant flow in a two stage turbine stator well rig at the University of Sussex. The test facility was developed to study the interaction of stator well cooling and main annulus air. Gas concentration measurements showed the amount of egress flow re-ingested into the downstream wheel-space was approximately 7% for the realistic sealing flow rates tested. The amount of re-ingestion reduced with increasing sealing flow.

Palafox *et al.* (2013) discussed a new 1.5-stage hot gas ingestion rig, designed to operate at near-engine conditions, including representative Mach and Reynolds numbers. The rig, shown in Figure 2.19, is designed with the capability of providing CO_2 gas concentration data, as well as pressure and temperature measurements.
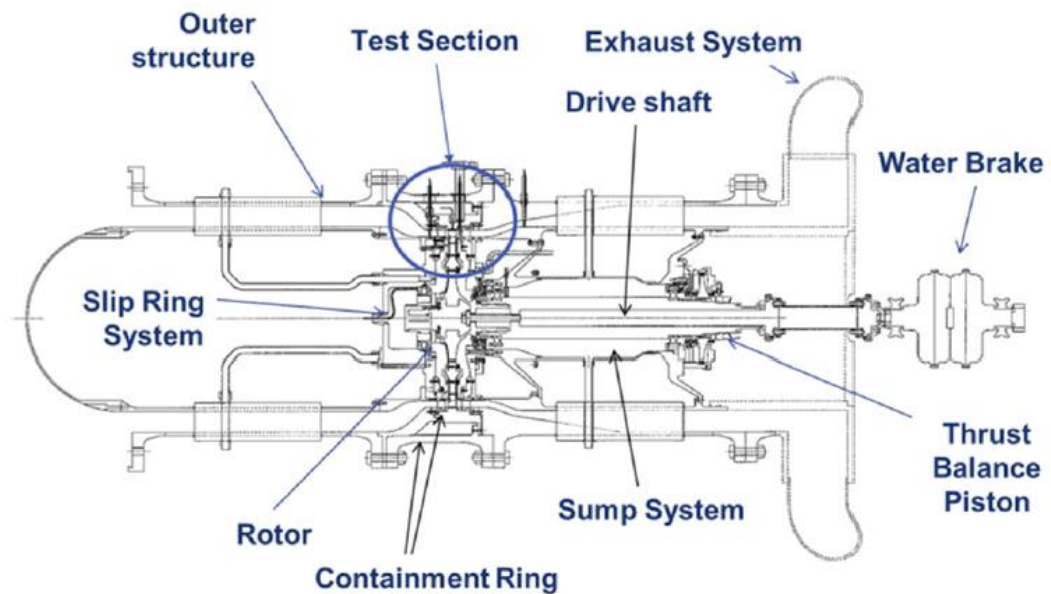
Figure 2.19: Section view of GE 1.5 stage hot gas ingestion rig - Palafox *et al.* (2013)

2.6 Ingestion research at the University of Bath

Owen (2011a) developed a theoretical model to predict ingress through the seal clearance in the absence of external flow. The model was derived for compressible and incompressible inviscid swirling flows, and the incompressible equations were solved analytically. The seal clearance was treated as an orifice ring, as shown in Figure 2.20. The inflow and outflow areas are represented by δA_i and δA_e respectively. Two discharge coefficients, C_{di} for ingress and C_{de} for egress, were used to account for viscous losses, similar to Johnson *et al.* (2008).
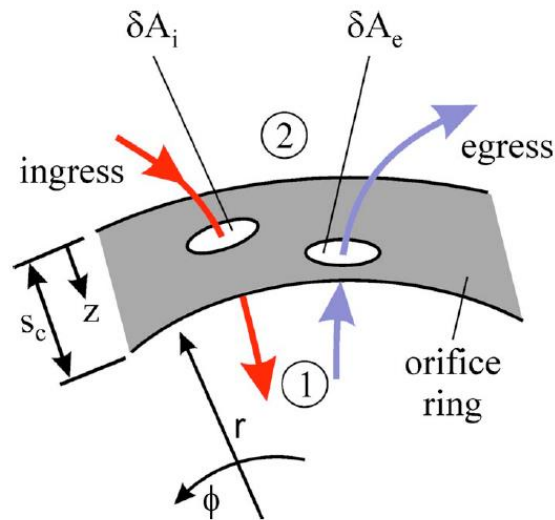
Figure 2.20: Orifice model ring – Owen (2011a)

To avoid using separate correlations, a new non-dimensional sealing parameter, Φ_0, was derived which combined $C_{w,0}$, G_c, and Re_ϕ into a single flow parameter as follows:

$$\Phi_0 = \frac{C_{w,0}}{2\pi G_c \, Re_\phi} = \frac{U}{\Omega b} \tag{2.5}$$

where U is the bulk-mean velocity through the rim-seal clearance.

As both Re_ϕ and $C_{w,0}$ include viscous terms which cancel in Eq. 2.5, Φ_0 is therefore an inertial parameter. The sealing effectiveness is therefore defined as:

$$\varepsilon = 1 - \frac{\Phi_i}{\Phi_e} = \frac{\Phi_0}{\Phi_e} \tag{2.6}$$

Assuming that the effect of the external swirl, β_2, was negligible (as shown by Graber *et al.* (1987)), the relationship between Φ_0 and ε was shown to be a function of the minimum $\Phi_{min,RI}$ and Γ_c, the ratio of the discharge coefficients. The definitions of both are as follows:

$$\Gamma_c = \frac{C_{d,i}}{C_{d,e}} \tag{2.7}$$

and

$$\Phi_{min,RI} = C_{d,e} C_{\beta 1}^{1/2} \tag{2.8}$$

where $C_{\beta 1}$ is the modified internal swirl ratio, defined as:

$$C_{\beta_1} = \beta_1^{2} \left(1 - \left(\frac{r_1}{r_2} \right)^2 \right) \tag{2.9}$$

For the basic theory case where $C_{de} = C_{di}$ ($\Gamma_c = 1$), and assuming $\Phi_{min,RI} = 0.097$, equivalent to the Bayley-Owen Criterion (calculated from Eq. 2.1), good agreement was found in comparison with the data of Graber *et al.* (1987). The theoretical overestimate of effectiveness as $\Phi_0 \to \Phi_{min,RI}$ was attributed to the effect of diffusion, which the model did not take into account.

Owen (2011b) extended the orifice model theory to cover externally induced ingress and combined ingress. The EI and combined orifice equations were derived from first principles, for compressible and incompressible inviscid swirling flow. Just as in Johnson *et al.* (2008), two empirical discharge coefficients, $C_{d,i}$ and $C_{d,e}$ for ingress and egress respectively, were used to account for viscous losses. To allow the equations to be solved analytically, a 'saw-tooth' profile was assumed for the circumferential variation in the annulus. For EI ingress with negligible external swirl (i.e. $\beta_1 = \beta_2 = 0$), the variation between of ε with Φ_0 was shown to depend only on two parameters $\Phi_{min,EI}$ and Γ_c, where:

$$\Phi_{min,EI} = \frac{2}{3} C_{d,e} \Delta C_p^{1/2} \tag{2.10}$$

and

$$\Delta C_p = \frac{\Delta p}{\frac{1}{2} \rho \Omega^2 b^2} \tag{2.11}$$

where Δp was the peak-to-trough circumferential pressure difference in the annulus.
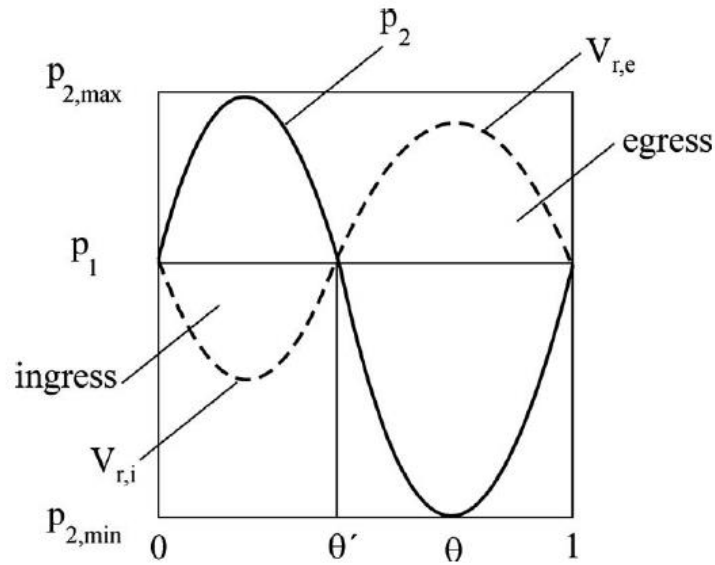
Figure 2.21: Arbitrary circumferential variation of pressure and radial velocity in external annulus - Owen (2011b)

The combined ingress orifice equations were solved for negligible external swirl to give the following ratio between the minimum sealant flow to prevent ingress for the combined and rotationally induced cases:

$$\frac{\Phi_{min,CI}}{\Phi_{min,RI}} = \frac{2}{3} \frac{C_{d,e,CI}}{C_{d,e,RI}} \frac{(1 + \Gamma_{\Delta p})^{3/2} - 1}{\Gamma_{\Delta p}} \qquad (2.12)$$

where the external pressure parameter is defined as:

$$\Gamma_{\Delta p} = \frac{\Delta C_p}{C_{\beta_1}} \qquad (2.13)$$

Flow conditions in the combined ingress regime are such that neither RI nor EI ingress dominate. The solution of the orifice equations in Figure 2.22 shows the transition between the EI and RI asymptotes as amplitude of the circumferential variation in pressure ($\Gamma_{\Delta p}^{1/2}$) increases.
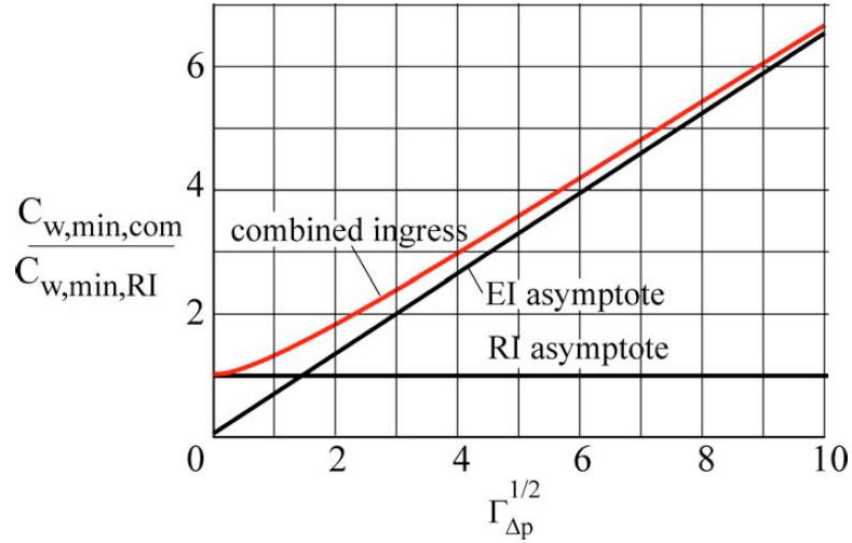
Figure 2.22: Theoretical variation of $C_{w,min,com}$ / $C_{w,min,RI}$ with $\Gamma_{\Delta p}^{1/2}$ according to Eq. 2.12 - Owen (2011b)

The EI orifice model was compared with the experimental data and numerical models of Johnson *et al.* (2006) and Johnson *et al.* (2008). Using equal discharge coefficients ($\Gamma_c = 1$), the agreement between theory and data was good. This assumption however, was not expected to provide a good fit for all experimental data, therefore a least-squares fit was recommended for future comparisons to determine Γ_c. Insufficient published data was available to validate the combined ingress theory.

Sangan *et al.* (2013a) presented an experimental study of EI ingress using the 1-stage facility described in Section 3. Measurements of CO_2 gas concentration were made at the design condition for two generic rim-seal geometries.

The authors used the EI orifice model developed by Owen (2011b) to form an explicit relationship between Φ_0 and ε:

$$\frac{\Phi_0}{\Phi_{min,EI}} = \frac{\varepsilon}{\left[1 + \Gamma_c^{-2/3}(1-\varepsilon)^{2/3}\right]^{3/2}} \tag{2.14}$$

This is known as the EI effectiveness equation. The model therefore provides an estimate of $\Phi_{min,EI}$ from experimental data without any knowledge of the pressure distribution in the annulus, or the associated rim-seal discharge coefficients, making it a powerful tool for rim-seal design.

The non-dimensional ingress flow into the wheel-space, Φ_i, was determined from the measurements of Φ_0 and ε using:

$$\Phi_i = \Phi_0(\varepsilon^{-1} - 1) \tag{2.15}$$

By combining Eqs. 2.14 and 2.15:

$$\frac{\Phi_{i,EI}}{\Phi_{min,EI}} = \frac{1-\varepsilon}{\left[1 + \Gamma_c^{-2/3}(1-\varepsilon)^{2/3}\right]^{3/2}} \tag{2.16}$$

Figure 2.23 shows the comparison between the experimental data and the theoretical variation of effectiveness, determined by Eq. 2.14, for the axial-clearance seal. For the design condition the data are shown to be characterised by $\Phi_{min,EI}$, which is independent of Re_ϕ. The ingested flow rate was also presented as $\Phi_{i,EI}$, along with the theoretical variation obtained using Eq. 2.16. The results showed the agreement between the optimum theoretical curves and the experimental data was very good. The radial-clearance seal was found to require 26% of the sealing flow rate to prevent ingestion compared to the axial-clearance seal.
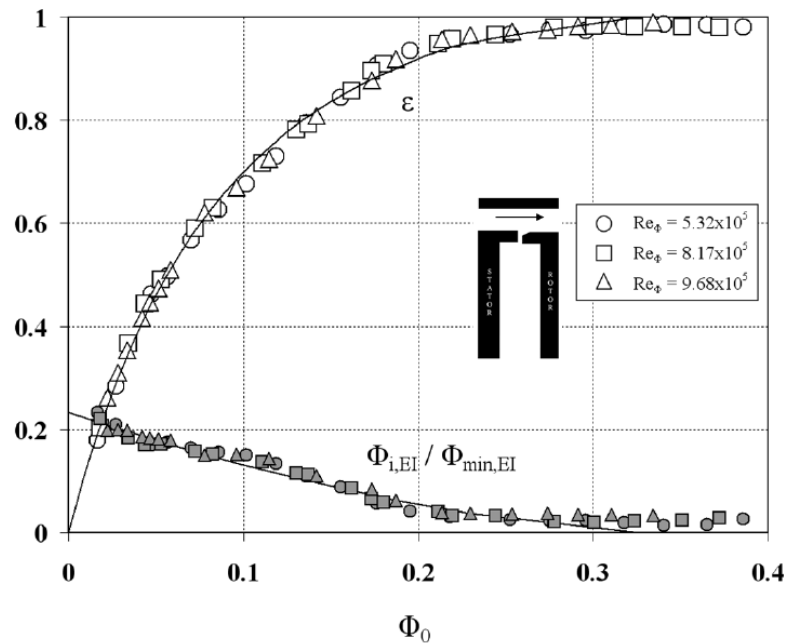
Figure 2.23: Comparison between theoretical effectiveness curves and experimental data for axial-clearance seal - Sangan *et al.* (2013a)

Sangan *et al.* (2013b) measured the variation of ε with Φ_0 for three values of Re_ϕ under RI ingress conditions. The same rim-seal geometries were used as Sangan *et al.* (2013a). The RI orifice model developed by Owen (2011a) was used to form an explicit relationship between Φ_0 and ε for the rotationally induced case:

$$\frac{\Phi_0}{\Phi_{min,RI}} = \frac{\varepsilon}{\left[1+(1-\varepsilon^{1/2})\right]\left[1+\Gamma_c^{-2}(1-\varepsilon)\right]^{1/2}} \qquad (2.17)$$

This is known as the RI effectiveness equation.

Once again in combination with Eq. 2.15, the non-dimensional ingress flow into the wheel-space for RI ingress can be derived from Eq. 2.17:

$$\frac{\Phi_{i,RI}}{\Phi_{min,RI}} = \frac{1-\varepsilon}{\left[1+(1-\varepsilon^{1/2})\right]\left[1+\Gamma_c^{-2}(1-\varepsilon)\right]^{1/2}} \qquad (2.18)$$

As shown in Figure 2.24, the ratio of $\Phi_{min,EI}$ / $\Phi_{min,RI}$ was determined as 3.9 for the axial seal and 2.9 for the radial-clearance seal.
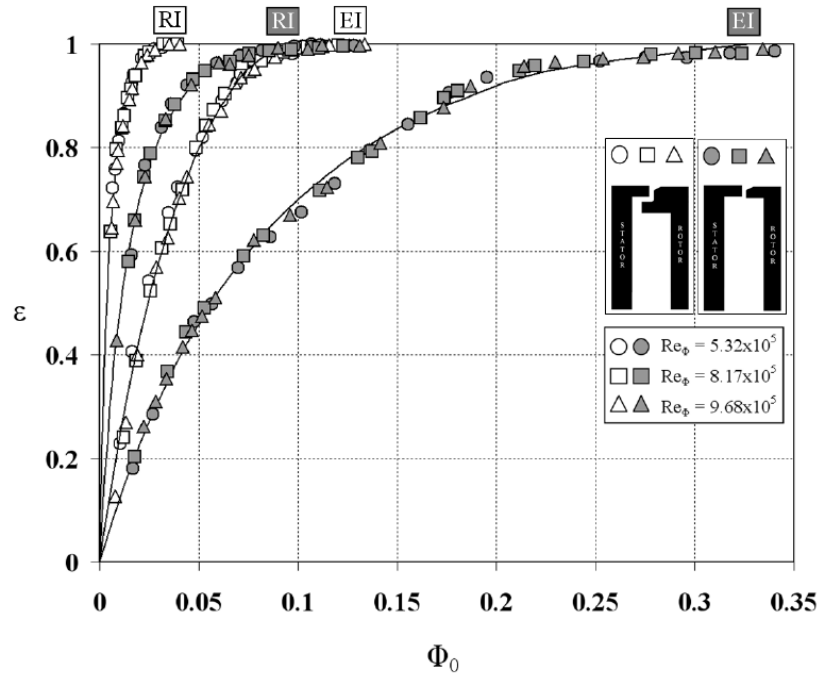
Figure 2.24: Comparison of sealing effectiveness for EI and RI ingress - Sangan *et al.* (2013b)

Zhou *et al.* (2013a) developed a statistical fitting technique based on a maximum likelihood method to determine the optimum values of $\Phi_{min,EI}$, $\Phi_{min,RI}$ and Γ_c in order to fit the solutions of Eqs. 2.14 and 2.17. It was shown that the model required a minimum of 16 data points to give acceptably close agreement with 'true values' in over 90% of the cases. The fitting error, σ, in addition to the 95% confidence limits for all three variables were calculated in the technique.

Owen *et al.* (2012a) compared sealing effectiveness values determined from the saw-tooth model for EI ingress with experimental data from Johnson *et al.* (2006). In addition, steady 3D CFD was used to compute the effectiveness at several values of sealing flow rate. The computations in Figure 2.25 shows how the value of ΔC_p varied throughout the annulus. The normalised axial and radial locations, x and y, used in this figure were defined as:

$$x = 2\frac{z}{s_c}, \quad y = \frac{r - r_{inner}}{r_{outer} - r_{inner}} \tag{2.19}$$

where r_{inner} and r_{outer} are the inner and outer radii, respectively, of the external annulus.

Locations of mathematical consistency were shown to exist, where the normalised pressure difference across the seal with no sealant flow, g^*, is consistent for the orifice model fit and the computations of pressure. The red dotted lines show the 'sweet spot' locations in the annulus where this consistency criterion is satisfied exist near the upstream and downstream edges of the seal clearance.
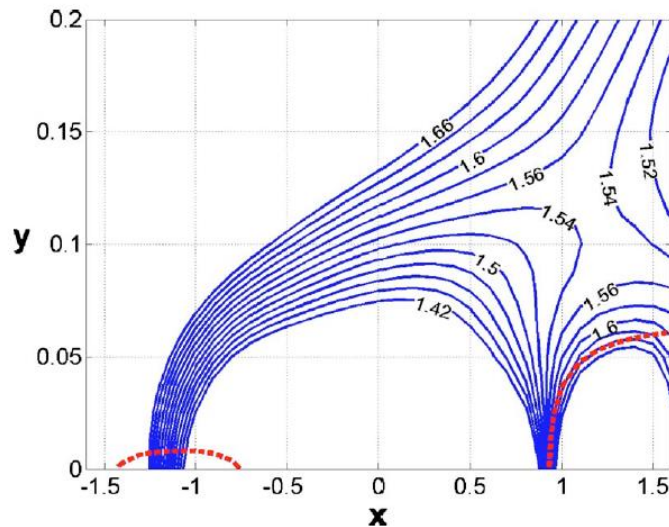
Figure 2.25: Close-up of contours of ΔC_p computed near seal clearance, dotted line corresponds to locus where the consistency criterion was satisfied - Owen *et al.* (2012a)

The combined ingress equations were validated by Owen *et al.* (2012b), using the data of Phadke and Owen (1998c). The agreement between the CI equation and the experimental data for an axial-clearance seal is shown in Figure 2.26. It was suggested, based upon the fit of the EI asymptote to data, that EI ingress occurs for $C_{w,min,CI} / C_{w,min,RI} = \Phi_{min,CI} / \Phi_{min,RI} > 2$, and below this value the effects of rotation cannot be ignored.
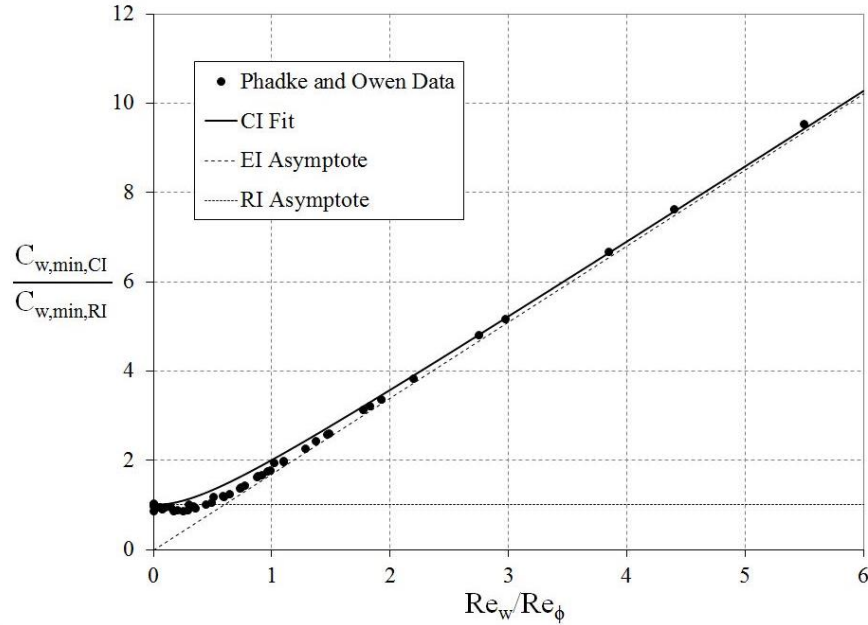
Figure 2.26: CI equation fitted to data of Phadke and Owen (1998c), CI fit is Eq. 2.12, EI asymptote is Eq. 2.10, and RI asymptote is Eq. 2.8 - adapted from Owen *et al.* (2012b)

Teuber *et al.* (2012) investigated the extrapolation of sealing effectiveness from experimental test rigs to gas turbine engine conditions. A scaling method was proposed to allow sealing flow rates to prevent ingestion, measured at incompressible flow conditions, to be extrapolated to engine-representative Mach numbers. The authors showed that, by correcting ΔC_p and assuming that the discharge coefficients are unaffected by Mach number, the sealing effectiveness, ε_c, determined by concentration measurements in an experimental rig at one Mach number, could be used to compute the effectiveness in an engine at another Mach number. Their suggested correction for Φ_{min} is:

$$\frac{\Phi_{\min,engine}}{\Phi_{\min,rig}} = \left(\frac{\Delta C_{p,engine}}{\Delta C_{p,rig}} \right)^{1/2} \tag{2.20}$$

where the ratio on the RHS of Eq. 2.19 is determined from the ratio of the Mach numbers. However, unless the location of the 'sweet spot' is known, where the consistency criterion is satisfied, the effectiveness cannot be related to the pressure differences in the engine. This makes the method of limited use to designers.
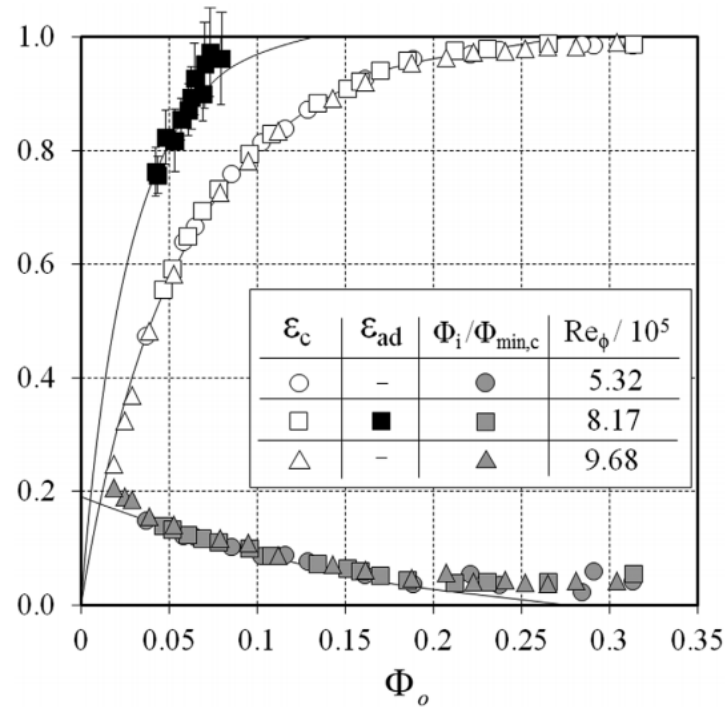
Figure 2.27: Variation of adiabatic and concentration effectiveness with non-dimensional sealing flow parameter – Pountney *et al.* (2013)

Pountney *et al.* (2013) made temperature measurements on the rotor side of the wheel-space using thermochromic liquid crystal (TLC), to determine the convective heat transfer coefficient, h, and the adiabatic surface temperature, T_{ad}. An adiabatic effectiveness, ε_{ad}, was defined for the rotor surface and from this a thermal buffer ratio, η, was derived as the ratio of $\Phi_{min,c}$ to $\Phi_{min,ad}$. Results for a mitred seal configuration, presented in Figure 2.27, showed the adiabatic effectiveness on the rotor, ε_{ad}, was significantly higher than the sealing effectiveness determined by concentration, ε_c, and consequently $\eta = 2.09$.

2.7 Summary

In conclusion this chapter has identified the most prominent literature relevant to the ingestion problem. It was shown the phenomenon can be categorised into three subsets: rotationally induced, externally induced and combined ingress. Although extensive research into RI and EI ingress exists, little experimental and theoretical consideration has been afforded to the scenario when the effects of both are significant. Combined ingress is of practical importance for gas turbines that regularly operate at off-design conditions, as well as in double seals where the pressure asymmetries that usually lead to externally induced ingress are damped out in an outer wheel-space, causing combined ingress to dominate across an inner seal.

Figure 2.28 shows the operating capabilities of current test facilities performing research into hot gas ingestion, many of which feature in this chapter. The operating points shown for each rig represent the test conditions found in the published literature and not the limitations of each individual facility. It should be noted this figure was produced using the definition of Re_w found in the nomenclature of this thesis, based on the characteristic disc radius, b. Using this definition, the flow coefficient C_F, analogous to the ratio Re_w / Re_ϕ, of the Bath single stage test rig is also plotted. The facilities that lie above this line correspond to a larger operating flow coefficient, and those that lie below equate to smaller flow coefficients. The figure shows that all the test facilities operate at similar flow coefficients.

Typical rotational Reynolds numbers found in gas turbine engines are of the order 2-3 $\times$ 10^7 (Childs (2011)). From Gentilhomme (2004), a typical design point flow coefficient for an industrial gas turbine is around $C_F = 0.6$, resulting in an axial Reynolds numbers of 1.2-1.8 $\times 10^7$.
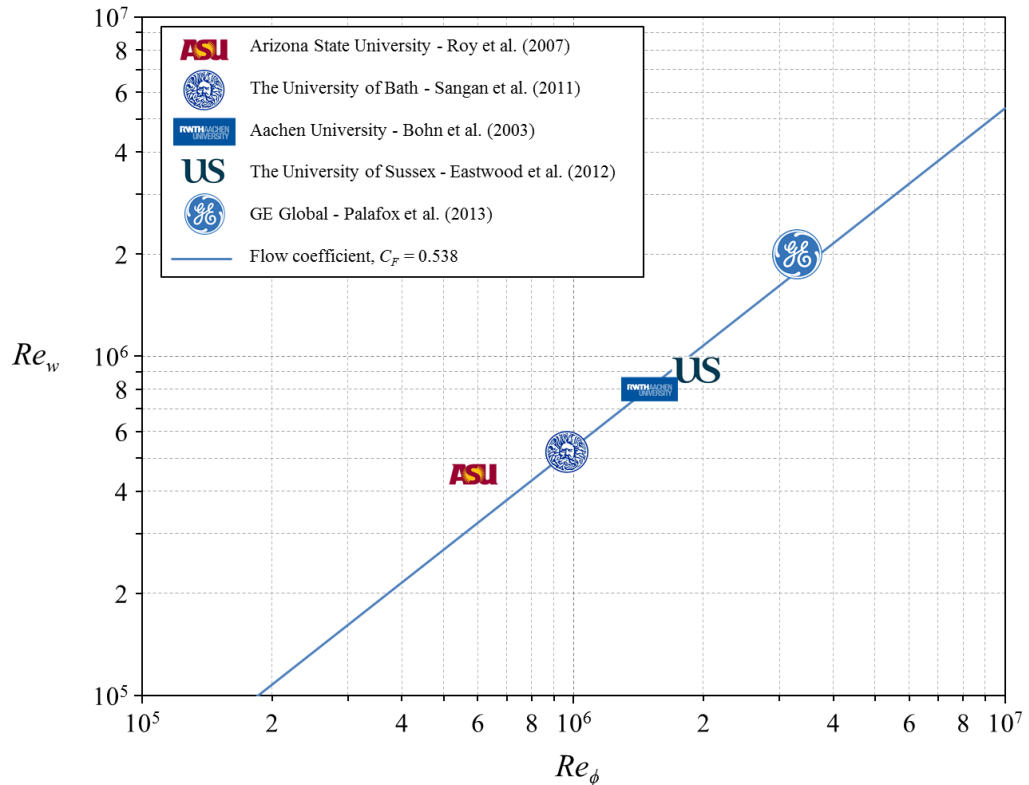
Figure 2.28: Operating capabilities of current rotating wheel-space test facilities

Other researchers have used alternative definitions of Re_w when presenting their work, usually based on vane axial chord length or vane exit velocity. Figure 2.29 shows the operating capabilities of the test facilities using the following definition of Re_w:

$$\mathrm{Re}_w{}^* = \frac{\rho W c_x}{\mu} \qquad (2.21)$$

Using this definition has allowed the new Penn State research rig to be included for comparison. This is a 1.5 stage facility currently under construction that can operate at near engine conditions, similar to the GE Global rig presented by Palafox *et al.* (2013). The reduction in axial Reynolds number capability for the Bath rig using this definition is due to the comparatively small axial size of the vane aerofoils used (c_x). Although Figure 2.23 and Figure 2.29 do not demonstrate a comparison of the complete individual rig capabilities, they do give an indication of the philosophies adopted by each research group.
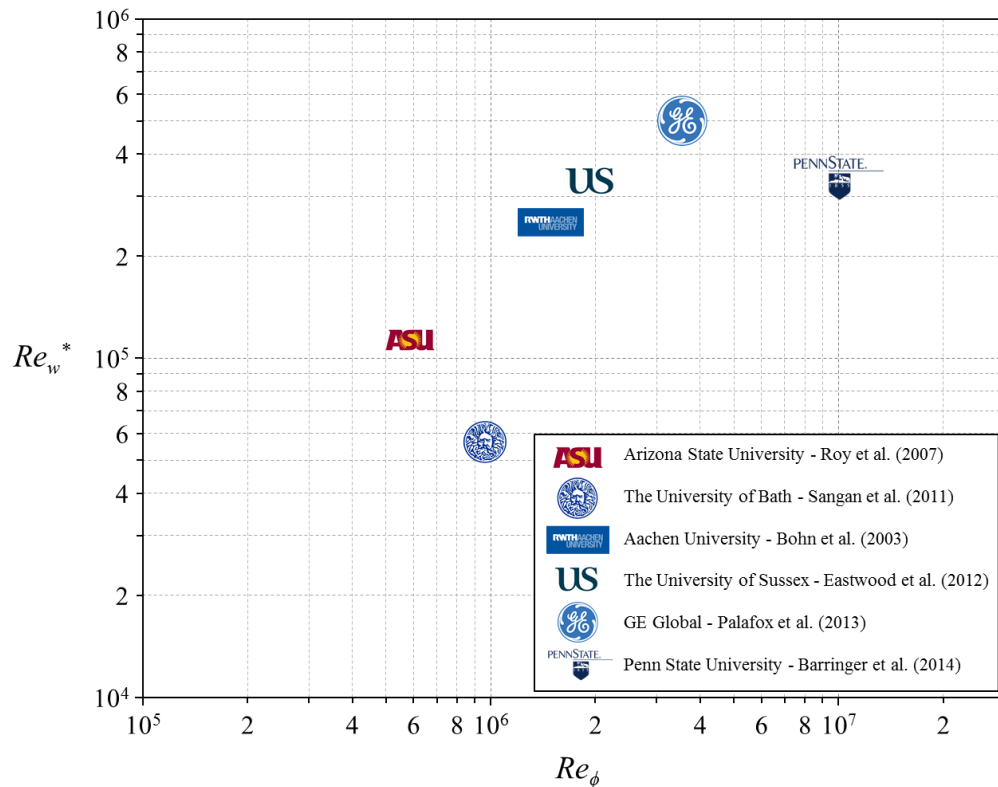
Figure 2.29: Operating capabilities of current rotating wheel-space test facilities – alternative definition of Re_w used

In practice it is uneconomical and sometimes impossible to make meaningful measurements using full size gas turbine replicas operating at real engine conditions. Consequently, research is often conducted using scaled test rigs to model the fluid dynamic behaviour at a more benign environment. Experiments using simpler geometries than those found in real engines are used to further understand the fundamental fluid dynamic principles involved. From these experiments, accurate results can be used to determine design criteria that can be scaled to engine operating conditions through the use of theoretical models. The experimental measurements also provide valuable CFD validation data. This allows for greater confidence to be gained when extrapolating results from computational codes to real life engine scenarios.

Chapter 3: Experimental measurements of ingestion through single and double rim seals

This chapter presents concentration sealing effectiveness measurements, pressure and swirl ratio measurements made experimentally using the University of Bath single-stage rig, for three rim seal geometries at EI and RI ingress conditions. Details of the test geometry, experimental operating conditions, concentration and pressure measurement techniques are all discussed in detail prior to the presentation of the experimental results. Finally, experimental uncertainty levels and practical implications are considered. The author of this thesis conducted all the experimental testing and analysis involved in this chapter.

3.1 Experimental test rig

This section summarises the University of Bath single-stage experimental gas turbine test facility. For a full description of the design and commissioning of this facility, the reader is directed towards Sangan (2011).

3.1.1 Test section

The 1-stage test rig experimentally simulates hot gas ingestion into the wheel space of an axial turbine stage. The test section of the facility, shown in Figure 3.1, features a single turbine stage with 32 vanes and 41 blades. The disc to which the blades were attached could be rotated by an electric motor. To avoid the necessity of a dynamometer to extract excess power, the blades were symmetric NACA 0018 aerofoils.

The vanes and blades, formed from nylon by rapid-prototyping, were secured to aluminium platforms which form the periphery of the stator and rotor respectively. Both the stationary and rotating discs (highlighted in red and blue, respectively, in Figure 3.1) were manufactured from transparent polycarbonate to allow optical access to the wheel-space for the application of thermochromic liquid crystal (TLC). The characteristic radius of the facility, b, measured from the centreline to the inside of the stator shroud was 190 mm.
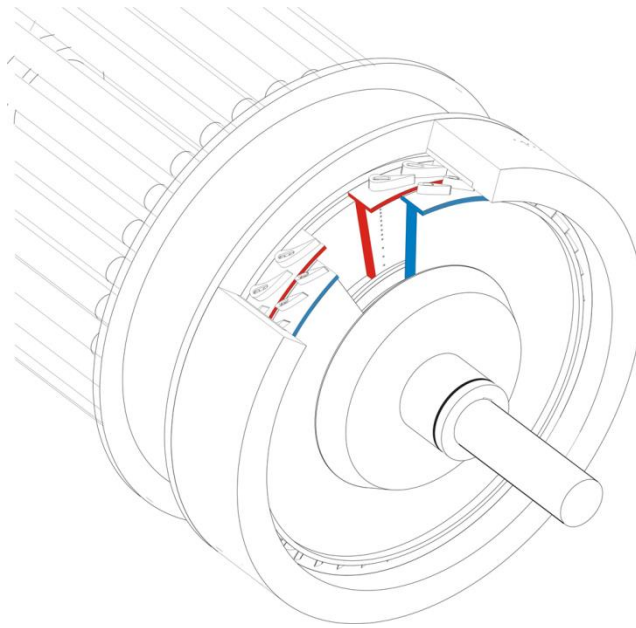
Figure 3.1: 1-stage rig test section showing turbine stage - the stator is shown in red and the rotor in blue

Displacement transducers were used to measure the axial deflection of the disc. The axial clearance of the seal was found to increase slightly when under rotation and when sealing flow pressurised the wheel-space, but at the maximum value of sealant flow tested the axial deflection was < 8% of the clearance. Displacement transducers were also used to measure the radial growth of the disc, rotor platform and radial-clearance of the seal under rotation. In all cases, the measured radial growth agreed with FEA predictions and was found to be linearly proportional to the square of the disc speed.

Compressed air is supplied to the rig for the external flow via a radial diffuser and 32 feed pipes (one per stator vane). The static pressure of the air in each feed pipe was measured to be axisymmetric to within ± 5%. The pipes in turn supplied a convergent transition section which fed into the test section annulus. The height of this annulus, *h*, was limited to 10 mm in order to create the necessary flow velocities at the design point for the largest rotational speed. Sangan (2011) estimated the boundary layer thickness to be 3.47% of the total flow area through the annulus using the one-seventh power law approximation. It was therefore concluded that a substantial amount of the ingestion into the wheel-space came from the mainstream flow rather than the boundary layer.

Figure 3.1 shows the different mass flows involved in the experiment. Both the sealant and external mass flow rates were measured using orifice plates manufactured to EN ISO 5167-2. The orifice plates were calibrated using a Rotameter to within ± 3% uncertainty.
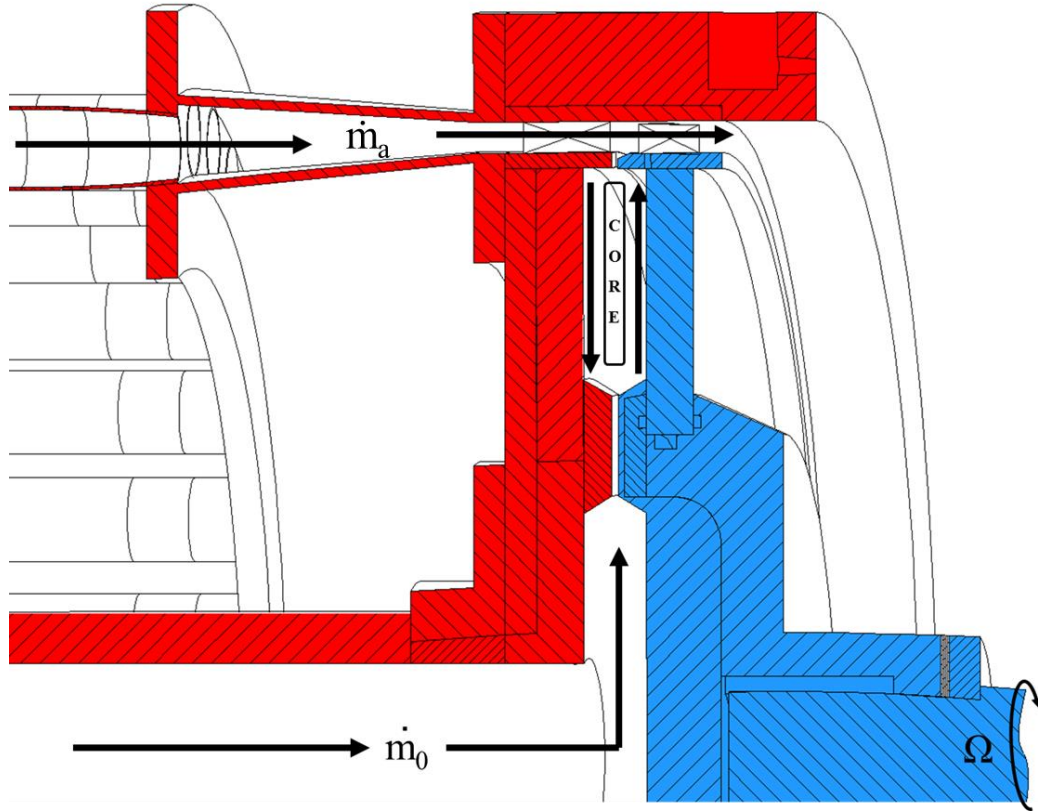
Figure 3.2: 1-stage rig test section showing sealing and mainstream flows- the stator is shown in red and the rotor in blue

The vanes and blades in the annulus produced a flow structure representative of those found in engines, albeit at lower Reynolds and Mach numbers. With reference to the velocity triangle in Figure 3.3, the air leaves the vane at an angle α with a velocity C and corresponding Mach number $M = C/a$. The design condition vane exit and blade inlet angles were determined from CFD analysis performed by Siemens as $\alpha = 73.5°$ and $\beta_0 = 56.7°$ respectively. From Saravanamuttoo *et al.* (2009):

$$\tan\alpha = \tan\beta_0 + \frac{1}{C_{F,0}}$$
(3.1)

which resulted in a design point flow coefficient ($C_{F,0} = Re_w / Re_\phi$) of 0.539, where Re_w is the Reynolds number based on the axial component of velocity in the annulus.

The disc could be rotated up to speeds of 4000 rpm, providing a maximum rotational Reynolds number, Re_ϕ (based on disc radius) up to 1.1×10^6. This value is typically an order-of-magnitude less than that found in gas turbines. However, for rotating flow the turbulent flow structure in the boundary layers is principally

governed by the turbulent flow parameter, λ_T, and depends only weakly on Re_ϕ [Owen and Rogers (1989)]. Hence the flow structure in the rig is considered to be representative of that found in the cooling systems of engines.
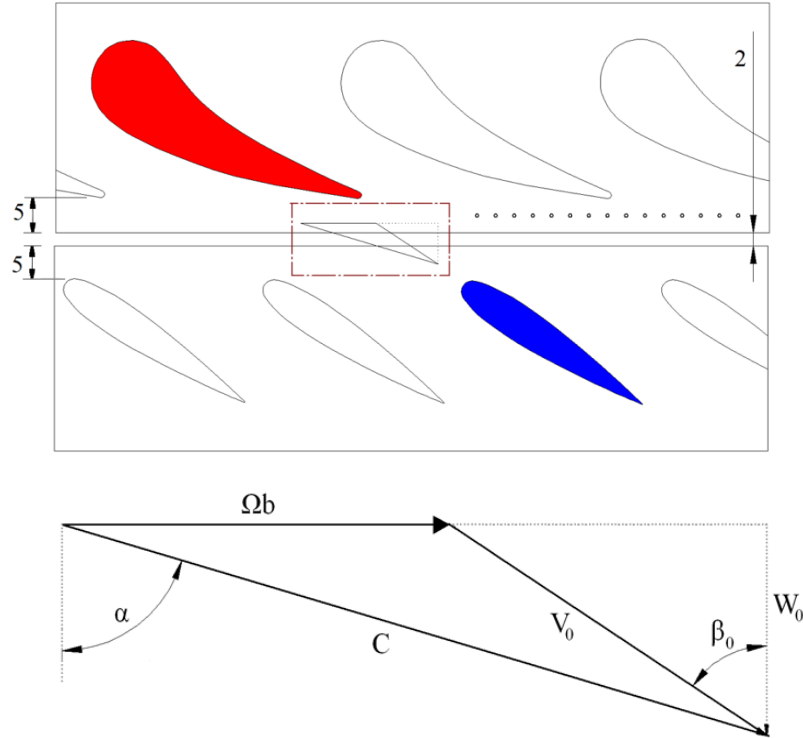
Figure 3.3: Profiles and velocity triangles for vanes and blades

Table 3.1 details the operating conditions at the three on-design rotational speeds tested. The flow exiting the vanes is virtually incompressible and near atmospheric pressure; the density, ρ, speed of sound, a, and air viscosity, μ, are determined from the static temperature and pressure measured inside the wheel-space on the stator at $r/b = 0.993$.

Parameter	Disc Speed (RPM)		
	2000	**3000**	**3500**
α		73.5°	
β_0		56.7°	
Re_w / Re_ϕ		0.538	
Re_ϕ	5.32×10^5	8.17×10^5	9.68×10^5
Re_w	2.86×10^5	4.40×10^5	5.21×10^5
Ωb	39.8 m/s	59.7 m/s	69.6 m/s
$\dot{m}_a$	0.33 kg/s	0.49 kg/s	0.58 kg/s
W_0	21.5 m/s	32.2 m/s	37.6 m/s
V_0	39.1 m/s	58.6 m/s	68.4 m/s
C	75.5 m/s	113.3 m/s	132.2 m/s
M	0.225	0.339	0.398

Table 3.1: Operating conditions for the three on-design rotational speeds

The axial spacing between the vane trailing edge and the blade leading edge was 12 mm, equivalent to 0.52 vane axial chords. The rim-seal clearance was 2 mm and located equidistant between the vane and blade. To take into account of radial growth under rotation, the rotor disc was designed with a 0.4 mm radial step. A chamfer was also machined onto the leading edge of the rotor shroud to prevent flow impingement.
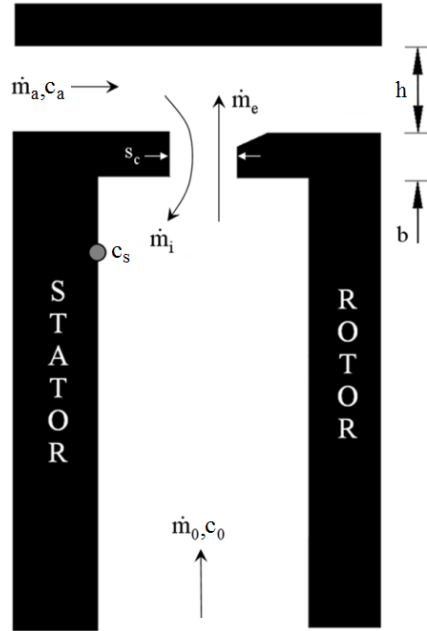
Figure 3.4: Simplified diagram of massflows and concentrations in test section for axial-clearance seal

The effectiveness ε used in the Bath theoretical orifice model is based on the ratio of the isentropic massflow rates of ingress and egress. The model ignores the friction, diffusion, heat transfer and mixing that occurs in the physical world. The term theoretical effectiveness is therefore used here for ε, which with reference to Figure 3.4 is defined as:

$$\varepsilon = 1 - \frac{\dot{m}_i}{\dot{m}_e} = \frac{\dot{m}_o}{\dot{m}_o + \dot{m}_i} \qquad (3.2)$$

where the subscripts e, i and 0 denote the egress, ingress and sealing flows respectively. It follows that the sealing effectiveness equals unity when the ingress is zero, and equals zero when there is no sealing flow. Expressed in terms of the flow parameter Φ, Eq. 3.2 becomes:

$$\varepsilon = 1 - \frac{\Phi_i}{\Phi_e} = \frac{\Phi_o}{\Phi_o + \Phi_i} \qquad (3.3)$$

It is difficult (and unnecessary) to determine ε experimentally; instead gas concentration measurements can be used to determine the concentration effectiveness, ε_c.

3.1.2 Concentration measurements

To measure the degree of ingestion, the sealant air was seeded with approximately 1% CO_2 and introduced into the wheel-space at a low radius ($r/b = 0.642$) through an inlet seal. The concentration of CO_2 was monitored at the entrance to the wheel-space, c_0, and in the unseeded upstream flow through the annulus, c_a. The variation of concentration c_s with radius ($0.55 < r/b < 0.993$) along the stator in the wheel-space was determined by sampling through 15 tubes of diameter 1.6 mm (shown in Figure 3.5). The gas was extracted by a pump, which delivered the samples to a Signal Group 9000 MGA dual channel infrared gas analyser. The analyser was calibrated using an alpha-grade pure N_2 as zero-gas and a 3% CO_2 in N_2 as the span-gas; this enabled a linear calibration of the analyser to take place. The pump was set to 0.3 l/min (equivalent to 0.000006 kg/s), which was the minimum sampling flow rate possible. In comparison, the sealant flow rate ($\dot{m}_0$) was varied between 0.001-0.07 kg/s therefore the disturbance to the boundary layer was deemed negligible.

Concentration sealing effectiveness, ε_c, was therefore determined from the CO_2 concentration measurements on the stator wall using the following equation:

$$\varepsilon_c = \frac{c_s - c_a}{c_o - c_a}$$

(3.4)

For consistency with Eqs. 3.2 and 3.3, $\varepsilon_c = 1$ when $c_s = c_0$ (zero ingress) and $\varepsilon_c = 0$ when $c_s = c_a$ (zero sealing flow).

The definition of effectiveness used in the orifice model is based upon the pressure difference between the annulus and wheel-space. The model does not consider diffusion resulting from the concentration difference across the rim-seal. It was assumed that the diffusion term was small and that $\varepsilon_c = \varepsilon$; this allowed the orifice equations to be fitted to the measured variation of ε_c with Φ_0.
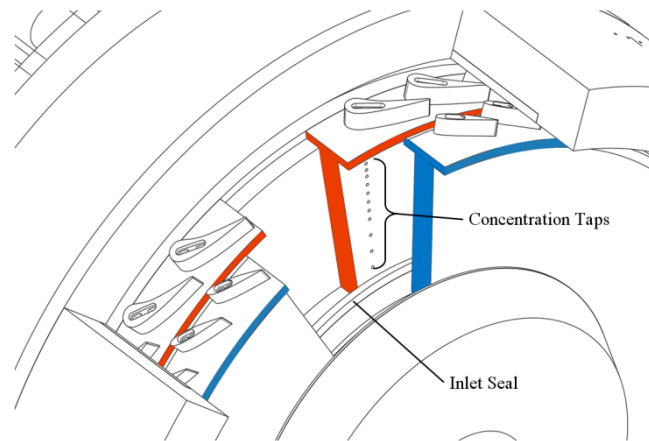
Figure 3.5: Rig test section showing concentration measurement locations - red represents stationary components, blue rotating

3.1.3 Pressure measurements

Steady pressure measurements were made at various locations in the test rig using a Scanivalve© system with Druck PDCR 22 transducers. The circumferential variation of static pressure in the annulus was measured at two locations: location A, on the stator shroud hub 2.5 mm downstream of the trailing edge of the vane; and B, in the outer casing above the centre-line of the seal clearance. At both locations the variation of static pressure was determined from 15 taps, each of 0.5 mm diameter, equally spaced across a single vane pitch $(0 < \theta < 1)$, as shown in Figure 3.3 and Figure 3.6. Data for location A was averaged over four vane pitches at 90° separations.
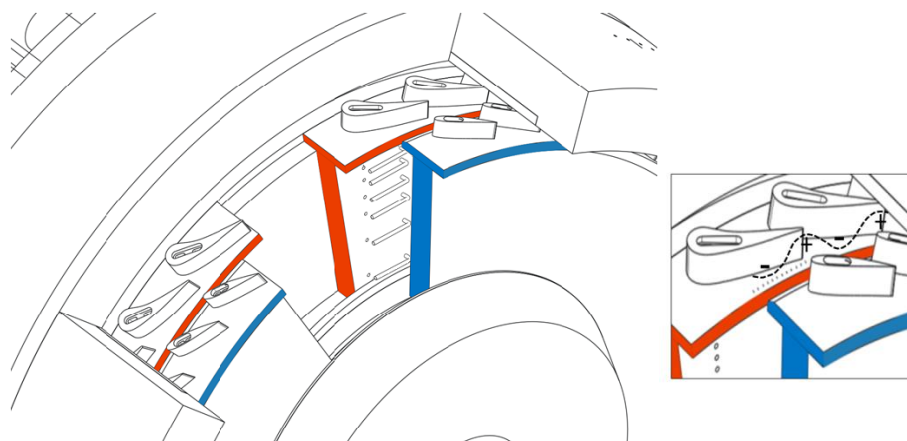
Figure 3.6: Rig test section showing pressure measurement instrumentation and typical pressure asymmetry in the annulus

The pressure coefficient, C_p, is defined as:

$$C_p = \frac{p_a - \bar{p}_a}{1/2 \rho \Omega^2 b^2}$$

(3.5)

where p_a is the local static pressure at the normalised angular measurement location between vanes, θ, and $\bar{p}_a$ the mean pressure across this pitch. The variation of C_p with θ at location A is plotted in Figure 3.7 for the design condition with $Re_\phi = 8.17 \times 10^5$ and zero sealant flow. i.e. $\Phi_0 = 0$.
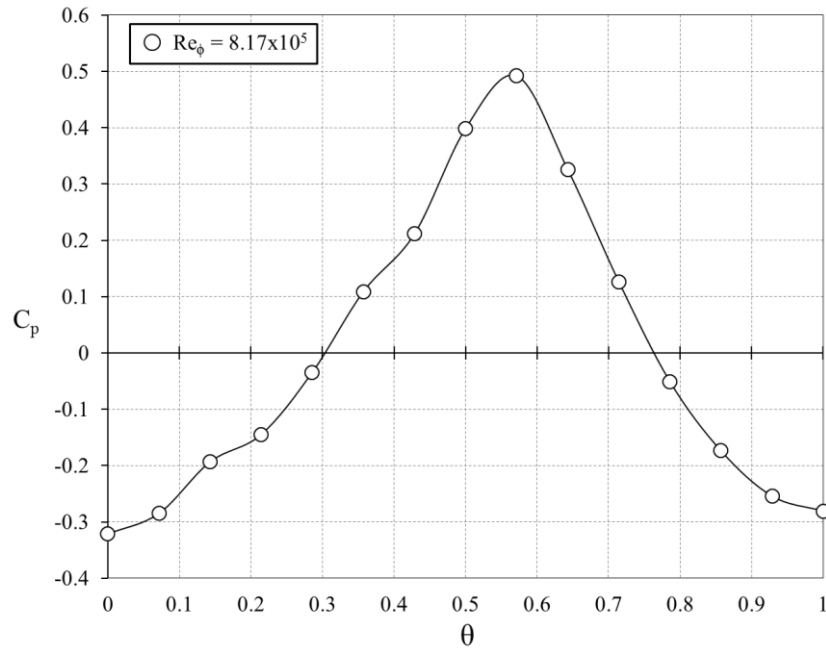
Figure 3.7: Circumferential distribution of C_p over non-dimensional vane pitch at design condition

It should be emphasised that this distribution is measured at an arbitrary location in a single stage rig with symmetrical rotor blades. It is expected that the inclusion of realistic turned blades would have had an effect on this pressure variation due to a stronger bow wave interaction from the rotor blades.

EI ingress is related to the non-dimensional pressure difference in the annulus, ΔC_p, where:

$$\Delta C_p = \frac{\Delta p_a}{1/2 \rho \Omega^2 b^2}$$

(3.6)

Δp being the peak-to-trough static pressure difference. From Figure 3.7, this non-dimensional driving potential ΔC_p is equal to 0.82. Sangan *et al.* (2011) showed that ΔC_p decreases slightly as the flow rate of sealing air increases. For the saw-tooth orifice model

derived by Owen (2011b), the sealing parameter for necessary to prevent EI ingress, $\Phi_{min,EI}$ is related to ΔC_p by:

$$\Phi_{min,EI} = \frac{2}{3} C_{d,e} \Delta C_p^{1/2} \qquad (3.7)$$

where C_{de} is the discharge coefficient for egress through the rim-seal. For mathematical consistency in the EI orifice model, it is necessary that there is zero ingress when $\Delta C_p = 0$. However, as ΔC_p will depend on where in the annulus it is measured, caution must be taken when comparing values from different studies.

Static pressure was also measured in the wheel-space at the same radial locations as the concentration measurements in order to determine the wheel-space fluid dynamics. Seven total pressure probes (shown in Figure 3.6) positioned at an axial position of $z/s = 0.25$ away from the stator disc were used to measure the variation of tangential velocity with radius. The swirl ratio of the fluid in the inviscid core between the boundary layers in the wheel-space is defined as:

$$\beta = \frac{V_\phi}{\Omega r} \qquad (3.8)$$

were V_ϕ is the tangential component of velocity in the core. In a rotating inviscid fluid the radial component of velocity must be zero and the axial gradients of the axial and tangential components of velocity must also be zero. All radial flow occurs inside the boundary layers, and the value of β adjusts to satisfy the continuity of the flow rate in the boundary layers.

3.2 Single rim-seal

3.2.1 Geometry of single seal

The geometry and static dimensions of the single radial-clearance rim seal are shown in Figure 3.8 and Table 3.2. This seal was bolted into the underside of the rotor shroud forming a seal lip positioned at a smaller radius than the stator shroud. A thumb-nail sketch of the seal configuration and measurement location (denoted by the white circle) is shown. It should be noted that the external flow is from left to right, i.e. from the stator towards the rotor. The seal-clearance ratio, $G_c = s_{c,ax} / b = 0.0105$ used in Eq.2.5 for all seal geometries, is based on an static axial clearance $s_{c,ax}$ of 2 mm.
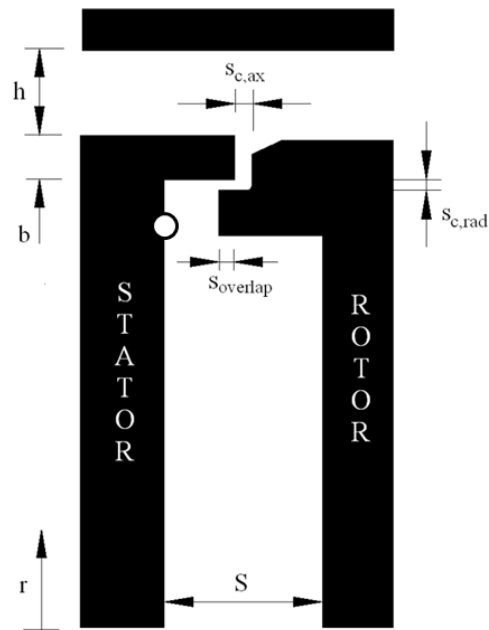
Figure 3.8: Geometry of radial-clearance seal

Geometric Symbol	Dimension
h	10 mm
b	190 mm
S	20 mm
$s_{c,ax}$	2 mm
$s_{c,rad}$	1.28 mm
$s_{overlap}$	1.86 mm

Table 3.2: Dimensions of radial-clearance seal

3.2.2 Experimental results of single seal
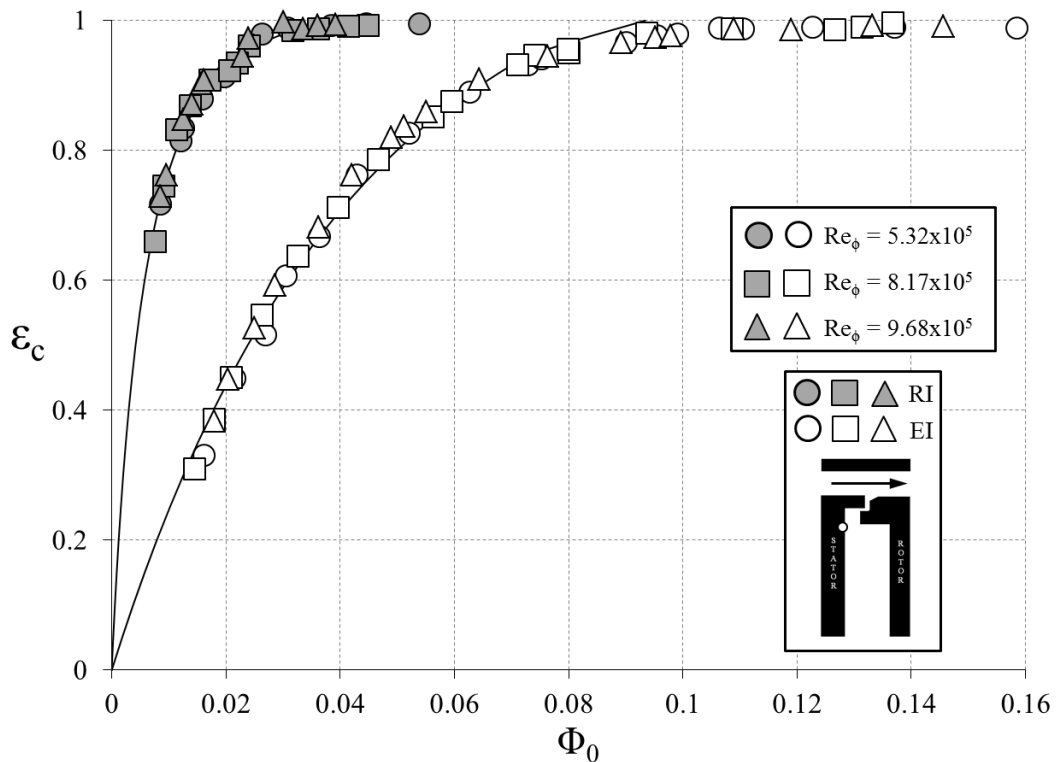
Figure 3.9: Variation of ε_c with Φ_0 for radial-clearance seal: EI and RI ingress (Symbols denote data; lines are theoretical curves)

For the results in Figure 3.9, the effectiveness values were based on the concentration measurements made on the stator surface at $r/b = 0.958$. The figure illustrates that ε_c increases with increasing Φ_0, as the sealing flow pressurises the wheel-space and reduces ingestion through the rim-seal. The data collapses onto a single curve, which is independent of rotational Reynolds number, Re_ϕ. The sealing effectiveness for the RI case is significantly greater than that for the EI case; i.e. for the same sealing flow rates, EI ingress causes much more ingestion. The RI tests were conducted with the inlet to the annulus closed but with the outlet open to the atmosphere. As the stationary vanes and rotating blades were still present in the annulus, rotation would have created swirl in the external fluid. However, as found by Graber *et al.* (1987), the external swirl did not appear to affect RI ingress, as confirmed by the collapse of the data in Figure 3.9 with rotational speed. The EI tests were conducted by adjusting the mainstream mass flow rate to maintain balanced velocity triangles for each rotational speed, as shown in Figure 3.3.

The theoretical effectiveness curves were based on Eqs.2.14 and 2.17, and were fitted to the data based on the maximum likelihood method described by Zhou *et al.* (2013a). The estimated values of Φ_{min} and Γ_c and their 95% confidence intervals are shown in Table 3.3 for both the EI and RI data. Also shown is the standard deviation, σ, between the data and the fitted curves. The ratio of $\Phi_{min,RI}/\Phi_{min,EI}$ is approximately 39%.

Parameter	EI	RI
Φ_{min}	0.0934	0.0361
Φ_{min}^{-}	0.0882	0.0330
Φ_{min}^{+}	0.100	0.0407
Γ_c	1.17	0.305
Γ_c^{-}	0.928	0.254
Γ_c^{+}	1.45	0.354
σ	0.0185	0.0131

Table 3.3: Parameters for radial-clearance seal at EI and RI ingress conditions

Both sets of data show very good agreement between the theoretical curves and the data, as highlighted by the relatively small values of σ in Table 3.3. It can be seen from Table 3.3 that the confidence intervals are around 10% of the estimated value of Φ_{min} for both cases. As Figure 3.9 shows, it is very difficult to determine the precise value of Φ_0 when ε first equals unity, and there is a consequential uncertainty in the determination of Φ_{min}. The value of Φ_0 at $\varepsilon = 0.95$ has a smaller associated uncertainty, and there is a case for using this rather than Φ_{min} as a design criterion for RI and EI ingress.
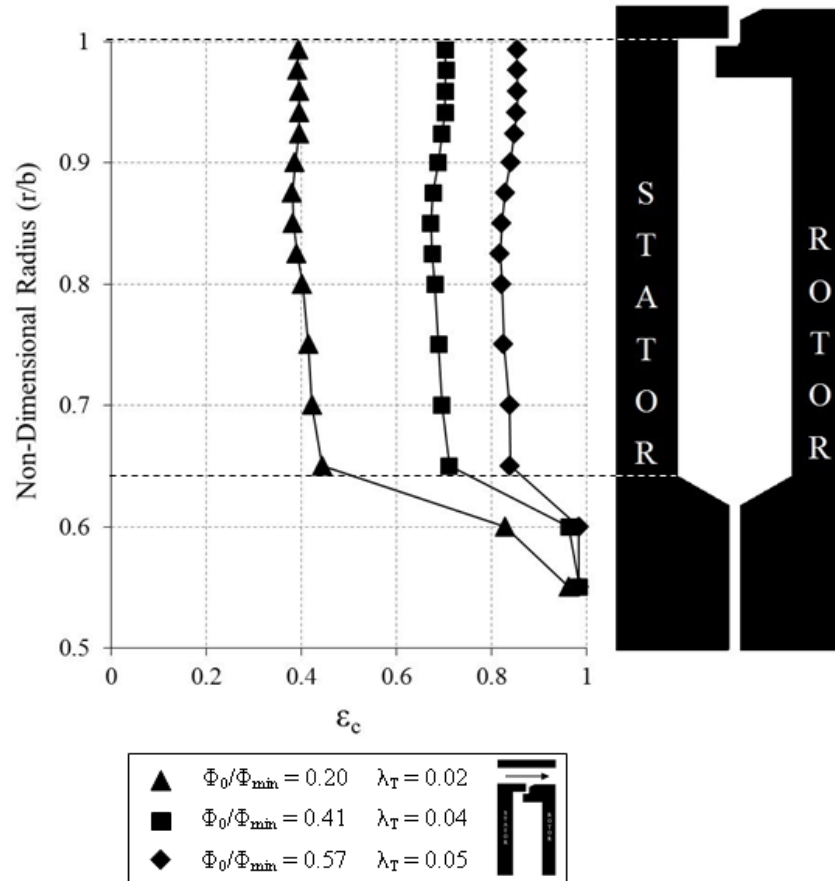
Figure 3.10: Effect of sealing flow rate on radial distribution of effectiveness

Figure 3.10 shows the radial variation of ε_c on the stator surface for tests at $Re_\phi = 8.17 \times 10^5$. The tests were conducted for several values of Φ_0/Φ_{min} and λ_T; in all cases ingress occurred. As expected, ε_c increases as Φ_0/Φ_{min} increases. For all sealant flow rates the effectiveness is broadly invariant with radius for $r/b > 0.65$, suggesting that near-complete mixing has occurred in a region very close to the rim-seal. If the flow was not fully mixed then there would be concentration gradients in the stator boundary layer and consequently a radial variation. The rapid increase in ε_c at the smaller radii is caused by the presence of the inner seal, which prevents or strongly reduces the ingestion of fluid into the region where the sealing flow is introduced.
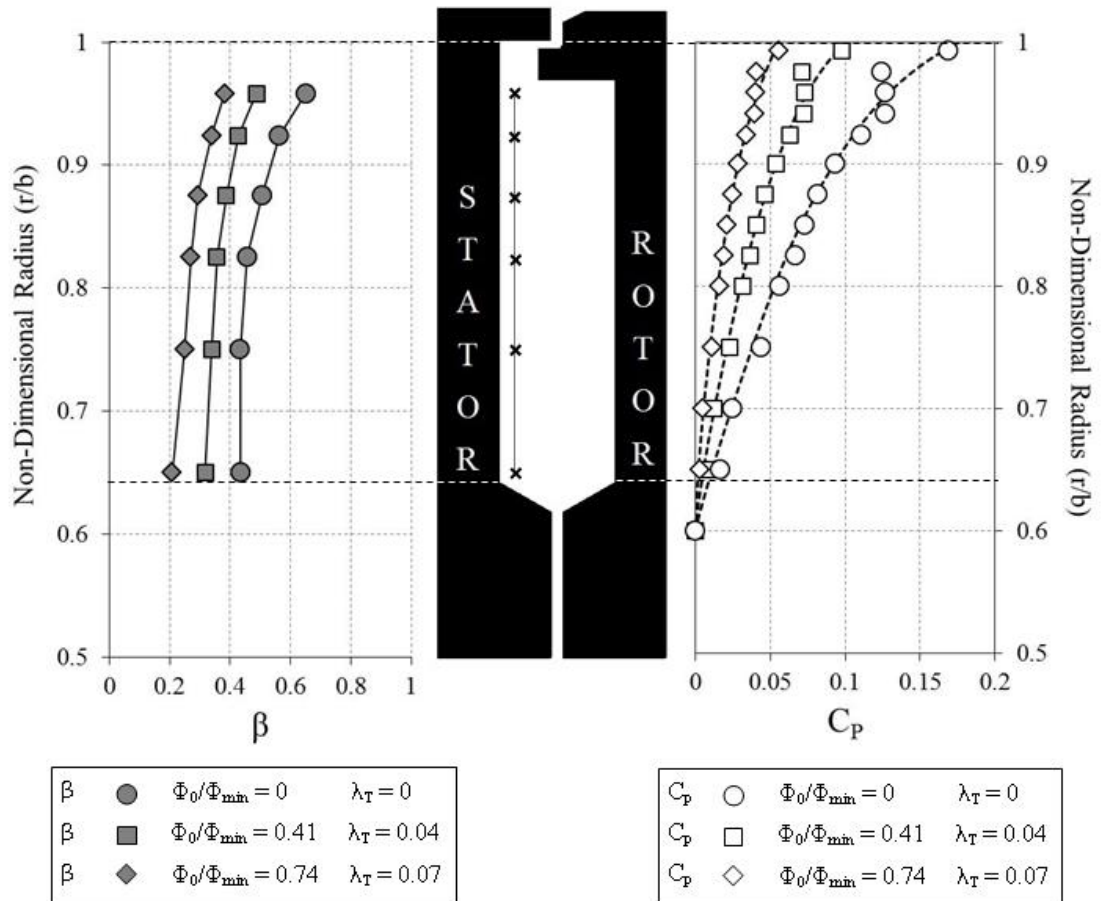
Figure 3.11: Effect of sealing flow rate on radial distribution of swirl ratio and static pressure coefficient for radial-clearance seal (Symbols denote measured values; lines denote fitted distribution for β and calculated distribution for C_p)

Figure 3.11 illustrates the variation of swirl ratio and static pressure coefficient in the wheel-space with non-dimensional radius at $Re_\phi = 8.17 \times 10^5$ for several values of λ_T and hence Φ_0. The measurement points for the total pressure in the wheel-space (at $z/S = 0.25$) are also shown on the silhouette in the middle of the figure. In all cases ingress occurred with an annulus swirl ratio, $\beta_a = 1.8$, determined from the isentropic velocity triangle shown in Figure 3.3. For $\lambda_T = 0$, there is no superposed flow and the core rotation $\beta = 0.44$ is observed for $r/b < 0.8$, in agreement with Daily et al (1964). The swirl ratio at the larger radii outside of the core region increases radially outward with the influence of highly swirling ingested flow. The case $\lambda_T = 0$ has the maximum ingress and the concentration effectiveness everywhere in the wheel-space is zero. Increasing the sealing flow caused a reduction in the core rotation as the wheel-space is pressurised. The level of swirl at the periphery of the wheel-space also reduced as the increased sealant flow decreased ingestion from the annulus.

Consider now the variation of C_p in the wheel-space, shown on the right hand side of Figure 3.11. For a rotating inviscid core, the radial momentum equation reduces to a balance between the pressure force and the centripetal acceleration so that:

$$\frac{1}{\rho}\frac{dp}{dr} = \frac{V_\phi^2}{r}$$

(3.9)

Using the definitions of C_p and β, Eq. 3.9 can be integrated to give:

$$C_p = \frac{p\text{-}p_{ref}}{0.5\rho\,\Omega^2 b^2} = 2\int_{x_{ref}}^{x} x\beta^2 dx$$

(3.10)

where p_{ref} is the pressure at $x = r/b = x_{ref}$; for the results presented here, $x_{ref} = 0.6$. The numerical integration was carried out using Simpson's rule, with values of β obtained from a least-squares cubic spline fitted to the experimental data.

The results show very good agreement between the calculated and measured distributions of C_p. This shows that the radial distribution of the swirl ratio determines the radial distribution of pressure in the wheel-space.

In an engine, the pressure distribution at the inlet to the wheel-space is fixed by the outlet pressure of the compressor and by the flow rate of the sealing air. For given conditions, the distribution of swirl and pressure in the wheel-space is also fixed by the flow rate, and as shown this determines the pressure near the outlet of the wheel-space. In principle therefore, if the variation of the swirl ratio with flow rate were known, the sealing effectiveness could be calculated.

3.3 Double rim seal

This section assesses the performance of a double radial-clearance seal. For turbine applications, the advantage of a double seal is that the annular cavity (or outer wheel-space) between the inner and outer seals acts as a damping chamber so that the circumferential pressure differences generated in the annulus are attenuated (as highlighted in Figure 3.12). The amount of sealing air required to prevent ingress through the inner seal (into the inner wheel-space) is therefore significantly less than that required for a single seal. If the pressure asymmetry in the outer wheel-space is eliminated, EI ingress will dominate for the outer seal and RI ingress for the inner one.

Figure 3.12: Variation of static pressure in a turbine annulus. Red and blue indicate regions of high pressure and low pressure with respect to the wheel-space, respectively. For the double rim-seal shown, the pressure asymmetry is attenuated in the outer wheel-space between the two seal clearances.

3.3.1 Definitions of sealing effectiveness for double seals
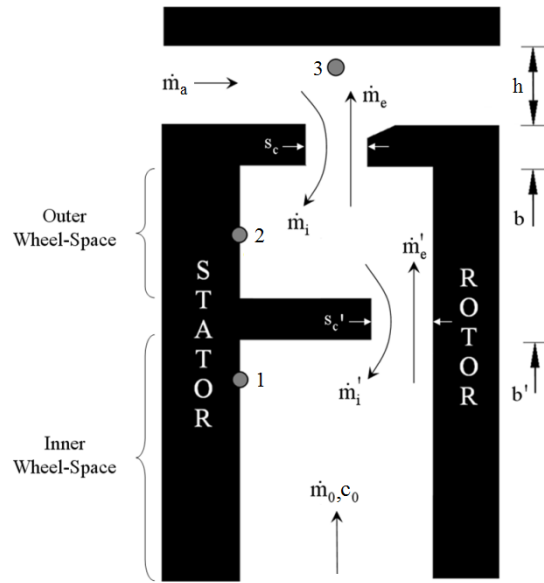
Figure 3.13: Simplified diagram of massflows and concentrations in test section for double seal

Figure 3.13 illustrates a double seal with inner and outer radii b' and b and clearances s_c' and s_c respectively, where primes are used to denote the inner seal. The concentrations c_0, c_1, c_2 and c_3 refer respectively to the concentration at positions at inlet, the stator at location 1 in the inner wheel-space, the stator at location 2 in the outer wheel-space, and the annulus at location 3.

There are several ways of defining the concentration effectiveness for the double seal. For example, the inner seal could have a concentration effectiveness $\varepsilon_{c,12} = 0$ when $c_1 = c_2$ and $\varepsilon_{c,12} = 1$ when $c_1 = c_0$. Hence, for the inner seal:

$$\varepsilon_{c,12} = \frac{c_1 - c_2}{c_0 - c_2} \tag{3.11}$$

For the outer seal, it could be assumed that $\varepsilon_{c,23} = 0$ when $c_2 = c_3$ and that $\varepsilon_{c,23} = 1$ when $c_2 = c_0$. Hence, for the outer seal:

$$\varepsilon_{c,23} = \frac{c_2 - c_3}{c_0 - c_3} \tag{3.12}$$

For the combined seals, it could be assumed that $\varepsilon_{c,13} = 0$ when $c_1 = c_3$ and that $\varepsilon_{c,13} = 1$ when $c_1 = c_0$. Hence, for the combined seals:

$$\varepsilon_{c,13} = \frac{c_1 - c_3}{c_0 - c_3} \qquad (3.13)$$

However, for the theoretical effectiveness based on the non-dimensional flow parameter, as shown in Eq. 3.3 for a single seal, there are only two appropriate definitions of effectiveness:

$$\varepsilon_{c,23} = \frac{\Phi_0}{\Phi_0 + \Phi_i} \qquad (3.14)$$

$$\varepsilon_{13} = \varepsilon_{12} = \frac{\Phi_0}{\Phi_0 + \Phi_i{}'} \qquad (3.15)$$

where Φ_i and $\Phi_i{}'$ are the respective non-dimensional ingress flow parameters for the outer and inner seals. This creates a paradox as there are now more definitions for ε_c than for ε. To understand this paradox, it can be shown for Eqs. 3.11 to 3.13 that:

$$\varepsilon_{c,12} = \frac{\varepsilon_{c,13} - \varepsilon_{c,23}}{1 - \varepsilon_{c,23}} \qquad (3.16)$$

For the general case of $\Phi_0 < \Phi_{min}$, Eq. 3.16 implies that $\varepsilon_{c,12} \neq \varepsilon_{c,13}$. This in turn means that these definitions produce two different values of $\Phi_i{}'$, the ingress parameter for the inner seal. This is physically impossible therefore Eqs. 3.11 and 3.13 are inconsistent.

From a physical, rather than a theoretical point of view, there is another factor. There may be differences between the concentration measured on the stator and that which exists elsewhere in the wheel-space. Therefore although c_2 might be the correct concentration to determine ingress through the outer seal, there is no reason to believe that it is the appropriate value for ingress through the inner seal. Because of this, only Eq. 3.13 is used for comparison of the performance of different double seals.

3.3.2 Geometry of double seal

A secondary inner radial-clearance seal was added to the single radial-clearance seal configuration to form the double seal shown in Figure 3.14. One advantage of this double seal design is that it can be assembled from both the axial and radial directions. For double seals, the effectiveness was determined in the inner wheel-space at $r/b = 0.85$ and in the outer wheel-space at $r/b = 0.958$.
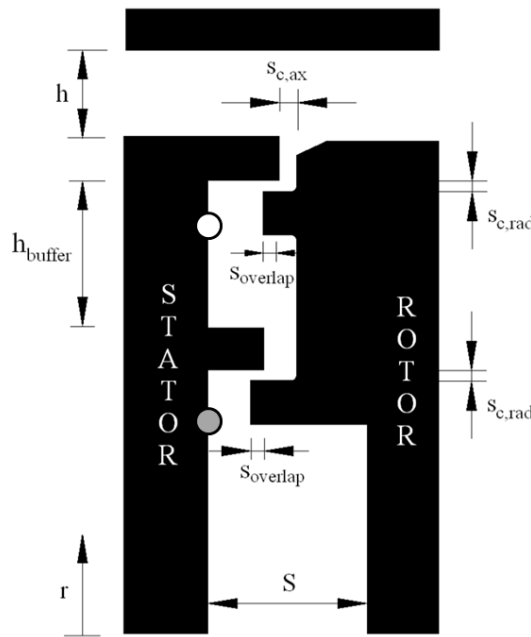
Figure 3.14: Geometry of double radial-clearance seal

Geometric Symbol	Dimension
h	10 mm
b	190 mm
S	20 mm
t	5 mm
$S_{c,ax}$	2 mm
$S_{c,rad}$	1.28 mm
$S_{overlap}$	1.86 mm
h_{buffer}	16.5 mm

Table 3.4: Dimensions of double radial-clearance seal

3.3.3 Experimental results of double seal
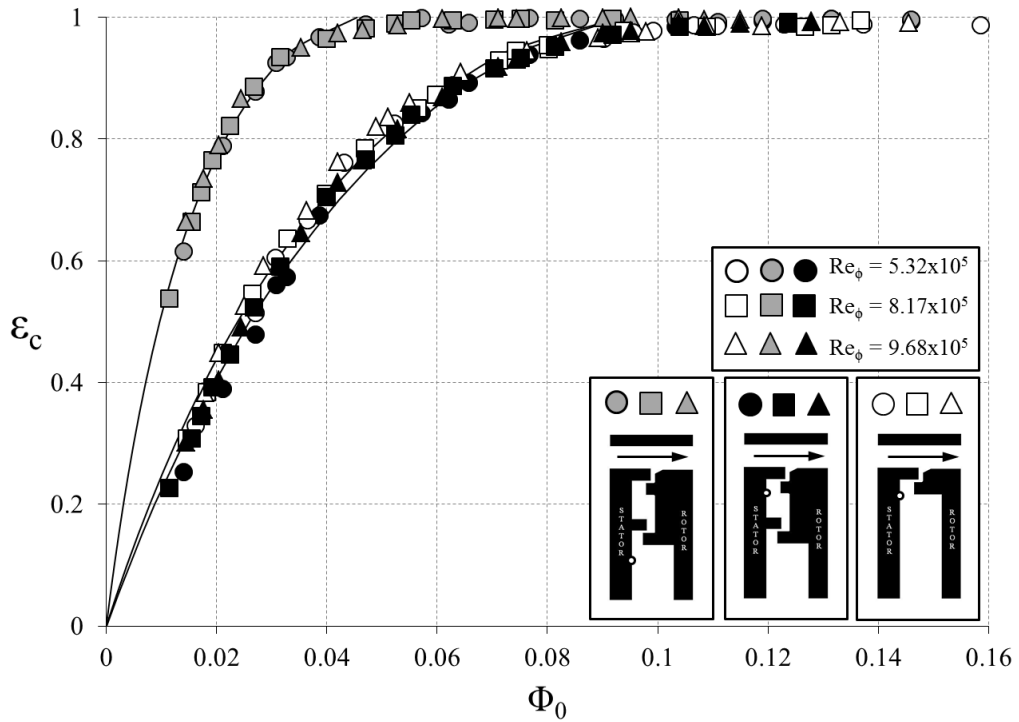
Figure 3.15: Variation of ε_c with Φ_0 for single and double radial-clearance seals: EI ingress (Symbols denote data; lines are theoretical curves)

Parameter	EI Inner	EI Outer
Φ_{min}	0.0455	0.0932
Φ_{min}^{-}	0.0435	0.0885
Φ_{min}^{+}	0.0433	0.0977
Γ_c	0.745	1.54
Γ_c^{-}	0.619	1.28
Γ_c^{+}	0.868	1.91
σ	0.0097	0.0179

Table 3.5: Parameters for inner and outer wheel-spaces for double radial-clearance seal at EI ingress conditions

Figure 3.15 shows the variation of measured concentration effectiveness for the double radial-clearance seal plotted versus Φ_0 for EI ingress. As before, EI measurements were made at three values of Re_ϕ corresponding to the operational design points listed in

Table 3.1. Also shown is the theoretical variation of effectiveness according to Eq.2.14; again the agreement between the optimised theoretical curves based on the method described by Zhou *et al.* (2013a) and the experimental data is very good despite the complexity of the fluid dynamics in the annulus and wheel-space. The values for $\Phi_{min,EI}$ and Γ_c, as well as their

upper and lower bounds and the standard deviation between the equation and the data, are shown in Table 3.5 for both the inner and outer wheel-spaces. The ratio of sealant flow rate required to seal the inner wheel-space of the double radial-clearance in comparison to the outer wheel-space seal was approximately 49%

Figure 3.15 also includes the data for the single radial-clearance seal, previously shown in Figure 3.9. The data for the double seal is presented in terms of $\varepsilon_{c,23}$ and $\varepsilon_{c,13}$ according to Eqs. 3.14 and 3.16 respectively. Both the outer seal, with effectiveness $\varepsilon_{c,13}$, and the inner seal, with effectiveness $\varepsilon_{c,23}$, are shown to be individually characterised by a unique value of $\Phi_{min,EI}$ which is independent of Re_ϕ. In the outer wheel-space of the double seal the effectiveness is virtually the same as the single seal results for the whole range of sealing flow rates tested; i.e. $\varepsilon_{c,23}$ for the double seal is virtually equal to ε_c for the single seal. However, in the inner wheel-space of the double seal the effectiveness is significantly higher, meaning $\varepsilon_{c,13} > \varepsilon_{c,23}$. From the respective values of $\Phi_{min,EI}$ in Table 3.5, sealing the inner wheel-space requires approximately 50% of the air required to prevent ingress through the outer seal.
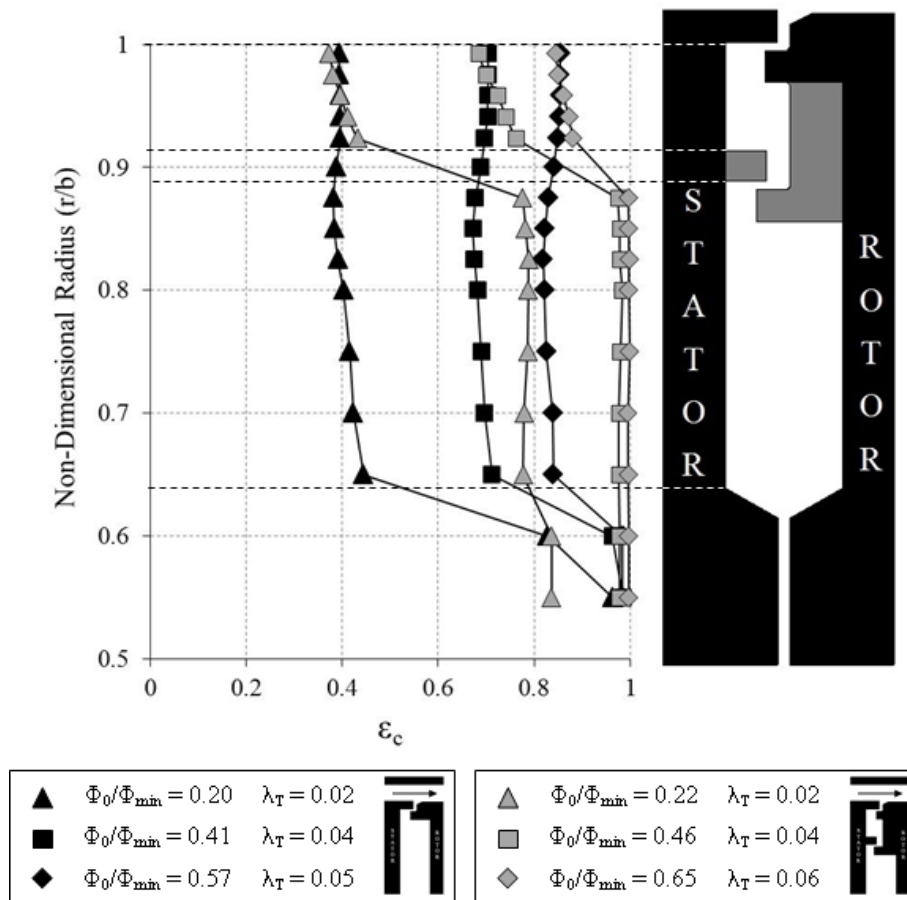
Figure 3.16: Effect of sealing flow rate on radial variation of effectiveness for single and double radial-clearance seals

The variation of ε_c with radius for the double radial-clearance seal is presented in Figure 3.16. The tests were performed for EI ingress at the design operating point equivalent to Re_ϕ = 8.17 × 10^5 for several values of Φ_0/Φ_{min} and λ_T. Also included is the data for the single radial-clearance seal at the same values of λ_T, previously presented in Figure 3.10. In the outer wheel-space of the double seal ($r/b > 0.913$), the effectiveness is virtually the same as the single seal equivalent for all radial locations. The slight variation of ε_c with r/b is possibly due to the proximity of the radial seal to the stator. In the inner wheel-space however, the effectiveness of the double seal is significantly higher than that of the single seal for the same sealing flow rates. Ingestion is therefore predominantly constrained within the outer wheel-space. This is consistent with the results presented in Figure 3.15.
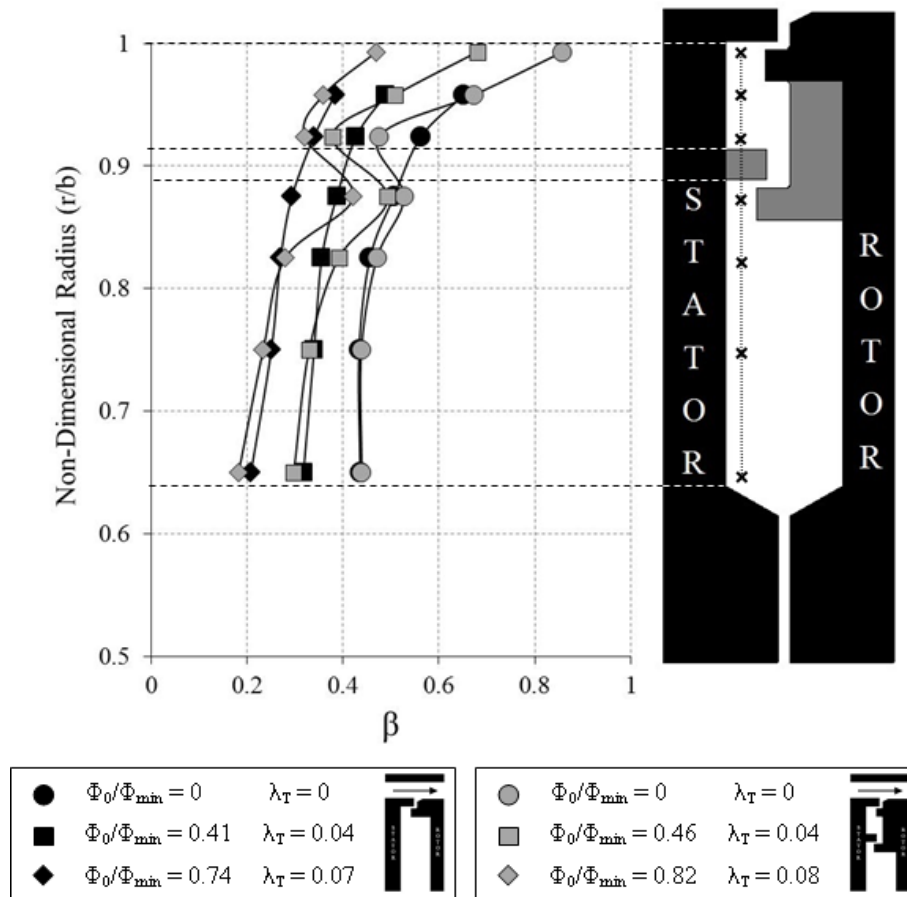
Figure 3.17: Effect of sealing flow rate on radial distribution of swirl ratio for single and double radial-clearance seals

Figure 3.17 shows the variation of swirl ratio with non-dimensional radius at Re_ϕ = 8.17 × 10^5 for the double radial-clearance seal. Once again, data for the single radial-clearance seal, previously presented in Figure 3.11, is included for comparison. As discussed above, at common values of λ_T there are significant differences in the amount of ingress between the

single and double seals. Despite this, the swirl ratios in the inner wheel-space for the two cases are similar, illustrating that β is governed principally by λ_T. The exception to this trend is at $r/b = 0.875$ where local effects of the lower portion of the rotating radial seal are observed for the double seal. In the outer wheel-space the swirl is seen to increase rapidly with radius from $\beta \approx 0.44$ to $\beta \approx 0.86$ for the $\lambda_T = 0$ case under the influence of highly swirling ingested flow.

In double rim-seals the circumferential variation of pressure that leads to EI ingress is attenuated in the annular space between the two seals. If the pressure asymmetry in the outer wheel-space is eliminated, EI ingress will dominate for the outer seal and RI ingress for the inner one. By definition, the performance limit for any double seal is one in which the inner seal is exposed to purely rotationally induced ingress.
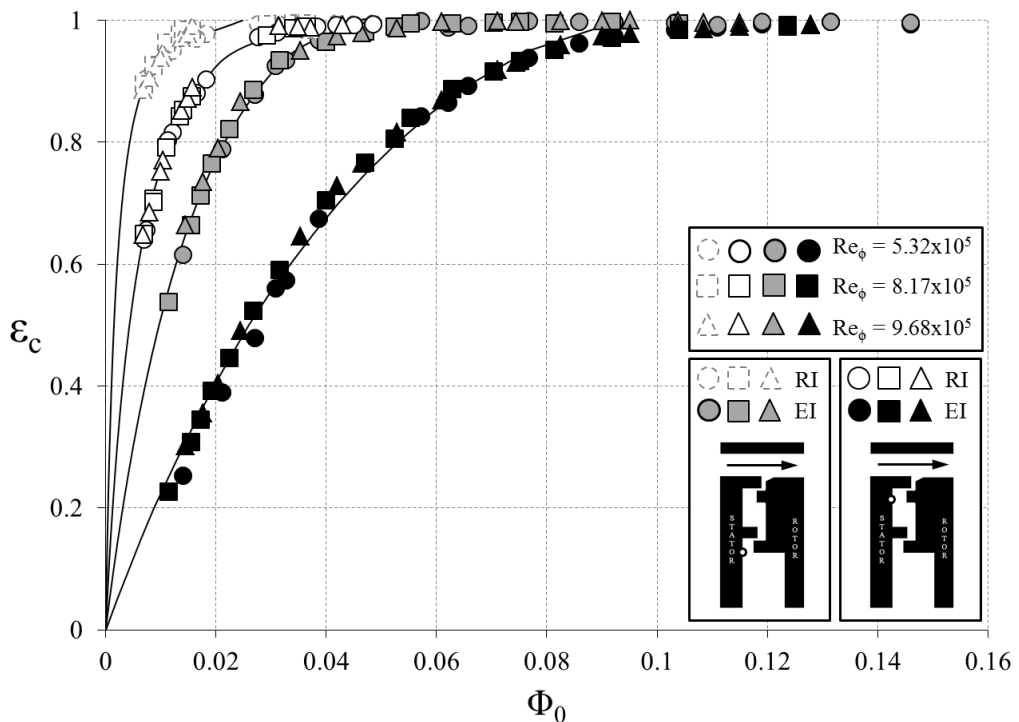
Figure 3.18: Variation of ε_c with Φ_0 for double radial-clearance seal: EI and RI ingress (Symbols denote data; lines are theoretical curves)

Figure 3.18 shows the variation of $\varepsilon_{c,23}$ and $\varepsilon_{c,13}$ for both EI and RI ingress. Values for both $\Phi_{min,EI}$ and $\Phi_{min,RI}$ can be determined which are independent of Re_ϕ. It can be seen for the inner seal, $\Phi_{min,EI} > \Phi_{min,RI}$, indicating the performance limit has not been reached and the pressure asymmetries have not been completely damped out in the outer wheel-space for this double seal design.

3.4 Finned rim seal

In the 1980s, Chew *et al.* (1988) used radial fins to reduce the pressure drop in rotating cavities with radial inflow. The fluid entered the system at disc speed and the fins kept the fluid swirl close to this rotational value as it flowed radially inward.

In Figure 3.12 the pressure asymmetry in a turbine annulus is shown to be attenuated in the outer wheel-space of a double rim-seal. As discussed above, the performance limit of the inner seal would be reached if the circumferential pressure asymmetries in the intermediate annulus were eliminated. Under these conditions the inner seal would experience rotationally-induced ingress. The concept behind the finned seal is to encourage the flow to reach solid-body rotation, and therefore help to damp out the pressure asymmetries.
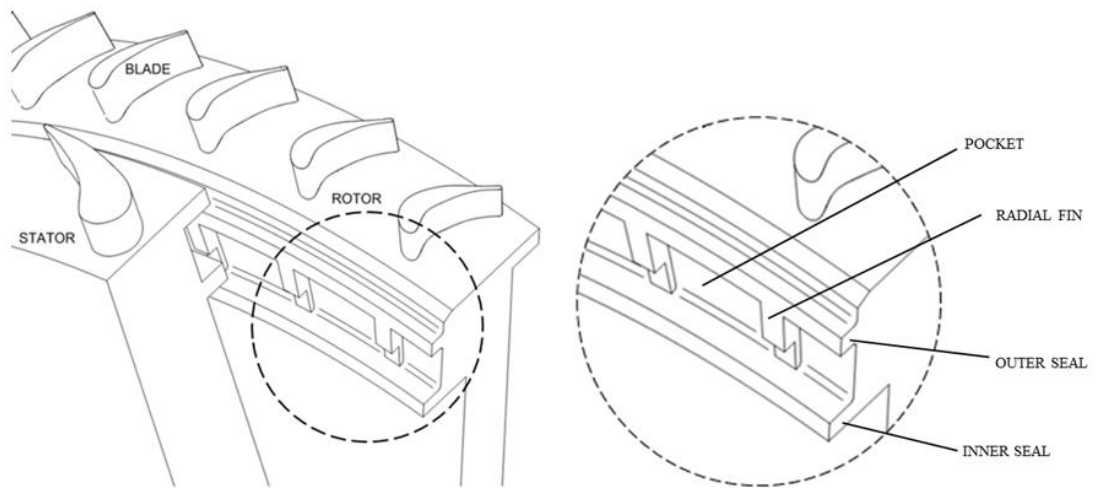
Figure 3.19: Isometric schematic of finned double seal

3.4.1 Geometry of finned seal

The configuration in Figure 3.20 featured the same geometry as the previous double radial-clearance seal including for the addition of 37 radial fins, introduced between the inner and outer seals. 37 was selected as the closest prime number to the blade count in order to avoid resonance issues. The fins extend the full radial height between the seal lips and created 'pockets' inside the double seal on the rotor side attachment. The dimensions of the seal are tabulated in Table 3.6 and an isometric view is shown schematically in Figure 3.19.
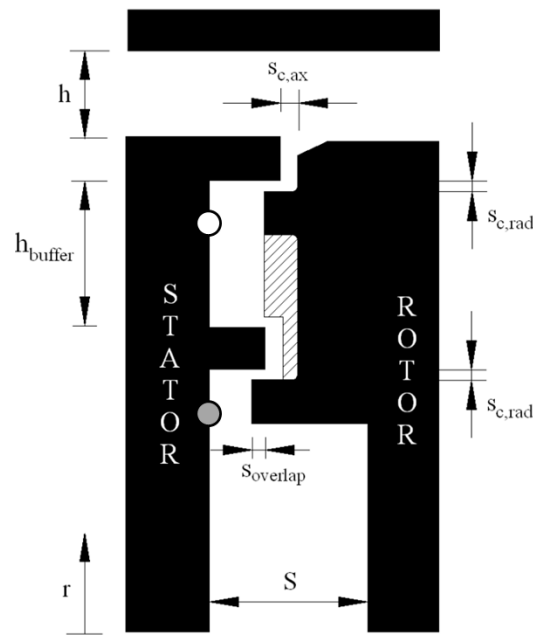
Figure 3.20: Geometry of finned rim-seal

Geometric Symbol	Dimension
h	10 mm
b	190 mm
S	20 mm
t	5 mm
$s_{c,ax}$	2 mm
$s_{c,rad}$	1.28 mm
$s_{overlap}$	1.86 mm
h_{buffer}	16.5 mm
No. pockets	37

Table 3.6: Dimensions of finned rim-seal

3.4.2 Experimental results of finned seal
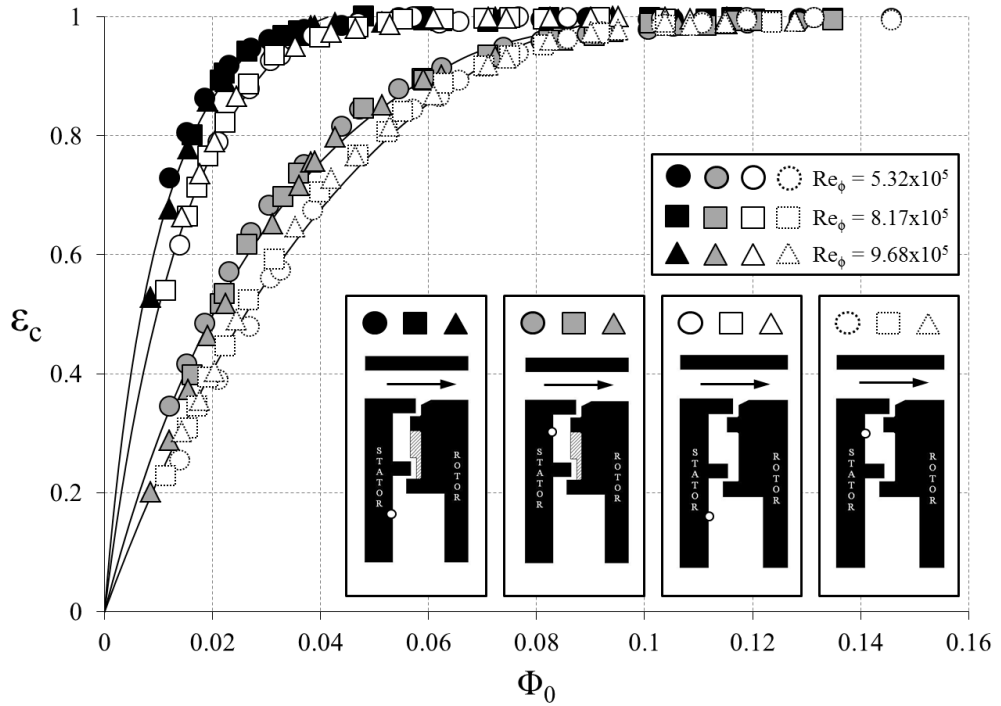
Figure 3.21: Variation of ε_c with Φ_o for seals double seal and double finned seal (Symbols denote data; lines are theoretical curves)

Parameter	EI Inner	EI Outer
Φ_{min}	0.0413	0.0956
Φ_{min}^{-}	0.0384	0.0885
Φ_{min}^{+}	0.0445	0.103
Γ_c	0.428	0.722
Γ_c^{-}	0.350	0.592
Γ_c^{+}	0.529	0.905
σ	0.0118	0.020

Table 3.7: Parameters for inner and outer wheel-spaces of finned double seal at EI ingress conditions

Figure 3.21 shows the variation of ε_c plotted versus Φ_0 for the finned double seal compared with the original un-finned version. It is clear from this figure that the addition of the radial fins to the datum double seal provides an improved sealing performance over the full range of Φ_0 in both the inner and outer wheel-spaces. The results of the statistical orifice model fit are included in Table 3.7. Using $\Phi_{min}*$ (the value of Φ_0 when $\varepsilon = 0.9$) as a ranking parameter, the ratio of $\Phi_{min}*$ for the finned seal compared to that for the datum double seal

is 80% and 90% for the inner and outer wheel-spaces respectively. This could result in a potentially significant reduction in sealing air for the engine designer.
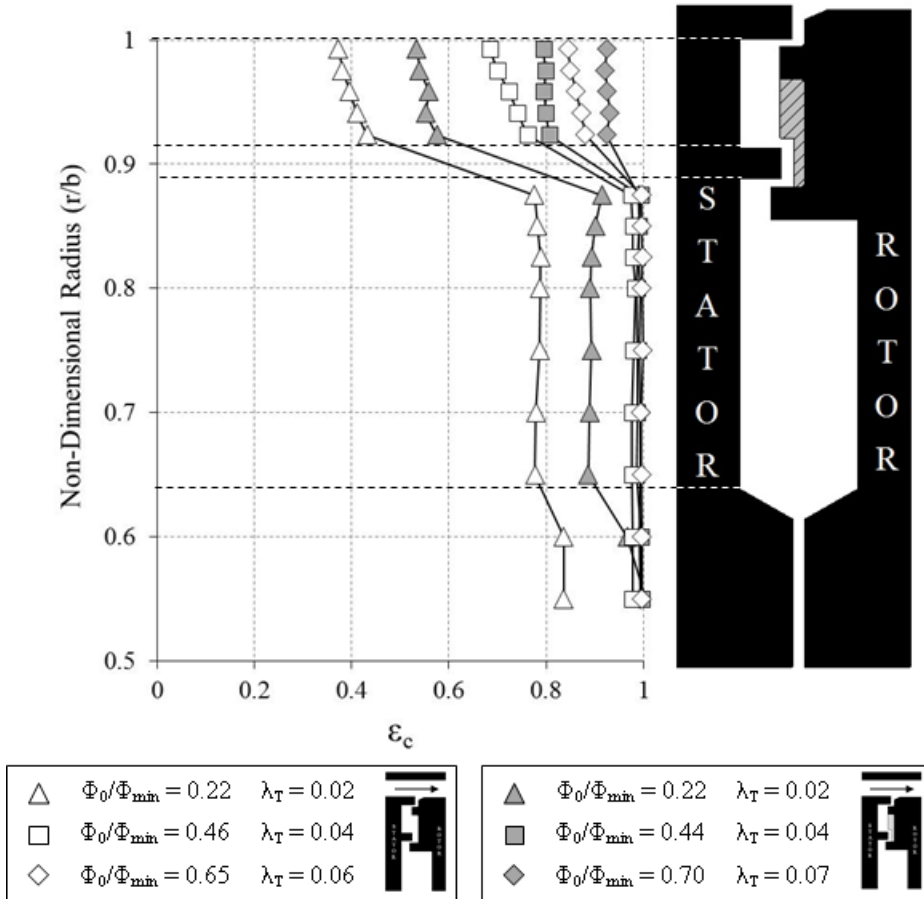
Figure 3.22: Effect of sealing flow rate on measured radial variation of effectiveness for finned and double radial-clearance seals (Open symbols denote double seal; shaded symbols denote double finned seal)

Figure 3.22 shows the radial variation of concentration sealing effectiveness ε_c, measured on the stator for both the datum double seal and the finned-seal. The experiments were conducted at $Re_\phi = 8.2 \times 10^5$ with $\lambda_T = 0.02$, 0.04 and 0.07. The values of Φ_0/Φ_{min} are also labelled. As mentioned above, there are differences between the values of Φ_{min} for the two seals; consequently at the same value of λ_T (hence the same Φ_0) there are some differences in the ingress through these seals into the wheel-space.

At all radii within both the inner and outer wheel-spaces, the finned seal provides an improved effectiveness over the datum seal. As expected, ε_c increases as λ_T increases. In the inner wheel-space for both seals the effectiveness is essentially constant for $0.65 < r/b < 0.85$, suggesting that near-complete mixing has occurred in a region very close to the inner

rim-seal. In the outer wheel-space ($r/b > 0.913$) there is a significant reduction in effectiveness as the ingress is contained between the two seals. For the finned seal, ε_c is again invariant with radius. However for the datum seal ε_c decreases with increasing radius, indicating that the flow here has not mixed fully. This suggests that the fins enhanced the mixing between ingress and egress within the intermediate annulus; the swirl data presented below supports this suggestion.

○	$\Phi_0/\Phi_{min} = 0$	$\lambda_T = 0$	●	$\Phi_0/\Phi_{min} = 0$	$\lambda_T = 0$
□	$\Phi_0/\Phi_{min} = 0.46$	$\lambda_T = 0.04$	■	$\Phi_0/\Phi_{min} = 0.44$	$\lambda_T = 0.04$
◇	$\Phi_0/\Phi_{min} = 0.82$	$\lambda_T = 0.08$	◆	$\Phi_0/\Phi_{min} = 0.82$	$\lambda_T = 0.08$
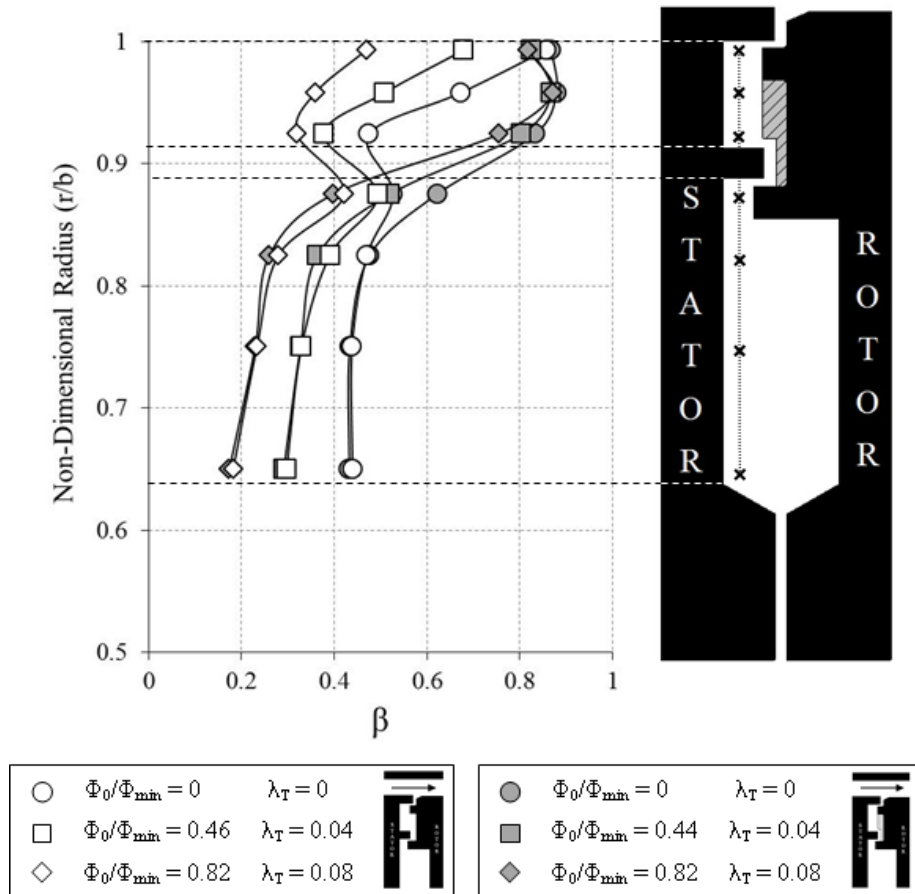
Figure 3.23: Effect of sealing flow rate on radial distribution of swirl ratio for finned and double radial-clearance seals

Figure 3.23 illustrates the variation of swirl ratio, β, with non-dimensional radius, again for both double seals. The seal geometry and measurement locations for total pressure in the wheel-space (at $z/S = 0.25$) are shown on the right of the figure. The data for both seals are shown for pairs of common superposed flow rates ($\lambda_T = 0$, 0.04 and 0.08) at $Re_\phi = 8.2 \times 10^5$.

Within the inner wheel-space ($r/b < 0.9$) the swirl ratio β for both seals is similar and is governed principally by λ_T; this indicates that the inner seal is able to constrict the ingress

predominantly within the outer wheel-space. Increasing the sealing flow (i.e. increasing λ_T) caused a reduction in the core rotation. For a given sealing flow rate, β (and the associated static pressure) increases with radius.

In the outer wheel-space there are significant differences in the distribution of swirl for the two seal geometries. As observed previously for the datum double seal, β increases rapidly with radius under the influence of highly-swirling ingress, with the distribution dependent on λ_T. In contrast, the finned seal produces a much higher swirl relative to the datum seal, with $0.8 > \beta > 0.9$ (virtually independent of λ_T) indicating near solid-body rotation. It is encouraging to see that the data support the concept behind the design of the finned seal discussed above, and the improved performance across the inner seal is probably linked to a reduction in the pressure asymmetry within the intermediate annulus.
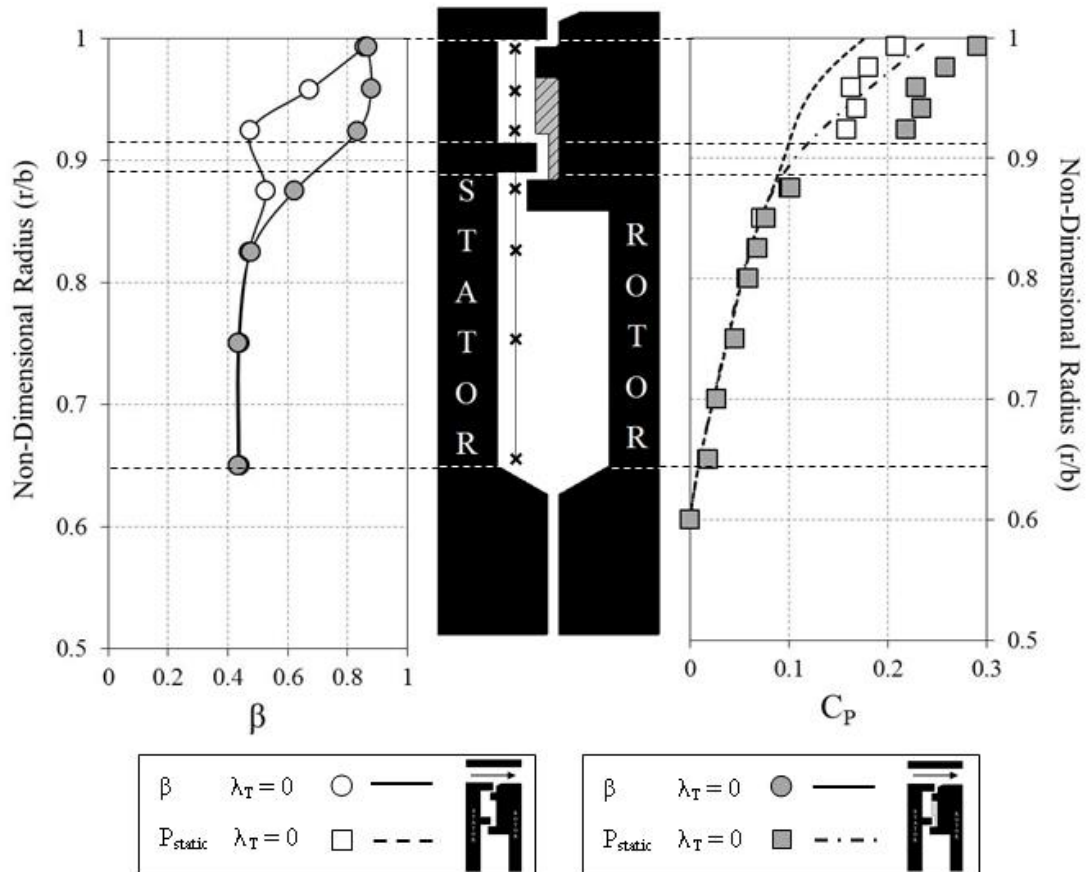
Figure 3.24: Radial distribution of swirl ratio and pressure coefficient (static) for finned and double radial-clearance seals (Symbols denote measured values; lines denote fitted distribution for β and calculated distribution for C_p)

Figure 3.24 shows comparisons between the distributions of C_p, calculated from Eq. 3.10, and the values obtained from the measured static pressures for the double and finned seals. The experiments were conducted at $Re_\phi = 8.2 \times 10^5$ with $\lambda_T = 0$. In both cases there is very good agreement between the calculated and measured distributions of C_p within the inner wheel-space, i.e. $r/b < 0.9$. This shows two important things: (i) the radial distribution of the swirl ratio determines the radial distribution of pressure in the wheel-space; (ii) the distributions of swirl and pressure are controlled by λ_T and there is very little effect of ingress on these distributions.

In the outer wheel-space the geometric features of both the datum seal and the finned seal, as well as the ingress into the intermediate annulus, have affected the distribution of swirl and pressure. Externally-induced ingress is controlled by the pressure difference between the annulus and the wheel-space near the rim-seal. Figure 3.24 shows that the finned seal increases the pressure in the immediate annulus relative to the datum seal, and this explains the superior performance across the outer seal. Clearly, ingress cannot occur if the pressure in the wheel-space, radially inward of the seal, is greater than the maximum pressure in the annulus.
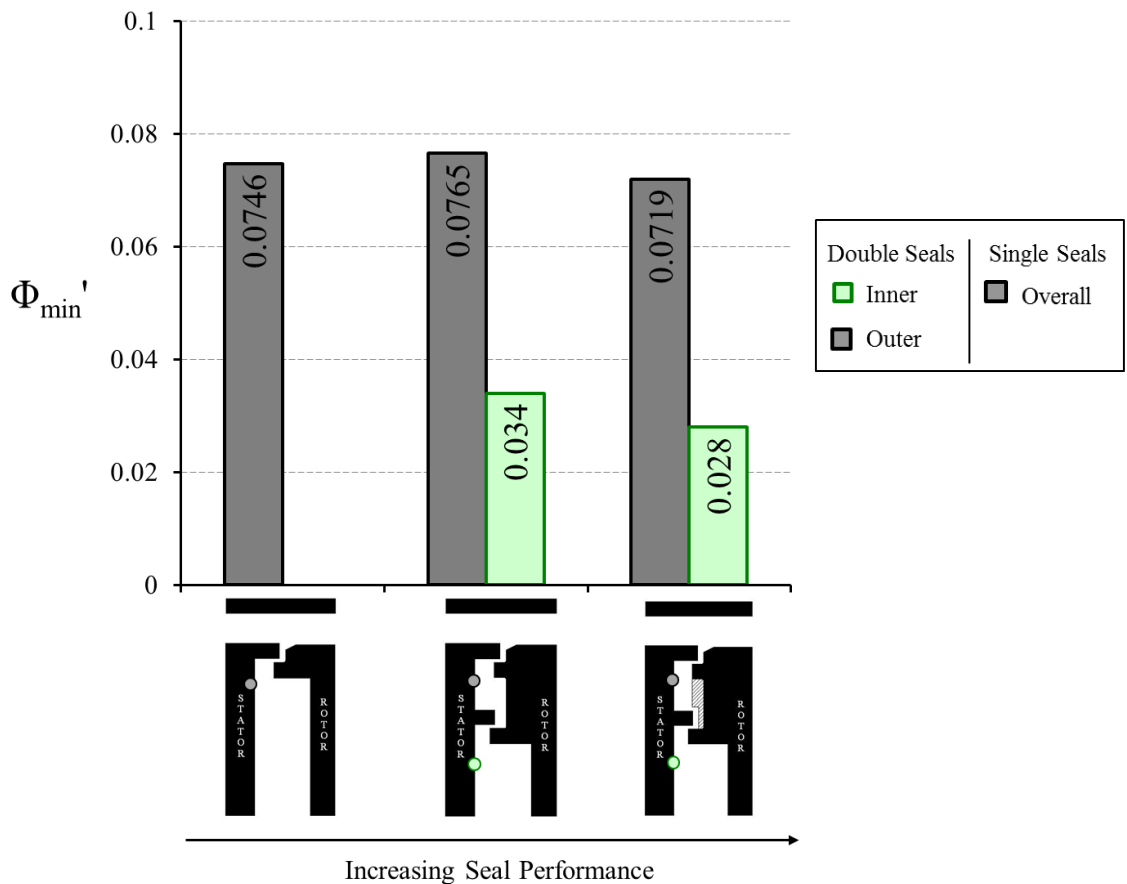
Figure 3.25: Seal performance ranking shown in order of magnitude of Φ_{min}'

Figure 3.25 shows a bar chart ranking the three geometries in order of sealing performance. As stated above, as the value of Φ_0 at $\varepsilon = 0.95$ has a smaller associated uncertainty, Φ_{min}' is used as a ranking criterion for both the inner and outer wheel-spaces. Although the single and double radial-clearance seals exhibit similar performance at the outer sampling location (in fact the single seal has a slightly lower value of Φ_{min}'), the benefit of protecting the inner wheel-space is evident. The ratio of Φ_{min}' for the finned seal compared to the datum double seal is 82% and 94% for the inner and outer wheel-spaces respectively. This could result in a potentially significant reduction in sealing air for the engine designer.

3.5 Measurement uncertainties

3.5.1 Uncertainty in effectiveness

The definition of sealing effectiveness is given in Eq. 3.4 where the subscripts a, o and s respectively denote the air in the annulus, the sealing air at inlet, and the surface of the stator. If δ_ε, δ_s, δ_0, δ_a are the uncertainties in ε, c_s, c_0, c_a respectively then:

$$\varepsilon \pm \delta_\varepsilon = \frac{c_s \pm \delta_s - (c_a \pm \delta_a)}{c_o \pm \delta_o - (c_a \pm \delta_a)} \tag{3.17}$$

$$= \frac{(c_s - c_a)[1 + (\pm \delta_s \pm \delta_a)/(c_s - c_a)]}{(c_o - c_a)[1 + (\pm \delta_o \pm \delta_a)/(c_o - c_a)]}$$

$$= \varepsilon \frac{[1 + (\pm \delta_s \pm \delta_a)/(c_s - c_a)]}{[1 + (\pm \delta_o \pm \delta_a)/(c_o - c_a)]} \tag{3.18}$$

If $(\pm \delta_0 \pm \delta_a) / (c_0 - c_a) \ll 1$ then:

$$\varepsilon + |\delta_\varepsilon| \le \varepsilon \left\{ 1 + \frac{|\delta_s| + |\delta_a|}{c_s - c_a} + \frac{|\delta_o| + |\delta_a|}{c_o - c_a} \right\} \tag{3.19}$$

hence:

$$\frac{|\delta_\varepsilon|}{\varepsilon} \le \left\{ \frac{|\delta_s| + |\delta_a|}{c_s - c_a} + \frac{|\delta_o| + |\delta_a|}{c_o - c_a} \right\} \tag{3.20}$$

If the uncertainty is a percentage of the full-scale range, which was the case in the experiments, then $\delta_s = \delta_0 = \delta_a = \delta$, say, and Eq. 3.20 simplifies to:

$$\frac{|\delta_\varepsilon|}{\varepsilon} \leq 2\delta \frac{1+\varepsilon^{-1}}{c_o - c_a} \tag{3.21}$$

or

$$|\delta_\varepsilon| \leq 2\delta \frac{1+\varepsilon}{c_o - c_a} \tag{3.22}$$

The average standard deviation, σ, in the range $0 < \varepsilon < 1$ can be calculated from Eq. 3.22 by:

$$\sigma = \frac{2\delta}{c_o - c_a} \sqrt{\int_0^1 (1+\varepsilon)^2 d\varepsilon} = 3.06 \frac{\delta}{c_o - c_a} \tag{3.23}$$

The CO_2 gas analyser had an overall uncertainty of 0.015% of each of its ranges. In the tests, where the 1% range was used, the concentration of gas in the sealing flow was close to the 1% range maximum. Hence $\delta / (c_0 - c_a) \approx 0.015$, and from Eq. 3.23 it follows that $\sigma \approx 0.046$. This value, which is an upper bound, exceeds the standard deviation found from the fitted $\Phi_0 - \varepsilon$ curves, the values of which are given in Tables 3.3, 3.5 and 3.7. If the experimental uncertainty of the measurements were also taken into account in the calculation of the standard deviation, the values presented in Tables 3.3, 3.5 and 3.7 would be expected to increase.

3.6 Summary

This chapter presents measurements of CO_2 gas concentration, pressure and swirl ratio inside the wheel-space of a single-stage axial turbine research facility. The results were used to assess the sealing performance of three rim seal geometries: a datum radial-clearance single seal, a radial-clearance double seal, and a double seal variant featuring a series of radial fins.

Although the ingestion through rim seals is a consequence of an unsteady, three-dimensional flow field, and the cause-effect relationship between pressure and the sealing effectiveness is complex, the experimental data is shown to be successfully calculated by the

simple effectiveness equations (Eqs. 2.14 and 2.17) developed from a theoretical orifice model. For all the seals tested, the data illustrated that the effectiveness can be correlated using two empirical parameters, which were independent of Re_ϕ.

The benefit of using a double seal was demonstrated: the ingested fluid was shown to be predominately confined to the outer wheel-space radially outward of the inner seal; in the inner wheel-space the effectiveness was shown to be significantly higher. In the practical situation of an engine, the inner stator wall could operate at an acceptably low metal temperature with the hot, ingested gas confined to the outer wheel-space protected by a more robust alloy.

A criterion for ranking the performance of the different seal designs was proposed. The performance limit for any double seal is shown to be one in which the inner seal is exposed to rotationally-induced ingress only.

The performance of the double rim-seal was further improved in both the inner and outer wheel-spaces by the addition of radial fins, over a wide range of sealant flow rates. Measurements of pressure and swirl in the outer wheel-space demonstrated that the fins helped to produce solid-body rotation. It is conjectured that this increase in swirl reduced the pressure asymmetries and consequently improved the performance of the inner seal. The fins also increased the pressure in the outer wheel-space and reduced ingress through the outer seal.

This improvement in sealing effectiveness could result in a potentially significant reduction in sealing air for the engine designer. However, by encouraging swirl within the intermediate annulus, the windage on the rotor will increase with a corresponding reduction in stage efficiency (The relative windage rise could be examined by monitoring the rotor torque with and without the finned seal installed). In mitigation, it is important to remember that the stage efficiency is also dependent on the mixing losses in the main annulus; these losses are influenced by the egress-mainstream interaction. If the sealing flow emerges from the wheel-space with a swirl closer to that of the mainstream (note $\beta_a > 1$) then these mixing losses may reduce.

Future optimisation studies of the finned design could examine the number of pockets, geometries more complex than the simple radial fins, or an improved aerodynamic profile. Any improvement arising from the introduction of intricate design features would compete against the disadvantage of increased manufacturing complexity.

As expected for all seals, the swirl ratios increased with increasing radius and decreased with increasing sealing flow rate. For a given sealing flow rate, there was little difference between the radial distribution of swirl ratio for the different seals, despite the difference in the amount of ingestion. The radial distribution of pressure was shown to be governed by the swirl ratio, and these swirl and pressure distributions were in turn governed by the turbulent flow parameter, λ_T.

Although the ingestion through the rim seal is a consequence of an unsteady, three-dimensional flow field, and the cause-effect relationship between pressure and the sealing effectiveness is complex, the experimental data is shown to be successfully calculated by simple effectiveness equations developed from a theoretical orifice model. The data illustrate that, for similar turbine-stage velocity triangles, the effectiveness can be correlated using two empirical parameters. In principle, these correlations could be extrapolated to a geometrically-similar turbine operating at engine representative conditions.

Chapter 4: Experimental measurements of ingestion at off-design conditions

All gas turbines spend some time (e.g. during starting, idling, reduced power, maximum power, acceleration and deceleration) at off-design conditions far removed from the design point of the turbine. Satisfactory off-design operation over a wide range of rotational speeds and inlet conditions is therefore an important requirement for all engines. In the case where the rotational speed of the engine is constant, such as in a single-shaft industrial turbine, performance can be improved by actively controlling the flow rate through the compressor using variable vanes. These vanes can be individually rotated around their axis which changes the design point of the compressor. However due to the harsher environment found in the turbine, the nozzle guide vanes are fixed therefore off-design operation is inevitable which may have a significant effect on ingestion.

The flow in the mainstream annulus of the turbine is usually characterised by the flow coefficient, C_F, defined as:

$$C_F = \frac{W}{\Omega b} \tag{4.1}$$

where W is the mean axial component of velocity in the annulus downstream of the turbine vanes, b is the outer radius of the turbine disc and Ω is its angular speed. For a given exit angle of the vanes, C_F defines the swirl ratio of the mainstream flow, and at the design point of engines $C_F \approx 0.5$. Modern turbines, with larger vane exit-angles, tend to operate at lower values of C_F than the older ones.

The pressure asymmetry in the annulus, and consequently EI ingress, increases as C_F increases. At the design point, where rotational effects are relatively small, EI ingress is usually assumed to dominate. However, at over-speed or low-C_F conditions rotation can have a significant effect on ingress, and the term *combined ingress (CI)* is used here to denote the ingestion that occurs when the effects of rotation and the external-pressure distribution are both significant. For off-design operation, it is important to consider combined ingress as the general case with EI and RI ingress as special or limiting cases.

The author of this thesis conducted all the experimental testing and analysis involved in this chapter.

4.1 Background

At the design point in a gas turbine, ingestion of hot gas through the rim seal is dominated by EI ingress. However, at off-design conditions, the effects of rotation can be significant. These conditions lead to combined ingress (CI) involving both externally-induced (EI) and rotationally-induced (RI) ingress.

Phadke and Owen (1988b and c) correlated $C_{w,min}$, the minimum sealing flow rate needed to prevent ingress, in a simple rotor-stator system with a number of different rim-seal geometries. Their tests were conducted without vanes and blades in the external annulus, and circumferential pressure asymmetries were created by blocking sections of the annulus with honeycomb and wire mesh. The tests showed that EI ingress was caused by the pressure asymmetry produced by the external flow. The axial Reynolds number is defined as:

$$\text{Re}_w = \frac{\rho W b}{\mu} \tag{4.2}$$

For $Re_w = 0$, where RI ingress occurs, $C_{w,min} \propto Re_\phi$; for large values of Re_w, where EI ingress dominates, $C_{w,min} \propto Re_w$. The term combined ingress is now used to denote the transition from RI to EI ingress.

Khilnani and Bhavnani (2001) investigated the sealing performance of an axial seal in a rig with external flow. In the absence of blades or vanes, eccentricity in the external annulus was assumed to have caused the circumferential variations in the external pressure. Static pressure measurements in the wheel-space were used to determine $C_{w,min}$ for a range of Re_w and Re_ϕ. Figure 2.15 shows the effect of Re_ϕ on the variation of $C_{w,min}$ with Re_w, and their results were broadly consistent with those of Phadke and Owen.

Owen *et al.* (2012b) fitted the CI equation developed from their orifice model (Owen (2011b)) to the experimental data of Phadke and Owen (1988c).

For the CI case, from Eq. 2.8:

$$C_{\beta_1} = \left[\frac{\Phi_{\min,RI}}{C_{d,e,RI}} \right]^2 \tag{4.3}$$

For simplicity, it is assumed here that $C_{d,e,CI} = C_{d,e,RI} = C_{d,e,EI}$.

The non-dimensional pressure difference can be correlated to the flow coefficient using:

$$\Delta C_p^{\;1/2} = k_a C_F \tag{4.4}$$

where k_a is found from least-squares fit to the experimental pressure data. It follows that:

$$\Gamma_{\Delta p} = k_c C_F^{\;2} \tag{4.5}$$

where

$$k_c = \left[\frac{k_a \, C_{d,e,RI}}{\Phi_{\min,RI}} \right]^2 \tag{4.6}$$

The CI equation (Eq. 2.12) can therefore be written as:

$$\frac{\Phi_{\min,CI}}{\Phi_{\min,RI}} = \frac{2}{3} \frac{\left[1 + k_c C_F^{\;2} \right]^{3/2} - 1}{k_c \, C_F^{\;2}} \tag{4.7}$$

where k_c is an empirical constant defined in Eq. 4.6. As:

$$\frac{\Phi_{\min,CI}}{\Phi_{\min,RI}} = \frac{C_{w,\min,CI}}{C_{w,\min,RI}} \tag{4.8}$$

and

$$C_F = \frac{\mathrm{Re}_w}{\mathrm{Re}_\phi} \tag{4.9}$$

Eq. 4.7 can be written as:

$$\frac{C_{w,\min,CI}}{C_{w,\min,RI}} = \frac{2}{3} \frac{\left[1 + k_c (\, \mathrm{Re}_w \, / \, \mathrm{Re}_\phi \,)^2 \right]^{3/2} - 1}{k_c \, (\, \mathrm{Re}_w \, / \, \mathrm{Re}_\phi \,)^2} \tag{4.10}$$

The RHS of equation (4.9) approaches the EI asymptote as $Re_w/Re_\phi \to \infty$, and Eq. 4.10 becomes:

$$\frac{C_{w,\min,CI}}{C_{w,\min,RI}} = \frac{2}{3} k_c^{\;1/2} \frac{\mathrm{Re}_w}{\mathrm{Re}_\phi} \tag{4.11}$$

The CI equation (Eq. 4.10) is shown fitted to the data of Phadke and Owen (1988c) in Figure 2.26 and to the data of Khilnani and Bhavnani (2001) in Figure 4.1. (The data shown in Figure 4.1 were obtained from the data shown in Figure 2.15; Figure 4.1 was not shown in the paper of Khilnani and Bhavnani (2001)) In both figures, the CI equation captures the

transition from RI to EI ingress and collapses the data obtained for a wide range of Re_w and Re_ϕ onto a single curve. The fact that the $C_{w,min}$ ratio in Figure 4.1 is much higher than that in Figure 2.26 was attributed to the fact that the pressure asymmetry in the annulus of the rig of Khilnani and Bhavnani was significantly higher than that in the rig of Phadke and Owen. It should also be noted that the departure of the CI curve from its EI asymptote increases as Re_w/Re_ϕ decreases.
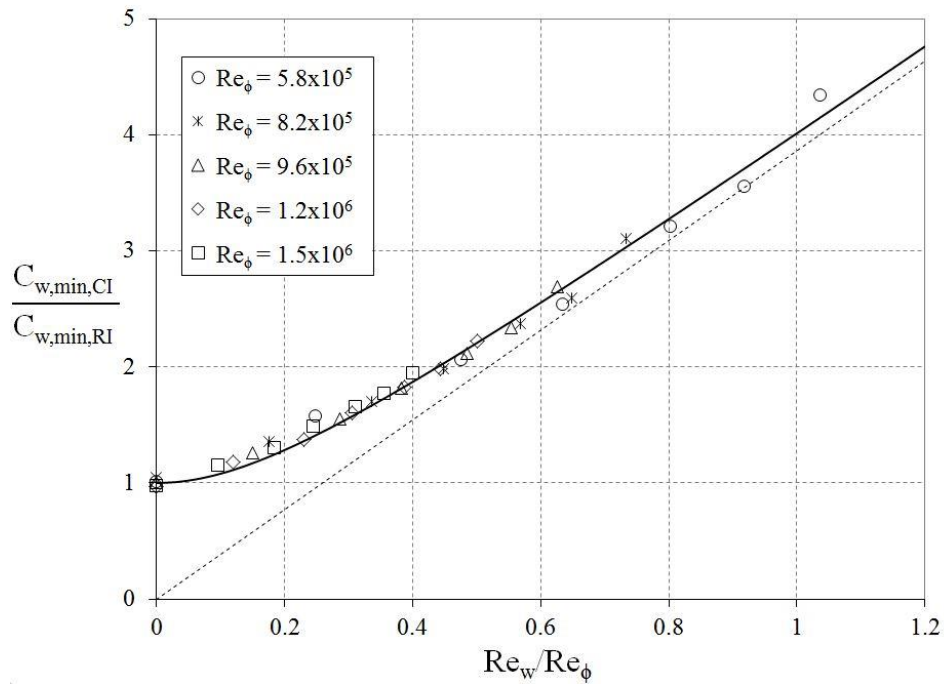
Figure 4.1: CI equation fitted to data of Khilnani and Bhavnani (2001) (Solid line is Eq. 4.10; broken line is Eq. 4.11)

4.2 Pressure measurements

All data presented in this section are for three rotational disc speeds (corresponding to $Re_\phi = 5.32 \times 10^5$, 8.17×10^5 and 9.68×10^5), with the mainstream flow-rate varied to create the *off-design* velocity triangles in the turbine annulus. At the design condition $Re_w/Re_\phi = 0.538$, where Re_w is the Reynolds number based on the axial component of velocity in the annulus. Off-design Re_w/Re_ϕ (which is analogous to the flow coefficient, C_F) is varied from zero (i.e. in the absence of external flow) up to 0.858. When $C_F < 0.538$, the rig was operating at an over-speed condition; when $C_F > 0.538$, the rig was said to be operating at an under-speed condition.

4.2.1 Flow direction relative to the blade

Figure 4.7 shows the velocity triangles for the vanes and the symmetrical blades at the design and an off-design condition. α and β are the respective angles of the resultant velocity of the flow, relative to the axial direction, in the stationary and rotating frames. In the rig, α was set at 73° and β_0, the blade angle, was 56°; at the design condition, $\beta = \beta_0$; at off-design conditions, β-β_0 is the 'deviation angle' between the resultant velocity in the rotating frame and the blade.
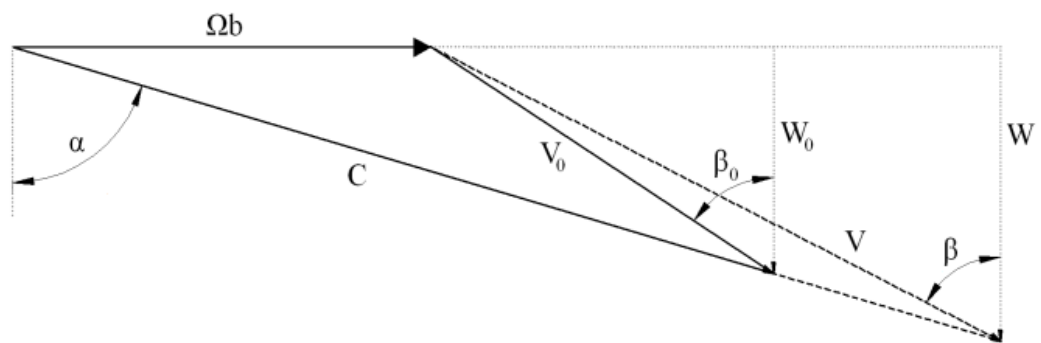
Figure 4.2: Velocity triangles shown for design and under-speed conditions
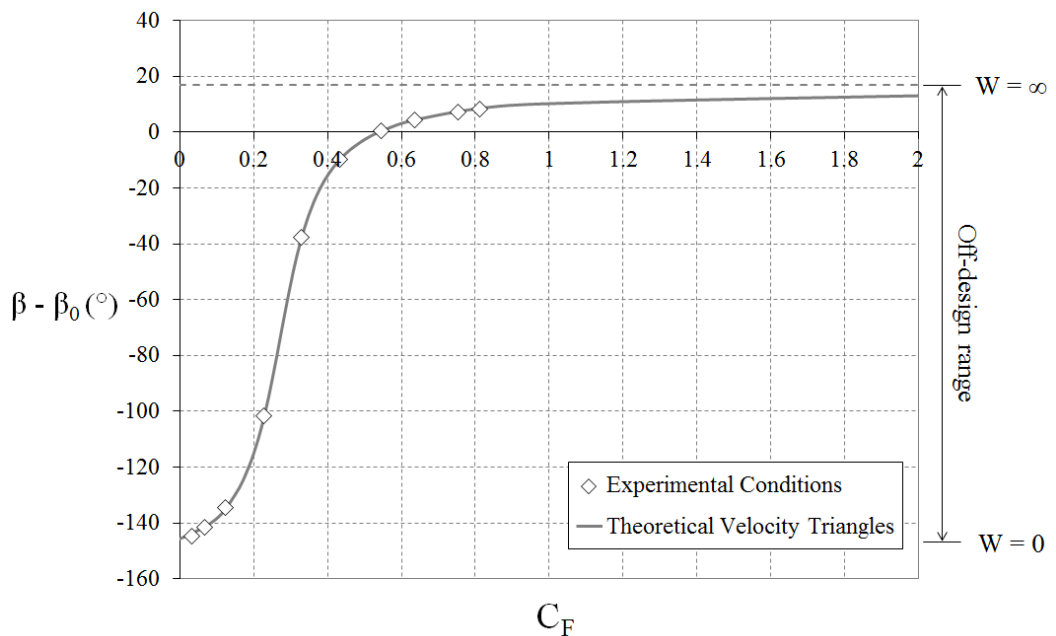
Figure 4.3: Variation of deviation angle with flow coefficient (Symbols denote where concentration measurements were made for axial-clearance seal)

From the velocity triangles, it follows that:

$$\tan\beta = \tan\alpha - \left(\frac{W}{\Omega b}\right)^{-1} = \tan\alpha - C_F^{-1} \tag{4.12}$$

At the design point, which is denoted by the subscript 0:

$$\tan\beta_0 = \tan\alpha - \left(\frac{W}{\Omega b}\right)_0^{-1} = \tan\alpha - C_{F,0}^{-1} \tag{4.13}$$

and, the flow coefficient at the design point for the rig was $C_{F,0} = 0.538$. For the *over-speed condition*, where $C_F < 0.538$, $\beta < \beta_0$; for the *under-speed condition*, $\beta > \beta_0$. When $\Omega = 0$ or $W\rightarrow\infty$, $\beta = \alpha$ and $\beta\text{-}\beta_0 = 17°$; when $W = 0$, $\beta = -\pi/2$ and $\beta\text{-}\beta_0 = -146°$.

Figure 4.3 shows the variation of the deviation angle, $\beta\text{-}\beta_0$, with the flow coefficient, and the symbols denote where measurements were made for the axial-clearance seal. The experimental range exceeded any range likely to be experienced in an engine, particularly at the low values of C_F.

4.2.2 Pressure measurements in the annulus
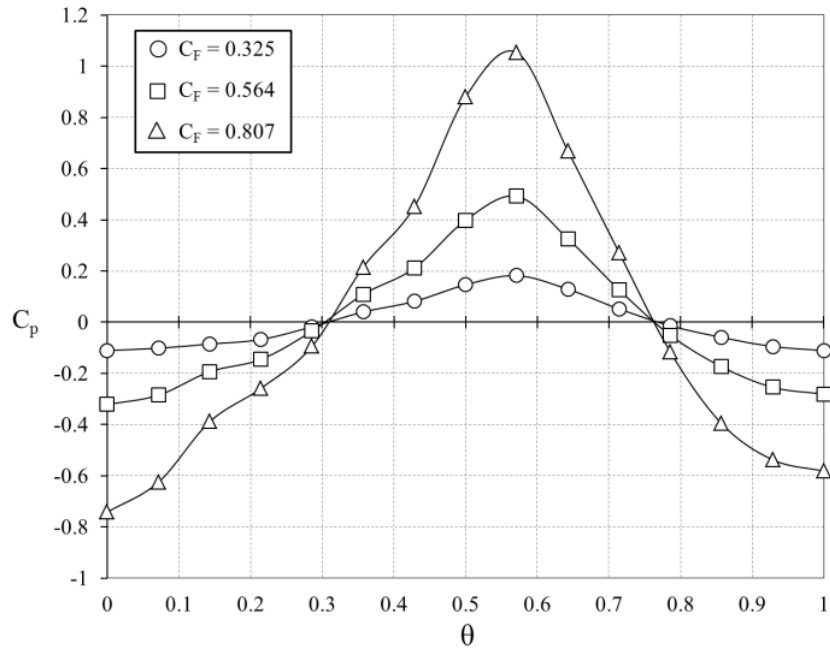
Figure 4.4: Circumferential distribution of C_p over non-dimensional vane pitch at three different flow coefficients

Figure 4.4 shows the effect of C_F on the circumferential distribution of C_p (defined by Eq. 3.5). The static pressures were measured on the vane platform downstream of the vanes in the absence of sealing flow, and $\bar{p}$ was the mean static pressure over one vane pitch.
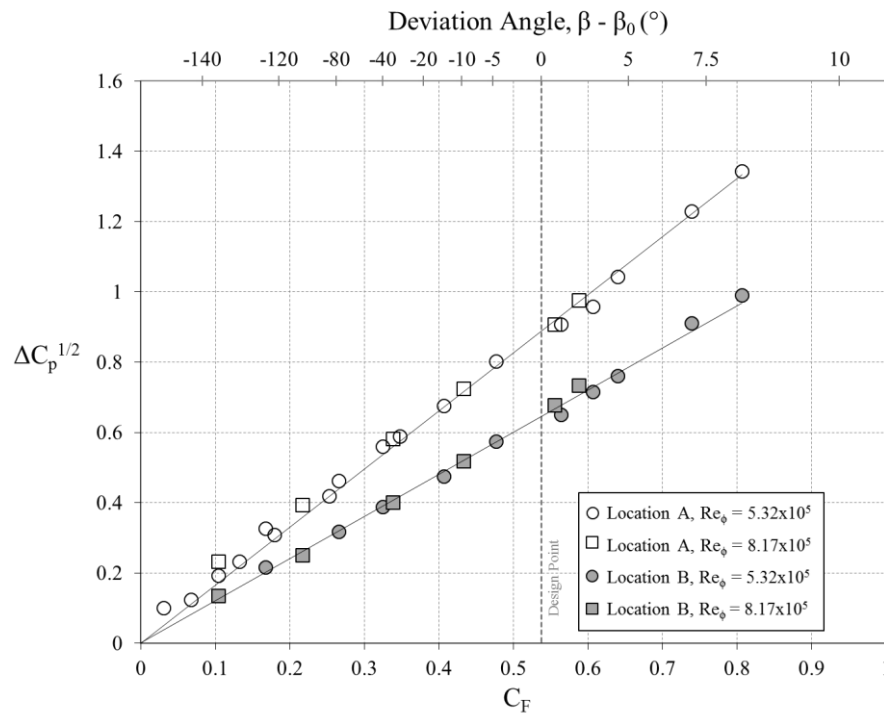
Figure 4.5: Measured variation of $\Delta C_p^{1/2}$ at locations A and B in annulus with flow coefficient and with deviation angle

According to the orifice model, summarised in Section 2.6, EI ingress is related to the non-dimensional pressure difference in the annulus, ΔC_p, defined by Eq. 3.6. ΔC_p, which is equivalent to the peak-to-trough difference of C_p, increases as flow coefficient increases.

Eq. 3.7 demonstrates how the sealing parameter necessary to prevent EI ingress, $\Phi_{min,EI}$, is related to ΔC_p. Sangan *et al.* (2011) showed that ΔC_p decreased slightly as the flow rate of sealing air increases.

For mathematical consistency in the EI orifice model, it is necessary that there is zero ingress when $\Delta C_p = 0$. However, as shown below, the value of ΔC_p depends on where in the annulus it is evaluated. As shown by Owen *et al.* (2012a) in Figure 2.25, the consistency criterion can only be satisfied in small regions near the rim seal, and the values of ΔC_p

measured in an experimental rig are unlikely to satisfy this criterion. This topic is discussed further in Chapter 5.

Figure 4.5 shows the measured variation of $\Delta C_p^{1/2}$ with the flow coefficient, and with the deviation angle β-β_0, measured at locations A and B in the annulus. The experimental measurements show no significant effect of Re_ϕ, and $\Delta C_p^{1/2}$ increases linearly with C_F; despite the large experimental range, there was no obvious effect of the deviation angle on this linear variation. The experimental data in Figure 4.5 for location A were correlated by Eq. 4.4, where $k_a = 1.66$.

4.3 Concentration measurements

Results for two single and one double seal are presented here, principally to illustrate the similarities between the off-design performance of different seals. There are, of course, quantitative differences in the effectiveness of these seals, as demonstrated in Chapter 3.

4.3.1 Variation of sealing effectiveness
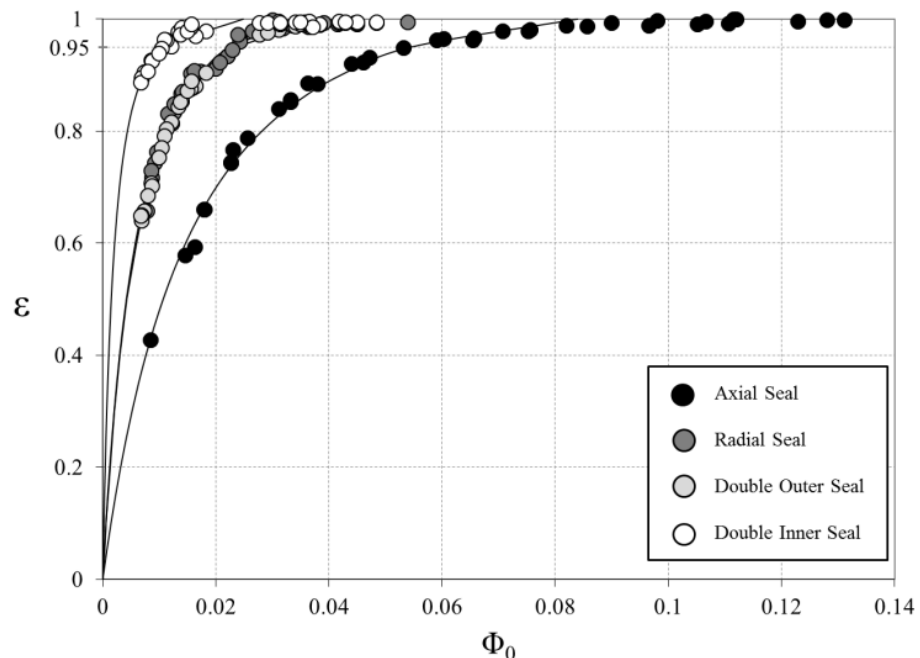
Figure 4.6: Variation of sealing effectiveness with Φ_0 for RI ingress for four seals (Symbols denote experimental data; lines are theoretical curves)

Figure 4.6 shows the variation of ε with Φ_0 for the case where the external flow was zero, which (as shown in Sangan *et al.* (2011b)) corresponds to RI ingress. The RI effectiveness equation (Eq. 2.17) was fitted to the experimental data using the statistical technique described in Zhou *et al.* (2013a), and the agreement between the theoretical curve and the data was very good for all four seals. It can be seen that the results for the outer seal of the double radial-clearance seal agree very closely with those for the single radial-clearance seal, and the radial-clearance seal was much more effective than the axial-clearance one.
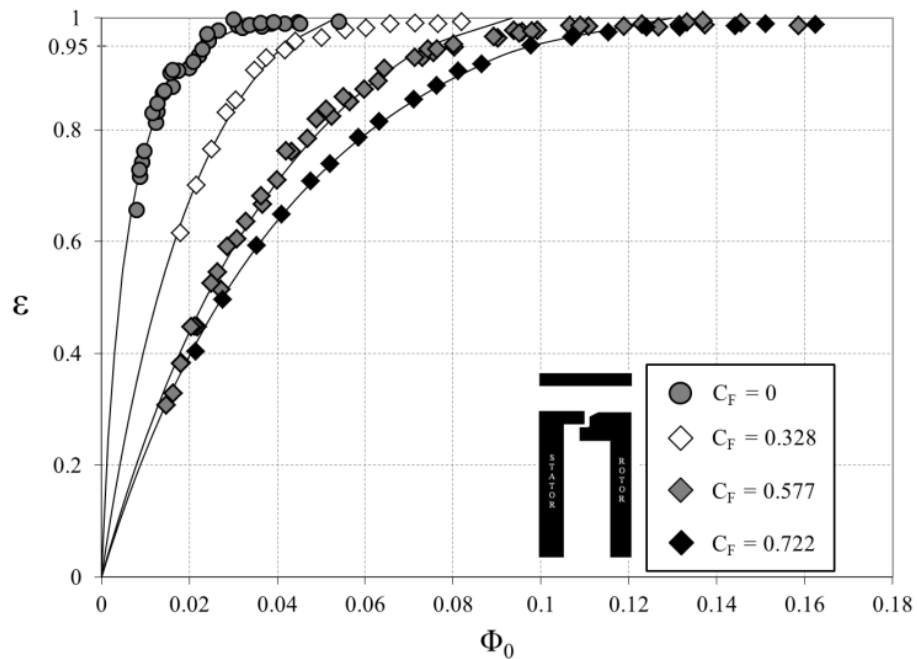
Figure 4.7: Effect of flow coefficient on variation of effectiveness with sealing parameter for radial-clearance seal (Symbols denote experimental data; lines are theoretical curves)

Figure 4.7 shows the effect of the flow coefficient on the variation of the sealing effectiveness with the sealing parameter, Φ_0, for the radial-clearance seal. The RI data and the EI design condition data are the same values as presented in Figure 3.8. The effectiveness decreased as C_F increased, which was consistent with the pressure measurements discussed in Section 4.2.2, where ΔC_p increased as C_F increases. In some of the experiments it proved impossible to achieve a fully sealed system but, apart from the values near $\varepsilon = 1$, the theoretical curves (with equation Eq. 2.14 used for $C_F > 0$ and Eq. 2.17 for $C_F = 0$) provide a good fit to the data.
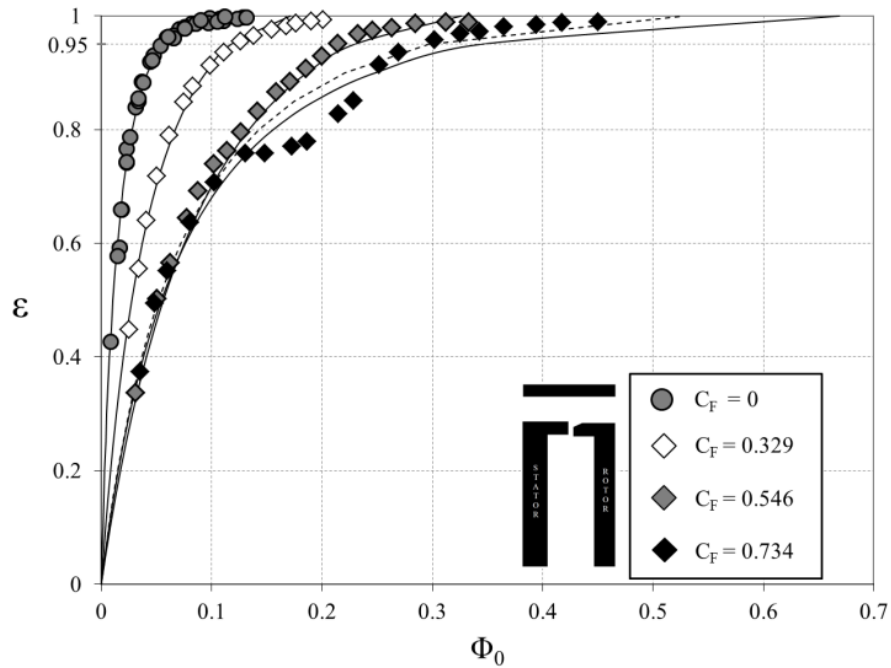
Figure 4.8: Effect of flow coefficient on variation of effectiveness with sealing parameter for axial-clearance seal (Symbols denote experimental data; lines are theoretical curves)

Noting the different scale from that in Figure 4.7, Figure 4.8 shows the effect of C_F on the variation of ε with Φ_0 for the axial-clearance seal. For any value of ε, the values of Φ_0 are significantly larger than those for the radial-clearance seal, which is consistent with measurements made at the design condition in the previous chapter. Although there was good agreement between the theoretical curves and the data for the three smaller values of C_F, the effectiveness data for the largest value display a distinct kink around $\Phi_0 \approx 0.2$. If the anomalous data are removed, the remaining data can be satisfactorily fitted, as shown by the broken curve in Figure 4.8.

The 'kink phenomenon' for the axial-clearance seal was also observed at the other under-speed conditions, which are not shown here. (The phenomenon was not observed for the other three seals, for which the sealing flow rates were significantly lower.) Tests were conducted with increasing and decreasing values of Φ_0 but the results were repeatable and no hysteresis effects were found. Although pressure measurements in the annulus shed no light on the kink phenomenon, it is speculated that it might be peculiar to the rig geometry and it could have been caused by the interaction between the sealing and mainstream flows at large sealing flow rates. The large sealant flow rates required to purge the wheel-space for the under-speed conditions could have impacted the discharge coefficients through the seal clearance. Future CFD research may be able to explain this behaviour. Interestingly,

Gentilhomme *et al.* (2002) observed similar behaviour in their effectiveness measurement curves, as shown in Figure 2.17.
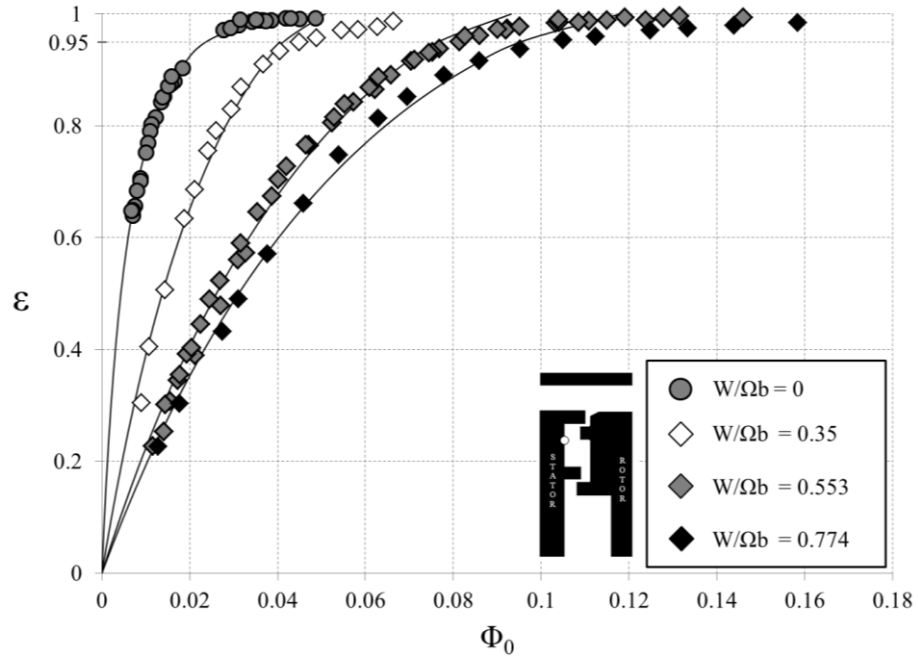
Figure 4.9: Effect of flow coefficient on variation of effectiveness with sealing parameter for outer sampling point of double seal (Symbols denote experimental data; lines are theoretical curves)

The effectiveness curves for the outer and inner sampling points of the double seal are shown in Figure 4.9 and Figure 4.10 respectively. The outer seal results are very similar to those shown in Figure 4.7 for the single radial-clearance seal. This is consistent with the conclusion drawn in Chapter 3, and demonstrates that the agreement shown in Figure 3.14 at the design condition can be extrapolated to off-design conditions. Again noting the change in scale from Figure 4.9, Figure 4.10 shows the values of Φ_0 to seal the inner seal are significantly smaller than for the outer one.
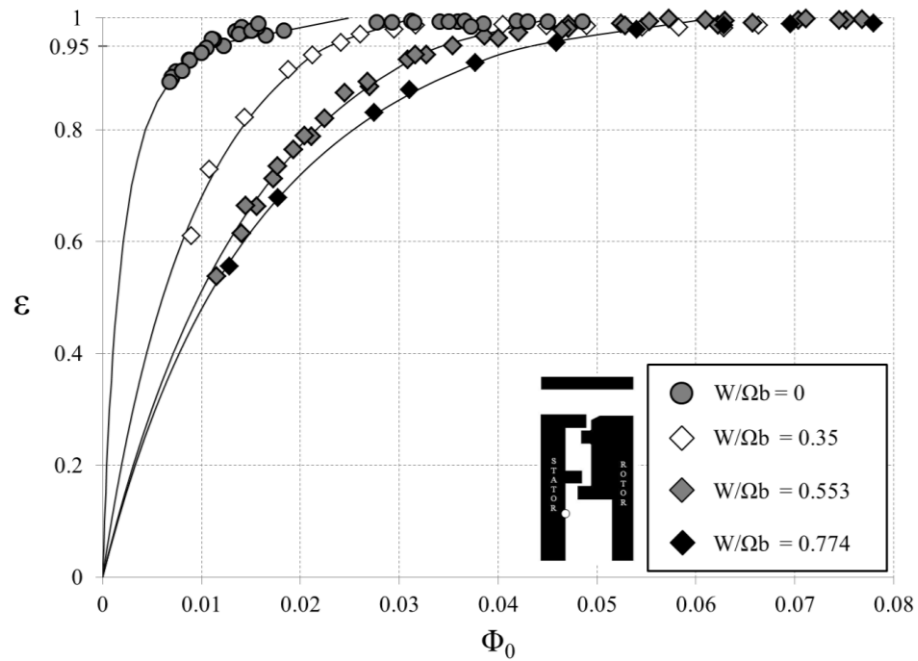
Figure 4.10: Effect of flow coefficient on variation of effectiveness with sealing parameter for inner sampling point of double seal (Symbols denote experimental data; lines are theoretical curves)

For each of the four seals tested, the values of Φ_{min} and their confidence intervals determined from the fitted effectiveness curves could be used to produce the variation of Φ_{min} with C_F. Before the above effectiveness curves were obtained, a separate series of concentration tests was conducted to determine Φ_{min} for the axial-clearance seal. As it was difficult, and sometimes impossible, to determine the precise value of Φ_0 when $\varepsilon = 1$, the value of Φ_0 when $\varepsilon = 0.95$ was used to define a new sealing parameter Φ_{min}'. The measured variation of Φ_{min}' with flow coefficient is discussed below.

4.3.2 Variation of Φ_{min}' with flow coefficient

Figure 4.11 shows the variation of Φ_{min}' with flow coefficient for the axial-clearance seal where, as stated above, Φ_{min}' denotes the value of Φ_0 when $\varepsilon = 0.95$. The direct measurements were of Φ_{min}' based on concentration measurements, at $r/b = 0.958$, for $Re_\phi = 5.52$, 8.17 and 9.68×10^5. The indirect values were calculated from the effectiveness curves discussed above, and the 'uncertainty bars' on the figure were based on the upper and lower bounds of the fitted effectiveness curves at $\varepsilon = 0.95$. It should be noted that, at large flow

coefficients where there was a kink in the effectiveness data, the effectiveness curves excluding the kinks (the dashed line in Figure 4.8) were used to determine Φ_{min}'.
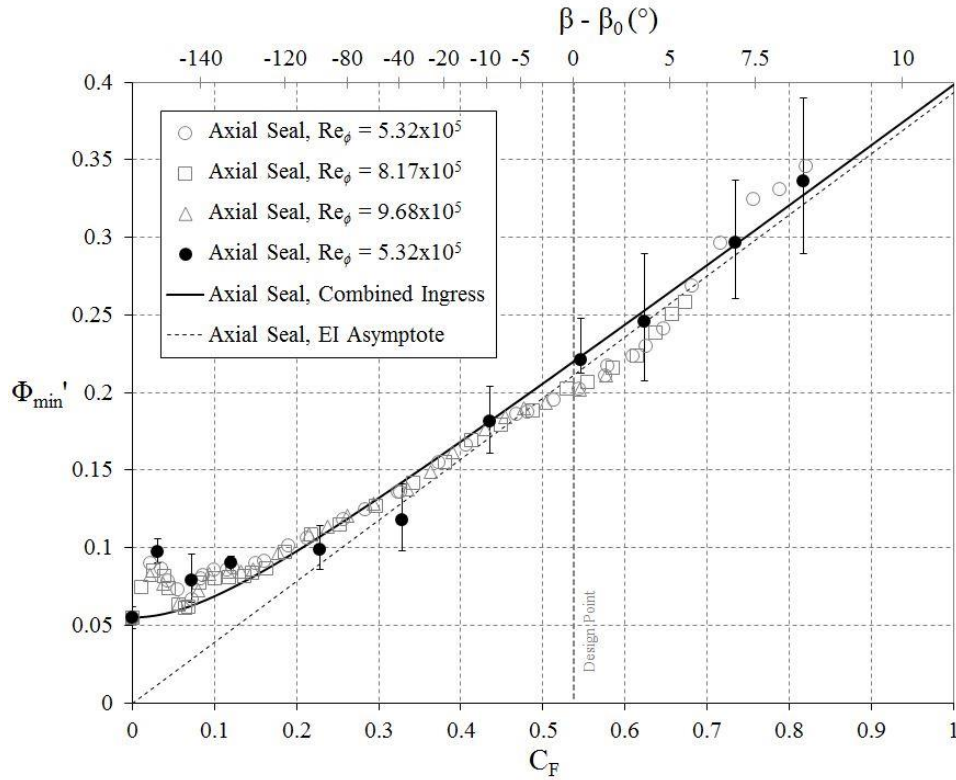
Figure 4.11: Variation of Φ_{min}' with flow coefficient for axial-clearance seal - Solid symbols denote indirect values of Φ_{min}' deduced from effectiveness curves; open symbols denote direct measurements of Φ_{min}'; solid line is fitted CI curve (Eq. 4.14); broken line is EI asymptote (Eq. 4.15)

The fitted CI curve was obtained from Eq. 4.7, which is rewritten here in terms of Φ_{min}' as:

$$\frac{\Phi_{min}'}{\Phi_{min,RI}'} = \frac{2}{3} \frac{\left(1 + k_c C_F{}^2\right)^{3/2} - 1}{k_c C_F{}^2} \tag{4.14}$$

where the constant k_c was found from a least-squares fit of the indirect measurements (Note: the redundant subscript CI has been omitted). For consistency with the other seals (where only indirect measurements were made), no direct measurements were used in the fit. As $C_F \to \infty$ and $\Phi_{min}' \to \Phi_{min,EI}'$, Eq. 4.14 reduces to

$$\frac{\Phi_{min,EI}'}{\Phi_{min,RI}'} = \frac{2}{3} k_c{}^{1/2} C_F \tag{4.15}$$

which is the equation for the EI asymptote shown in Figure 4.11. For the axial-clearance seal, $\Phi_{min,RI}' = 0.055$ and $k_c = 115$; these values and those for the other seals are shown in Table 4.1. As discussed previously, owing to the increasing effect of rotation, the difference between the EI asymptote and the CI curve increases as C_F decreases.

Figure 4.11 has a similar form to Figures 2.26 and Figure 4.1, which show the CI curve fitted to the data of Phadke and Owen (Figure 2.26) and Khilnani and Bhavnani (Figure 4.1). Unlike the rig used here, there were no vanes or blades in the external annuli of the rigs used by these two pairs of researchers; the circumferential external pressure variations in their two rigs were caused by eccentricities or partial blockages in the annuli. As noted for Figures 2.26 and Figure 4.1, the deviation between the CI curve and the EI asymptote in Figure 4.11 increases as C_F decreases and as the effects of rotation increase. It can be seen that even at the design point ($C_F = 0.538$) there is a small difference between the CI curve and the EI asymptote.

Based on the observation that $V_{r,max} = 0.105\Omega r$ near a rotating free disc using the 1/7th power law velocity profile from Von Kármán, Hamabe and Ishida (1992) expressed the increased pressure coefficient due to the rotor pumping action and compared it to the non-dimensional external pressure gradient. They proposed the following parameter:

$$k = \frac{0.011}{\Delta C_{p,max}}\left(\frac{\mathrm{Re}_{\theta}}{\mathrm{Re}_{w}}\right)^2 \tag{4.16}$$

where if k >> 1, the rate of ingestion will be affected by the disc pumping and if k << 1, by the external flow. This order of magnitude analysis was later confirmed by Chew *et al.* (1994).

It should be noted however that $\Delta C_{p,max}$ will depend where in the annulus it is evaluated at. For the data measured at location A in Figure 4.5, $k = 1$ at a flow coefficient, $C_F \approx 0.25$. This agrees with the results presented in Figure 4.11, where the effects of rotation are significant at $C_F < 0.25$. Owen *et al.* (2012b) suggested that that EI ingress occurs for $\Phi_{min,CI}$ / $\Phi_{min,RI} > 2$, and below this value the effects of rotation cannot be ignored. Again, this is consistent with the results in Figure 4.11.

The solution of the CI orifice equations captures the transition from RI to EI ingress as the amplitude of the circumferential variation of pressure increases. Any departure of the data from this curve must therefore be related to the effect of the blades.

There appears to be no systematic departure between the measured values and the CI curve in Figure 4.11 until $C_F < 0.1$. The sudden increase in Φ_{min}', which is shown by the

direct and indirect measurements of Φ_{min}' at these small values of C_F, is thought to be caused by massive separation of the flow over the blades at extreme deviation angles ($|\beta-\beta_0| > 130°$). Although many additional measurements were conducted to confirm that this 'blade effect', which also occurred for the other seals tested, was repeatable, it was surprising that the deviation angle appears to have no significant effect for $|\beta-\beta_0| < 130°$.
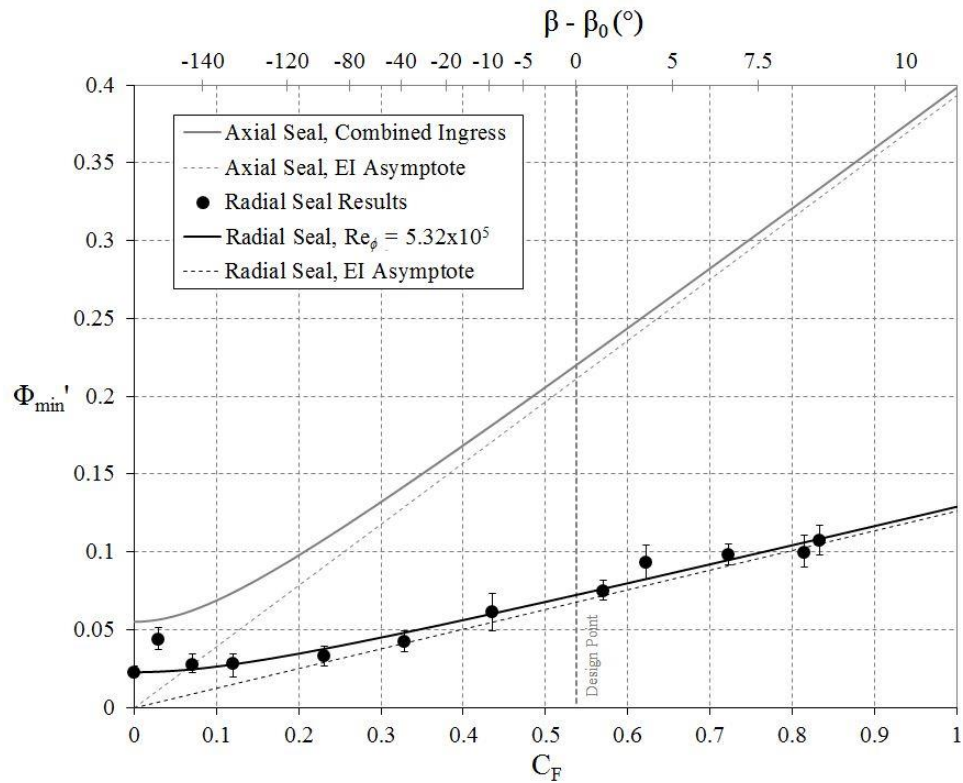
Figure 4.12: Variation of Φ_{min}' with flow coefficient for radial-clearance and axial-clearance seals - Solid symbols denote indirect values of Φ_{min}' deduced from effectiveness curves; solid lines are fitted CI curves (Eq. 4.14); broken lines are EI asymptotes (Eq. 4.15)

Figure 4.12 shows the variation of Φ_{min}' with flow coefficient for the radial-clearance seal. It can be seen that Φ_{min}' is significantly smaller than for the axial-clearance seal, which is consistent with the results presented in Sangan *et al.* (2011) for EI and RI ingress in single seals. As for the radial-clearance seal, the 'blade effect' for the axial-clearance seal occurs only at very large deviation angles.
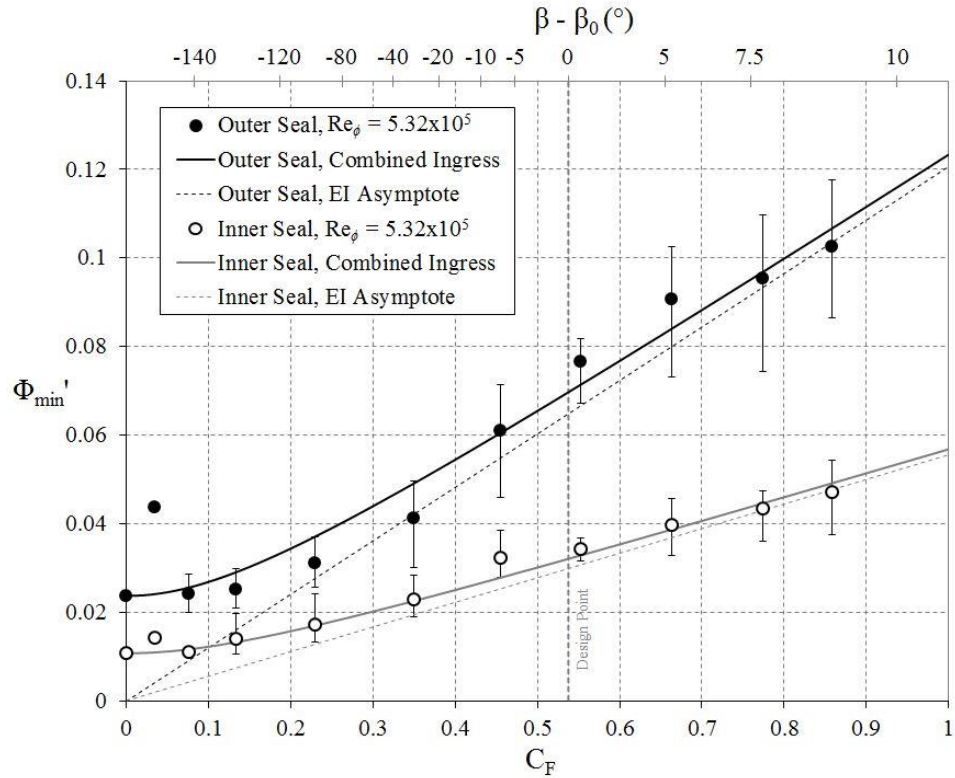
Figure 4.13: Variation of Φ_{min}' with flow coefficient deduced from effectiveness curves for double seal - Solid symbols denote indirect values of Φ_{min}' deduced from effectiveness curves; solid lines are fitted CI curves (Eq. 4.14); broken lines are EI asymptotes (Eq. 4.15)

Figure 4.13 shows the variation of Φ_{min}' with flow coefficient for the double seal. The results for the outer seal are similar to those shown in Figure 4.12 for the single radial-clearance seal, and the values of Φ_{min}' for the inner seal are significantly smaller than for the outer one. Again this is consistent with results presented in Chapter 3 for EI ingress in double seals.

The sharp increase in Φ_{min}' at small C_F occurs at similar deviation angles to that found for all the seals tested. This suggests that the 'blade effect' is insensitive to seal geometry.

Parameter	Axial-Clearance Seal	Radial-Clearance Seal	Double Outer Seal	Double Inner Seal
k_c	115	70.4	58.3	60.3
$\Phi_{min,RI}'$	0.055	0.0226	0.0237	0.0107
$C_{d,e,EI}'$	0.357	0.115	0.109	0.0503

Table 4.1: Parameters for CI fit for four seals tested

It is important to note that the results presented were obtained for incompressible flow in a rig with symmetrical blades and over a C_F range much larger than the normal operating range of engines. It was shown above that the effect of blades is complicated and depends on the geometry and relative location of the vanes, blades and seal: in some studies, the blades had a favourable effect on ingress; in others, the effect was adverse. Except under extreme conditions, the current results showed no significant effect of the blades for any of the seals tested. Although the 'blade effect', or systematic departure of the measured values of Φ_{min}' from the CI curves, only occurred here at extremely low values of C_F, it would be unsafe to conclude that this effect could not occur inside the operating range of a real turbine. (The fact that the measurements were made for incompressible flow is considered to be of secondary importance: extrapolation of effectiveness data from incompressible to compressible flow is discussed in Teuber *et al.*(2012))

It might seem surprising that the measured values of ΔC_p provided no evidence of the 'blade effect': even at the smallest values of C_F measured, the variation of $\Delta C_p^{1/2}$ with C_F remained linear. However, it has been shown computationally (see Zhou *et al.* (2013b)) that ingress is controlled by the magnitude of ΔC_p near the seal clearance: presumably the measurements made on the vane platform and on the outer surface of the annulus were insensitive to the effects near the seal itself. This topic is discussed further in Chapter 5.

4.4 Summary

This chapter presents off-design results for both over-speed, where the (symmetrical) blades rotate faster than at the design point, and under-speed conditions. The design flow coefficient was $C_F = 0.538$, and tests were conducted for $0 < C_F < 0.9$, which is a larger range than the operating range of engines. The 'deviation angle' between the flow over the blades and vanes, which increases as C_F decreases, varied between zero, at the design point, to 146° at $C_F = 0$. Single and double seals were tested for rotational Reynolds numbers were in the range $5.32 < Re_\phi/10^5 < 9.68$, and the flow was incompressible. The sealing effectiveness, ε, was determined using concentration measurements with CO_2 tracer gas, and pressure measurements were made using a Scanivalve system.

For both rotationally-induced (RI) and externally-induced (EI) ingress, the Bath effectiveness equations were used to correlate the variation of ε, the sealing effectiveness, with Φ_0, the nondimensional sealing flow parameter. The effectiveness equations were also used to determine Φ_{min}', the value of Φ_0 at $\varepsilon = 0.95$, and the combined ingress (CI) equation

was used to correlate the variation of Φ_{min}' with C_F and to determine the EI asymptote for each of the seals.

The principal conclusions are listed below:

- The pressure measurements showed that $\Delta C_p^{1/2}$ (where ΔC_p is the nondimensional peak-to-trough pressure difference in the annulus) was proportional to C_F. This proportionality occurred even at low values of C_F, where the deviation angle between the blades and vanes was very large ($> 130^\circ$).

- For $C_F > 0.1$, and for all the seals tested, the CI equation was in mainly good agreement with the variation of Φ_{min}' determined from the effectiveness curves; this implies that for a wide variation of C_F either side of the design point, the blade-deviation angle did not influence the degree of ingress.

- For $C_F < 0.1$ and deviation angles $> 130^\circ$, there was a sharp increase in Φ_{min}'; this is believed to be a 'blade effect' caused by separation of the flow over the blades.

- The difference between the CI correlations and the EI asymptotes increased as C_F decreased, and there was even a small but significant difference at the design point of $C_F = 0.538$.

It should be noted that these conclusions were drawn from data obtained in an experimental rig, with symmetrical blades and no fillet radii, operating over a C_F range much larger than that experienced in engines. The 'blade effect', which only occurred in the rig for $C_F < 0.1$, might occur at larger values of C_F in the operating range of a real turbine.

In principle, and within the limits of dimensional similitude, the results presented here should apply to a geometrically-similar engine operating at the same fluid-dynamic conditions. It is shown for a large range of operating conditions, Φ_{min}' is proportional to $\Delta C_p^{1/2}$, and it is tentatively suggested that this relationship could be used to extrapolate the results from and experimental rig to an engine.

Chapter 5: Use of pressure measurements to determine sealing effectiveness

Until this point, the 1-stage test rig has been used to determine ε_c, the sealing effectiveness based on gas concentration measurements. However, design codes for internal air systems usually estimate effectiveness from pressure, ε_p, rather than concentration. The orifice model can be used to relate the amount of ingress to the pressure difference across the rim seal but, the effectiveness determined in this way is strongly affected by the locations where the pressures are measured. In order to incorporate the model into design codes, the designer needs to know where in the turbine pressures should be evaluated. More broadly, it is necessary to understand the relationship between ε_c and ε_p in order to extrapolate measurements obtained from experimental rigs to engine conditions.

In this section a theoretical model has been developed to enable the value of ε_p to be determined from pressure measurements made at any arbitrary location on the vane platform, upstream of the seal clearance in a rig or engine. The model is based on the hypothesis that there is a unique location, referred to as the 'sweet spot', where the pressure distribution on the vane platform would ensure that $\varepsilon_c = \varepsilon_p$ for all sealing flow rates. Pressure and concentration measurements made in the 1-stage test rig are used to validate the theoretical model and to determine the corresponding values of ε_c and ε_p.

The author of this thesis conducted all the experimental testing and analysis involved in this chapter. Additional CFD analysis performed by a co-author of Owen *et al.* (2014) has been included in Section 5.3 for completeness.

As discussed in Section 2.5, pressure criteria have been used previously by Phadke and Owen (1988), Green and Turner (1994) and Bohn *et al.* (1995 and 1999) to quantify ingestion levels. The non-dimensional static pressure difference across the shroud, p^*, was defined as:

$$p^* = \frac{p(r) - p_{hub}}{p_{hub}} \tag{5.1}$$

where $p(r)$ is the static pressure measured at a certain radial location, and p_{hub} is the mean static pressure over one vane pitch on the stator shroud hub in the annulus. It follows when p^* is negative ingress will occur, and when $p^* = 0$, ingestion has been prevented. As noted

by Phadke and Owen (1988b), this definition is arbitrary and other criteria may be more appropriate, such as the maximum pressure in the annulus rather than the arithmetic mean.

5.1 Use of orifice model to calculate effectiveness

The Bath orifice model derived in Owen (2011a and b) and summarised in Section 2.6 was based on pressures. It was assumed that EI ingress is related to Δp, the peak-to-trough pressure difference in the annulus, where:

$$\Delta p = p_{2,\max} - p_{2,\min} \tag{5.2}$$

The sealing effectiveness in the model is related to g, the normalised pressure difference across the seal, where:

$$g = \frac{p_1 - p_{2,\min}}{\Delta p} \tag{5.3}$$

As shown by Figure 2.20, the subscripts 1 and 2 refer to locations in the wheel-space and annulus respectively, and these locations were not specified in the orifice model. The relationship between p_1 and p_2 is shown diagrammatically by Figure 2.21; it follows that ingress will be prevented from occurring when p_1 reaches $p_{2,\max}$ and therefore $g = 1$.

By assuming a linear saw-tooth model for the circumferential distribution of pressure in the annulus, the orifice equations were solved by Owen (2011b) to give:

$$\frac{\Phi_o}{\Phi_{\min}} = g^{3/2} - \Gamma_c(1-g)^{3/2} \tag{5.4}$$

It was also shown from the orifice equations that:

$$\varepsilon_p = 1 - \Gamma_c \left[\frac{1-g}{g} \right]^{3/2} \tag{5.5}$$

As discussed above, ε_p is the sealing effectiveness based on pressure differences, and Γ_c is the ratio of the discharge coefficients for ingress and egress through the seal clearance ($C_{d,i}/C_{d,e}$).

In practice, g (and therefore ε_p) depends on the sealing flow rate, and it also depends on where the pressures are measured. That is, $g = g(\Phi_o, x)$, where x is that axial location in the annulus where Δp is measured. At the sweet spot (where $x = \hat{x}$, $\varepsilon_p = \hat{\varepsilon}_p = \varepsilon_c$ and $g = \hat{g}$), Eq. 5.5 becomes:

$$\hat{\varepsilon}_p = \varepsilon_c = 1 - \Gamma_c \left[\frac{1-\hat{g}}{\hat{g}} \right]^{3/2}$$

(5.6)

Using Eq. (2.14), the effectiveness equation for ε_c, it follows from Eq. 5.6 that:

$$\hat{g} = \frac{1}{1 + \Gamma_c^{-2/3}(1-\varepsilon_c)^{2/3}}$$

(5.7)

Defining $\hat{g}* = \hat{g}$ when $\Phi_o = 0$, and $\varepsilon_c = 0$, it follows from Eq. 5.7 that:

$$\hat{g}* = \frac{\Gamma_c^{2/3}}{1 + \Gamma_c^{2/3}}$$

(5.8)

It is shown in the following section how $\hat{g}$ and $\hat{\varepsilon}_p$ can be determined from experimental measurements.

5.1.1 Determination of effectiveness from pressure measurements

In the model developed below, it is assumed that the *sweet spot*, where $g* = \hat{g}*$, can be found on the vane platform upstream of the clearance. This is consistent with the results of Owen *et al.* (2012a) shown in Figure 2.25, who used steady 3D CFD based on the geometry of the Bath rig (but without blades and with an axial-clearance seal) to determine the sealing effectiveness.

In the annulus, $p_{2,min}$, $p_{2,max}$ and Δp depend on both Φ_o and x, where x is the nondimensional axial distance from the centre of the seal clearance; in the wheel-space, p_1 is invariant with x and depends only on Φ_o. To make these dependencies explicit, Eq. 5.3 is rewritten as:

$$g(\Phi_o,x) = \frac{p_1(\Phi_o) - p_{2,min}(\Phi_o,x)}{\Delta p(\Phi_o,x)}$$

(5.9)

Similarly, at location A where the pressures are measured in the annulus, $x = x_A$ and:

$$g(\Phi_o,x_A) = \frac{p_1(\Phi_o) - p_{2,min}(\Phi_o,x_A)}{\Delta p(\Phi_o,x_A)}$$

(5.10)

Eliminating p_1 from Eqs. 5.7 and 5.8, it follows that:

$$g(\Phi_o,x) = \frac{\Delta p(\Phi_o,x_A)}{\Delta p(\Phi_o,x)} g(\Phi_o,x_A) + \frac{p_{2,\min}(\Phi_o,x_A) - p_{2,\min}(\Phi_o,x)}{\Delta p(\Phi_o,x)} \qquad (5.11)$$

Using a 'separation-of-variables' approach, it is assumed that:

$$\Delta p(\Phi_o,x) = \zeta(x) \Delta p(\Phi_o,x_A) \qquad (5.12)$$

and

$$[p_{2,\min}(\Phi_o,x) - p_{2,\min}(\Phi_o,x_A)] = \chi(x) \Delta p(\Phi_o,x_A) \qquad (5.13)$$

where $\zeta(x)$ and $\chi(x)$ are *similarity parameters* that depend on x but are assumed to be invariant with Φ_o. At location A, $\zeta(x_A) = 1$ and $\chi(x_A) = 0$.

Eq. 5.11 can now be written as:

$$g(\Phi_o,x) = \zeta(x)^{-1}[g(\Phi_o,x_A) - \chi(x)] \qquad (5.14)$$

Consequently, at the sweet spot where $x = \hat{x}$ and $g = \hat{g}$, Eq. 5.14 becomes:

$$g(\Phi_o,\hat{x}) = \hat{g}(\Phi_o) = \zeta(\hat{x})^{-1}[g(\Phi_o,x_A) - \chi(\hat{x})] \qquad (5.15)$$

As $\zeta(\hat{x})$ and $\chi(\hat{x})$ are constants, Eq. 5.15 can be expressed more simply as

$$\hat{g}(\Phi_o) = B\,g(\Phi_o,x_A) + C \qquad (5.16)$$

where the constants B and C are given by

$$B = \zeta(\hat{x})^{-1} = \frac{\Delta p(\Phi_o,x_A)}{\Delta p(\Phi_o,\hat{x})} \qquad (5.17)$$

$$C = -\frac{\chi(\hat{x})}{\zeta(\hat{x})} = -\frac{p_{2,\min}(\Phi_o,\hat{x}) - p_{2,\min}(\Phi_o,x_A)}{\Delta p(\Phi_o,\hat{x})} \qquad (5.18)$$

As $x_A \to \hat{x}$ then $B \to 1$ and $C \to 0$.

Knowing $\hat{g}$ from Eq. 5.7, the constants B and C in Eq. 5.16 can be found from linear regression of $\hat{g}$ versus the measured values of $g(\Phi_o,x_A)$; this is shown in Section 5.3.

The sealing effectiveness $\hat{\varepsilon}_p$, which in principle could be determined from pressure measurements at the sweet spot, can be calculated from Eq. 5.6 where:

$$\hat{\varepsilon}_p(\Phi_o) = 1 - \Gamma_c \left[\frac{1 - C - Bg(\Phi_o,x_A)}{Bg(\Phi_o,x_A) + C} \right]^{3/2} \qquad (5.19)$$

As shown in Section 5.3, Eq. 5.19 ensures that the sealing effectiveness determined from pressure measurements is equivalent to that determined from concentration measurements.

5.1.2 Calculation of discharge coefficients at sweet spot

The discharge coefficient for egress, determined from measurements at location A, can be calculated from Eq. 2.10 by:

$$C_{d,e}(x_A) = \frac{3}{2} \frac{\Phi_{\min}}{[\Delta C_p(x_A)]^{1/2}} \tag{5.20}$$

This value depends on where the measurements are made, and the correct value to use is the one determined at the sweet spot, where:

$$C_{d,e}(\hat{x}) = \frac{3}{2} \frac{\Phi_{min}}{[\Delta C_p(\hat{x})]^{1/2}} \tag{5.21}$$

At the sweet spot, Eq. 5.17 shows that:

$$\frac{\Delta p(\Phi_o, x_A)}{\Delta p(\Phi_o, \hat{x})} = B \tag{5.22}$$

where, as described above, the constant B is found from linear regression of the pressure measurements. It follows from Eq. 5.22 that:

$$\Delta C_p(\hat{x}) = B^{-1} \Delta C_p(x_A) \tag{5.23}$$

Substitution in Eq. 5.21 gives

$$C_{d,e}(\hat{x}) = B^{1/2} C_{d,e}(x_A) \tag{5.24}$$

Similarly, for ingress,

$$C_{d,i}(\hat{x}) = B^{1/2} C_{d,i}(x_A) \tag{5.25}$$

As shown in Section 5.5, the discharge coefficients determined from measurements in an experimental rig could be used to compute the ingress through an engine rim seal.

5.2 Radial-clearance rim seal

This section details the experimental validation of the theoretical model using a radial-clearance rim seal. Location A on the vane platform as shown in Figure 3.5 is used to determine p_2.
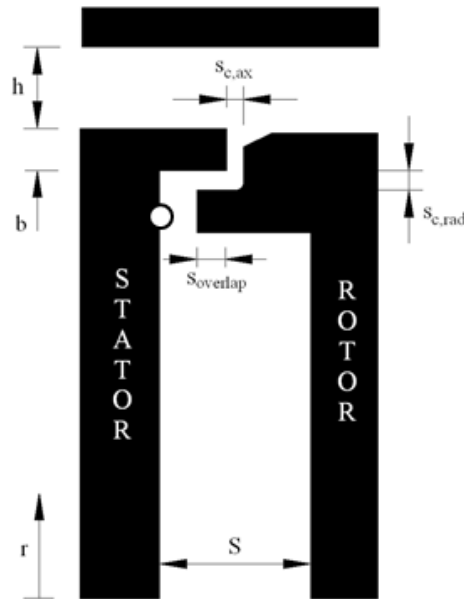
Figure 5.1: Geometry of radial-clearance seal

Geometric Symbol	Dimension
h	10 mm
b	190 mm
S	20 mm
$s_{c,ax}$	2 mm
$s_{c,rad}$	2.4 mm
$s_{overlap}$	3.7 mm

Table 5.1: Dimensions of radial-clearance seal

Figure 5.1 illustrates the geometry of the radial-clearance rim-seal tested in this section. This seal slightly differs from the radial seal presented in Section 3.2, therefore the geometric dimensions indicating the wider axial and radial clearances are given in Table 5.1.
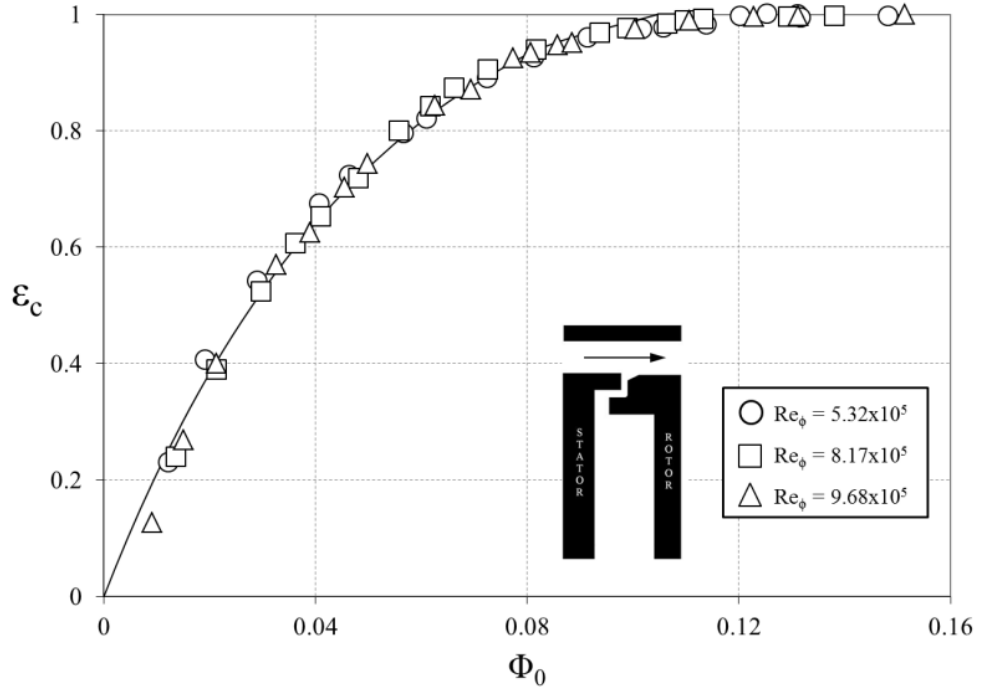
Figure 5.2: Variation of ε_c with Φ_0 for radial-clearance seal: EI ingress (Symbols denote data; lines are theoretical curves)

Parameter	EI
Φ_{min}	0.105
Φ_{min}^{-}	0.0999
Φ_{min}^{+}	0.110
Γ_c	1.35
Γ_c^{-}	1.12
Γ_c^{+}	1.64
σ	0.0172

Table 5.2: Parameters for radial-clearance seal at EI ingress conditions

Figure 5.2 shows comparisons between the theoretical curve, Eq. 2.14, and the experimental values of ε_c based on the concentration measured on the stator at a non-dimensional radius $r/b = 0.958$. Φ_{min} and Γ_c were calculated from a statistical fit of the data using the maximum likelihood method described by Zhou *et al.* (2013a). Their respective values were found to be 0.105 and 1.35 for the radial-clearance seal, as shown in Table 5.2. Once again the experimental data are in good agreement with the theoretical curve. Figure 5.2 also shows that Re_ϕ, the rotational Reynolds number, has no significant effect on the variation of effectiveness.

5.3 Computation of sweet spot location

In this section, CFD analysis performed by a co-author of Owen *et al.* (2014), is used to support the experiments which validate the theoretical model. The principal object of the CFD was to determine the location of the sweet spot and to test the hypothesis that its location was invariant with the sealing flow rate. As it was shown in the Chapter 4 that the blades had a negligible effect on ingress at the design condition, computations were performed with vanes but in the absence of rotating blades.

Although, as shown above, the sealing effectiveness and the discharge coefficients can be calculated without knowing the location of the sweet spot, its location is needed if the experimental results are to be applied to an engine rim seal. As shown below, its location can be determined computationally using Eqs. 5.3 and 5.7.

Figure 5.3 shows the computed axial distribution of $g(x)$, based on Eq. 5.3, for five values of Φ_o/Φ_{min}. The horizontal lines represent the five corresponding values of $\hat{g}$, which were calculated from Eq. 5.7 with the values of ε_c and Γ_c determined from the concentration measurements. The intercept of these two curves occurs at the point where $g = \hat{g}$ and consequently where $x = \hat{x}$. The vertical line corresponds to the mean of the computed values of $\hat{x}$. (The values of p_1 were computed on the stator surface at $r/b = 0.958$, which is the location used for the experimental measurements discussed in Section 5.4.)
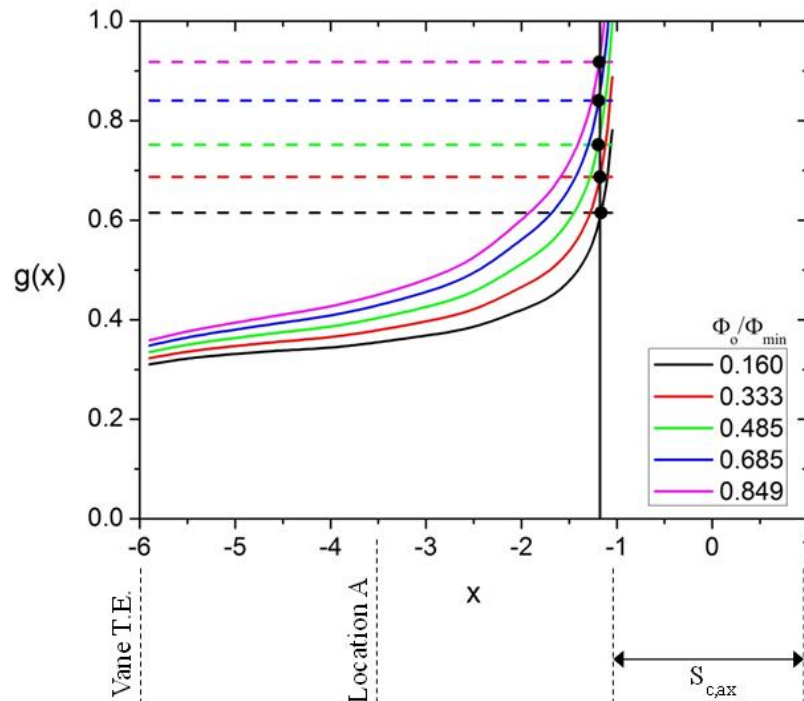
Figure 5.3: Effect of Φ_0/Φ_{min} on computed variation of $\hat{g}$ and g with x showing location of sweet spot - Horizontal broken lines show values of $\hat{g}$ from Eq. 5.7; solid curve shows computed variation of $g(x)$ from Eq. 5.3; solid vertical line shows mean value of computed $\hat{x}$

Figure 5.4 shows the computed values of $\hat{x}$ for the 22 values of Φ_o/Φ_{min} used for the pressure measurements described in Section 5.4. The mean value of $\hat{x}$ for the radial-clearance seal was 1.18, which is just 0.18 mm upstream of the seal clearance in the experimental rig. Although there is no reason to believe that this value will be the same for all seals, it is consistent with the previous computations for an axial-clearance seal in the same rig, shown in Figure 2.25. The fact that there is no significant effect of the sealing flow rate on the computed values of $\hat{x}$ provides support for the assumption that $\hat{x}$ is invariant with Φ_o.
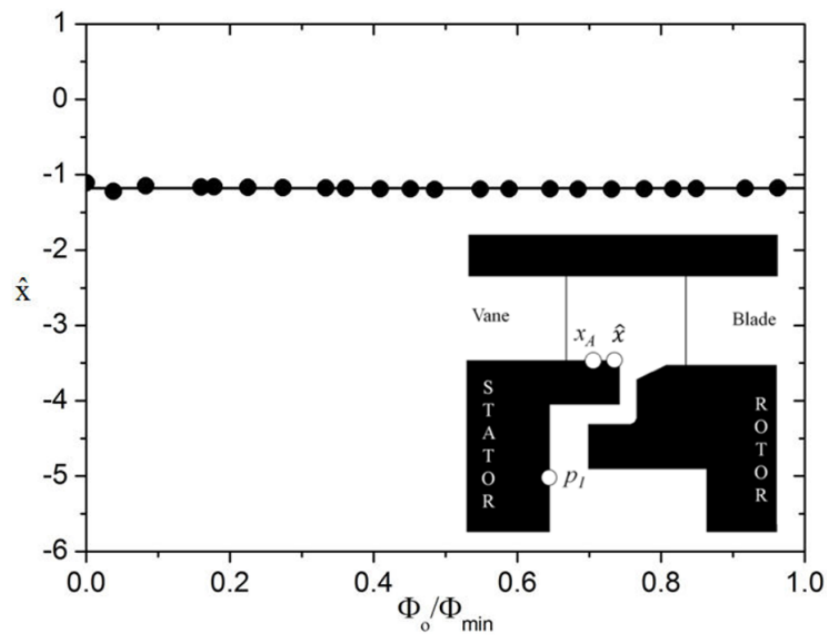
Figure 5.4: Computed variation of $\hat{x}$ with Φ_o/Φ_{min} - Solid line shows mean value of $\hat{x}$, with its geometric position shown in relation to the seal clearance (inset)

5.4 Experimental measurements
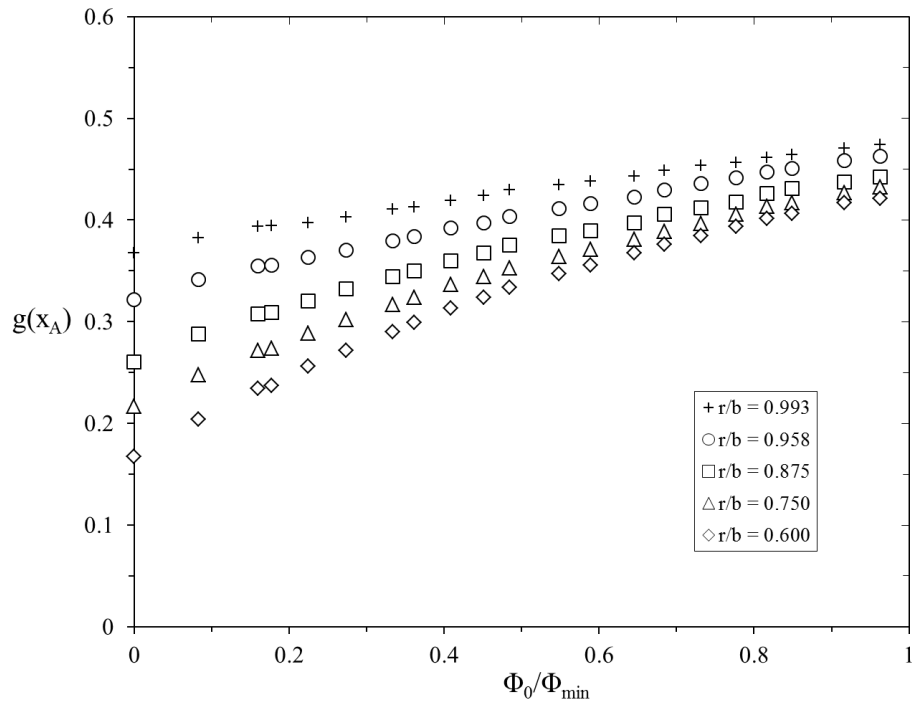
Figure 5.5: Effect of *r/b* on measured variation of *g(x_A)* with *Φ_o/Φ_min* for radial-clearance seal

The pressure measurements were obtained for the radial-clearance seal at $Re_\phi = 8.17 \times 10^5$. Figure 5.5 shows the measured variation of $g(x_A)$ with Φ_o/Φ_{min}. As shown in Figure 3.5, the static pressure on the surface of the stator, p_1, was measured at 14 different radial locations ($0.600 < r/b < 0.993$) in the wheel-space. For clarity, only five of these measurements are shown in Figure 5.5. It can be seen that there is no location of r_1/b that ensures that $g(x_A) = 1$ when $\Phi_o/\Phi_{min} = 1$, which confirms the fact that location A cannot be the sweet spot, and consequently these uncorrected measurements cannot be used to determine the effectiveness.

Although, in theory, the variation of $g(x_A)$ with Φ_o/Φ_{min} should be slightly nonlinear, the fact that the nonlinearity shown in Figure 5.5 increases as *r/b* decreases is attributed to the swirl in the wheel-space. The swirl creates a nonlinear radial pressure gradient, and the difference between the pressures at the measurement radius *r* and the seal radius *b* increases as *r/b* decreases.

There are two extremes to avoid in choosing a suitable location of *r/b* to measure p_1. As shown by Bohn *et al.* (1995) in Figure 2.13, if the radius is too close to the seal then the pressure in the wheel-space will be non-axisymmetric; if the radius is too small, the effects

of swirl will be significant. (The effect of swirl on the radial distribution of pressure in the wheel-space of the rig used here is discussed in Chapter 3). A value of $r/b = 0.958$ was chosen here as a compromise; this was also the radial location used to make the concentration measurements from which ε_c was determined.
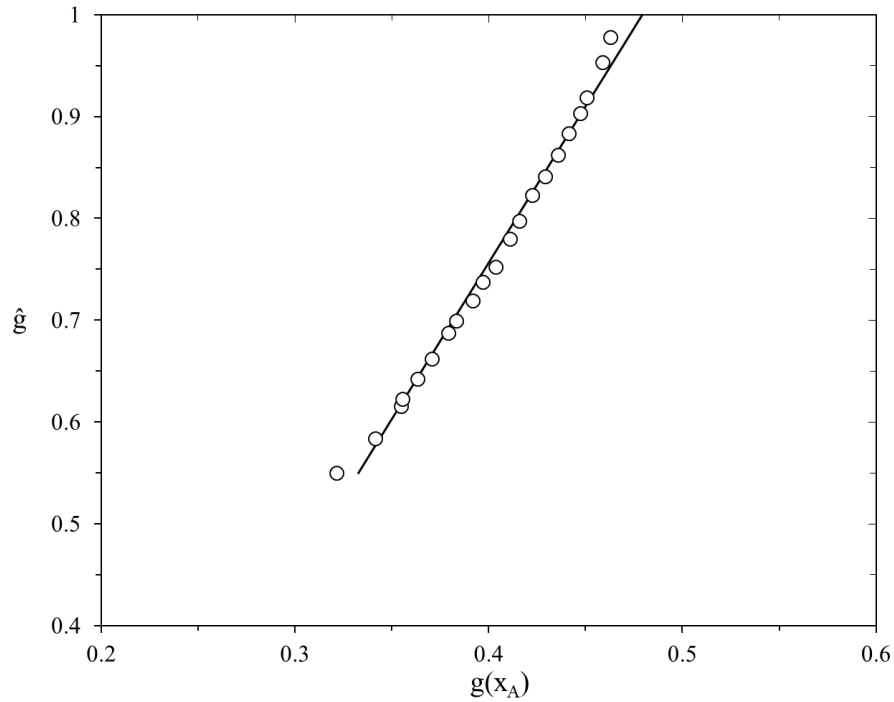
Figure 5.6: Variation of $\hat{g}$ with measured values of $g(x_A)$ for radial-clearance seal (Solid line shows linear regression of data)

Figure 5.6 shows the variation of $g(x_A)$, the values of which were measured at $r_I/b = 0.958$, versus $\hat{g}$, calculated from Eq. 5.19. Linear regression was used to determine the values of the constants, and it was found that $B = 3.07$ and $C = -0.472$. The standard deviation between the experimental values of $g(x_A)$ and the correlation was 0.012; in Section 5.6, the uncertainty in the measured value of $g(x_A)$ was estimated to be ≤ 0.0077. These results support the assumptions made in deriving eqs. (5.17 and 5.18).
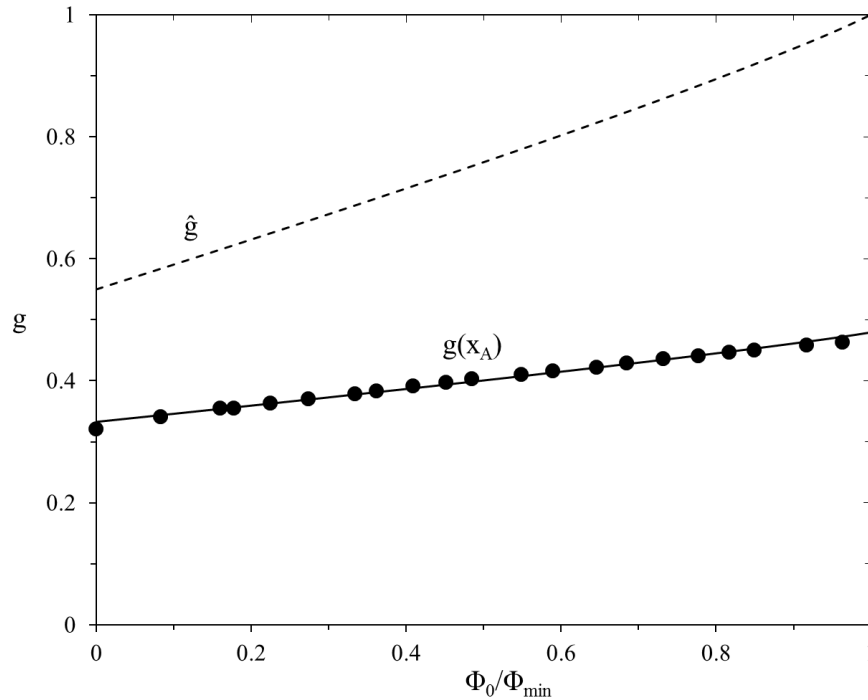
Figure 5.7: Variation of $\hat{g}$ and $g\,(x_A)$ with Φ_o/Φ_{min} for radial-clearance seal

Figure 5.7 shows the variation of $g(A)$ and $\hat{g}$ with Φ_o/Φ_{min}, where the curve for $\hat{g}$ was based on Eq. 5.7 and the values of $g(x_A)$ are the same as those shown in Figure 5.6. The results for $\hat{g}$ demonstrate the consistency requirement that g equals unity at the sweet spot location, when Φ_o is equal to Φ_{min}, as determined from the concentration measurements. For $\Phi_o = 0$, $\hat{g} = \hat{g}^*$, and it follows from Eq. (5.8) (with $\Gamma_c = C_{d,i}/C_{d,e} = 1.32$) that $\hat{g}^* = 0.546$.

Figure 5.8 shows the comparison of sealing effectiveness determined from both pressure and concentration with Φ_o/Φ_{min}. The values of ε_p were calculated from Eq. 5.19, using the values of B and C given above and the measured values of $g(x_A)$ shown in Figure 5.7. The values of ε_c were obtained from the concentration measurements, and Eq. 2.14 was used to produce the effectiveness curve; this data is repeated from Figure 5.2.

The standard deviation between the calculated values of ε_p and the effectiveness curve was 0.017, and that between the measured values of ε_c and the curve was 0.019. (Note: these standard deviations were based on the differences between the individual calculated or measured values and the theoretical curve and not on the uncertainties described in Section 5.6). The results in Figure 5.8 give confidence in the theoretical model described in Section 5.1.
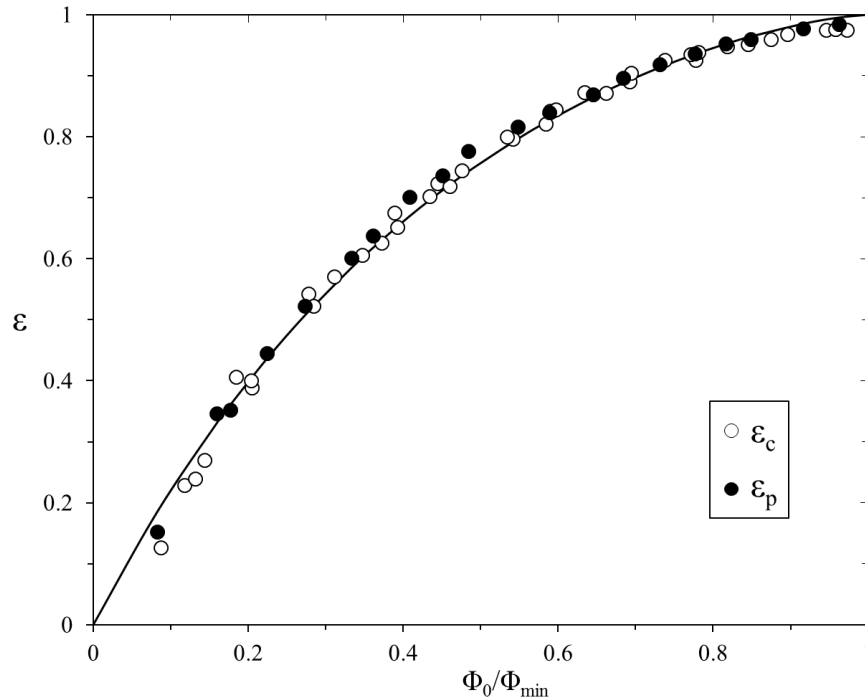
Figure 5.8: Variation of sealing effectiveness with Φ_o/Φ_{min} for radial-clearance seal - Solid symbols denote values of ε_p from pressure measurements; open symbols denote values of ε_c from concentration measurements; solid curve is based on effectiveness equation (Eq. 2.14)

The values of $C_{d,e}$ and $C_{d,i}$ for the radial-clearance seal determined from the measurements of ΔC_p at location A were 0.177 and 0.239 respectively. Using Eqs. 5.24 and 5.25 with $B = 3.07$, the values of $C_{d,e}$ and $C_{d,i}$ at the sweet spot are 0.310 and 0.419 respectively. It is shown below how the model could be used by the engine designer.

5.5 Extrapolation of effectiveness data from rig to engine

In principle, orifice models provide a simple method of extrapolating the experimentally-measured effectiveness of a particular rim seal to a turbine with similar seal geometry. However, the conditions – particularly the Mach number and temperatures – in engines are usually significantly different from those in the experimental rig. Also, the design codes used for internal air systems usually estimate ingress from pressures rather than from the concentration measurements made in most rigs. Care and attention to mathematical consistency are needed if orifice models are used to extrapolate rig measurements to engine conditions. In particular, the 'correct' pressures must be used in the engine, and the theoretical model discussed above was developed to ensure that consistency.

The Mach number effect was considered by Teuber *et al.* (2012) who showed, theoretically and computationally for the Bath rig, that the magnitude of ΔC_p increases as the Mach number increases. They showed that, by correcting ΔC_p and assuming that the discharge coefficients are unaffected by Mach number, the sealing effectiveness, ε_c, determined by concentration measurements in an experimental rig at one Mach number, could be used to compute the effectiveness in an engine at another Mach number. Their suggested correction for Φ_{min} is given in Eq. 2.19. However, unless the location of the sweet spot is known, the effectiveness cannot be related to pressure differences in the engine. This makes the method of limited use to designers.

The location of the sweet spot in the engine has to be determined using CFD, as described in Section 5.3. In the engine, unsteady CFD would be required to account for the turbine blades. However, as shown in Chapter 4, the symmetric blades used in the rig had little effect on ingress at the design condition. Therefore the steady CFD results presented did not include the blades. The mean value of $\hat{x}$ could then be determined from computations made for a range of sealing flow rates. An approximate value could be found by computing $\hat{x}$ only for the case where the sealing flow rate is zero. For this case, $\hat{g} = \hat{g}^*$ where, as shown in Section 5.1.1:

$$\hat{g}^* = \frac{p_1^* - p_{2,\min}^*(\hat{x})}{\Delta p^*(\hat{x})} = \frac{\Gamma_c^{2/3}}{1 + \Gamma_c^{2/3}} \tag{5.26}$$

and Γ_c is known from the concentration measurements in the rig. The value of p_1^* could be evaluated at any convenient radial location in the wheel-space of the engine, bearing in mind the qualifications given in Section 5.4. The approximate value of $\hat{x}$ could then be found by computing $p_{2,min}^*(x)$ and $\Delta p^*(x)$ for different values of x, on the vane platform upstream of the seal clearance, until Eq. 5.26 is satisfied.

In the proposed method, it is assumed that the discharge coefficients at the sweet spot for the rim seal in the engine are equal to those at the sweet spot in the rig. As $C_{d,e,engine} = C_{d,e,rig} = C_{d,e}$, it follows that:

$$\Phi_{\min,engine} = \frac{2}{3} C_{d,e} \Delta C_{p,engine}^{1/2} \tag{5.27}$$

where $\Delta C_{p,engine}$ is the time-average value determined at the sweet spot in the engine. As proposed by Teuber *et al.*, this relationship is assumed to apply for all Mach numbers.

For the case where $\Phi_0 < \Phi_{min}$, it is necessary to calculate $\hat{g}$ *for any flow rate* by:

$$\hat{g} = \frac{p_1 - p_{2,\min}(\hat{x})}{\Delta p(\hat{x})} \qquad (5.28)$$

Knowing $\hat{g}$, the sealing effectiveness can be calculated from Eq. 5.6 where:

$$\hat{\varepsilon}_p = 1 - \Gamma_c \left[\frac{1 - \hat{g}}{\hat{g}} \right]^{3/2} \qquad (5.29)$$

The uncertainties in $\hat{\varepsilon}_p$ depend on the uncertainties in $\hat{g}$, which, as shown in Section 5.6, depend on the uncertainties in the pressures determined for the engine.

The above method of extrapolation requires validation by experiments and CFD at engine-representative Mach numbers and density ratios not achievable in the existing Bath rig. Experimental rigs like the large HGIR rig described by Palafox *et al.* (2013) and the Sussex rig used by Gentilhomme *et al.* (2003) are more suitable for this purpose. A new 1.5 stage ingestion rig described in Chapter 6, featuring realistic turbine blade and vane geometries, is under construction at the University of Bath. It is hoped in the future this rig will be able to provide the data necessary to thoroughly test theoretical models that could then be used with confidence by engine designers.

5.6 Uncertainty in pressure measurements

From Eq. 5.3:

$$g = \frac{p_1 - p_{2,\min}}{p_{2,\max} - p_{2,\min}} = \frac{X}{Y} \qquad (5.30)$$

where $X = p_1 - p_{2,min}$ and $Y = p_{2,max} - p_{2,min}$. Hence:

$$dg = \frac{\partial g}{\partial X} dX + \frac{\partial g}{\partial Y} dY \qquad (5.31)$$

$$= \frac{dX}{Y} - X \frac{dY}{Y^2} \qquad (5.32)$$

The magnitude of the relative uncertainty in g is then bounded by:

$$\left| \frac{\delta_g}{g} \right| \leq \left| \frac{\delta_X}{X} \right| + \left| \frac{\delta_Y}{Y} \right| \qquad (5.33)$$

where $|\delta_X| = |\delta_{p1}| + |\delta_{p2,min}|$ and $|\delta_Y| = |\delta_{p2,max}| + |\delta_{p2,min}|$, and δ_g, δ_{p1}, $\delta_{p2,min}$, $\delta_{p2,max}$, are the uncertainties in g, p_1, $p_{2,min}$, $p_{2,max}$ respectively. Hence:

$$\frac{\left|\delta_g\right|}{g} \leq \left\{ \frac{\left|\delta_{p1}\right| + \left|\delta_{p2,\min}\right|}{p_1 - p_{2,\min}} + \frac{\left|\delta_{p2,\max}\right| + \left|\delta_{p2,\min}\right|}{p_{2,\max} - p_{2,\min}} \right\} \tag{5.34}$$

When the uncertainty is a percentage of the full-scale range, which was the case in the experiments, then $|\delta_{p1}| = |\delta_{p2,min}| = |\delta_{p2,max}| = \delta$, say, and Eq. 5.34 simplifies to:

$$\frac{\left|\delta_g\right|}{g} \leq \frac{2\delta}{p_{2,\max} - p_{2,\min}}\left(1 + g^{-1}\right) \tag{5.35}$$

or

$$\left|\delta_g\right| \leq \frac{2\delta}{p_{2,\max} - p_{2,\min}}\left(1 + g\right) \tag{5.36}$$

The Druck PDCR 22 Scanivalve pressure transducers used in the experiments had a stated uncertainty of ±0.06% (Best Straight Line) across a range of 70 mbar, which implies that $\delta = 0.042$ mbar. In the experiments, $p_{2,max} - p_{2,min} \approx 16.3$ mbar, and $g(x_A) < 0.5$, so from Eq. 5.36, $|\delta_g| \leq 0.0077$.

5.7 Summary

The main object of this chapter was to relate the sealing effectiveness determined from concentration measurements (ε_c) in an experimental rig to the effectiveness computed from pressure differences (ε_p) in an engine.

A theoretical model was developed to calculate the axial location (denoted by $\hat{x}$ and referred to as the 'sweet spot') where the pressures should be measured on the vane platform to ensure that $\varepsilon_p = \varepsilon_c$. The assumption was made that $\hat{x}$ should be invariant with Φ_o, the sealing flow parameter.

Concentration and pressure measurements were made on a single-stage turbine rig fitted with a radial-clearance rim seal. The concentration measurements were used, in conjunction with a previously published orifice model, to correlate the variation of ε_c with Φ_o for externally-induced ingress.

A nondimensional pressure difference, referred to as $g(x_A)$, was determined from measurements at an arbitrary location (location A) in the annulus of the rig. The pressure measurements showed that, as predicted by the model, $\hat{g}$, the nondimensional pressure difference at the sweet spot, varied linearly with $g(x_A)$ for $0 < \Phi_o/\Phi_{\min} < 1$, where $\Phi_{\min}$ is the minimum value of Φ_o needed to prevent ingress through the seal clearance.

Linear regression of $\hat{g}$ versus $g(x_A)$ was used to determine two constants, B and C, from which it was possible to calculate the variation of ε_p with $\Phi_o/\Phi_{\min}$. The calculated values of ε_p were in good agreement with the measured values of ε_c and with the effectiveness equation derived from the orifice model.

Steady 3D CFD, based on the geometry of the experimental rig but without the rotating blades, was used to compute the value of $\hat{x}$ for $0 < \Phi_o/\Phi_{\min} < 1$. These computations showed that, as assumed in the model, $\hat{x}$ was virtually invariant with Φ_o. In agreement with Owen *et al.* (2012a), the computed value of $\hat{x}$ was found to be very close to the upstream edge of the seal clearance.

Using the model, $C_{d,e}(\hat{x})$ and $C_{d,i}(\hat{x})$, the discharge coefficients for egress and ingress at the sweet spot, could be related to $C_{d,e}(x_A)$ and $C_{d,i}(x_A)$, the discharge coefficients determined experimentally at location A in the rig.

It was shown how, in principle, the theoretical model could be used to determine the effectiveness for the rim seals in an engine. This would involve the use of CFD, together with the values of $C_{d,e}(\hat{x})$ and $C_{d,i}(\hat{x})$ determined from an experimental rig with a similar rim seal, to compute the sweet spot for the engine seal.

Chapter 6: Design of a 1.5 stage experimental test facility

This chapter details the design of a novel 1.5 stage research facility which experimentally models hot gas ingestion into a downstream, as well as an upstream wheel-space. A requirement was identified for a new rotating experimental facility capable of measuring the effects of ingress with turned rotor blades. The downstream wheel-space differs significantly in some important ways: the axial flow in the annulus is from the rotor towards the stator, and the swirl of the ingested fluid can be in the opposite sense to the direction of rotation of the turbine disc.

The rig was specifically designed for detailed instrumentation access in a more benign environment than is typically found in a gas turbine. Once again CO_2 gas measurements will be used to ascertain the effectiveness of rim seal designs in both wheel-spaces. Infrared sensor technology is employed to determine the adiabatic surface temperatures, adiabatic effectiveness and Nusselt numbers for the rotating surfaces. Static and total pressure measurements will also be made to determine the external driving pressure, and the fluid dynamics in the wheel-spaces.

The methodology behind the design process is outlined, and the technical aspects of the rig are documented. Initial calculations were conducted to assess the running conditions for the rig. The test section design was determined in conjunction with Siemens, who provided the vane and blade profiles. The rig is due to be operational and commissioned in July 2014.

The author of this thesis completed the design work described in this chapter in conjunction with a colleague, based on knowledge and experience gained from operating and conducting experiments using the single stage facility described in Section 3.1.

6.1 Conceptual design of the rig

The rig featured a 1.5 stage (vane, blade, vane) axial turbine, where two stators separated by a rotor disc created two separate wheel-spaces. Sealant flow entered the upstream wheel-space through the centre of the stator disc. In the downstream wheel-space, flow could be supplied at two radial locations either side of an inlet-seal. In both cases, flow moved radially-outward through the wheel-space, emerging through rim-seals into an external

annulus. The project proposal provided by Siemens required the provision for leakage flow from the nozzle guide vane and the inner carrier ring gap in the upstream wheel-space to be modelled. Additionally, both sets of stator vanes were manufactured as split blings (bladed rings) in order to allow for radially assembled seal designs to be tested.

The addition of turned rotor blades results in an engine representative flow-field in the external annulus. This did however necessitate the drive system to be capable of removing the power generated by the turbine through a dynamometer, and cope with the resulting temperature and pressure drop across the stage.

By moving to a larger, more representative annulus, the interaction between the main and secondary flow gas paths can be studied in greater detail. Additional design challenges arise from the larger mass flows, greater rotational speeds and making simultaneous measurements in both wheel-spaces.

Experience gained from operating and conducting experiments using the single stage facility heavily influenced the design of the 1.5 stage rig. Repeatability in the assembly and set-up between tests was identified as crucial if the relative performance of different seal designs was to be determined. It was therefore decided to mount the drivetrain assembly carriage on linear guide rails to ensure repeatability in lining up the discs, whilst allowing for access to both the upstream and downstream wheel-spaces.
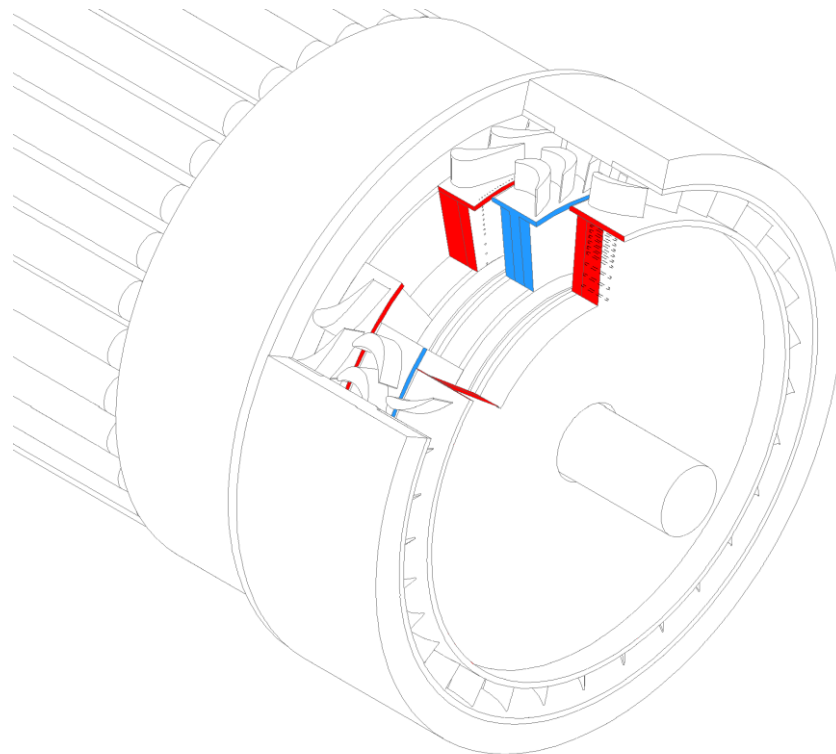
Figure 6.1: 1.5-stage rig test section showing turbine stage - the stator is shown in red and the rotor in blue

6.2 Design operating conditions

The first step in the design process was to determine the approximate running conditions. The rig was specified with two design operating points corresponding to rotational speeds of 3000 and 4000 rpm. The blade and vane profiles and the corresponding velocity triangle angles were determined from CFD analysis performed by Siemens. The vane-blade-vane count was chosen as 32 upstream vanes, 48 rotor blades, followed by a further 32 downstream vanes. This allowed for a convenient CFD sector model of 2-3-2. Each design point had geometrically similar velocity triangles to ensure the same non-dimensional driving potential, ΔC_p, in the annulus for the different rotational speeds.

6.2.1 Non-isentropic calculations

The flow conditions through the turbine stage were calculated using non-isentropic gas relationships and by applying conservation of mass. These values were calculated using an iterative process, assuming an inlet temperature of 303 K and atmospheric static pressure at exit of the turbine. To account for losses in the vane and blade rows, loss coefficients were applied to the isentropic calculations. Values of λ_N and λ_R were arbitrarily chosen as 0.05 and 0.11 respectively, resulting in an isentropic stage efficiency, $\eta_s = 0.925$. The operating conditions for the two design points are shown in Table 6.1.

Parameter	Disc Speed (RPM)	
	3000	4000
Rotational Reynolds Number (Re_ϕ)	8.64×10^5	1.25×10^6
Axial Reynolds Number (Re_w)	3.41×10^5	4.94×10^5
Flow Coefficient (Re_w / Re_ϕ)	0.395	0.395
Mass Flow Rate ($\dot{m}_a$)	1.08 kg/s	1.56 kg/s
Vane Exit Mach Number (M)	0.345	0.464
Degree of Reaction (Λ)	0.0675	0.0675
Blade Loading Coefficient (ψ)	3.4	3.4
Isentropic Coefficient of Vanes (λ_N)	0.05	0.05
Isentropic Coefficient of Blades (λ_R)	0.11	0.11
Isentropic Efficiency of Stage (η_s)	0.925	0.925
Power Generated by Stage (W_s)	7.8 kW	20 kW
Torque Generated by Stage (T_s)	24.9 Nm	47.9 Nm
Stage Pressure Ratio ($P_{0,1} / P_{0,4}$)	1.10	1.18
Stage Pressure Loss ($P_{0,1} - P_{0,4}$)	98.1 mbar	185 mbar
Stage Temperature Loss ($T_{0,1} - T_{0,4}$)	7.2 °C	12.8 °C

Table 6.1: Non-isentropic design point calculations

Two key non-dimensional parameters used to achieve the appropriate fluid dynamics are the axial and rotational Reynolds numbers. The ratio of these numbers gives the flow coefficient ($C_F = Re_w/Re_\phi$). In line with current industrial gas turbine engine designs, and in order to ensure a sufficient driving potential for externally induced ingress, a target flow coefficient of 0.4 was chosen. This approximately matches the mean value of the first 10% span of a Siemens gas turbine engine design.

The magnitude of Re_ϕ was made as large as possible given the constraints of the design. At the fastest rotational design speed, this was in the region of 1×10^6. To ensure turbulent flow, Re_ϕ should be greater than 3×10^5 (Theodorsen and Regier (1944)). Typical values of Re_ϕ found in gas turbine engines are in the order of 2-3 $\times 10^7$ (Childs (2011)). Although the rig is operating at an order of magnitude below this, Owen and Rogers (1989) showed that, for rotating flow, the flow structure in the boundary layers is principally governed by the turbulent flow parameter, λ_T, and depends only weakly on Re_ϕ. Hence the flow structure in both wheel-spaces of the rig is considered to be representative of that found in the cooling systems of engines.

For consistency with the 1 stage rig, a characteristic radius $b = 190$ mm was maintained for the new design. An annulus height of 25 mm was selected, providing a hub to tip ratio (R_i/R_o) of 0.89, which is typical of the first few stages of many gas turbines (Khilnani and Bhavnani (2001)). This resulted in a much larger air flow rate capacity to supply the annulus than was previously available. A new compressor was purchased in order to meet the requirement of 1.5 kg/s that enabled in the target flow coefficient to be obtained. This equated to vane exit Mach number of 0.46, which was considered within the incompressible flow regime.

The blade loading coefficient, ψ, (also known as temperature drop coefficient) expresses the work capacity of the stage. The degree of reaction, Λ, indicates the fraction of the stage expansion that occurs in the rotor. As shown in Table 6.1, the blade loading coefficient was 3.4, and the degree of reaction for the stage design was less than 7%.

6.2.2 Velocity triangles
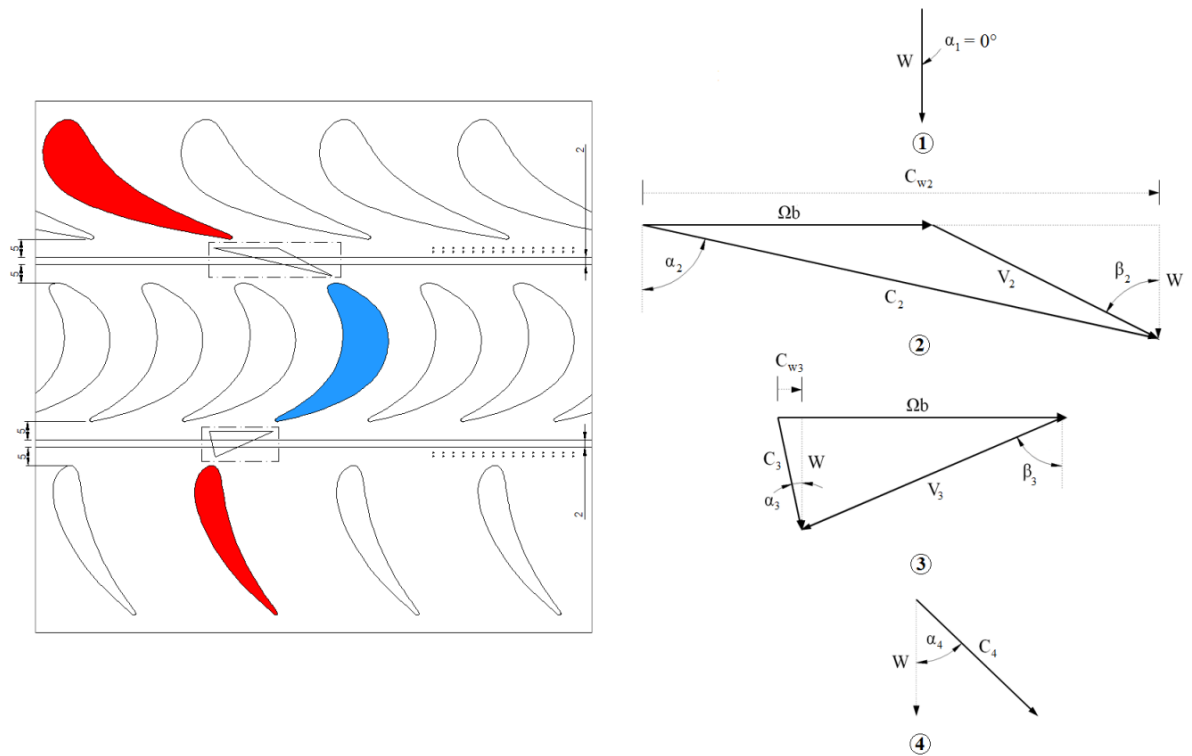
Figure 6.2: Velcoity triangles for the 1.5 stage axial turbine

The velocity triangles for the axial turbine stage are given in Figure 6.2 and the corresponding angles and velocities are given in Table 6.2. As the experimental rig models the first stage of a gas turbine, air entered the first stage of vanes with a purely axial flow velocity component, W; the vane 1 inlet angle, α_1, was therefore equal to zero. It then left the vanes with a velocity C_2 and an angle $\alpha_2 = 77.5°$, in the stationary frame of reference. In the rotating frame of reference, this is equivalent to a velocity V_2 and an angle β_2. At the design condition, β_2 therefore determined the geometric metal angle of the blade. A blade turning angle (equivalent to $\beta_2 + \beta_3$) of approximately 130° was deemed similar to that found in a modern day gas turbine designs. V_3 and β_3 were the relative blade exit velocity and angle respectively. In the stationary frame of reference, the air is turned by the blade back to almost completely axial flow, thus minimising α_3. The flow was then turned 34.5° by the downstream set of vanes to an angle of α_4 and a resulting velocity C_4, in the stationary frame of reference.

Velocity Triangle Parameter	Disc Speed (RPM)	
	3000	4000
Vane 1 Inlet Angle (α_1)	$0°$	
Vane 1 Exit Angle (α_2)	$77.5°$	
Blade Inlet Angle (β_2)	$63.2°$	
Blade Turning Angle ($\beta_2 + \beta_3$)	$129.9°$	
Blade Exit Angle (β_3)	$66.7°$	
Vane 2 Inlet Angle (α_3)	$11.8°$	
Vane 2 Exit Angle (α_4)	$46.3°$	
Rotational Velocity (Ωb)	59.7 m/s	79.6 m/s
Axial Velocity (W)	25.8 m/s	34.3 m/s
Vane 1 Exit Velocity (C_2)	119 m/s	159 m/s
Blade Inlet Velocity (V_2)	57.1 m/s	76.2 m/s
Blade Exit Velocity (V_3)	65.1 m/s	86.8 m/s
Vane 2 Inlet Velocity (C_3)	26.3 m/s	35.1 m/s
Vane 2 Exit Velocity (C_4)	37.3 m/s	49.7 m/s

Table 6.2: Velocity Triangle Parameters

Due to noise considerations, the value of the stage exit velocity C_4 is limited. In the case this acceptable value was exceeded, a third set of de-swirl vanes were designed to return the flow to the axial direction and reduce the velocity. However the velocities in Table 6.2 for the two design conditions were deemed acceptable, therefore the de-swirl vanes were not required; this saved manufacturing costs and physical space in the rig.
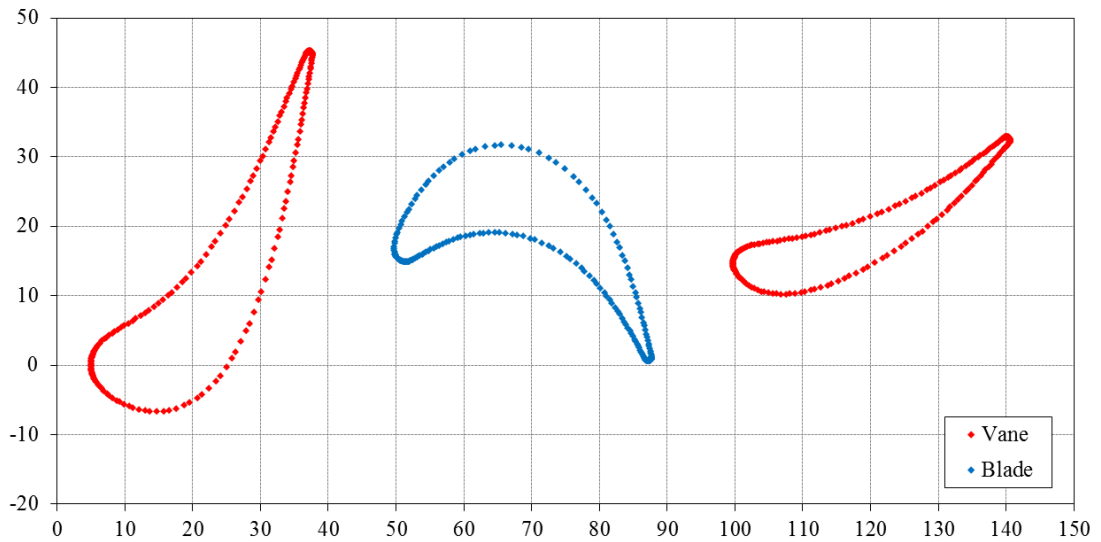
(A)
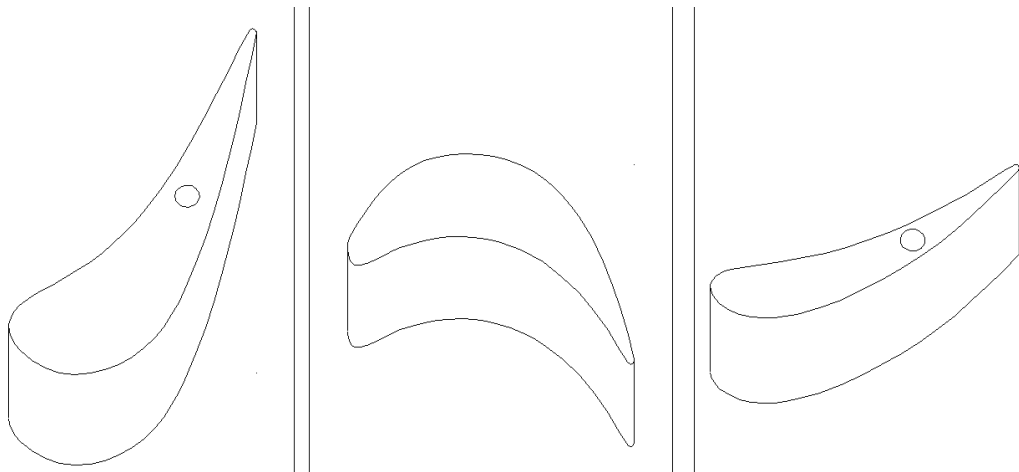
(B)

Figure 6.3: Vane and blade profiles; (A) Co-ordinate geometries, (B) Representative modelling

The vane-blade-vane co-ordinate system was obtained with 12 mm separations between each aerofoil and shown in Figure 6.3. The CAD modelling of these geometries and the resulting manufactured parts are shown in Figure 6.4.
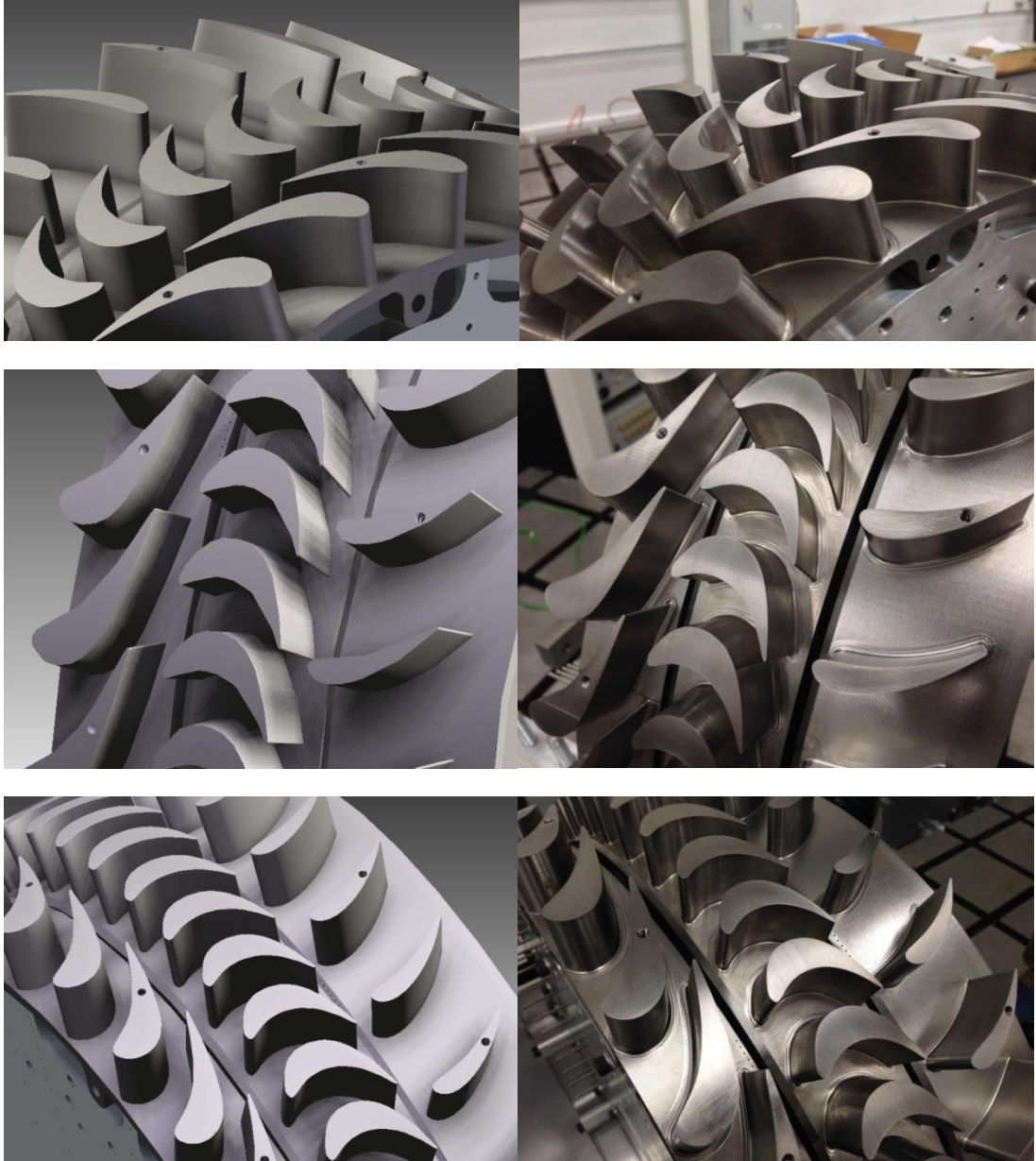
Figure 6.4: Vane and blade profiles showing CAD representation and manufactured parts

6.2.3 Free vortex design

As the linear blade speed, U, increases with increasing radius, the shape of the velocity triangles will vary from the root to tip of the blade. However as the tip to hub radius ratio in the stage is low, it was fair to assume the conditions at the mean diameter of the annulus represent an average of what happens to the mass flow as it passes through the stage.
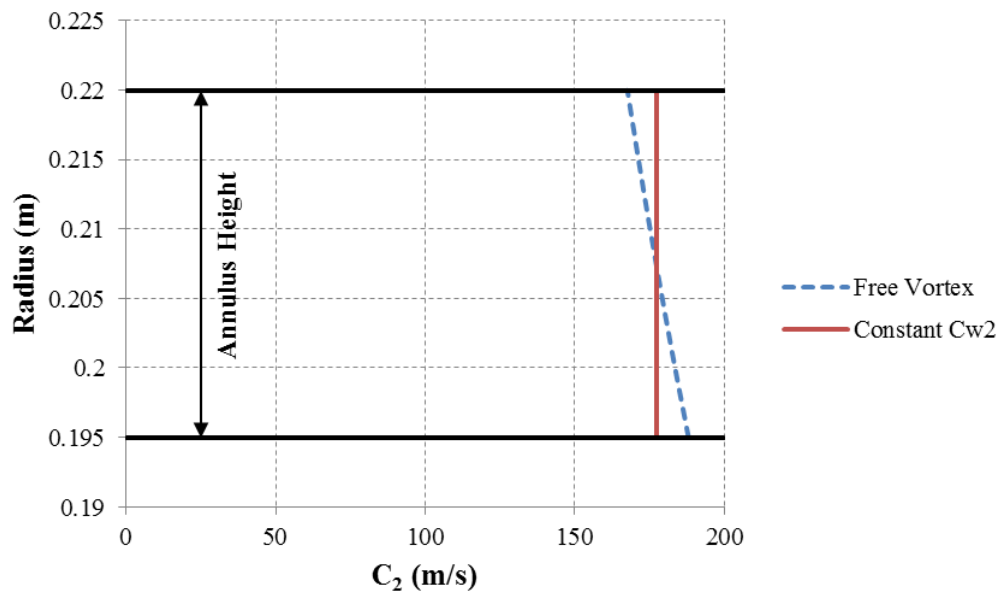
Figure 6.5: Radial variation of C_2 across annuls height

Figure 6.5 shows the radial variation of C_2 with annular height for the free vortex case and the design case where C_{w2} is constant. For a free vortex design, it was calculated that a root to tip variation of 1.5° in vane angle, α_2, would be required to ensure the $C_{w2}r = $ constant condition is met. It was deemed that the added complexity and manufacturing cost to produce twisted vanes was unfeasible for such a small change in angle.

6.2.4 Temperature entropy diagram
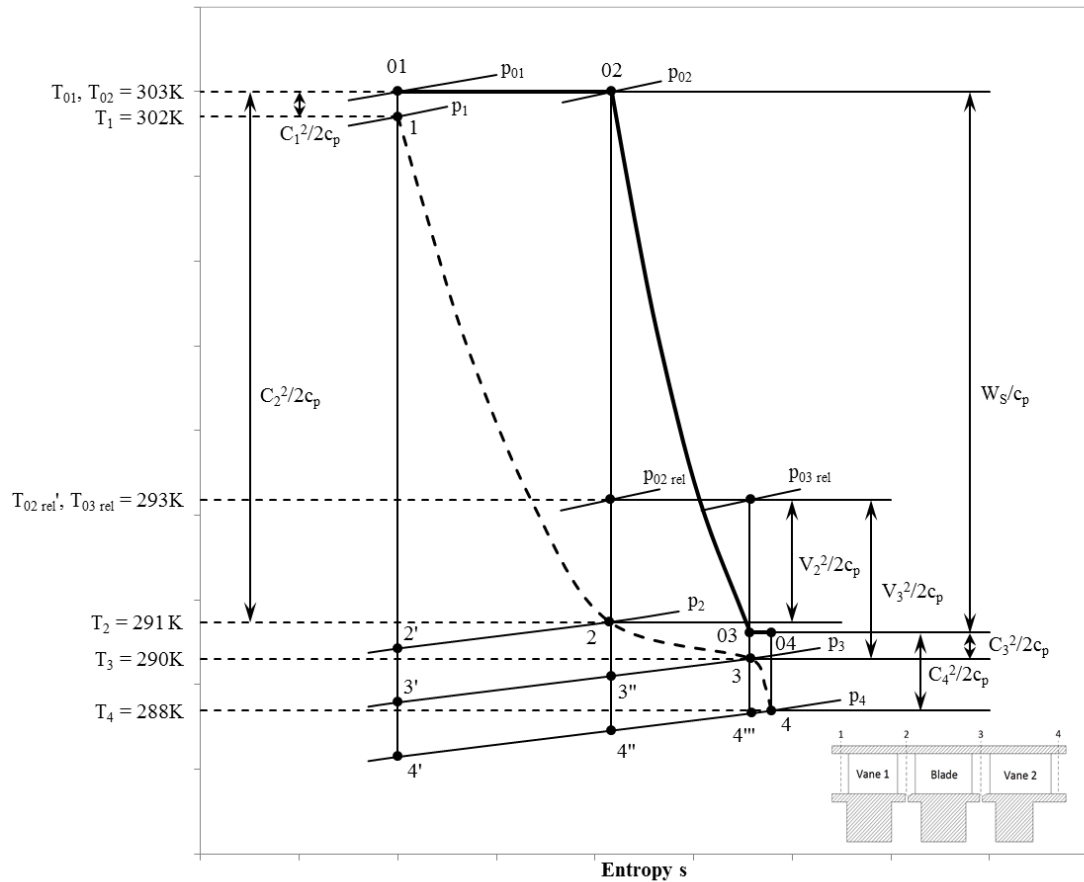
Figure 6.6: T-s diagram of 1.5 stage facility

The resulting temperature-entropy diagram for the stage is shown in Figure 6.6. Isentropic expansions are represented by the superscript dashed notation, and the thick full and dashed lines connect the total and static states respectively. The definitions of the velocities are given by the velocity triangles in Figure 6.2. No change in total temperature occurs across the first set of vanes as no work is done to the flow ($T_{01} = T_{02}$). However a change in total pressure occurs (p_{01} - p_{02}) due to friction in the vanes. Further expansion in the moving blade passages reduces the pressure to p_3. The associated total temperature drop (T_{02} - T_{03}) is equivalent to the stage work output per unit mass flow, W_s, divided by the specific heat capacity of air.

6.3 Design of experimental section

Each of the numbers in this section refers to the exploded component view shown in Figure 6.7.

The mainstream flow from the co-axial pipe (1) supplied a radial diffuser (2) featuring 32 (one per vane) flow guides manufactured from carbon-fibre. These ensured a smooth transition through the change in radius, whilst also helping to establish axisymmetric flow in the mainstream annulus. A sealed flange was used to connect the guides to the co-axial pipe, and a steel plate provided support from the bedplate whilst allowing the connection to the stub pipes to be made.

In order to link the radial diffuser to the annular transition, the use of thirty-two 1-inch aluminium inlet feed pipes (3) from the previous rig design was replicated. This was advantageous as it allowed for access to instrumentation at the rear of the upstream stator disc. Unlike an alternative plenum chamber design, the space in-between each pipe enabled instrumentation cables and tubing to be passed out from the inside of the rig. However, as an alternative to the hosing sleeve and jubilee clip arrangement, used to connect the pipe lengths to the stub pipes at either end in the previous rig, a new joining mechanism was sourced. A coupling device manufactured by Straub® was used that allowed for the quick release and removal of the pipes, increasing the ease of access to the rear of the upstream stator disc, whilst also creating a seal between the two pipe faces.

In order to determine the required length of the pipes, a calculation was performed to establish the fully developed flow entrance length. From White (2011), for Re $\leq 10^7$ the following equation is used:

$$\frac{L_e}{d} = 1.6 \, \text{Re}_d^{1/4} \qquad (6.2)$$

where Re_d is calculated for the maximum flow rate through the one inch pipe, which resulted in a velocity of 77.1 m/s in each pipe which was deemed acceptable. The maximum entrance length was therefore calculated as 0.772 m.

The 2-inch sealant line from the co-axial pipe supplied a fibreglass transition (4) which allowed for the change in profile from a circular pipe, to square sections for the two mesh heaters, then back to a circular section which supplied the upstream wheel-space. The fibreglass downstream of the mesh heaters was lined with Rohacell to prevent heat transfer through the surfaces.

Rig Components		
Number	Description	
(1)	Co-axial Inlet Pipe	
(2)	Radial Diffuser	
(3)	32 Inlet Pipes	
(4)	Sealant Line	
(5)	Annular Transition	
(6)	Upstream Stator Disc	
(7)	Rotor Disc	
(8)	Downstream Stator Disc	
(9)	Outer Annulus	
(10)	Bearing Unit	
(11)	Flexible Coupling	
(12)	Dynamometer	
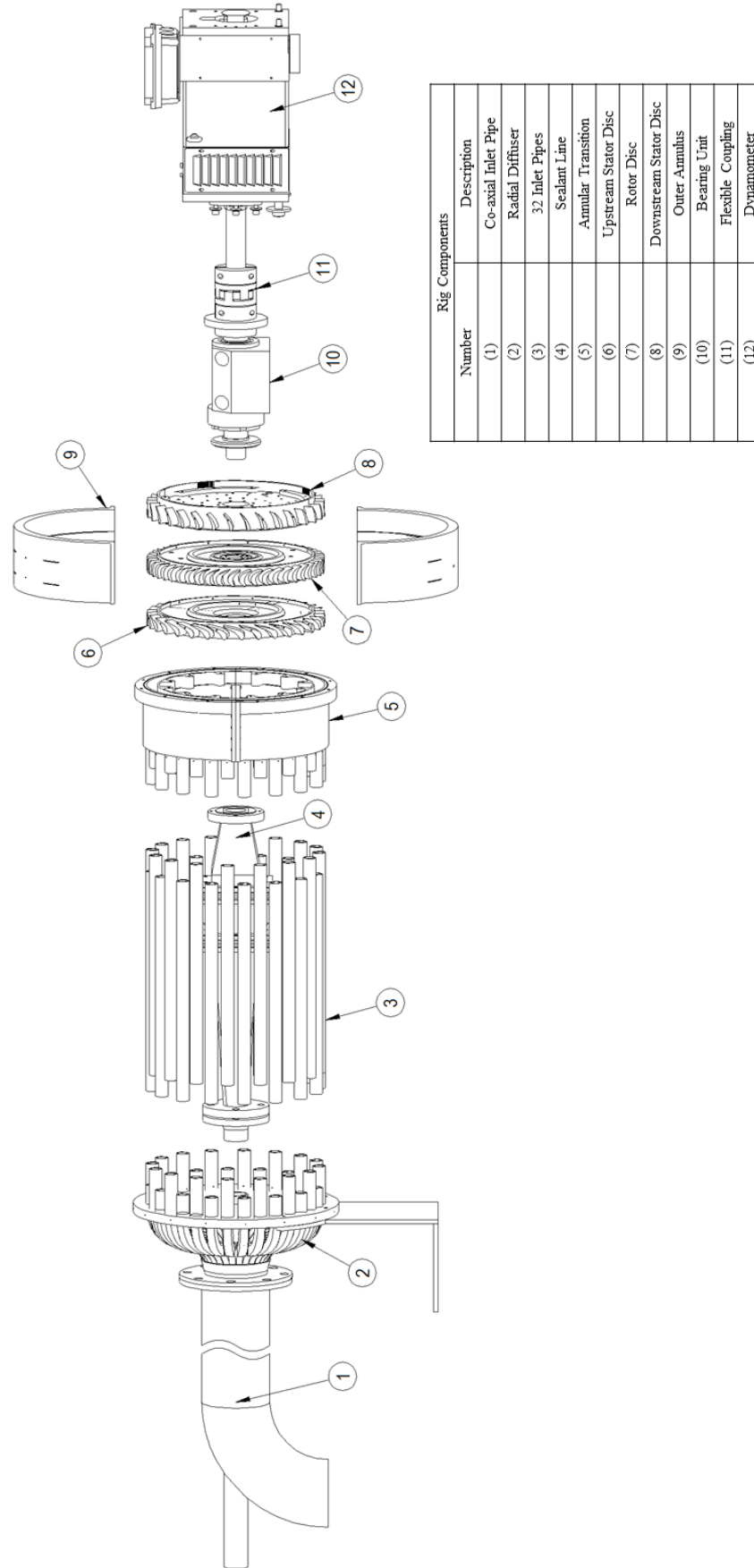
Figure 6.7: Exploded component model of rig configuration

The annular transition (5) was manufactured as two 180° split sections, which allowed for improved access to the instrumentation at the rear of the upstream stator disc (6). It also featured carbon-fibre inserts that acted as flow straighteners to promote transition from the 32 one-inch circular pipes to the mainstream annulus.

The outer annulus (9) was also manufactured as two sections to provide improved access to the turbine stage. Outer diameter rings where bolted to both vane sets to ensure no tip leakage occurred between the stator vanes and the outer casing. A steel cradle structure (not shown in Figure 6.7) provided the support for both the upstream stator disc and the outer casing.

The titanium rotor disc (7) was attached to the shaft using a Tollok® locking assembly. When tightened, this device creates an interference fit between the disc bore and the shaft hub. This allowed for the rotor disc to be removed easily and quickly, providing access to the downstream wheel-space, whilst ensuring accuracy when the disc is re-attached. The geometry of the TL 133 Tollok, and an aluminium ring on the downstream sides of the disc, ensured that no axial movement relative to shaft occurred during tightening. A shaft end cap was manufactured to cover the Tollok bolts and provide a smooth surface for the Rohacell lining. In the case of failure of the Tollok, this end cap and the aluminium ring prevented the disc from colliding with other components.

The downstream stator disc (8) was supported by the bearing housing (10). Sufficient space was left at the rear of the disc to prevent impingement of the flow exiting the stage on the support structure, and allow for a volute to be installed for future heat transfer experiments in the downstream wheel-space. Thrust bearings resisted axial movement caused by the pressure imbalances between the two wheel-spaces, and the axial component of the loaded rotor blades. The rotor was connected to the dynamometer (12) via a flexible coupling (11). This ensured any movement or vibration caused by the drive system was not transferred to the turbine section, which would have altered the radial and axial clearances during operation.

The drivetrain assembly carriage was mounted to linear guide rails to allow for movement of the rotor and downstream stator assemblies. This allowed for access to the upstream wheel-space, and by removing the rotor disc, access to the down-stream wheel-space. Bosch Rexroth® torque-resistant profiled ball rails were chosen which provided location accuracy up to 10 μm, ensuring repeatability when lining up the discs. A lead-screw was included to allow for precision movements when aligning the rotor-stator system. The

rig assembly, with support structures and guide rails mounted to the bedplate in the retracted position, is shown in Figure 6.8.
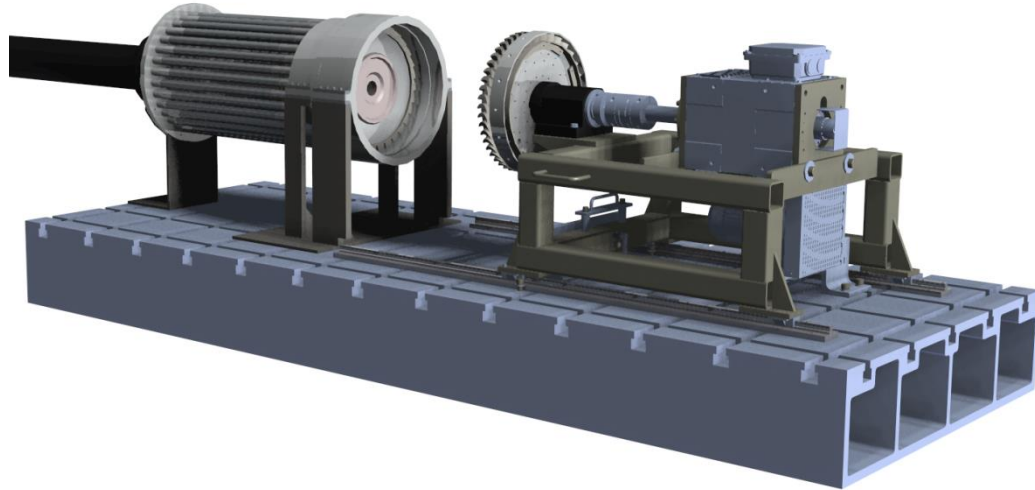
Figure 6.8: Experimental facility in retracted position

The dynamometer was a VASCAT MAC HS4 132 S asynchronous servomotor. This unit was capable of operating in 'drive' mode, where in the absence of air loading the blades it acted as a motor, rotating the turbine up to operating speed. The rotational speed was measured internally by the dynamometer to an accuracy of ± 1 rpm. When the blades were under load from the mainstream flow, the dynamometer was able to extract up to 34.4 kW of energy from the turbine through an electrical inverter.

The rotor could also be locked in position to prevent rotation during tests in order to capture the EI asymptote, as shown in Figure 4.9. Five different angular positions were chosen in order to investigate the effect of the blade leading edge location, relative to the vane exit angle.
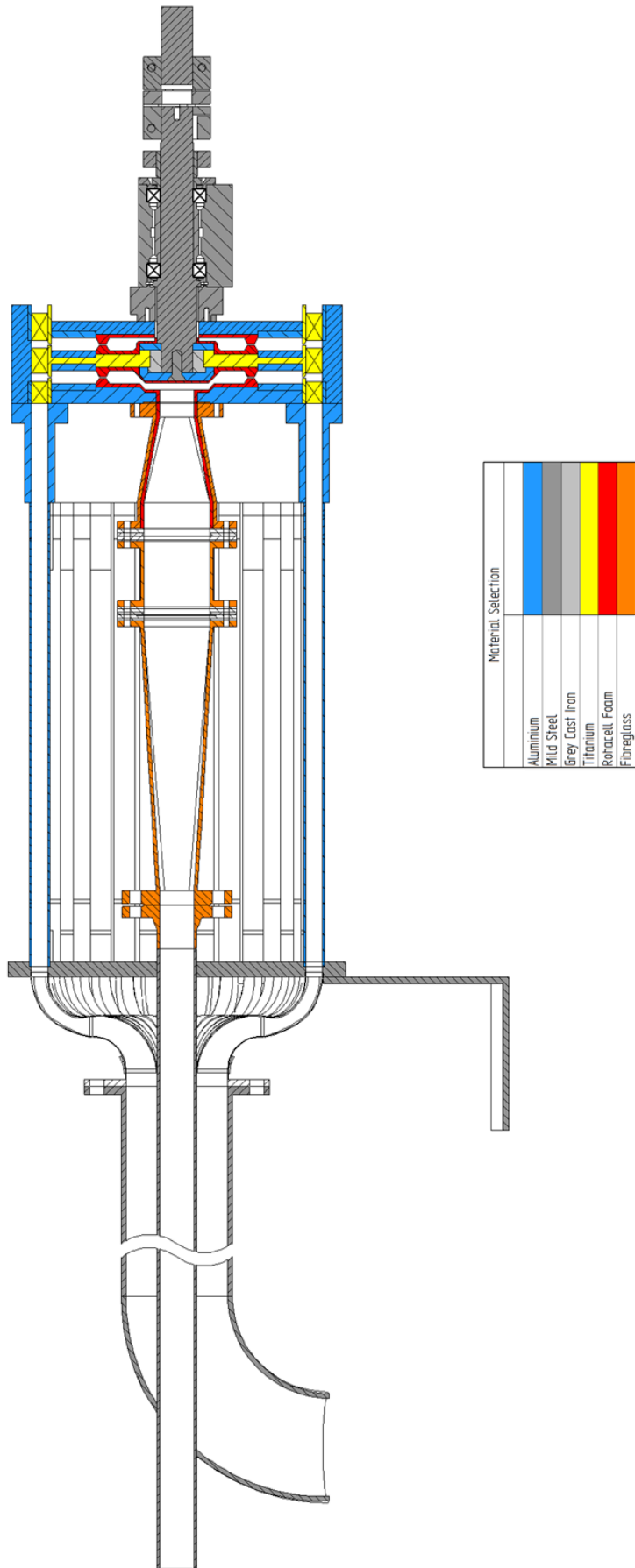
Figure 6.9: Sectioned general assembly of rig

6.3.1 Turbine stage geometry
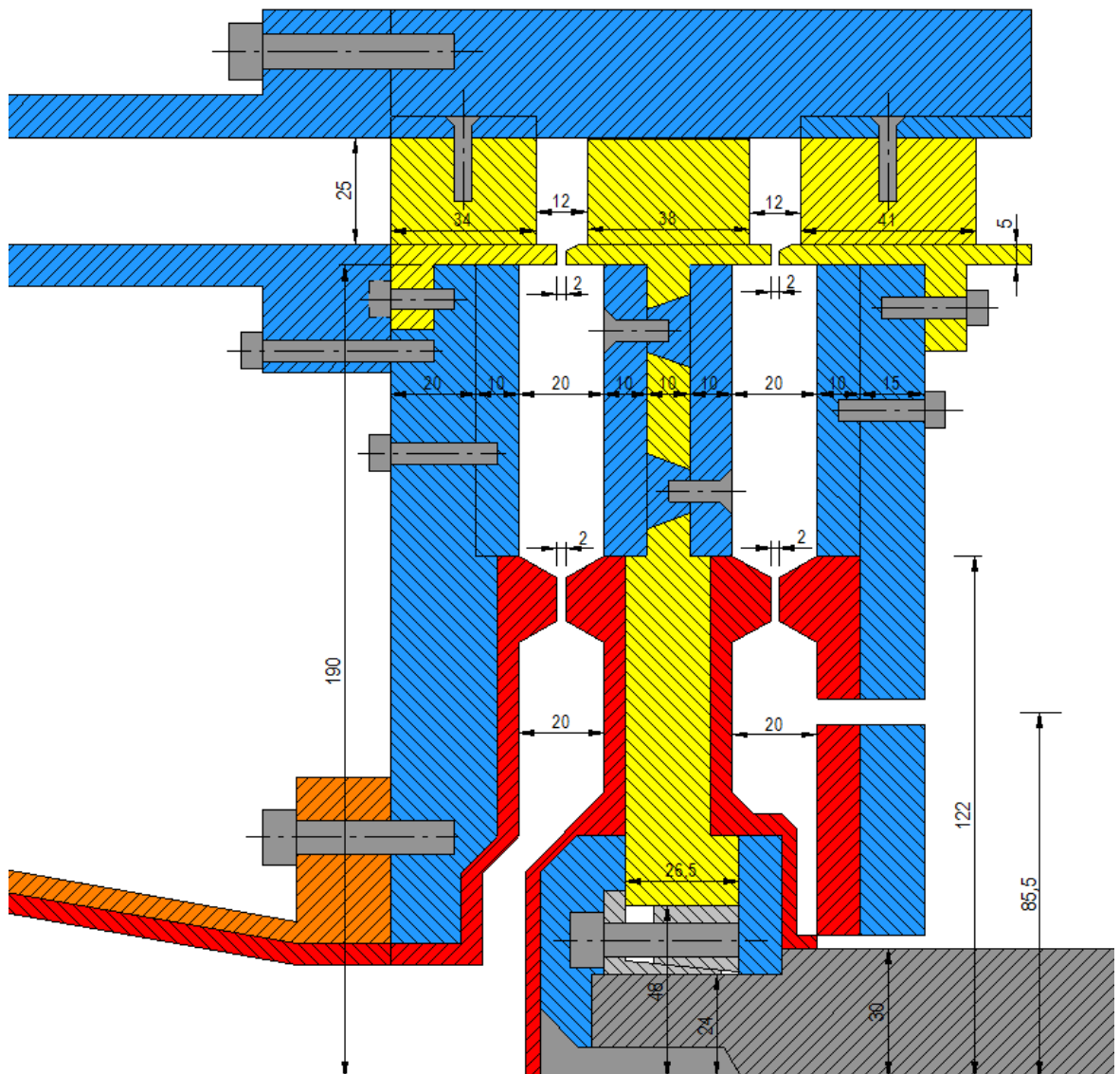
Figure 6.10: Dimensioned section of turbine stage (dimensions in mm)

For consistency with the 1 stage rig, many of the key geometric dimensions, including the characteristic radius, vane blade spacing, wheel-space width and rim seal gap were maintained for the new design. Some of the important dimensions, along with the attachment arrangement for each of the components, are shown in Figure 6.10.

Similar to the single stage rig, the datum setup once again featured simple axial clearance seals, formed by the shrouds at the wheel-space peripheries. 30° chamfers of 1/3 depth were included at the leading edge of the rotor and downstream stator platforms to prevent flow impingement and to resemble real gas turbine designs. Modular holes located on the

underside of both the stators and rotor shrouds allowed for different seal geometries to be attached. Inner seals located approximately half way down the cavities ensured turbulent Couette flow entered both wheel-spaces with the appropriate swirl. The radial length of this inlet seal was reduced from the previous design to allow a larger lower wheel-space in both the upstream and downstream sides.

An estimate of the boundary layer thickness in the annulus was conducted treating the inner and outer end walls as a pair of adjacent flat plates. Using the $1/7^{th}$ power law for the turbulent boundary layer shape, the displacement thickness, δ^*, was estimated using:

$$\delta^* = \frac{0.046x}{Re_x^{0.2}} \tag{6.1}$$

where the Reynolds number was calculated using the estimated curve-linear length of the vane channel (62.4 mm) and the free-stream velocity, estimated as the vane 1 exit velocity, C_2. For the 3000 rpm design case, δ^* was calculated as 0.2 mm, resulting in a blockage factor equal to 1.7% of the 25 mm annulus height. This was deemed acceptable and ensured a substantial amount of the ingested fluid came from the mainstream flow and not just from the boundary layer.
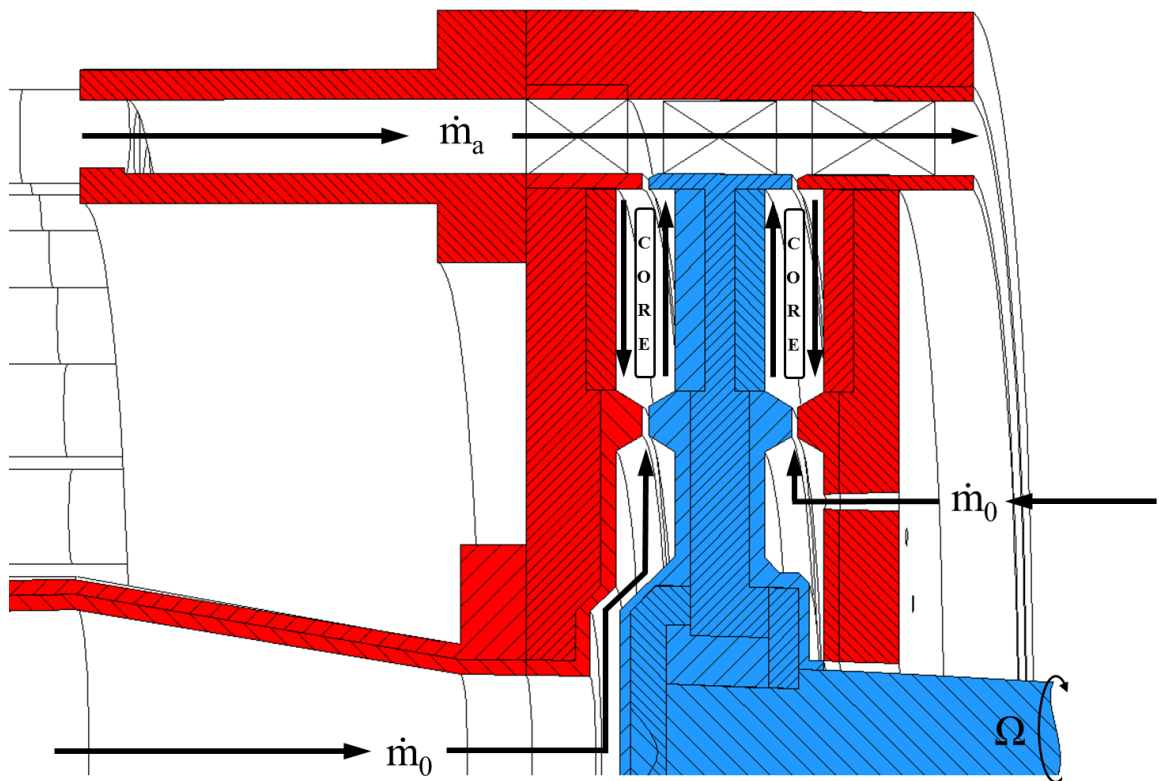
Figure 6.11: Rig test section showing mainstream, and upstream and downstream sealing flows (red – stationary, blue – rotating)

Upstream sealing flow was supplied to the turbine section along the centreline, as shown in Figure 6.11. In order to conduct reverse heat transfer experiments, this flow was heated using mesh heaters. A transition section was formed from the circular inner co-axial 2 inch pipe, to the square section mesh heaters, then back to the round profile. This transition was flanged to the back of the upstream stator disc. In the downstream wheel-space, flow was supplied at a radial height, $r/b = 0.45$, through 16 circumferentially distributed holes of 6 mm in diameter. Equal distribution of this flow to each hole was ensured using a manifold.

For future heat transfer experiments in the downstream wheel-space, sufficient space at the rear of the stator disc was left to accommodate a volute. This circumferentially contracting device would feature a mesh heater and Rohacell lining on the inner surfaces to evenly distribute the flow to the individual holes whilst preventing heat transfer.

An alternative sealant flow arrangement is shown in Figure 6.12, where air is supplied to turbine stage at larger radius ratios. To satisfy the design criteria provided by Siemens, these additional sealant line holes were included in both the upstream and downstream wheel-spaces. This allowed for the effects of leakage flow from the nozzle guide vane and the inner carrier ring gap to be experimentally simulated. Flow could also be extracted through the downstream wheel-space holes to replicate flow arrangements found in gas turbine engines.
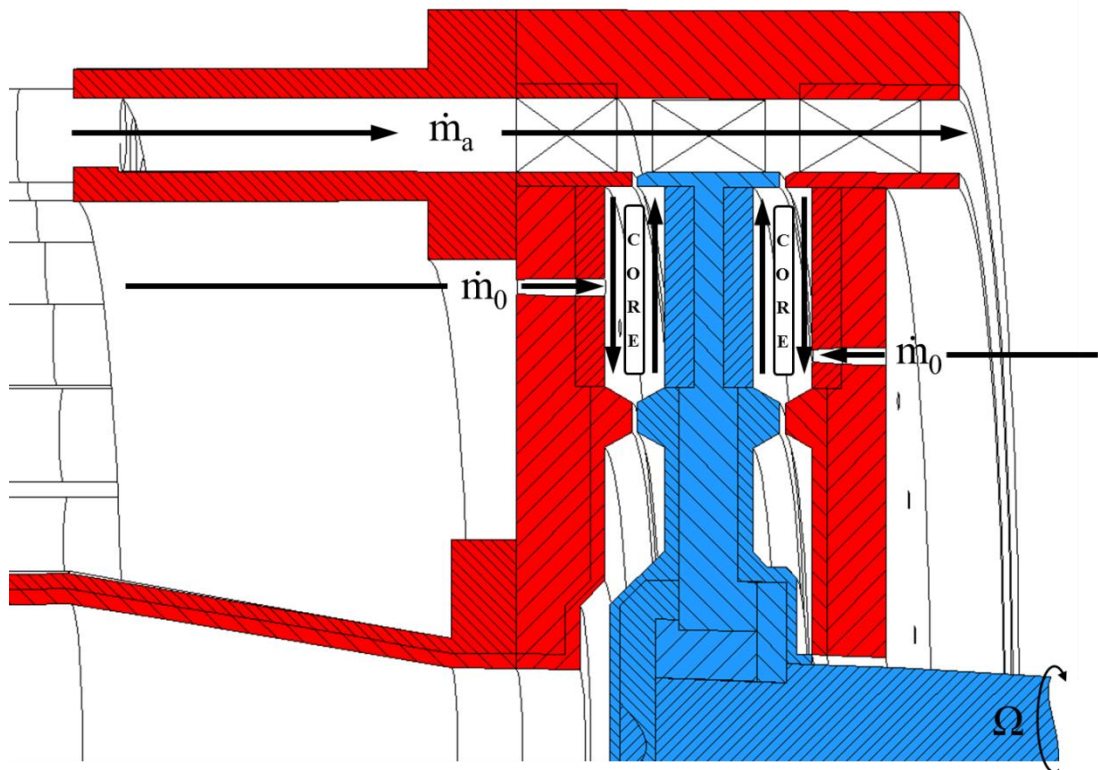
Figure 6.12: Rig test section showing alternative sealing flow entrance locations in upstream and downstream wheel-spaces (red – stationary, blue – rotating)

6.3.2 Materials

To prevent heat transfer to the metallic components, Rohacell 51 insulating foam lining was used on the stator and rotor surfaces. Rohacell is a low density grade material with a very high strength to weight ratio, and a low thermal conductivity. As shown by Table 6.3, the thermal conductivity is very close to the value for air (equal to 0.0257 W/mK).

Titanium was chosen for the manufacture of the rotor blisc, and also the stator vane blings, for its strength properties in comparison with aluminium, and also a dramatically reduced thermal conductivity value. This negated the use of mitred seal inserts used in the previous rig to help prevent heat transfer to the underside of the stator and rotor shrouds.

To ensure the structural integrity of the rotor blisc, the 0.2% proof stress was compared with the maximum calculated stress experienced under rotation. Because materials such as titanium do not readily exhibit a yield point based on the shape of the stress-strain curve, an arbitrarily defined offset yield point, or proof stress, is usually used.
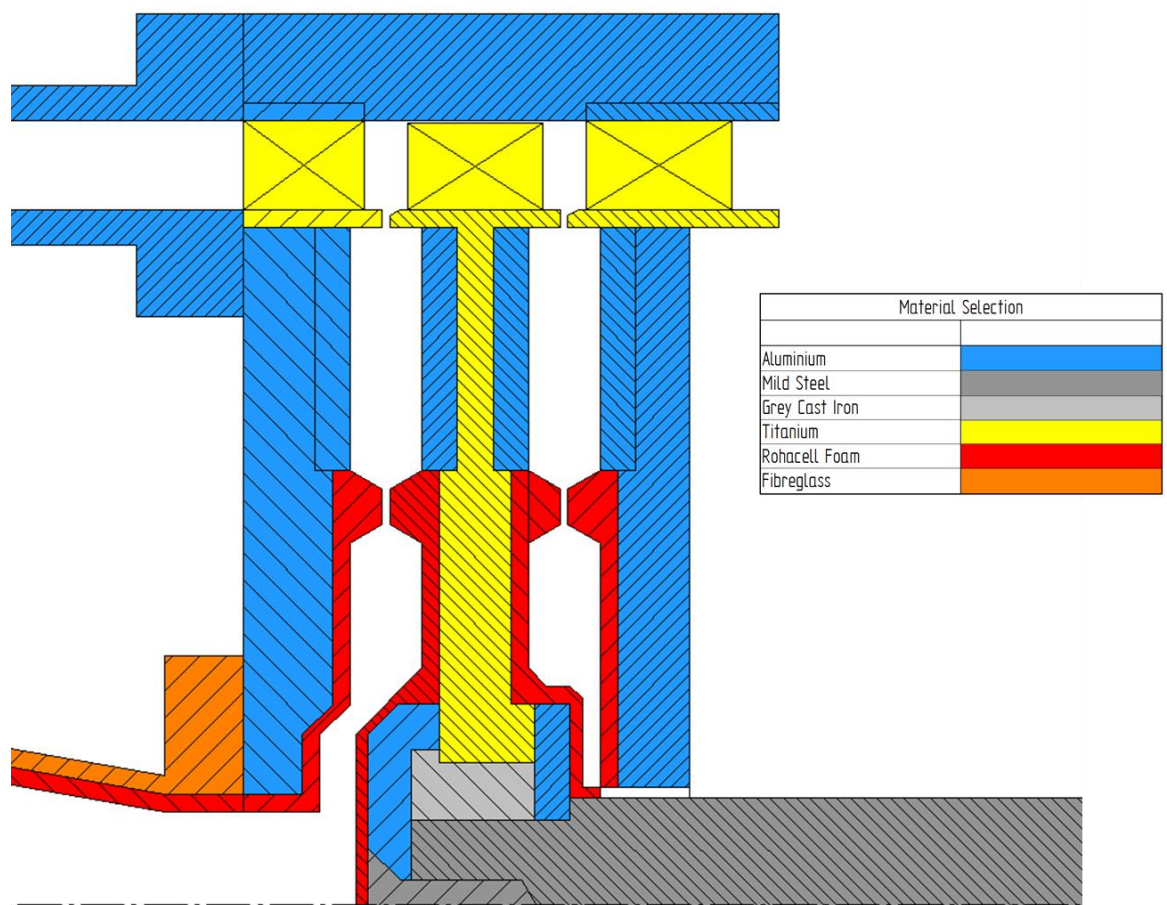
Figure 6.13: Material selection of turbine section

Property	Material		
	Titanium	Aluminium	Rohacell
Type	Ti A6AI-4V	Al 7075 T6	51 IG-F
Density	4500 kg/m^3	2800 kg/m^3	52 kg/m^3
Young's Modulus	116 GPa	72 GPa	70 MPa
Poisson's Ratio	0.34	0.33	0.25
0.2 % Proof Stress	880 MPa	505 MPa	1 MPa
Thermal Conductivity	8.73 W/mK	250 W/mK	0.033 W/mK

Table 6.3: Mechanical properties of materials used

6.3.3 Rotor growth

The chosen Tollok design allowed torque to be transmitted between the disc and the shaft by creating an interference fit between the two components. However, due to the difference in materials the disc will grow radially under rotation at a greater rate than the Tollok, resulting in a relaxation of this interference. The growth of the titanium disc therefore has to be investigated. A simplified diagram of the Tollok and disc arrangement is shown in Figure 6.14.
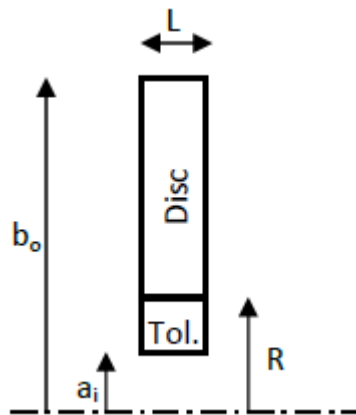
Figure 6.14: Simplified diagram of Tollok and disc arrangement

From Table 6.1, the maximum torque occurs generated by the stage is 47.9 Nm at 4000 rpm. The force, F, generated by the interference at the interface between the Tollok and the disc is related to the contact surface area, A, by:

$$F = A\mu p = (2\pi RL)\mu p \qquad (6.3)$$

where, as shown in Figure 6.14, R is the radius of the interface and L is the contact length. The torque, T, is therefore related by:

$$T = RF = 2\pi R^2 L\mu p \qquad (6.4)$$

For an interference fit the pressure, p (equivalent to the radial stress at the disc bore, σ_r) is related to the interference by:

$$p = \frac{\delta}{R\left[\dfrac{1}{E_o}\left(\dfrac{b_o^2 + R^2}{b_o^2 - R^2} + v_o\right) + \dfrac{1}{E_i}\left(\dfrac{R^2 + a_i^2}{R^2 - a_i^2} - v_i\right)\right]} \qquad (6.5)$$

where E and v are the modulus of elasticity and Poisson's ratio respectively. The subscript o symbols refer to the outer component, in this case the disc, and the subscript i the inner component, i.e. the Tollok. The required interference to transmit the torque is therefore found by combining Eqs. 6.4 and 6.5:

$$\delta = \frac{T\left[\dfrac{1}{E_o}\left(\dfrac{b_o^2 + R^2}{b_o^2 - R^2} + v_o\right) + \dfrac{1}{E_i}\left(\dfrac{R^2 + a_i^2}{R^2 - a_i^2} - v_i\right)\right]}{2\pi R L\mu} \qquad (6.6)$$

Using the dimensions shown in Figure 6.10, and a coefficient of friction, μ, between titanium and grey cast iron of 0.49, the interference to transmit this torque is calculated from Eq. 6.6 as 3.35×10^{-8} m, which equates to a pressure at the bore of the disc of 324 KPa.

For an unconstrained titanium disc spinning at 4000 rpm, the expected radial growth at the bore is 1.09×10^{-5} m, significantly larger than that required to transmit the torque. Using Eq. 6.5, the pressure required to create this interference is 24.5 MPa. The Tollok TL 133 creates a surface pressure on the bore of the disc of 120 MPa, a factor of almost 5 times larger.

In reality, the disc is statically pre-stressed by the Tollok, which in turn will affect the growth. This results in a circular problem, as the interference pressure under rotation is dependent on the growth, and the growth is dependent on the interference pressure. As this is a rather complicated problem to solve computationally, the unconstrained case was considered worst case. The maximum hoop stress, determined using a 1D calculation of the unconstrained titanium blisc at 4000 rpm was estimated as 32 MPa. From Table 6.3, the 0.2% proof stress of the titanium used was 880 MPa, resulting in a safety factor of 27.5. This allowed a large margin to account for potential stress raisers caused by the geometry.

In order to prevent further stressing of the disc by threading the titanium for the cover-plate attachment, tapered captive nuts were used on both sides of the rotor. These were

distributed circumferentially over 12 positions at two radial locations. The attachment arrangement for the cover-plates is shown in Figure 6.10.

6.3.4 Rotor whirl

One consideration that had to be taken into account during the design phase was whether whirl of the disc was an issue. For a cantilevered rotating mass, the whirling or critical speed is given by:

$$\Omega_c = \sqrt{\frac{3EI}{mL^3}} \tag{6.7}$$

where I is the second moment of area of the shaft, m the mass of the disc and L the length of the overhang from the bearings. The deflection, y, of the mass is given by:

$$y = \frac{e}{\left(\dfrac{3EI}{m\Omega^2 L^3} - 1\right)} \tag{6.8}$$

where e is the distance of the centre of mass from the axis of the shaft. The rotor was dynamically balanced to BS ISO1940-1:2003 to within turbine specification Grade 2.5 (2.5 mm/s), resulting in a centre of mass offset of 0.6 μm. When the denominator of Eq. 6.8 is equal to zero, that is $3EI / m\Omega^2 L^3 = 1$, the deflection becomes infinite and whirling takes place. Figure 6.15 shows the deflection of the shaft at speeds up to 35,000 rpm. The critical speed, calculated by Eq. 6.7, is shown as 27,800 rpm, where the deflection tends to an asymptote. At speeds greater than this value the deflection tends to the static imbalance. At the 4,000 rpm design case the deflection was 2 μm, ensuring whirl is not a problem within the operating range.
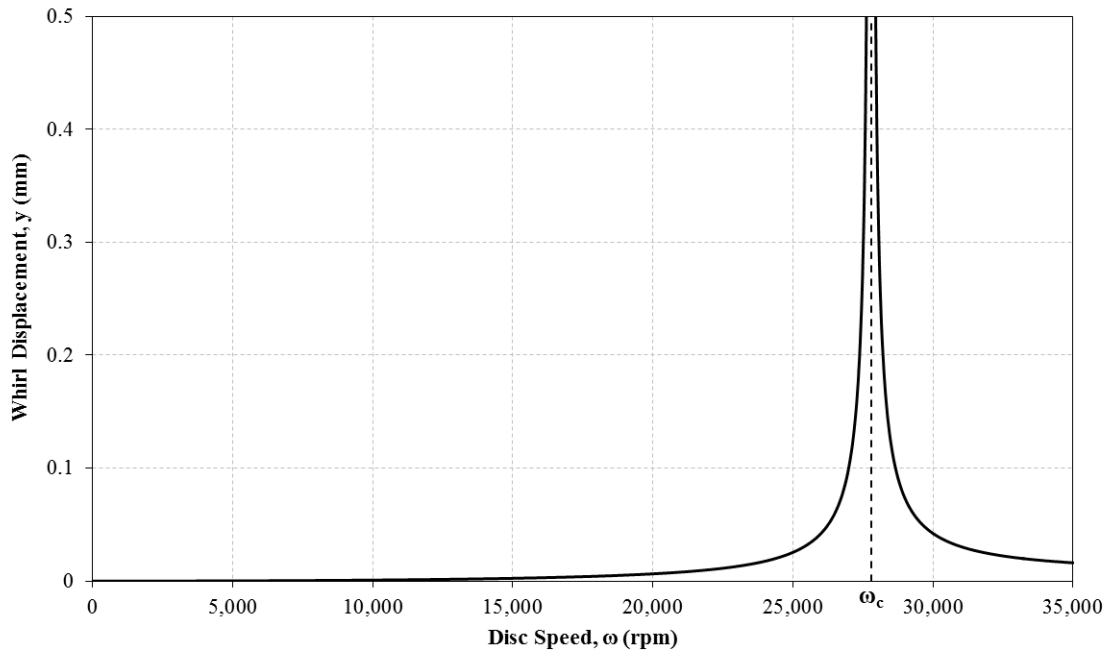
Figure 6.15: Calculated whirl displacement of disc with rotational speed

6.3.5 Split vane construction

To allow for the testing of radial overlap seals, both the upstream and downstream stator vane blings were manufactured as two 180° segments. This enabled the stator platforms to be radially assembled as shown in Figure 6.16. Clearance holes in specifically designed lugs allowed for the attachment of these segments to the rear of the stator discs without interfering with the instrumentation tappings.

Both the outer annulus casing and the annular transition sections were also manufactured as split sections to allow for access to the annulus and the rear of the upstream stator disc.
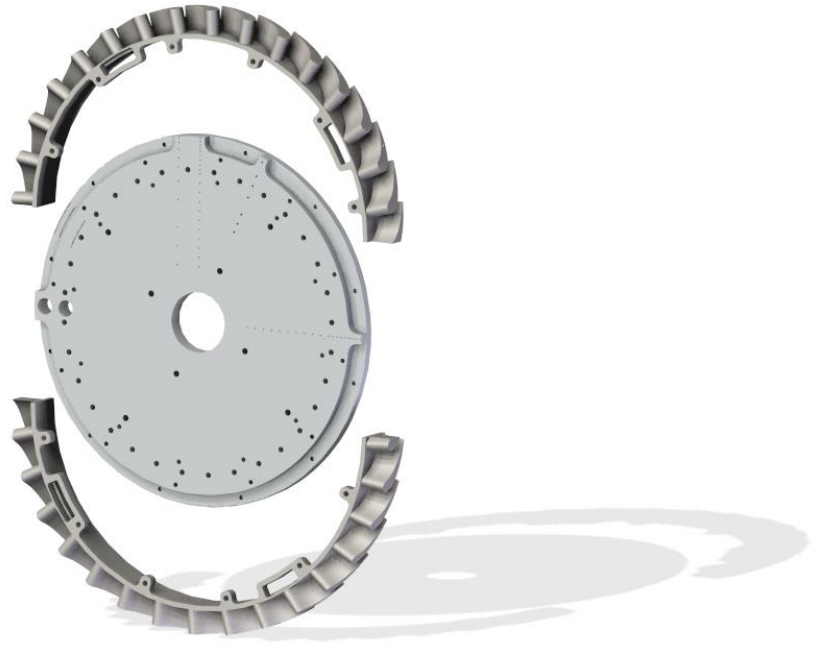
Figure 6.16: Split vane arrangement of upstream stator bling

6.3.6 Designing for heat transfer experiments

The rig was specifically designed to accommodate infrared temperature sensors for heat transfer measurements on the rotor surface. This novel approach will enable the effects of ingress on the rotor side of the wheel-space to be established. A transient reverse heat transfer experiment is used, where the sealant line temperature is raised to above the ambient mainstream flow temperature (reverse in the sense that this is the opposite of what occurs in the engine). It is therefore important that heat transfer to surfaces downstream of the mesh heaters in the sealant line is minimised.

Detachable cover-plates on both sides of the upstream and downstream wheel-spaces allowed for different surface materials to be easily attached. Modifications to these cover-plates to incorporate future instrumentation could also be easily made without the need to disassemble the whole test facility. The test section is shown in Figure 6.17 with the heat transfer cover-plates in place. These ensured near adiabatic surfaces through Rohacell lining of both sides of each wheel-space.
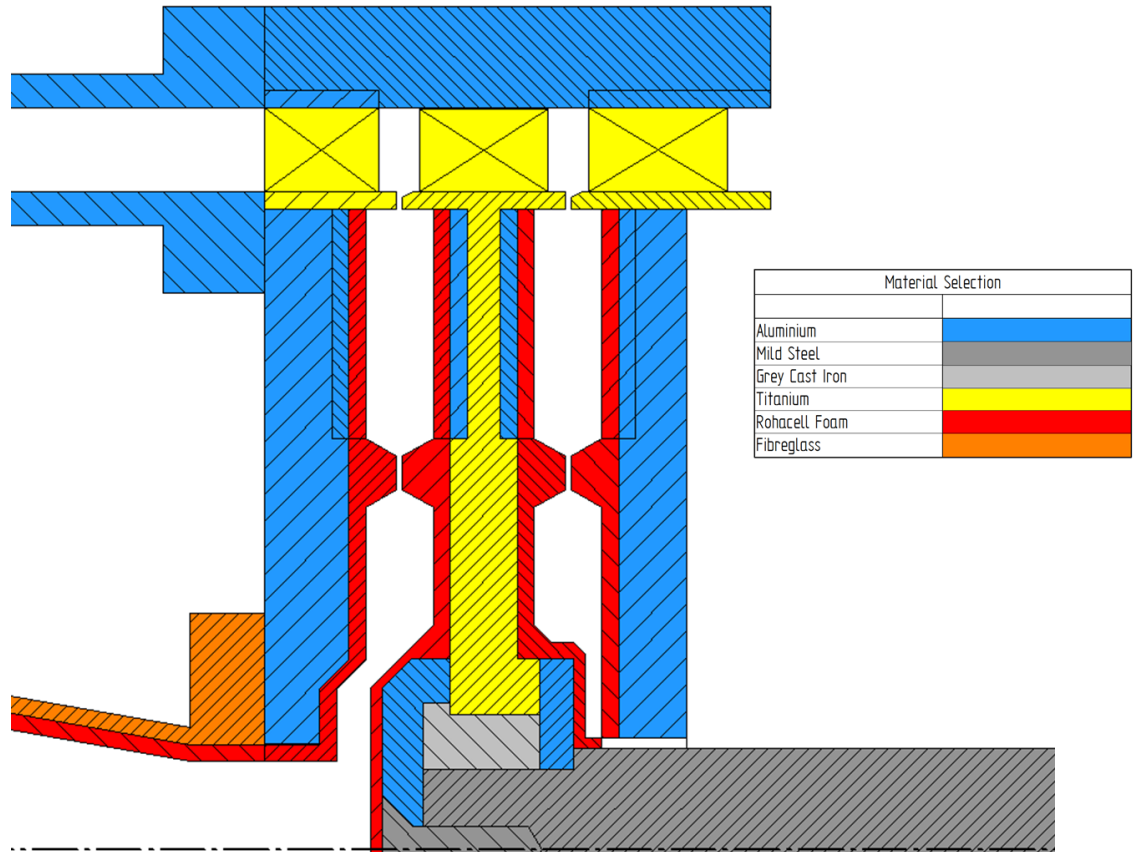
Figure 6.17: Turbine section in heat transfer configuration

The mesh heater design used in the sealant line was replicated from the 1 stage rig (see Sangan (2011) for details). Two heaters were installed in series in the sealant line; one to increase the temperature of the air to ambient conditions, and a second to step the temperature by approximately 40°C. These were manufactured using fine wire meshes soldered to bus bars, and insulated using Tufnol.

6.4 Gas turbine laboratory

Figure 6.18 shows an isometric schematic of the gas turbine research laboratory used to house the 1.5 stage experimental facility. As part of the project the laboratory was completely refurbished to include a new larger test cell, capable of accommodating multiple rigs, and a separate control room divided by a soundproof wall. In order to achieve the straight length requirements for the measurement devices, the air lines were looped into and around the control room, then back into the test cell.

Mainstream flow air (shown in red) was supplied directly from a dedicated Atlas Copco ZS160+VSD compressor through 6-inch Victaulic piping. The compressor was capable of delivering up to 4,578 m³/hr of air (equivalent of 1.53 kg/s at atmospheric conditions) at pressures of up to 1.2 bar gauge. Direct control of the compressor motor speed enabled variation of the mass flow supplied to the rig. As the compressor raised the temperature of the air to above ambient conditions, heat exchangers supplied by EJ Bowman were used to extract up to 120 kW of power, ensuring the air supplied the rig was at a safe working temperature. Two PK250 shell and tube heat exchangers were used in parallel in order to reduce the pressure drop. Water from the department's existing blast cooler network was used as the cooling medium (shown in dark blue). The mainstream flow rate was then measured using a Bronkhorst 6-inch thermal mass flow meter.

Both the upstream and downstream sealant flow lines (shown in light blue) were supplied by the existing high pressure compressed air line through 2-inch pipes. The flow was split on entrance to the laboratory and each separately pressure regulated down from 7 to 2 bar gauge to ensure minimal feedback interactions. Shut-off valves were included to isolate each line if required. Massflow rates in both lines were regulated and measured using Bronkhorst mass flow controllers. An additional orifice plate was installed in the upstream sealant line as a checking device. This line was then merged with the 6-inch mainstream flow line to form a co-axial pipe which supplied air to the upstream end of the test facility.
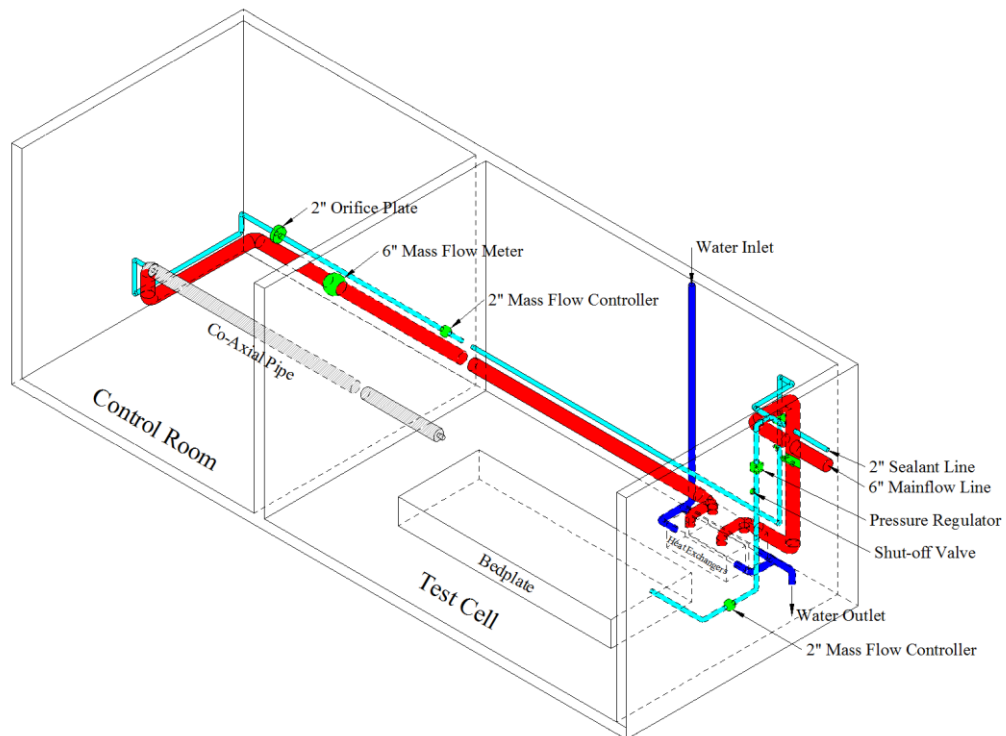
Figure 6.18: Isometric schematic diagram of the laboratory layout

6.5 Instrumentation and control

The cross-sectioned view in Figure 6.19 shows the axial and radial locations where the different measurements are made. Due to the cover-plate system, not all of these measurements in the wheel-spaces are made during the same testing set. For example, the large infrared probe holes can be covered during the concentration tests when they are not required, and the thermocouples can be removed as to not interfere with the total pressure measurements. Data acquisition for all measurements and control of the rig was performed by the CADET automation system.
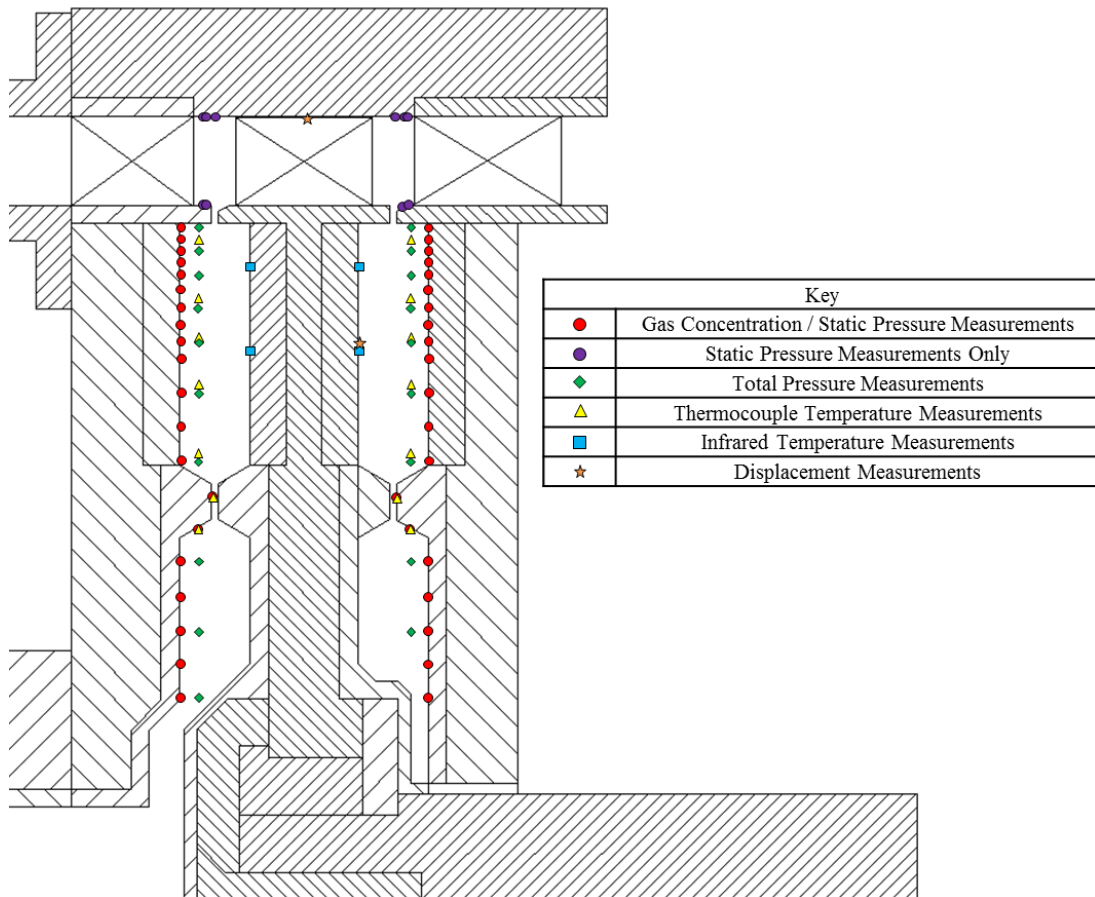
Figure 6.19: Global instrumentation map showing measurement locations

6.5.1 Wheel-space instrumentation

1. Static pressure tappings were located on the stator wall to measure the radial distribution of pressure in both the upstream and downstream wheel-spaces. The locations are outlined in Table 6.4, and were chosen in line with the previous rig design, with an emphasis on the outmost positions corresponding to the area of greatest interest. Additional locations were added radially inward of the inlet seal to determine the fluid dynamics of the lower wheel-space. Measurements were made through the stator discs and cover-plates using hypodermic tubing of 1.65 mm diameter. The tappings were then connected via flexible polyurethane tubing to a Scani-value with a calibrated pressure transducer. This allowed for multiple pressure measurements to be made in the same testing set using a consistent measurement device.

2. Total pressure probes were used in conjunction with the static pressure taps to determine the tangential velocity in the wheel-space. The probes were located one quarter of the axial distance across the wheel-space ($z/s = 0.25$), and at every second radial location of static pressure. The probes were aligned perpendicular to the flow direction, although as this was not possible at the radially outermost position, this was aligned at 3.9° (as shown in Figure 6.20). From Tropea *et al.* (2007), for an accuracy of approximately 1% of dynamic head, the sensitivity to yaw angle of a square-ended Pitot probe is ± 11°.

3. Circumferentially located pressure tappings were also included at three radial positions to check for asymmetries in the wheel-space. Bohn *et al.* (1995) showed these asymmetries can exist at radius ratios larger than 0.972 (Figure 2.13). Measurements were made at 15 locations across one vane pitch, corresponding to an 11.25° sector. This enabled the degree of pressure asymmetry damping to be quantified for different double seal designs.

4. CO_2 gas concentration tappings were included on both stator walls at various radial locations, consistent with the static pressure measurement positions given in Table 6.4. These were then connected to a Signal Group 9000 MGA dual channel infrared gas analyser, again with flexible polyurethane tubing to determine the concentration of CO_2. To allow multiple measurements to be made within the same testing set, two 20 channel multiplexors were used to switch been the different measurement locations. As the tappings were fabricated from the same 1.65 mm hypodermic tubing used for the pressure measurements, it would have been possible to measure pressure and gas concentration using the same taps. However, in order to make both types of measurements simultaneously, separate concentration taps were included at a 90°

separation. By making measurements at each angle, the effect of circumferential variation in concentration could be determined, although from the literature, this effect is expected to be marginal.

5. Fast-response thermocouples made temperature measurements in the rotating core. These provided valuable information that quantified the heat transfer that took place between the air and the surfaces as the fluid flowed radially down the stator surface. The thermocouples were manufactured internally using 10 micron wire beads fitted inside a ceramic sleeve of diameter 2.34 mm.

6. Infrared sensors were used to make temperature measurements on the rotating surfaces of both sides of the rotor disc. These measurements were used to calculate the heat transfer coefficient of the disc, as well as the adiabatic effectiveness based on temperature. The sensors were 17 mm in diameter including a copper sleeve, which acted as thermal mass to help maintain a constant internal sensor temperature, and a Rohacell covering for insulation. The sensors acquired data over a spot size area 6 mm in diameter at an axial distance of 20 mm (equivalent to the width of the wheel-space). Four sensors were included that produced data at two different radial locations in both the upstream and downstream wheel-spaces. It was envisaged this would provide temperature measurements either side of a generic double seal rotor attachment.

Key	
1	Radial Static Pressure Taps
2	Pitot Tubes
3	Circumferential Static Pressure Taps
4	Concentration Taps
5	Thermocouples
6	Infrared Sensors
	Rohacell
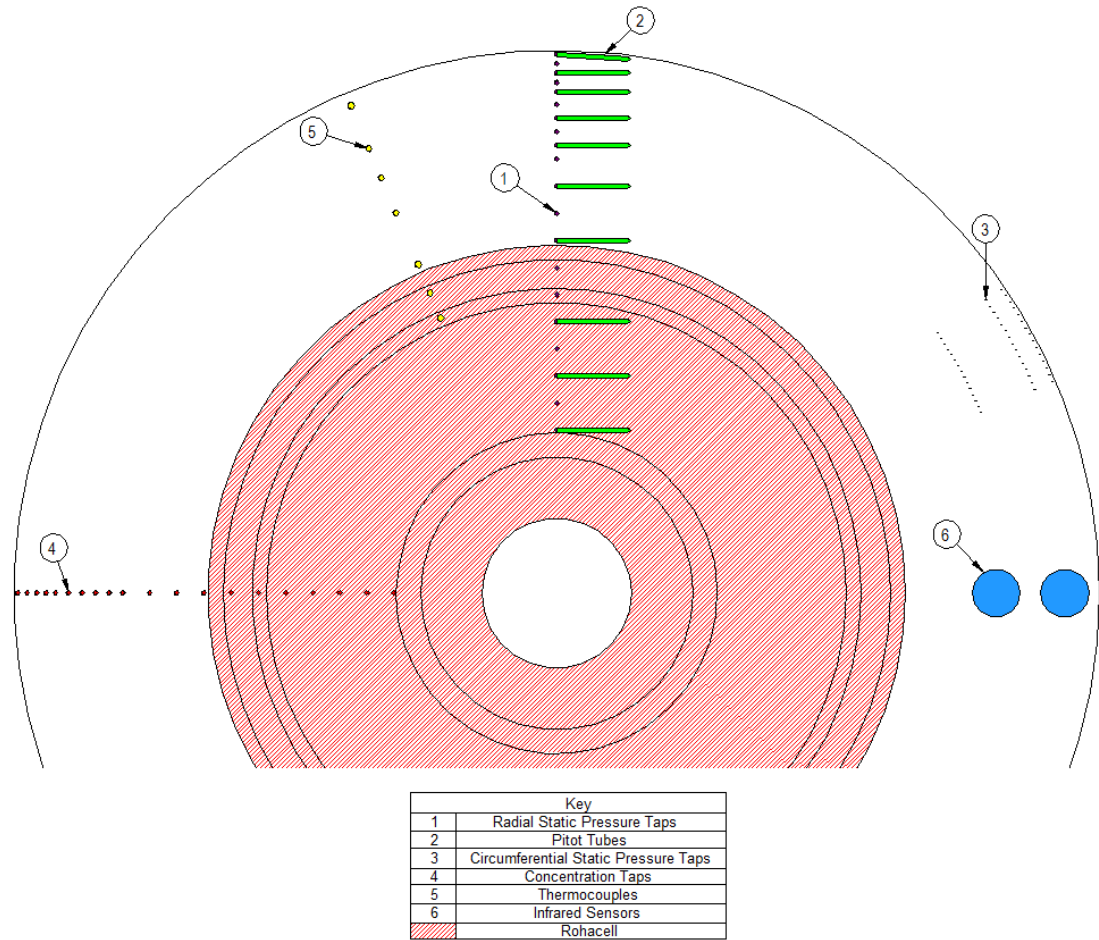
Figure 6.20: Upstream wheel-space instrumentation

r/b	r (mm)
0.993	188.7
0.976	185.4
0.958	182.1
0.941	178.8
0.924	175.5
0.9	171
0.875	166.25
0.85	161.5
0.825	156.75
0.8	152
0.75	142.5
0.7	133
0.65	123.5
0.6	114
0.55	104.5
0.5	95
0.45	85.5
0.4	76
0.35	66.5
0.3	57

Table 6.4: Wheel-space concentration and pressure taps locations

6.5.2 Annulus instrumentation

In order to quantify the driving potential for externally induced ingress to occur, the circumferential variation of pressure in the annulus was measured at ten locations, each averaged over two vane pitches. As highlighted in Figure 6.22, measurements were made at four axial locations on the vane hub, shown in blue at a radius of 195 mm. These corresponded to 2.5 and 3.5 mm downstream of the stator 1 vane trailing edge, and 2.5 and 3.5 mm upstream of the stator 2 vane leading edge. In the outer annulus casing, shown in red for a radius of 220 mm, measurements were made at the same four axial locations, and at an additional two locations in the middle of each rim seal clearance. The magnitude of measured static pressure is expected to be larger at the outer annulus due to the radial gradient of pressure. 15 measurements were made at each location across a single vane pitch (θ), which corresponded to an 11.25° sector. The first and last taps at the edges of the sector were therefore duplicates within the pressure profile, ensuring data was captured for the whole vane pitch.
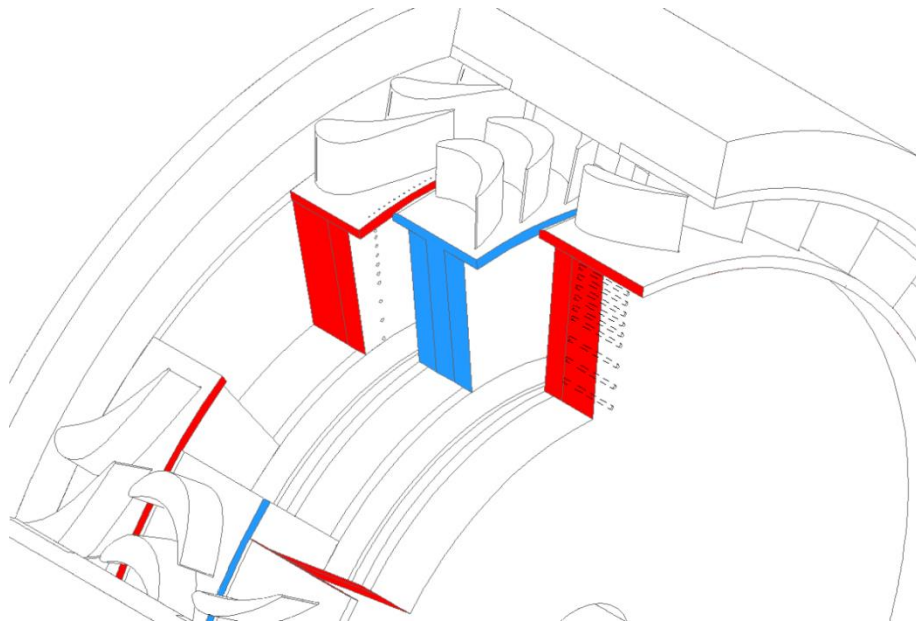
Figure 6.21: Closeup of rig test section showing annulus and wheel-space instrumentation
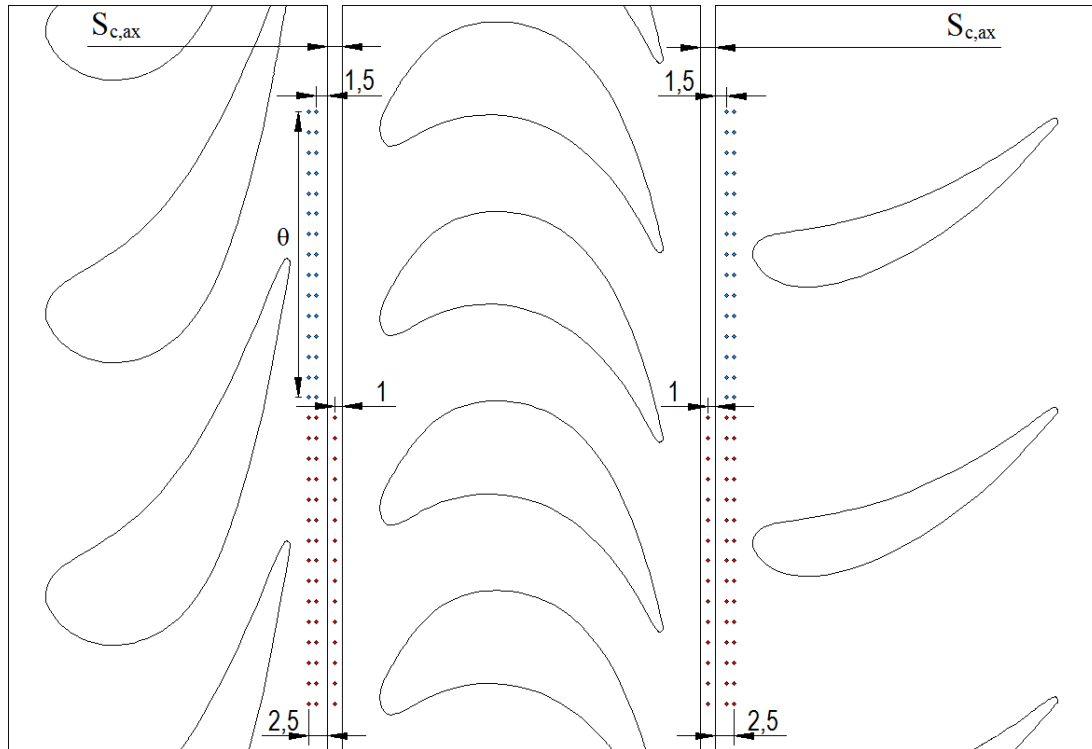
Figure 6.22: Pressure tap locations in the mainstream annulus – blue refers to the vane hub and red to the outer annulus

The additional axial locations should provide greater detail of the axial decay of pressure asymmetry in comparison to the previous 1-stage rig design. If it is assumed that the rate of axial decay in pressure is the same for the two radial positions, the pressures on the vane hub could be extrapolated to the middle of the seal clearance. The multiple axial locations should also give an indication of swirl in the annulus as the maximum and minimum pressure locations should change circumferentially with axial distance.

It is unclear what the static pressure measurements gathered in the region between the blade trailing edge and downstream stator vane leading edge will show. Ingress in the downstream wheel-space is expected to be dominated by the pressure asymmetries caused by the blade and therefore are therefore likely to be unsteady. The tappings in the outer casing downstream from the blade are also likely to be affected by tip leakage.

Figure 6.23 shows how the pressure taps were taken out though the vane platforms and outer annulus casing. The tappings were 0.5 mm in diameter which expanded to the larger size of 1.65 mm to allow hypodermic tubes to be inserted. These were again connected to a calibrated pressure transducer via a Scani-valve.
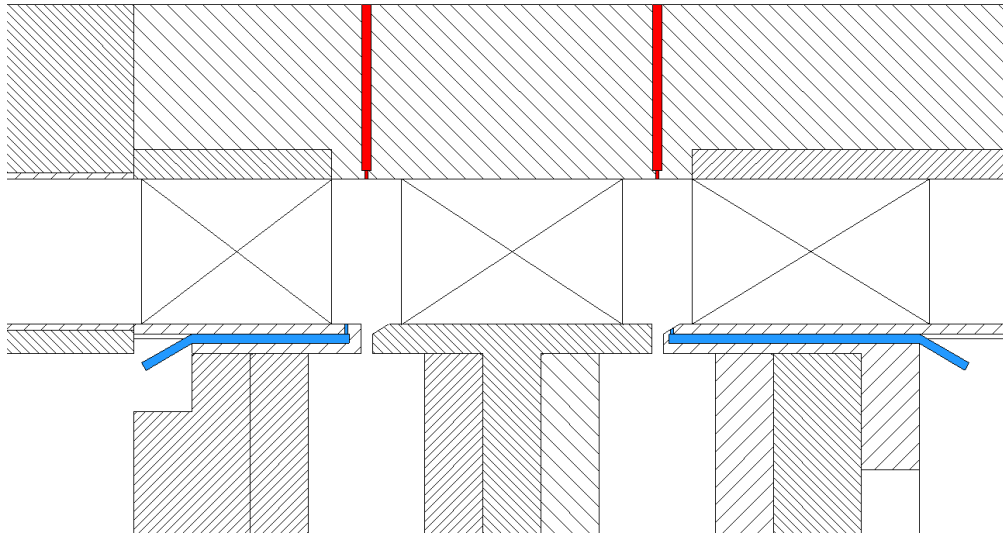
Figure 6.23: Instrumentation taps in mainstream annulus

Figure 6.24 indicates the axial locations where static pressure measurements were made over one vane pitch in the annulus. Each measurement location featured 15 taps and were averaged over two circumferential positions. This equated to 300 pressure tappings in total, distributed around the outer annulus.
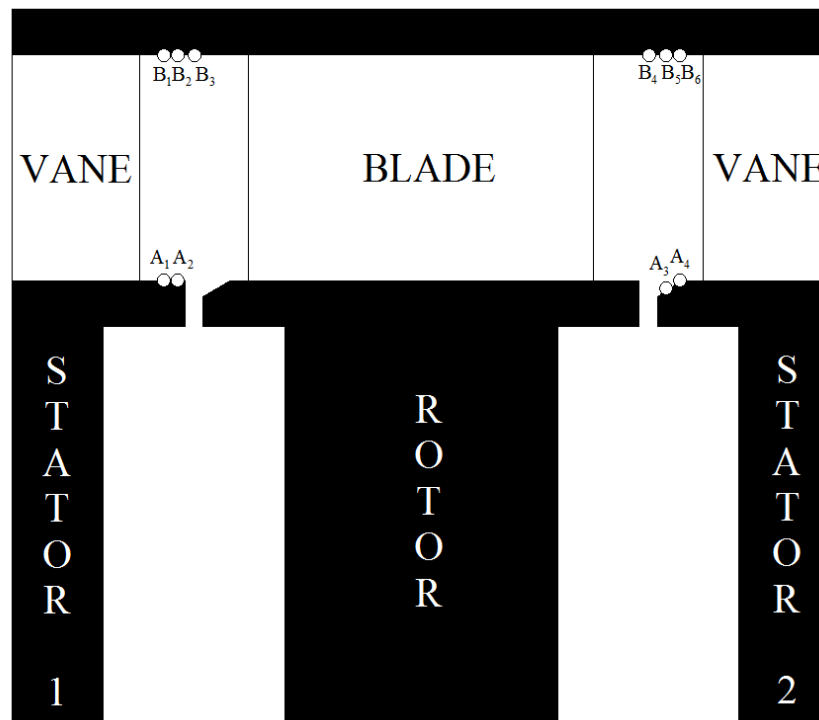
Figure 6.24: Static pressure measurement locations in the mainstream annulus

6.5.3 Additional instrumentation

In order to determine the radial growth and axial deflection of the rotor disc, capacitance based displacement probes were used in the outer annulus and downstream wheel-space. The measurement locations of both are shown in Figure 6.19. The radial probe was used to ensure the tip clearance of 0.5 mm was maintained and only registered measurements when a blade tip passed by the sensor. Axial movement of the rotor could occur under loading from the stage or pressurising the wheel-spaces. The axial displacement probe could also be used to ensure the downstream stator was correctly aligned to the rotor disc. As a safety feature, if either sensor registered a value outside of the nominal operating range a signal was sent from the CADET control system to stop the rig and cut the air supply to the rig.

Mass flow measurements in both the sealing and mainstream flow lines were primarily made by thermal mass flow controllers, supplied by Bronkhorst. These devices were accurate up to ±1% of the full scale range and maintained linearity at the smallest flow rates. The meters used for both sealant lines were coupled with control valves to regulate the flow. This enabled a sealant flow rate to be set within the rig control system, causing the mass flow controllers to iterate within a feedback loop until this desired level was reached.

One additional orifice plate was included in the upstream sealant flow line as a confirmation device, manufactured and calibrated to EN ISO 5167-2:2003. The throat diameter was 25 mm and the inner pipe diameter 50 mm, resulting in a β value of 0.5. Orifice plates were deemed less desirable as the principal mass flow measurement device due to their reduced accuracy, lack of linearity at small sealant flow rates, and susceptibility to offset drift.

6.6 Summary

This chapter details the design of a novel 1.5 stage research facility which will experimentally simulate the fluid dynamics in an upstream and a downstream wheel-space of a gas turbine. The uniqueness of this facility is the ability to operate at conditions more conducive to producing high quality measurements, whilst matching the relevant parameters required for scaling to engine conditions.

Turned rotor blades and representative fillet radii in a larger mainstream annulus will allow for a more engine representative flow-field in the external gas path, especially at off-design conditions. This will enable a more detailed study on the effects of the interaction

between the mainstream and sealant flows on the ingestion process to take place. The provision for leakage flows in both wheel-spaces will allow for an investigation into the fluid dynamic consequences of introducing an addition flow path. The use of a second tracer gas would allow for this flow to be tracked as it interacts with the wheel-space fluid dynamics.

By incorporating a downstream wheel-space into the design, the causes of ingestion into this cavity can be investigated. As this is downstream of the blade, ingress into this wheel-space is expected to be dominated by unsteady pressure effects. The use of fast response, unsteady pressure transducers are likely to be required to fully understand the pressure field in this region. The modular nature of the rig design allows for alterations to incorporate additional instrumentation to easily be made at a future stage. Re-ingestion of sealing flow could also be investigated by seeding the upstream sealant line and making measurements in the downstream wheel-space.

Figure 6.25 shows how the operating capability of the 1.5 stage facility compares with the other research test rigs shown in Figure 2.29. Once again the alternative definition, given by Eq. 2.21, is used in this chart. The figure shows the small increase, in both rotational and axial Reynolds number, gained by the 1.5 stage facility in comparison with the previous single stage rig. It also emphasises that although large investment is required in order to marginally increase these parameters, none of the rigs featured are capable of reaching actual conditions found in real gas turbines.
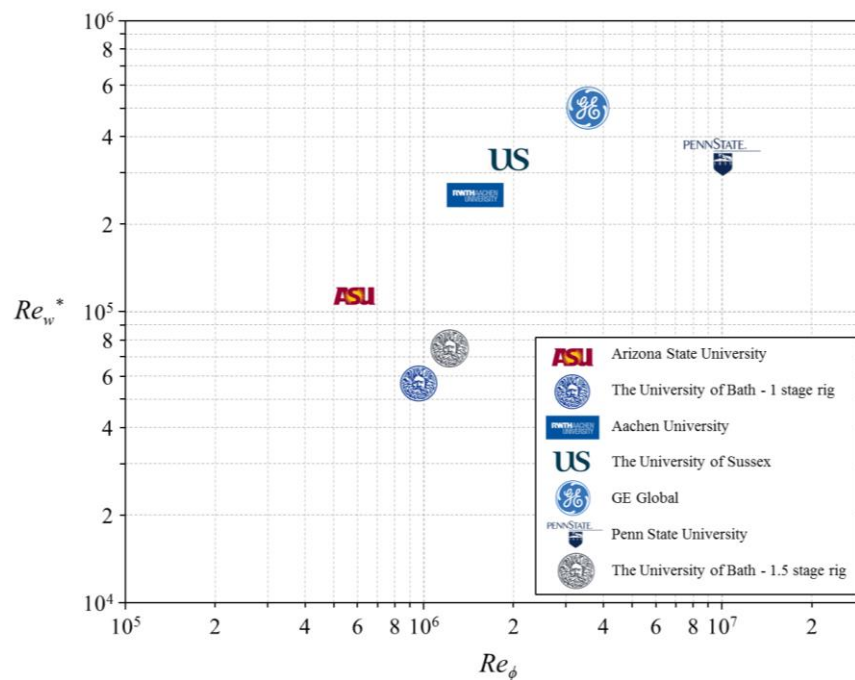

Figure 6.25: Comparison of 1.5 stage rig operating capabilities with other test facilities – alternative definition of Re_w used

Chapter 7: Conclusions

7.1 Design point testing

Measurements of gas concentration, pressure and swirl ratio were made in the wheel-space of the Bath single stage test rig to assess the sealing performance of three rim seal geometries: a datum radial-clearance single seal, a radial-clearance double seal, and a double seal variant featuring a series of radial fins. The data were collected at the design condition for $Re_\phi = 5.32 \times 10^5$, 8.17×10^5 and 9.68×10^5. Although the ingestion through the rim seal is a consequence of an unsteady, three-dimensional flow field, and the cause-effect relationship between pressure and the sealing effectiveness is complex, the experimental data is shown to be successfully calculated by simple effectiveness equations developed from a theoretical orifice model. The variation of ε with Φ_0 was presented for the externally induced and rotationally induced cases, along with radial distributions of ε, swirl ratio and static pressure coefficient at constant sealant flow rates.

The benefit of using a double seal over a single seal design was demonstrated. The ingested fluid was shown to be predominately confined to the outer wheel-space, radially outward of the inner seal. This resulted in protection of the inner wheel-space, where the effectiveness was shown to be significantly higher. Using the statistical model, the ratio of sealing flow rate to prevent ingress for the inner wheel-space of the double radial-clearance seal to that required for the single radial-clearance was found to be approximately 49%.

Further improvements were gained by encouraging swirl within the intermediate annulus through the addition of radial fins. It is conjectured that this increase in swirl reduced the pressure asymmetry, which governs the ingress, and consequently improved the performance of the inner seal. The fins also increased the pressure in the outer wheel-space and reduced ingestion through the outer seal.

The addition of radial fins will have the effect of increasing the windage on the rotor, corresponding to a reduction in stage efficiency of the engine. However, by encouraging swirl at the rim seal periphery, the sealing flow will emerge from the wheel-space with a swirl ratio closer to that of the mainstream flow. This could have the effect of reducing mixing losses in the main annulus, therefore increasing the efficiency of the stage.

For all the seals tested the swirl ratios increased with increasing radius and decreased with increasing sealing flow rate. For a given sealing flow rate, there was little difference

between the radial distribution of swirl ratio for the different seals, despite the large difference in the amount of ingestion. The radial distribution of pressure was shown to be governed by the swirl ratio, and these swirl and pressure distributions were in turn governed by the turbulent flow parameter, λ_T.

7.2 Off-design testing

Experiments were also conducted at off-design conditions, where the flow coefficient was varied over a large range either side of the design condition. Gas concentration measurements were again made to determine the effect on ingress for an axial-clearance seal, a radial-clearance seal and a double radial-clearance seal.

For all the seals, the combined ingress orifice equation was in good agreement with the experimental data for flow coefficient values greater than 0.1. This implied for a large variation of flow conditions, the blade-deviation angle (β-β_0) did not influence the degree of ingress. At lower values of flow coefficient the agreement was less good, owing to a sharp increase in $\Phi_{min}{}'$, believed to be caused by a 'blade effect'. As this increase was observed for all seal geometries tested, boundary layer separation of the flow over the blades was suggested as a possible explanation for the effect.

Time averaged static pressure measurements at two locations in the external annulus showed that the square root of the non-dimensional peak-to-trough pressure difference, $\Delta C_p{}^{1/2}$, was proportional to the flow coefficient, C_F. This variation remained linear even at the smallest values of flow coefficient, where the ingestion measurements showed a departure from the CI theory. However the magnitude of ΔC_p will depend on where in the annulus pressure measurements are made. It is postulated that if measurements were taken at a location closer to the seal clearance, where the pressures controlling the level of ingestion could be evaluated at, the effect of the blade would have been evident.

It should be noted that the results were obtained for incompressible flow conditions in an experimental rig with symmetrical blades, operating over a C_F range much larger than that experienced in engines. For a turbine with turned rotor blades and fillet radii, the 'blade effect' could have an influence on ingestion at flow coefficients within the operational range of a real gas turbine.

7.3 Effectiveness from pressure measurements

The effectiveness measurements determined from gas concentration were then used to establish a new effectiveness based on pressure. A hypothetical location on the vane platform, known as the 'sweet-spot', was assumed to exist where the measured pressures would ensure consistency between the two definitions. A theoretical model was developed to calculate this location, based on the assumption that it would be invariant with sealing flow rate.

Experimental measurements for a radial clearance seal showed that as predicted by the theoretical model, the normalised pressure difference across the seal at this hypothetical location was linearly related to the pressure difference at an arbitrary position (location A) in the annulus of the rig.

The variation of ε_p with sealant flow rate was calculated using two constants determined by linear regression of the experimental data. When compared to the original concentration effectiveness measurements, good agreement was found with the values of effectiveness determined by the theoretical pressure model.

Steady 3D CFD has been used to show the computed location of the sweet-spot was very close to the upstream edge of the seal clearance, and virtually invariant with sealant flow rate. If the pressure asymmetries were able to be measured at this sweet-spot location, any influence of the blade would be expected to have been captured.

It was shown in principle how parameters obtained from measurements of pressure and concentration in a rig could be used to calculate the sealing effectiveness in an engine. Using CFD to compute pressures in the mainstream annulus and wheel-space of a real design, values of discharge coefficients for ingress and egress could be extrapolated to determine the sweet spot location for the engine.

7.4 Design of a new test facility

A requirement was identified for a novel 1.5 stage experimental gas turbine facility, capable of measuring the effects of ingress with turned rotor blades, and within a secondary downstream wheel-space.

Experience gained from conducting experiments in the previous single stage rig factored greatly in design of the new rig. The improvement of the alignment allowing for greater repeatability in the experiments was a key priority for the new facility. The 1.5 stage design featured linear guide rails and a precision lead screw that ensured the rig returned to same position after each reassembly. It is envisaged that a large proportion of time will be saved lining the rig up from these design modifications.

Large consideration was also given to designing the rig with heat transfer experiments in mind. All surfaces downstream of the mesh heaters in both sealant flow lines were either lined with Rohacell, or in the case of the wheel-spaces, had the capability to do so through the interchangeable cover-plates. This ensured minimal heat transfer to metallic surfaces took place during testing.

Turbine stage velocity triangles were used to determine the running conditions of the rig, and ensure the correct flow field was set up in the external annulus for ingestion to take place. This led to a series of calculations governing the flow characteristics at each station, and allowed geometric CAD models to be created providing the dimensions of the rig.

Two design operating points were chosen relating to rotational disc speeds of 3000 and 4000 rpm. The rig featured a 25 mm annulus height, upstream vane with a 77.5° turning angle, turned rotor blades with an engine representative angle of 130°, and a downstream set of vanes with an angle of 34.5°. An eddy current dynamometer was used to absorb the power produced by the stage.

The rig was instrumented with a series of static pressure taps in the annulus, used to determine the driving potential for externally induced ingress to occur. Concentration measurements in the wheel-space using CO_2 tracer gas are used to determine the effectiveness of different rim seal geometries. Additional instrumentation such as total pressure Pitot tubes, infrared sensors, thermocouples and capacitance based displacement probes were also implemented.

The facility will serve as a testing ground for interchangeable generic rim seal designs, aimed at increasing fundamental knowledge, as well as company proprietary seals which will have a direct impact on gas turbine efficiencies. Siemens anticipate that new, improved rim seal designs will improve thermal efficiencies by 0.4%.

7.5 Future work

The next stage of the research programme is to build and commission the new 1.5 stage facility. This will involve cross referencing measurements for consistency with the previous data obtained from the single stage rig as a form of validation. It is envisaged many of the generic seal tests will be repeated, including the axial, radial and double radial-clearance seals, before complicated Siemens proprietary seals are tested, including radially assembled geometries. Similar measurements of gas concentration, pressure and swirl ratio will be made to determine the performance of each design in the new facility.

A distinct lack of data exists in the open literature on hot gas ingestion into a downstream wheel-space. The double cavity design will allow for many combinations of rim seal geometries to be tested. To account for these different combinations, a design of experiments approach is recommended.

Although many researchers have investigated the topic, the influence rotor blades have on the ingestion process is still undetermined. By repeating the off-design measurements in the new facility, the effect of turned rotor blades and fillet radii can be looked at. The true effect of the blades could be isolated by manufacturing a bladeless rotor and repeating the measurements. It is highly likely that unsteady pressure measurements will be required to fully understand the influence of the blade on the ingestion process. The modular rig design is adaptable to accommodate these alterations, should additional instrumentation be required in the future.

By virtue of the double wheel-space design, re-ingestion of sealant flow could be looked at within the new facility. By seeding the upstream sealant line with tracer gas, concentration measurements could be made in the downstream wheel-space to determine the degree of re-ingestion that takes place. The dependence of this effect on the seal geometry of both wheel-space peripheries could also be investigated.

In a real gas turbine, the temperature difference between the flow in the annulus and that in the wheel-space results in a significant density difference between the two flows. This is expected to have a large effect on the ingestion process and is the subject of an ongoing research programme at the University. By using 100% CO_2 gas as the sealant flow and a gas analyser with a 0-100% range, the sealant to mainstream flow density ratio found in an engine (approximately 1.6:1) could be replicated through the difference in density between the two fluids. Momentum or mass flux ratios may prove more useful in correlating these results.

References

Abe, T., Kikuchi, J. and Takeuchi, H., 1979, "An Investigation of Turbine Disk Cooling (Experimental Investigation and Observation of Hot Gas Flow into a Wheel Space)," CIMAG - 13th International Congress on Combustion Engines.

ASME, 2007, "The World's First Industrial Gas Turbine Set at Neuchâtel (1939)," ASME International Historic Mechanical Engineering Landmark, H135.

Balasubramanian, J., Junnarkar, N., Zhou, D.W., Roy, R.P., Kim, Y.W., Moon, H.K., 2011, "Experiments on Aft-Disk Cavity Ingestion in a Model 1.5-Stage Axial-Flow Turbine," ASME Paper GT2011-45895.

Batchelor, G. K., 1951, "Note on the Class of Solutions of the Navier-Stokes Equations Representing Steady Rotationally Symmetric Flow," Quarterly Journal of Applied Mathematics, 4 (1), pp. 29-41.

Bayley, F. J. and Owen, J. M., 1970, "Fluid Dynamics of a Shrouded Disk System with a Radial Outflow of Coolant," ASME J. Eng. Power, 92(3), pp. 335-341.

Bohn, D. E., Johann, E. and Kruger, U., 1995, "Experimental and Numerical Investigations of Aerodynamic Aspects of Hot Gas Ingestion in Rotor-Stator Systems with Superimposed Cooling Mass Flow," ASME Paper 95-GT-143.

Bohn, D. E., Rudzinski, B., Surken, N. and Gartner, W., 1999, "Influence of Rim Seal Geometry on Hot Gas Ingestion into the Upstream Cavity of an Axial Turbine Stage," ASME Paper 99-GT-248.

Bohn, D., Rudzinski, B., Sürken, N. and Gärtner, W., 2000, "Experimental and Numerical Investigation of the Influence of Rotor Blades on Hot Gas Ingestion into the Upstream Cavity of an Axial Turbine Stage," ASME Paper 00-GT-284.

Bohn, D. E., Decker, A., Hongwei, M. and Wolff, M., 2003, "Influence of Sealing Air Mass Flow on the Velocity Distribution in and Inside the Rim Seal of the Upstream Cavity of a 1.5-Stage Turbine," ASME Paper GT2003-38459.

Bohn, D. E. and Wolff, M., 2003, "Improved Formulation to Determine Minimum Sealing Flow - Cw, min – for Different Sealing Configurations," ASME Paper GT2003-38465.

Bohn, D. E., Decker, A., Ohlendorf, N. and Jakoby, R., 2006, "Influence of an Axial and Radial Rim Seal Geometry on Hot Gas Ingestion into the Upstream Cavity of a 1.5-Stage Turbine," ASME Paper GT2006-90453.

Cao, C., Chew, J. W., Millington, P. R. and Hogg, S. I., 2004, "Interaction of Rim Seal and Annulus Flows in an Axial Flow Turbine," J. Eng. Gas Turb. Power 126(4): pp. 786-793.

Chew, J.W., Farthing, P.R., Owen, J.M. and Stratford, B., 1988, "The Use of Fins to Reduce the Pressure Drop in a Rotating Cavity with a Radial Inflow," ASME Paper 88-GT-58.

Chew, J. W., 1991, "A Theoretical Study of Ingress for Shrouded Rotating Disk Systems With Radial Outflow," ASME J. Turbomach. 113(1): pp. 91-97.

Chew, J. W., Dadkhah, S. and Turner, A. B., 1992, "Rim Sealing of Rotor-Stator Wheelspaces in the Absence of External Flow," ASME J. Turbomach., 114(2), pp. 433-438.

Chew, J. W., Green, T. and Turner, A. B., 1994, "Rim Sealing of Rotor-Stator Wheelspaces in the Presence of External Flow," ASME Paper 94-GT-126.

Childs, P. R. N., 2011, *Rotating flow*, Oxford: Butterworth-Heinemann.

Cumpsty, N., 2003, *Jet propulsion*, 2nd ed. Cambridge: Cambridge University Press.

Dadkhah, S., Turner, A. B. and Chew, J. W., 1992, "Performance of Radial Clearance Rim Seals in Upstream and Downstream Rotor-Stator Wheelspaces," ASME J. Turbomach., 114(2), pp. 439-445.

Daily, J. W. and Nece, R. E., 1960, "Chamber Dimension Effects on Induced Flow and Frictional Resistance of Enclosed Rotating Disks," Journal of Basic Engineering, 82(1), pp. 217-230.

Diakunchak, I., Kiesow, H. J. and McQuiggan, G., 2008, "The History of the Siemens Gas Turbine," ASME Paper GT2008-50507.

Eastwood, D., Coren, D.D., Long, C.A., Atkins N.R., Childs, P.R.N., Scanlon, T.J. and Guijarro-Valencia, A., 2012, "Experimental Investigation of Turbine Stator Well Rim Seal, Re-Ingestion and Interstage Seal Flows Using Gas Concentration Techniques and Displacement Measurements," ASME J. Turbomach., 134, pp. 082501.

Gentilhomme, O., Hills, N. J., Turner, A. B., and Chew, J.W., 2002, "Measurement and Analysis of Ingestion through a Rim Seal," ASME J. Turbomach., 125. pp. 505-512.

Gentilhomme, O.J.P, 2004, "Turbine Rim Seal Investigation," University of Sussex, PhD.

Graber, D. J., Daniels, W. A. and Johnson, B. V., 1987, "Disc Pumping Test, Final Report," Air Force Wright Aeronautical Laboratories, Report No. AFWAL-TR-87-2050.

Green, T. and Turner, A. B., 1994, "Ingestion into the Upstream Wheelspace of an Axial Turbine Stage," ASME J. Turbomach., 116(2), pp. 327-332.

Hamabe, K. and Ishida, K., 1992, "Rim Seal Experiments and Analysis of a Rotor-Stator System with Nonaxisymmetric Main Flow," ASME Paper 92-GT-160.

Hills, N.J., Green, T., Turner, A. B., and Chew, J. W., 1997, "Aerodynamics of Turbine Rim-Seal Ingestion," ASME Paper No. 97-GT-268.

Hills, N. J., Chew, J. W., and Turner, A. B., 2002, "Computational and Mathematical Modeling of Turbine Rim Seal Ingestion," ASME J. Turbomach., 124. pp. 306-315.

Hunt, R. J., 2011, "The History of the Industrial Gas Turbine: Part 1- The First Fifty Years 1940-1990," IDGTE Paper 582.

Jakoby, R., Zierer, T., Lindblad, K., Larsson, J., deVito, L., Bohn, D. E., Funcke, J., and Decker, A., 2004, "Numerical Simulation of the Unsteady Flow Field in an Axial Gas Turbine Rim Seal Configuration," ASME Paper No. GT2004-53829.

Johnson, B. V., Mack, G. J., Paolillo, R.E. and Daniels, W.A., 1994, "Turbine Rim Seal Gas Path Flow Ingestion Mechanisms," AIAA Paper 94-2703.

Johnson, B. V., Jakoby, R., Bohn, D. E. and Cunat, D., 2006, "A Method for Estimating the Influence of Time-Dependent Vane and Blade Pressure Fields on Turbine Rim Seal Ingestion," ASME Paper GT2006-90853.

Johnson, B. V., Wang, C. Z. and Roy, R. P., 2008, "A Rim Seal Orifice Model with Two Cd's and Effects of Swirl in Seals," ASME Paper GT2008-50650.

Khilnani, V. I. and Bhavnani, S. H., 2001, "Sealing of Gas Turbine Disk Cavities Operating in the Presence of Mainstream External Flow," Exp. Therm. Fluid. Sci., 25(3-4), pp. 163-173.

Owen, J. M. and Rogers, R. H., 1989, *Flow and heat transfer in rotating-disc systems*, Volume 1: Rotor-stator systems, Taunton: Research Studies Press Ltd.

Owen, J. M., Lock, G. D., Sangan, C. M., Tham ,K. M., Laurello, V.P., and Lee, C. P., 2011, "Finned Seal Assembly for Gas Turbine Engines," USPTO patent application, 2012P08852US.

Owen, J. M., 2011a, "Prediction of Ingestion through Turbine Rim Seals. Part I: Rotationally Induced Ingress," ASME J. Turbomach., 133(3), pp. 031005.

Owen, J. M., 2011b, "Prediction of Ingestion through Turbine Rim Seals. Part II: Externally Induced and Combined Ingress," ASME J. Turbomach., 133(3), pp. 031006.

Owen, J. M., Zhou, K., Pountney, O. J., Wilson, M., and Lock, G. D., 2012a, "Prediction of Ingress through Turbine Rim Seals. Part 1: Externally-Induced Ingress," ASME J. Turbomach., 134, p.031012.

Owen, J. M., Pountney, O. J., and Lock, G. D., 2012, "Prediction of Ingress through Turbine Rim Seals. Part 2: Combined Ingress," ASME J. Turbomach., 134, p.031013.

Palafox, P., Ding, Z., Bailey, J., Vanduser, T., Kirtley, K., Moore, K., and Chupp, R., 2013, "A New 1.5-Stage Turbine Wheelspace Hot Gas Ingestion Rig (HGIR) – Part I: Experimental Test Vehicle, Measurement Capability and Baseline Results," ASME Paper GT2013-96020.

Phadke, U. P. and Owen, J. M., 1983, "An Investigation of Ingress for an Air-Cooled Shrouded Rotating-Disk System with Radial Clearance Seals," ASME J. Eng. Power, 105(1), pp. 178-183.

Phadke, U. P. and Owen, J. M., 1988a, "Aerodynamic Aspects of the Sealing of Gas-Turbine Rotor-Stator Systems. Part 1: The Behavior of Simple Shrouded Rotating Disk Systems in a Quiescent Environment," Int. J. Heat Fluid Flow, 9(2), pp. 98-105.

Phadke, U. P. and Owen, J. M., 1988b, "Aerodynamic Aspects of the Sealing of Gas-Turbine Rotor-Stator Systems. Part 2: The Performance of Seals in a Quasiaxisymmetric External Flow," Int. J. Heat Fluid Flow, 9(2), pp. 106-112.

Phadke, U. P. and Owen, J. M., 1988c, "Aerodynamic Aspects of the Sealing of Gas-Turbine Rotor-Stator Systems. Part 3: The Effect of Nonaxisymmetric External Flow on Seal Performance," Int. J. Heat Fluid Flow, 9(2), pp. 113-117.

Pountney, O. J., Sangan, C. M., Lock, G. D. and Owen, J. M., 2013, "Effect of Ingestion on Temperature of Turbine Discs," ASME J. Turbomach., 135, p. 051010.

Rolls-Royce, 1996, *The jet engine*, 5th ed. Derby: Rolls-Royce plc.

Roy, R.P., Zhou, D.W., Ganesan, S., Wang, C.Z., Paolillo, R.E. and Johnson, B.V., 2007, "The Flow Field and Main Gas Ingestion in a Rotor-Stator Cavity," ASME Paper GT2007-27671.

Sangan, C. M., 2011, "Measurement of Ingress through Gas Turbine Rim Seals," University of Bath, PhD.

Sangan, C. M., Pountney, O. J., Zhou, K., Wilson, M., Owen, J. M., and Lock, G. D., 2013a, "Experimental Measurements of Ingestion through Turbine Rim Seals. Part 1: Externally-Induced Ingress," ASME J. Turbomach., 135, p.021012.

Sangan, C. M., Pountney, O. J., Zhou, K., Wilson, M., Owen, J. M., and Lock, G. D., 2013b, "Experimental Measurements of Ingestion through Turbine Rim Seals. Part 2: Rotationally-Induced Ingress," ASME J. Turbomach., 135, p.021013.

Sangan, C. M., Pountney, O. J., Scobie, J.A., Wilson, M., Owen, J. M., and Lock, G. D., 2013c, "Experimental Measurements of Ingestion through Turbine Rim Seals. Part 3: Single and Double Seals," ASME J. Turbomach., 135, p.051011.

Saravanamuttoo, H. I. H., Rodgers, G. F. C., Cohen, H. and Straznicky, P. V., 2009, *Gas turbine theory*, 7th ed. London: Pearson Prentice Hall.

Scobie, J. A., Sangan, C. M., O. J., Owen, J. M., Wilson, M., and Lock, G. D., 2014, "Experimental Measurements of Hot Gas Ingestion through Turbine Rim Seals at Off-Design Conditions," Proc. IMechE Part A: J. Power and Energy, published OnlineFirst on March 25, 2014.

Stewartson, K., 1953, "On the Flow Between Two Rotating Coaxial Discs," Proceedings of the Cambridge Philosophical Society, 49(1), pp. 333-341.

Teuber, R., Wilson, M., Lock, G. D., Owen, J. M., Li, S., and Maltson, J. D., 2013, "Computational Extrapolation of Turbine Sealing Effectiveness from Test Rig to Engine Conditions," Proc. IMechE Part A: J. Power and Energy, 227, 167-178.

Teuber, R., 2014, "Computation of Rim-Seal Ingestion for Gas Turbines," University of Bath, PhD.

Tropea, C., Yarin, A.L., and Foss, J.F., 2007, *Springer handbook of experimental fluid mechanics*, Heidelberg: Springer.

Wang, C. Z., Johnson, B. V., Mathiyalagan, S. P., Glahn, J. A. and Cloud, D. F., 2012, "Rim Seal Ingestion in a Turbine Stage from 360-Degree Time-Dependent Numerical Solutions," ASME J. Turbomach., 136, p.031007.

White, F. M., 2011, *Fluid mechanics*, 7th ed. McGraw-Hill.

Zhou, D.W., Roy, R.P., Wang, C.-Z., Glahn, J.A., 2011, "Main Gas Ingestion in a Turbine Stage for Three Rim Cavity Configurations," ASME J. Turbomach., 133, p.031023.

Zhou, K., Wood, S. N., and Owen, J. M., 2013a, "Statistical and Theoretical Models of Ingestion through Turbine Rim Seals," ASME J. Turbomach., 135, p.021014.

Zhou, K., Wilson, M., Owen, J. M., and Lock, G. D., 2013b, "Computation of Ingestion through Gas Turbine Rim Seals," Proc. IMechE Part G: J. Aerospace Engineering, 227, 1101-1.